Nano-Bio-Interactions on Intracellular Plasmonics and Mechanobiology of Human Cells

Ahmad Sohrabi Kashani

A Thesis

in the Department

of

Mechanical, Industrial and Aerospace Engineering

Presented in Partial Fulfilment of the Requirement

For the Degree of

Doctor of Philosophy (Mechanical Engineering) at

Concordia University

Montreal, Quebec, Canada

March 2020

CONCORDIA UNIVERSITY

SCHOOL OF GRADUATE STUDIES

This is to certify that the thesis prepared

By: **Ahmad Sohrabi Kashani**

Entitled: **Nano-Bio-Interactions on Intracellular Plasmonics and Mechanobiology of Human Cells**

and submitted in partial fulfilment of the requirement for the degree of

Doctor of Philosophy (Mechanical Engineering)

complies with the regulations of this university and meets the accepted standard with respect to originality and quality.

Signed by the Final Examining Committee:

Dr. Zhibin Ye	Chair
Dr. Krishnan Venkatakrishnan	External Examiner
Dr. Alisa Piekny	External to Program
Dr. Zahangir Kabir	Examiner
Dr. Rama Bhat	Examiner
Dr. Sivakumar Narayanswamy	Examiner
Dr. Muthukumaran Packirisamy	Thesis Supervisor

Approved by

Dr. Ivan Contreras, Graduate Program Director

March 19, 2020

Dr. Amir Asif, Dean
Gina Cody School of Engineering & Computer Science

Abstract

Nano-Bio-Interactions on Intracellular Plasmonics and Mechanobiology of Human Cells

Ahmad Sohrabi Kashani, Ph.D.
Concordia University, 2020

Cancer is a complex disease that originates from various mutations in cells, influencing cellular growth and proliferation. During cancer progression, the biophysical properties of cells, as well as their responses to surrounding mechanical stimuli, are altered. These alterations impact their interactions and communications with their microenvironment and enhance the motility of cancer cells, allowing them to detach from the primary tumor and invade other healthy tissues/organs. Progress in nanotechnology and nanoscience has resulted in the nano-bio-interaction field in which the interaction between nanoparticles and cells are studied to develop innovative nanomedicines to optimize and revolutionize classical methods for cancer treatment and management. While nanomedicines could directly and selectively target cancer cells and deliver anti-cancer reagents to cancer cells, their presence into cells (even without drugs) could cause significant changes in the mechanobiological properties of cells. Although many studies showed that nano-bio-interaction could induce cytoskeletal changes in cancer cells, it is not yet clearly known or understood how these changes could potentially influence cancer progression.

This dissertation focused on how cell-nanoparticle interactions and the resulting mechanobiological change in cancer cells would influence their cellular functions. Here, we utilized three different types of gold particles with different physicochemical properties to study their interactions with both healthy and cancer cells. In the first step of this research, we employed various nanotechnology and microscopic techniques including fluorescent imaging, SEM, Raman spectroscopy, dark-field imaging and hyperspectral imaging to study the behavior of gold nanoparticles in cells in terms of cellular uptake, cytotoxicity, internalization level, and subcellular localization. The findings revealed that all types of particles, sphere-shaped, star-shaped, and Swarna Bhasma, are non-toxic to the cells even with increasing doses and exposure times. Raman

enhancement results highlighted the importance of nano-morphology in mediating changes in the affinity of gold nanoparticles to different chemical structures in cells, which is essential for developing nanomedicines. The hyperspectral technique was then utilized to detect particles in different regions of cells with measuring the intracellular plasmonic responses of nanoparticles. It was found that the regional-dependent plasmonic shifts of gold nanoparticles could be used to estimate the subcellular localization of nanoparticles. Nanospheres showed higher accumulation in cells, and they exhibited a greater plasmonic shift with more sensitivity to their neighboring medium compared to Swarna Bhasma and nanostars.

This dissertation then used Atomic Force Microscopy for mechanobiological measurements and to study their alterations upon incubation with gold nanoparticles. Imaging techniques confirmed morphological and cytoskeletal changes in cancer cells after uptake of gold nanoparticles. Migration assays revealed that nanospheres cause stronger changes than nanostars in the dynamic capability of cancer cells, by significantly slowing down their migration. In support of this, biomechanical measurements showed that internalized gold nanospheres reduce the elasticity of cancer cells by 66% more compared to nanostars. The same trend was also observed in the adhesion levels of treated cells. We observed that nanospheres are mainly distributed in regions where force is generated and translocated for cell migration, and their distribution reasons why their impacts are stronger than nanostars. Furthermore, our simulations showed that the bulk stiffness of cells has contradictory effects on cell deformation and overcoming forces at the cell-substrate interfaces required for cell migration. To approximate the migratory capability of cells, we defined a stiffness-dependent energy term, migratory index, to uniquely capture the effects of both phenomena. Our modeling revealed that there is an optimal stiffness value/range associated with maximal migration, and when bulk stiffness deviates from the optimal range, the rate of migration is predicted to decrease. Our experimental results showed that nanospheres could change the bulk stiffness of cancer cells outside of the optimal range for efficient migration, and we hypothesize that this could suppress their metastatic potential of cancer cells.

Acknowledgments

In the name of God

Over the four and half years of my Ph.D. journey (2015-2020), many people helped me accomplish my dissertation, and definitely, it would not have been possible without them.

First, I would like to express my sincere gratitude to my Ph.D. advisor, Professor Muthukumaran Packirisamy, who trusted me and provided me with this opportunity to achieve one of my life dreams. I very much appreciate his continues support, invaluable guidance, creative advice, ideas, and encouragement during these past four years, without which I could not have completed this dissertation. Second, I am extremely grateful of Dr. Alisa Piekny, from the Biology Department of Concordia University and a member of my Ph.D. dissertation committee, who had a major contribution to this dissertation. I much appreciate her favors, supports, guidance, and discussion, especially in the biological aspects of this research.

Then, I am very thankful to Dr. Simona Badilescu, who always supported and motivated me during this journey. I appreciate her support, advice, and discussion about my experimental work. I should also extend my thanks to my Ph.D. dissertation committee, Dr. Krishnan Venkatakrishnan, Dr. Rama Bhat (Mechanical Engineering), Dr. Sivakumar Narayanswamy (Mechanical Engineering), and Dr. Zahangir Kabir (Electrical Engineering) for accepting this role, putting their precious time, and providing helpful insight in my research. I also would like to acknowledge the financial support from the Quebec government (FRQNT) and Concordia University faculty engineering during my Ph.D. program.

I have to thank my lab-mate Kiran Kuruvinashetti, Daniel Beaudet (from Alisa Piekny's lab), and Dilan Jaunky (from Alisa Piekny's lab) for their collaboration, idea, support, and discussion in the study presented in Chapter 3. I also express my gratitude to Kevin Larocque (from Alisa Piekny's lab) for his supports/helps for the biological experiments in the studies presented in Chapters 5 and 9. Special thanks to the administrative staff at the MIAE department of Concordia University, Leslie Hossein, Arlen Zimmerman, Sophie Merineau, and Maureen Thuringer. I also would like to thank Dr. Chris Law (Concordia University) in the "Centre for Microscopy and Cellular Imaging" for his training, technical supports and helps on microscopic images, Mr. Mazen Samara (Concordia University) for his assistance with SEM imaging, Ms. Moraille Patricia

(University of Montreal) for her assistance with AFM measurement, Mr. Gwenaël Chamoulaud (UQAM University) for his training on Raman spectroscopy, and Ms. Hoda Yasini for her help with schematic drawings and editing figures. I also thank Jaya Indian Medicine Pharmaceutical Pvt. Ltd., Maduravoyal, Chennai, Tamilnadu, India for providing information on Swarna Bhasma.

It has been my pleasure to be a member of the "Optical Bio-Microsystem lab", and I am very thankful to my wonderful lab-mates with whom I shared lots of moments and discussions, and without their help, I could not pave this hard way. Thank you, Dr. Pierre, Dr. Jalal, Dr. Mostapha, Durai, Kiran, Srinivas, Ehsan, Naghmeh, Shervin, Vahid, Mohammad Reza, Mehdi, and Mahdi.

My deepest heartfelt gratitude goes out to my beloved and beautiful wife, Hoda, for her unconditional love, support, and patience throughout this entire process. She stood by my side during this journey as a best friend and made countless sacrifices to help me get this point. She has been extremely supportive of me and was always happier than me for every single success. Words simply cannot express my gratitude to my parents, Hossein and Fatemeh, for their invaluable love and endless support. I inherently gained a strong faith from them. I wish them a long healthy, and happy life. I also have to thank my siblings, Maryam, Mostafa, and my brother in law, Amir, who have always provided me through moral and emotional support in my life. They made a great devotion by covering my responsibilities during my absence at home. I am also extremely grateful to my parents in law, Kamal and Homa, for their unfailing support, prayers, and kindness.

Finally, I would like to thank one of my best friends, Dr. Mohammad Mastiani (Arizona State University), who supported and helped me pursue my education at the PhD level before I moved to Montreal. Mohammad, I never forget your favors.

To: my wife, ***Hoda,***

and my parents, ***Hossein*** *and* ***Fatemeh***

Contribution of Authors

Chapter 3

This chapter is based on the two following published papers, and I included sections/parts to which I contributed.

- **Ahmad Sohrabi Kashani**, Kiran Kuruvinashetti, Daniel Beaudet, Simona Badilescu, Alisa Piekny, and Muthukumaran Packirisamy. "Enhanced Internalization of Indian Ayurvedic Swarna Bhasma (Gold Nanopowder) for Effective Interaction with Human Cells." Journal of nanoscience and nanotechnology 18, no. 10 (2018): 6791-6798. 2).
- Daniel Beaudet, Simona Badilescu, Kiran Kuruvinashetti, **Ahmad Sohrabi Kashani**, Dilan Jaunky, Sylvie Ouellette, Alisa Piekny, and Muthukumaran Packirisamy. "Comparative study on cellular entry of incinerated ancient gold particles (Swarna Bhasma) and chemically synthesized gold particles." Scientific Reports 7, no. 1 (2017): 10678.

Contributions of co-authors: Dr. Muthukumaran Packirisamy (Professor), Dr. Alisa Piekny (Associate Professor), and Dr. Simona Badilescu (Research Associate) supervised the works. Daniel Beaudet and Dilan Jaunky trained me and helped with biological experiments (Nuclear assays presented in **Section 3.3.5, Figure 3-11,** and **Figure 3-12**). Kiran Kuruvinashetti helped with cell culture and characterization of nanoparticles.

Chapter 9

This chapter is based on the two following submitted papers.

- **Ahmad Sohrabi Kashani**, Kevin Larocque, Alisa Piekny and Muthukumaran Packirisamy, “Regulation of Migratory Capabilities of Human Lung Cancer Cells through Nano-Bio-Interaction”

Contributions of co-authors: Dr. Muthukumaran Packirisamy (Professor), Dr. Alisa Piekny (Associate Professor), supervised the work. Kevin Larocque helped with scratch assay (imaging and analyzing its data) presented in **9.3.5,** and **Figure 9-10 b and c.**

Table of Contents

List of Figures

List of Tables

Nomenclature

3D	Three Dimensional
a.u.	Arbitrary Unit
AFM	Atomic Force Microscopy
AgNPs	Silver Nanoparticles
ATP	Adenosine Triphosphate
AuNPs	Gold Nanoparticles
CAD	Computer Aided Design
CCD	Charged Coupled Device
CP	Contractile Pressure
DIC	Differential Interference Contrast
DK	Dark-Field
DLS	Dynamic Light Scattering
DMEM	Dulbecco's Modified Eagle's Medium
DNA	Deoxyribonucleic Acid
ECM	Extracellular Matrix
EDS	Energy Dispersive Spectroscopy
ELS	Electrophoretic Light Scattering
EMT	Epithelial-Mesenchymal Transition
EPR	Enhanced Permeability And Retention Effects
EQS	Equivalent Elastic Strain
FBS	Fetal Bovine Serum
FEM	Finite Element Method
FSI	Fluid Structure Interaction
F-SPL	Filtered Spectral Library
FTIR	Fourier-Transform Infrared spectroscopy
HSI	Hyperspectral Images
ICP-MS	Inductively-Coupled Plasma Mass Spectroscopy
IF	Immunofluorescence Imaging

LSPR	Localized Surface Plasmon Resonance
MB	Mechanobiological Properties
MEMS	Micro-Electro-Mechanical System
MP	Micropipette
MT	Microtubules
MTC	Magnetic Twisting Cytometry
NBI	Nano Bio Interaction
NP	Nanoparticles
NR	Nanorods
NTA	Nanoparticles Tracking Analysis
OP	Optical Tweezer
PDMS	Polydimethylsiloxane
PTFE	Polytetrafluoroethylene
ROI	Region of Interest
RS	Raman Spectroscopy
SAM	Spectral Angle Mapper
SB	Swarna Bhasma
SEM	Scanning Electron Microscopy
SERS	Surface Enhanced Raman Spectroscopy
SPL	Spectral Library
SU8	Negative Photo Resist
TCA	Trichloroacetic Acid
TEM	Transmitted Electron Microscopy
TIRF	Total Internal Reflection Fluorescence
UV	Ultraviolet
VIR	Visible Infrared
XRD	X-Ray Diffraction

List of Symbols

$\overline{\varepsilon^*}$	Average equivalent elastic strain
$\overline{\lambda_\iota}$	Deviatoric principal stretches
$\overline{\sigma^*}$	Average Von Mises stress
Q_f	Quality factor
δ_{ij}	Kronecker delta
ε^*	Equivalent elastic strain
ε_d	Dielectric constant
μ_o	Initial shear moduli
σ^*	Von Mises stress
σ_{ij}	Stress
$\Delta\lambda_{max}$	Maximum plasmonic shift
ΔP	Pressure difference
Δn	Refractive index changes
A	Area
A_e	Effective area
A_p	Projected area of particles
C_D	Drag coefficient
D	Diffusion coefficient
d*	Relative AFM cantilever deflection
d_0	Initial deflection of AFM cantilever
d_d	Thickness of the dielectric
d_a	Thickness of the analyte
d_h	Hydrodynamic diameter
d_p	Diameter of particles
E	Elasticity

Ec	Elasticity of cancer cells
E_{cyto}	Cytoplasm Elasticity
En	Elasticity of normal cells
f	Henry's function
F	External force
F_D	Buoyancy force
F_e	External force
F^T	Total fluid loading
I	Raman intensity
I_p	Specific polar momentum of inertia
k	Stiffness
k_b	Boltzmann constant
k_o	Initial bulk moduli
L	Length
l_d	Electromagnetic-field-decay
L_{eq}	Equivalent length
m	Refractive index of the particles
m_p	Mass pa particle
n	Normal unit vector
η	Viscosity
P	Pressure
Q	Flow rate
R	Hydrodynamic resistance
r	Rigidity index
Re_p	Particles Reynolds number
t	time
T_e	Trapping efficiency
u	Velocity field

U	Energy
U_e	Electrophoresis mobility
u_p	Velocity of particles
u_r	Relative particle velocity
v	Mean velocity
w	Full width at half of maximum
X_a	Non-adherent proportion of cells
z	Vertical Position of AFM sensor
z*	Relative vertical position of AFM cantilever
z_o	Initial contact point
δ	Indention (AFM)
ε_{ij}	Strain
λ	LSPR band
μ	Migratory index
ρ	Density
ν	Poisson's ratio
ζ	Zeta potential
σ	Stress
φ	Opening angle of sharp cone of AFM

Chapter 1
Literature Review and Scope

This chapter, as a review paper, will be submitted to the "*SN Applied Science* Journal."

1.1. Introduction to Cancer-Nano-Interactions

Our bodies continuously produce abnormal cells, and in cancer, there is no control on proliferation of these cells[1]. Cancer is one of the leading causes of death in the world. According to the recent report by "International Agency for Research on Cancer" in 2018, 9.6 million people estimated to die due to cancer in 2018[2]. In Canada, cancer is the main reason of death. Based on the "Canadian Cancer Statistic" in 2019, half of Canadians are expected to get cancer in their lifetime, and half of them will die. Lung cancer is responsible for more cancer death among Canadians compared to breast, colorectal, and prostate cancers. Early cancer detection and effective treatment enhance the possibility of cancer management; however, when cancer becomes metastasis, the survival rate is dramatically reduced. Metastasis is the main cause (90%) of cancer-related mortality[3](**Figure 1-1a**). Over the past decades, intensive efforts have been made to develop new and effective methods for treatment of cancer. The classical techniques for cancer treatment are based on surgery, radiation, and chemotherapy. There are some significant limitations in using these traditional methods. Surgery and radiotherapy are effective methods for non-metastasis cancer, but they are not useful when cancer spreads throughout the body[1]. In surgery also, the eradication of cancer tumor cannot be performed entirely, and it might damage the healthy organs. In chemotherapy, which is a widely used technique in cancer treatment, the drugs are administrated to the whole body, trying to suppress tumor growth and control cancer progression ineffectively. Due to the non-specifically distribution of drugs, this technique induces severe toxic side effects within the body as both healthy and cancerous cells are treated[4][5]. Therefore, developing novel therapeutic approaches to overcome the drawbacks of conventional therapy is one of the important challenges in the treatment of cancer.

In recent years, with progressing nanotechnology techniques, the concept of targeted therapy has received considerable attention to design medicine and drug-delivery systems. In the targeted therapy, nanoparticles with specific properties, nanomedicine, are designed to specifically transport therapeutic agents to tumor sites. These strategies can significantly improve cancer treatment outcomes by distinguishing malignant cells from non-malignant cells and selectively kill

malignant cells[6]. With the aid of NPs-based drug delivery systems, the amount of the drug needed to effectively treat the cells can be significantly reduced while the concentration of drugs on the tumor sites is increased without inducing side effects to the patient compared to the classical methods. With the NP-based drug delivery system, the anti-cancer drugs at the injury sites can be released under controlled conditions, which protects the therapeutic agents, and reduces toxicity to healthy cells[7]. Two main processes are used for specific targeting and to differentiate cancer cells from normal cells (**Figure 1-1b**): active and passive targeting. In the active targeting, NPs are driven to the target site by conjugating the NPs surface with specific ligands for molecular recognition of antigens on the surface of cells, which are expressed during cancer[8]. Once conjugated NPs reach to target sites, drugs are released under controllable conditions. Passive targeting takes advantage of physical changes at the tumor vasculatures, making them relatively leaky compared to the structure of the normal vasculature. During this process, the endothelium of blood vessels becomes more permeable than in the healthy state[9]. Due to this phenomenon, enhanced permeability and retention effects (EPR), the concentration of NPs may be increased in the target site [6]. In order to control and predict drug release from nanocarriers, different stimuli such as temperature, redox potential, pH, enzymatic activity, and others can be used to induce changes in physiological environment of NPs.

Nanoparticles are generally smaller than 100 nm (at least in one dimension) and are used as carriers to transport drugs to the place of cancer. The outstanding and tuneable properties of NPs have made them a good candidate for biomedical applications, particularly for cancer therapies. A wide range of NPs, such as metal-based NPs, liposomes, quantum dots, peptide, carbon nanotube, and nano-diamonds, can be used for therapeutic application[7]. Bio-distribution, biocompatibility, biodegradability, and systemic clearance are the general challenges of using NPs and targeted therapy[10]. Drugs can be integrated to NPs or can be attached to the surface of particles. An effective NP-based drug delivery system should be able to predict and control the fate of NPs in a biological environment[11]. In order to develop a rational nanosystem and achieve an efficient drug delivery system, we need to enhance our understanding of the dynamic interactions between NPs and complex heterogeneous biological environments [12]. At the cellular level, the nano-bio-interaction (NBI) occurs at the interface of NPs' surface and cell membranes. The interaction behavior of NPs is highly dependent on the physical and chemical properties of NPs. Therefore, it is essential to enhance our understanding of NBI to design efficient and safe NPs by tuning the

physicochemical properties of NPs and control cellular uptake and targeting[13]. NPs surface in contact with biological fluids such as blood and cell-culture media absorbs biomolecules including proteins, known as protein corona, and might alter the designed function of NPs in cells [13], [14].

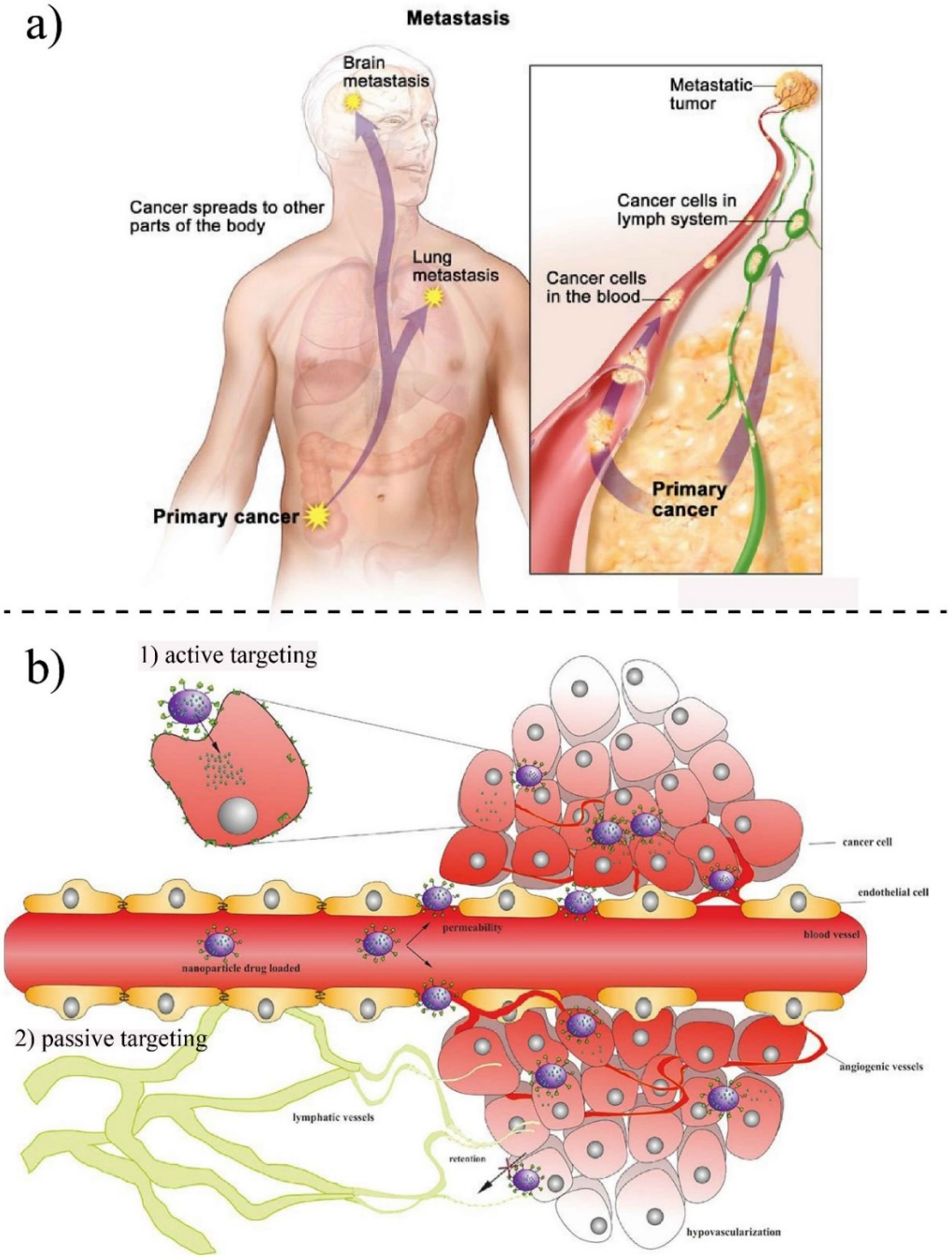

***Figure 1-1**. **a)** Metastasis process during cancer progression (© (2020) Terese Winslow LLC, U.S. Govt. has certain rights), **b)** two possible methods for targeting tumors; 1) active targeting using recognizing ligands, 2) passive targeting using EPR*[15]

Furthermore, NPs before reaching the target cells must interact with the tumor microenvironment, and exposing to this environment might change the properties of NPs, and consequently, affect their interactions with cells. The cellular uptake of NPs can be achieved through the endocytosis mechanism, an energy-dependent process. In this process, NPs are engulfed in the membrane of cells to form endocytic vesicle swimming within cells to reach out to the specific intracellular compartments and then exclude out of the cells. However, in some cases, the NPs might get out of the endosomes, and enter into the cell cytoplasm. By bypassing the lysosomal degradation, NPs have a chance to enter other organelles and directly interact with intracellular compartments[13][16][17]. There are five different endocytosis mechanisms: phagocytosis[1], pinocytosis[2], Clathrin[3]-mediated and Caveolae[4]-mediated endocytosis, and Clathrin/Caveolae independent endocytosis. Intracellular trafficking is a complex process through which NP-loaded vesicles are shuttled along cytoskeletal structures within cells to reach their intracellular destinations and plays a critical role in the fate of NPs and their therapeutic efficacy/toxicity[18]. The physicochemical properties of NPs, such as size, composition, shape, surface charge, and surface functionalization, influence the endocytosis process and intracellular trafficking[13].

In the nano-bio-interactions field (**Figure 1-2**), researchers mostly have focused on the effects of NPs' physicochemical properties on NPs cellular uptake, NPs cytotoxicity, and NPs intracellular fate. However, in the nano-bio-interaction field, less attention has been paid to NPs' effects on cell mechanics and biological functions. Cellular uptake of NPs and their interactions with intracellular compartments can affect the cytoskeletal structures, and consequently, the cell mechanic. Cellular functions such as migration, differentiation, and wound healing are influenced by the mechanical properties of cells. Therefore, it is worthwhile to investigate how intracellular NPs affect mechanobiological properties and cellular functions. In order to cover both the above-

[1] Phagocytosis is the process by which a cell uses its plasma membrane to engulf a large particle, giving rise to an internal compartment called the phagosome.

[2] In cellular biology, pinocytosis, otherwise known as fluid endocytosis and bulk-phase pinocytosis, is a mode of endocytosis in which small particles suspended in extracellular fluid are brought into the cell through an invagination of the cell membrane, resulting in a suspension of the particles within a small vesicle inside the cell.

[3] Clathrin is a protein that plays a major role in the formation of coated vesicles.

[4] In biology, Caveolae, which are a special type of lipid raft, are small invaginations of the plasma membrane in many vertebrate cell types, especially in endothelial cells, adipocytes and embryonic notochord cells.

mentioned aspects of nano-bio-interactions, the following background review section is divided into two major parts. In the first part, the effects of important NPs physicochemical properties on nano-bio-interaction are reviewed, and in the second part, the interactions between nanomaterials and cells are discussed in the context of cell mechanics.

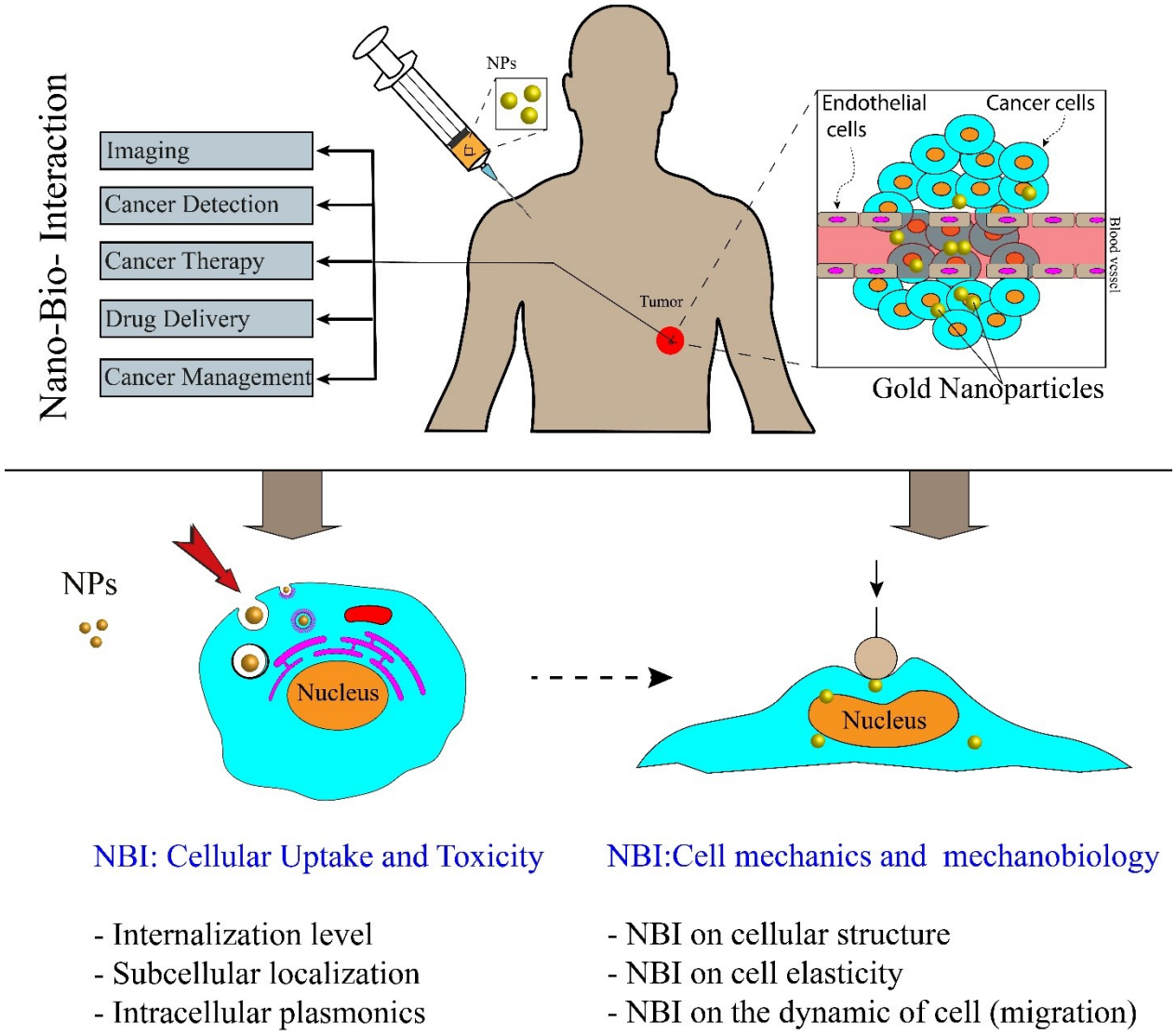

***Figure 1-2**. Nan-bio-interaction from two different perspectives; 1) study the cellular uptake and toxicity, and intracellular plasmonics, 2) study the mechanics and mechanobiology of cells after cellular uptake of NPs*

1.1.1. Nano-Bio-Interaction: Cellular Uptake and Toxicity

To design nanomedicines for cancer therapy, we need to efficiently deliver NPs to tumor sites in the body with cellular and oftentimes subcellular precision. In order to provide an effective NP-based drug delivery system, it is critical to have full control over NPs cellular uptake, NPs

internalization level, NPs localizations, and NPs distributions within cells. Nano-bio-interaction is a complex, dynamic, and multi-parametric phenomenon [18]. Before engineering NPs for therapeutic application, we need to enhance our fundamental understanding of how NPs' physicochemical properties affect their interactions with biological systems. Before testing NPs *in vivo* at tissue or organs, we have to evaluate them *in vitro* at the cellular level. Biocompatibility and toxicity are two important parameters that are used to assess NPs for therapeutic purposes. Biocompatibility shows the ability of NPs to provide the designed and desired functions in terms of cancer therapy without inducing undesirable local and systematic effects in the recipient. In the same context, the toxicity is defined as the ability of NPs to adversely affect the normal physiology of cells and directly disrupt the structure of cells or tissue[19]–[21]. Several investigations have shown that the properties of NPs also influence biocompatibility and toxicity. Apart from physicochemical properties of NPs, other factors or conditions such as cell lines[22], cell size[23], cell sex[24], incubation time[25], NPs concentration[25], protein absorption[26], and evaluating methods might affect the biocompatibility and toxicity of NPs[27]. In the following parts, the effects of NPs properties on the quality of the nano-bio-interaction in terms of cellular uptake, internalization, toxicity potential, and biocompatibility are discussed with a focus on gold nanoparticles.

1.1.1.1. Effects of NPs Size

The cellular uptake of nanoparticles strongly depends on the nanoparticle size. With the aid of the endocytosis process, cells are able to uptake biomolecules, and due to a similar size of NPs, they can enter into cells through the same mechanism. As earlier mentioned, NPs can be taken up by cells, either with binding to cell surface receptors such as Clathrin or Caveolae or by other mechanisms like pinocytosis and phagocytosis[13][28](**Figure 1-3**). It has been shown that each type of particle may prefer a different pathway for its cellular internalization. Regarding the different endocytic mechanisms, there are specific dynamic and size rules of entering[25][26]. Larger solid particles generally can enter cells through phagocytosis with good efficiency. This process might take thirty minutes to several hours with respect to cell type and NPs properties. Nanoparticles with a size of 200-1500 nm in diameter can be taken up by phagocytosis[13]. Smaller particles (less than 120 nm) can enter cells through receptor-mediated endocytosis. This process takes places in the area of plasma membrane which is rich in Clathrin and Caveolae proteins[13]. The ability of nanoparticles to enter the cells may be increased by reducing their sizes. However,

smaller nanoparticles due to their low binding tendency to receptors, have less chance to be engulfed by the membrane, so they need to form clusters on the cell membrane[30]. It has been observed that gold NPs with a size of 50 nm can enter mammalian cells with high efficiency while they have a fast wrapping up.

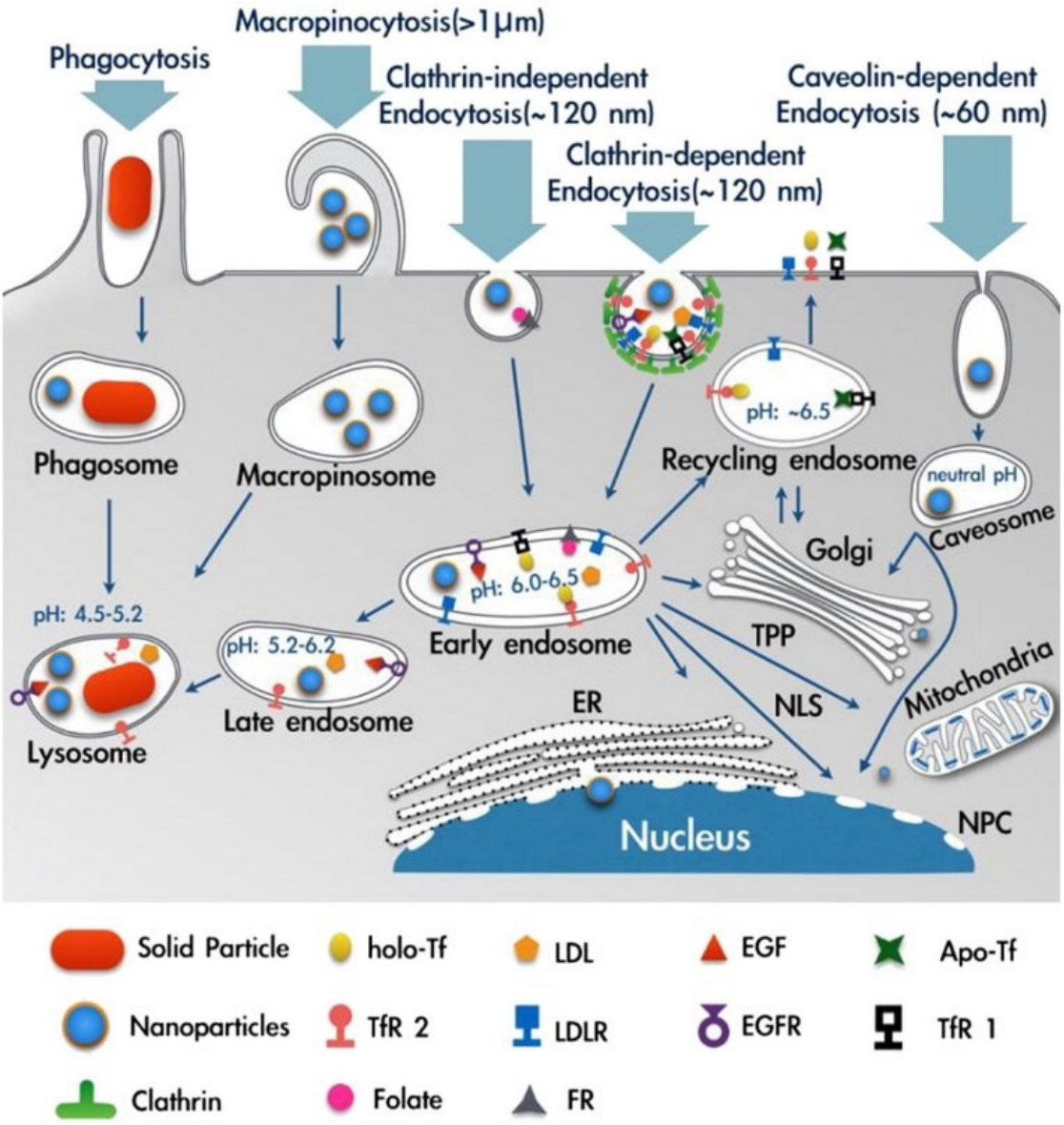

Figure 1-3. *Different endocytosis mechanisms by which NPs could enter cells through passing the membrane*[31]

Several investigations have shown that 50 nm is the optimal size for cellular uptake of gold NPs[32][33]. *Wk et al.* [34] reported that spherical nanoparticles having a size of 30~50 nm have higher internalization efficiency to human adipose-derived stem cells (ADSCs), compared to NPs

of 15, 75 and 100 nm. NPs aggregation also might affect quantitatively cellular uptake. *Albanese et al.* [35] showed that the average uptake of gold NPs is reduced by 25% compared to non-aggregated NPs. Moreover, as the size of NPs plays a significant role in the endocytosis efficiency of nanoparticles, the cytotoxicity of gold NPs may be influenced by particle size. Some studies have shown that gold NPs with smaller size are more toxic to the cells compared to larger NPs. Smaller nanoparticles have a higher surface area to volume, enabling them to interact more effectively with cellular and subcellular compartments. On the other hand, smaller particles have a better chance to penetrate intracellular locations such as mitochondria and nucleus, making them more toxic [31][32]. *Pan et al.* [38]investigated the toxicity of gold NPs with different range (0.8~15 nm) in HeLa and L929 cell lines. Their finding revealed that gold NPs with 1.4 nm induce the highest cellular toxicity.

1.1.1.2. Effects of NPs Shape

In addition to the size of nanoparticles, their morphologies may influence NPs internalization ability and NPs toxicity potential. Due to their shape, NPs may interact differently with cellular and subcellular compartments of cells. Spherical NPs have shown more effective internalization, compared to their non-spherical counterparts[39]. While nanospheres are good candidates for drug delivery, anisotropic nanostructure could provide better efficiency due to their higher ratio of surface area to volume, and they can carry more drug concentration to the desired sites[10]. NPs with different shapes exhibit different abilities to enter cells because of the different contact areas with the cell membrane. For example, nanorods exhibit lower internalization ability compared to spherical particles and they need a longer time for endocytosis. However, by reducing the aspect ratio of nanorods (length to width of particles), their cellular uptake can be significantly enhanced. The findings of *Chithrani et al.* [40] revealed that sphere-shaped gold NPs with a size of 14 nm and 74 nm are taken up 5 and 3.75 times more than 74 ×14 (nm) rod-shaped gold NPs, respectively by human breast cancer cells (MCF-7). *Xueping Xie et al.* [41] studied the effects of various shapes of gold NPs on their internalization ability. They considered nanostars, nanorods and, triangle-shaped nanogolds with similar sizes coated with mPEG (methoxy polyethylene glycol) to investigate their internalization level to mouse leukemic monocyte macrophage. They found that the triangle-shaped particles tend to enter the cells with higher efficiency, compared to other shapes, and gold nanostars displayed the lowest ability. Furthermore, they observed that each particle may tend to penetrate the cell membrane through a different endocytosis process, showing

that NPs depending on their geometry may be used for different intracellular fate. In another work, *Herd et al.*[42] suggested that spherical NPs prefer to penetrate cells through Clathrin-mediated endocytosis, while worm-like NPs undergo phagocytosis.

1.1.1.3. Effects of NPs Surface Charge and Coating

NPs surface charge affects the electrostatic interactions between cell membranes and NPs. It has been shown that both sides of a bilayer phospholipid membrane of cells are negatively charged, and it has a hydrophobic surface[29][43]. Theoretically, it has been studied the importance of surface charge on the interactions of NPs and cell membranes. It was shown that cationic charged NPs have better thermo-dynamical interaction with phospholipid membranes[44]. In contrast to anionic and natural NPs, the positively charged NPs adhere readily to the cell membrane and enhance the membrane-engulfing process[13][29]. Negatively charged NPs induce local disorders in their local contact with cell membranes, making their interaction unfavorable. In work performed by *Cho et al.* [45], the uptake of cationic gold NPs was found to be fivefold higher than anionic counterparts. Their findings revealed that gold NPs could even directly diffuse to cells through generating holes in the cell membrane, whereas negatively charged and neutral gold NPs are internalized only through endocytosis. In another study, *Arvizo et al.* [46] reported that cationic gold NPs depolarize the cell membrane (the permeabilization potential of cell membrane) and increase the concentration of Ca^{2+} within cells. The depolarization might reduce the proliferation and viability of normal cells by changing the intracellular pathways. The uptake of very negative and very positive gold nanorods was studied into HeLa cells by *Hauck et al.* [47] at different concentrations. They showed that maximum and minimum uptake take place for positive and negative, respectively. *Jiang et al.* [48] demonstrated that surface charge might modulate NPs size-dependent uptake into cells. They observed that with anionic gold NPs, cellular uptake is decreased as their size is increased whereas, for cationic gold NPs, the level of internalization is enhanced by reducing their sizes.

Understanding the role of surface coating on the internalization ability and the intracellular pathways is also needed to design efficient nanomedicine. It has been shown that the surface functionalization significantly influences the intracellular pathways, so with the aid of engineering the surface coating, we can dictate NPs to interact differently with biological systems. In order to control the NPs delivery to a specific site for therapeutic purposes, the surface of the NPs is functionalized with biomolecules such as peptide ligands, antibodies, or various chemical

groups[48][49]. These ligands can guide NPs to the intended sites by recognizing specific receptors on the surface of cells, and NPs can then be taken up via receptor-mediated endocytosis. In addition, the surface coating can be used to improve the stability and biocompatibility of NPs. The findings of *Bartczak et al.* [50] showed that with the diacetylene-containing ligand, the stability of gold NPs could be remarkability increased under different pH and temperatures. *Chompoosor et al.* [51] studied the effects of the surface functionality of gold NPs on their cytotoxicity. Their results revealed that the toxicity of NPs in HeLa cells depends on the hydrophobicity, and by increasing the hydrophobicity of particles, the cytotoxicity is increased.

1.1.2. Nano-Bio-Interactions: Cell Mechanics and Mechanobiology

As earlier mentioned, NBI behaviors can be evaluated from the mechanics point of view. The presence of NPs within cells might directly or indirectly impact the function of cells, and their effects can be reflected in the mechanics or mechanobiology of cells. Mechanobiology is an emerging multidisciplinary field at the crossroads of biology, bioengineering, and biophysics. Mechanobiology describes how cell mechanics and mechanical forces influence cell behavior, cell morphogenesis, and disease like cancer[52][53]. The mechanotransduction by which cells can sense and respond to mechanical forces at their external surroundings and mechanical characterization of cells are two main aspects of mechanobiology [54][55]. The mechanical properties and the behavior of cells are determined by their cytoskeletal structures that play a significant role in the field of mechanobiology. Because of this cellular structure (Cytoskeleton), cells are able to resist the deformation induced by their microenvironment and alter their shapes during movement by polymerizing or fluidizing the polymeric composition of the cytoskeleton[56]–[58]. During this process, the structural stiffness of the cells is either reinforced or reduced, helping cells to maintain their physiological processes and continue their biological functions.

The cytoskeleton is involved in cell migration during wound healing and cancer metastasis, so in NBI, as NPs could interact with cellular organelles[5] and cytoskeletal structures, they might influence cell mechanics and consequently alter cellular processes such as cell migration, cell adhesion, and cancer metastasis. In the following sections, first, the biomechanics of cells are

[5] An organelle is a tiny cellular structure that performs specific functions within a cell. Organelles are embedded within the cytoplasm of eukaryotic and prokaryotic cells

reviewed, and the effects of NPs on the cytoskeleton organization, cell migration, and cell stiffness are then discussed.

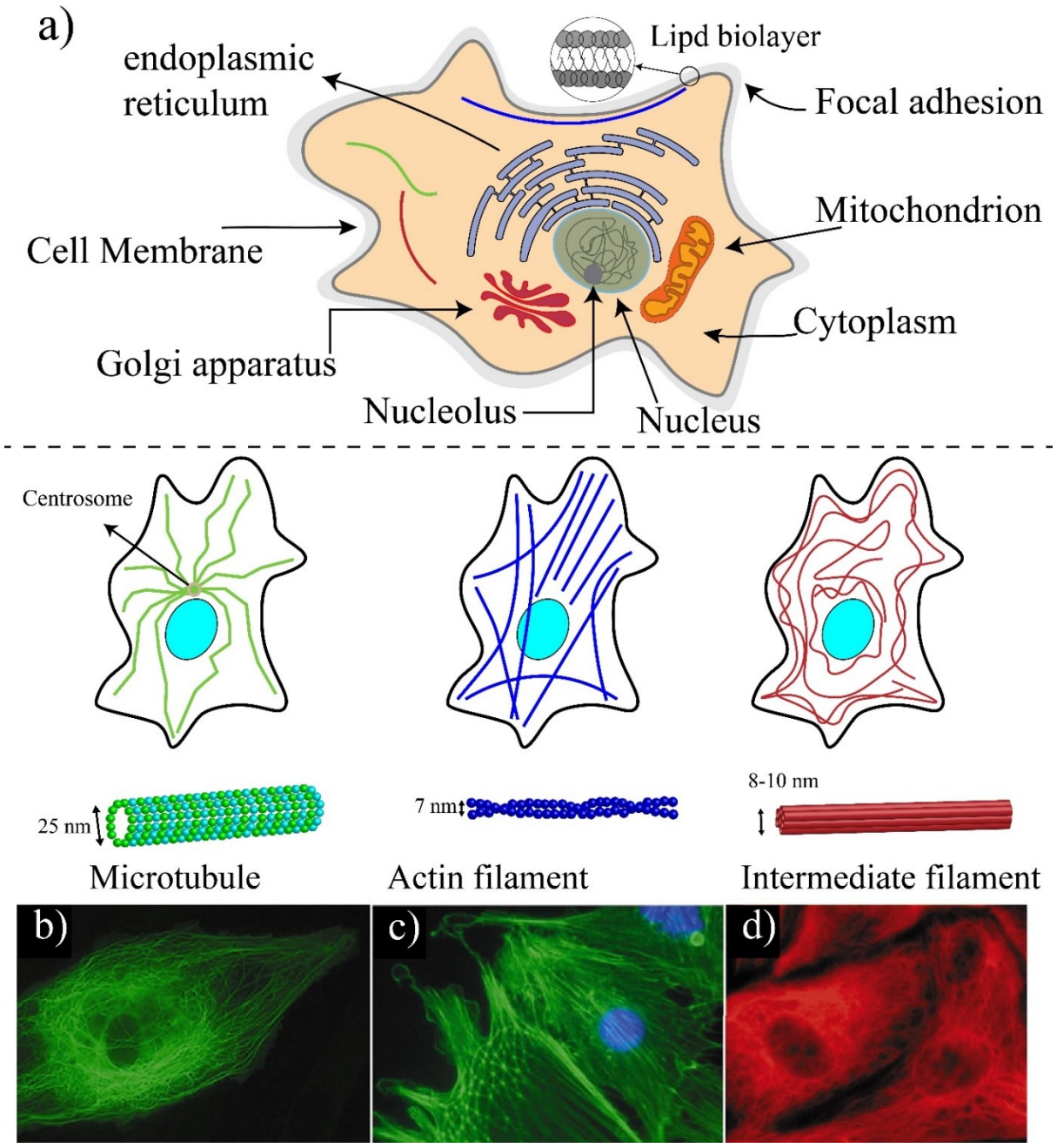

Figure 1-4. a) *A schematic showing a typical Eukaryote cells,* ***b)*** *microtubules (large region of cytoplasm and are in curved format),* ***c)*** *actin filaments or long stress fibers (they are in linear format),* ***d)*** *intermediate filament (they are extending from the nucleus to the periphery of cells)*[59]

1.1.2.1. Basic Components of Cells and Biomechanics

Cells are the basic functional unit of living organisms. Unlike plant cells (prokaryotic), animal

cells (eukaryotic) do not have enclosing cell walls, and they are surrounded only by cell membranes (**Figure 1-4a**). Therefore, a specialized structure is required to retain their structural integrities. The physical properties and behavior of cells are determined by the cellular structure that plays a significant role in cell mechanics and Mechanobiology. However, the contribution of other components such as the membrane, the nucleus, and the cytoplasm to the mechanics of cells cannot be overlooked. The cellular membrane is a thin (5-10 nm thickness) and permeable lipid bilayer, which controls the flow and movements of ions and molecules between the interior of cells (cytosol) and the extracellular environment.

A schematic drawing of a eukaryotic cell is illustrated in **Figure 1-4a**. The nucleus, the mitochondria, endoplasmic reticulum, Golgi apparatus, and cytoskeleton are main components of the internal part of a typical eukaryotic cell [60]. The nucleus of the cells is the largest organelle among sub-cellular components[61] and is located within the central region of cells and includes two regions: the internal region containing DNA and proteins, and the outer boundary of the nucleus or karyotheca[6], which is a lipid bilayer similar to the membrane of cells. Regulating the gene expression is the main role of the nucleus, and to some extent, it contributes to cell mechanics[62]. The cytoplasm of eukaryotic cells includes all the material within the cell and outside of the nucleus, such as proteins, protein complexes, and organelles[63]. Cells are dynamic living systems that have mechanical properties, and they can sense microenvironmental changes and convert stimuli and changes into biological signals [64][65].

The cytoskeleton determines the cell's shape, structure, and internal organization. The cytoskeleton is made with a complex network of protein fibers and biopolymers embedded in the cytoplasm. Besides maintaining the integrity of cells, the cytoskeleton provides pathways for molecular motor proteins to shuttle cargo between different regions of cells and generates and transmit cellular forces[66]. In response to the mechanical changes in their microenvironments, cells are either able to reinforce their cytoskeleton by polymerizing their structural, and filamentous proteins, or fluidize their cytoskeleton to reduce their stiffness. Microtubules (MT), intermediate filament, and actin filament (F-actin) are three major fiber parts of the cytoskeleton (see **Figure 1-4**). Microtubules (diameter ~ 25 nm) are stiff and hollow structures of the cytoskeleton, radiating outward from the central organelle. Microtubules are composed of two subunit tubules

[6] Karyotheca is double-layered membrane surrounding the nucleus of a eukaryotic cell, separating the nucleoplasm from the cytoplasm

(**Figure 1-5a, b**). Two subunits (α- and β-tubulin) form a dimer, then multiple dimers assemble into a protofilament, and then multiple protofilaments align and form a tube to make the microtubule polymer. Microtubules are major structural components of the cell, and they can generate force via dynamic instability. Microtubules also provide transportation highways for kinesin and dynein motor proteins to shuttle cargo through cells[56].

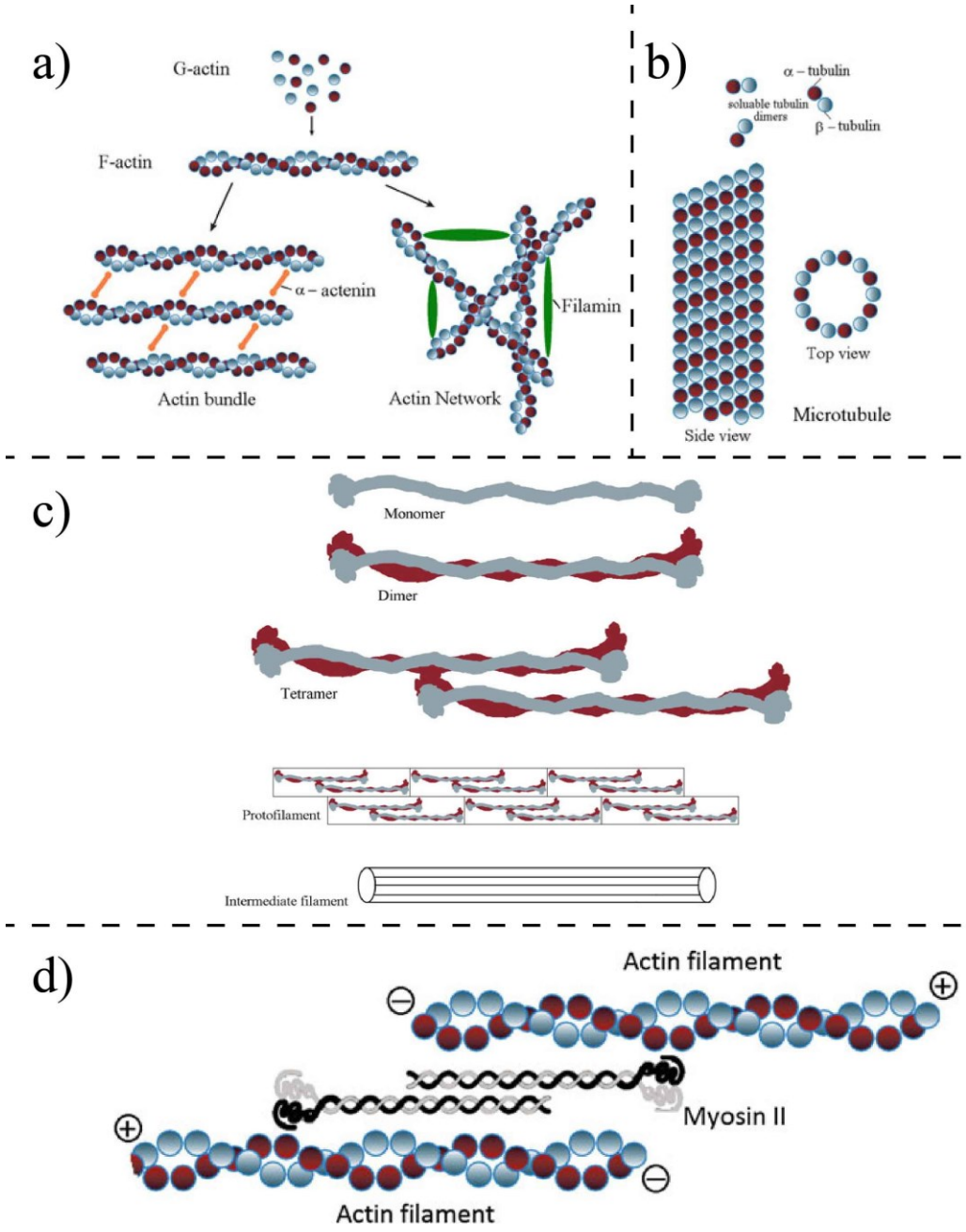

***Figure 1-5**. **a**) schematic representing an actin filament, **b)** microtubule, **c)** intermediate filaments, d) interaction of myosin filament with two actin filaments. The signs show the polarity of actin*[67]

On the other hand, the strength, integrity, organization of both cell and nucleus are provided

by intermediate filaments. The intermediate filaments (**Figure 1-5c**) with diameter of ~10 nm are composed of a variety of proteins known as proto-filaments (protein lamin, vimentin, keratin). These proteins are bundled around each other in a rope-like structure to form the final intermediate filaments. Intermediate filaments have Young's modulus between 1 to 5 GPa, and their length is between 1-3 micrometers. Intermediate filament within the cytoplasm acts as "stress absorber" and organizes the position of organelles in cells [68]. Actin filaments are the main structural component of the cytoskeleton, and with the help of non-muscle myosin II proteins, they provide required forces for movement and contraction of cells (**Figure 1-5 a**, **d**). Actin filaments are in two forms G-actin (or globular actin) and F-actin. G-actin monomers are polymerized to form stiff, polarized and double-helical F-actin with modulus elasticity between 1 to 2 GPa. [56][69].The dimeter of F-actin varies from 5 to 9 nm and has a length in the order of ten micrometers. During cell migration, F-actin filaments are linked to each other through Arp2/3 proteins to form branches at 70 degree angle from the original filament, enabling cell membranes to protrude outward[56]. Unbranched F-actin tends to behind the leading edge and in the back of cells. With the aid of non-muscle myosin II, two or more F-actin filaments are bundled in parallel to provide stress fibers. Myosin is a molecular motor that makes F-actin filaments to slide past each other to generate forces within cells[70]. Myosin converts chemical energy from ATP[7] into mechanical energy. The force generated by myosin is transmitted through focal adhesions, aggregates of cytoplasmic proteins at inners surface of the membrane, to the interface of the integrin and extracellular matrix, and these forces are considered as traction forces to help cells to move forward during cell migration[56][68].

Among these three different components of the cytoskeleton, actin filament plays the most crucial role in the structural integrity and deformability of the cell. Intermediate filaments are also able to tolerate some reasonable extent of deformations. Microtubules have minor shear or tensile resistance and do not contribute significantly to the mechanical integrity of cells. However, they could provide stability for the cytoskeleton.

1.1.2.2. Techniques for Mechanobiological Characterizations

Various techniques can be implemented to measure the mechanobiological properties of cells, such as viscoelasticity and deformability. Elastic modulus and viscosity modulus are typically used to express the mechanical properties of cells. In the elastic modulus, the applied forces are

[7] Adenosine triphosphate (ATP), energy-carrying molecule found in the cells of all living things

related to cell deformation, while in the viscosity, time-dependency stress relaxation is measured in response to a step displacement[71][65]. Forces have to be applied to the cells in order to measure the mechanical properties of cells. Based on the types of forces, different methods have been developed so far. The most used methods for experimental measurements are shown in **Figure 1-6**. Classical methods such as Atomic Force Microscopy (AFM)[72], micropipette aspiration[73], optical tweezer[74] and magnetic twisting cytometry (MTC)[75] are preferred because of their high resolution. However, they are tedious, and the performing measurements takes a long time. On the other hand, with MEMS-based[76] systems and microfluidic devices[77], biomechanical measurements can be done at higher speed, but their resolution is not as high as that of classical methods, and most of them are able only to measure deformability-related parameters not elastic and viscous modulus. To enhance the accuracy of these methods, in parallel to experimental measurements, computational analyses need to be carried out; however, they impose a level of complexity. **Table 1-1** shows the limitation and advantages of different techniques. Depending on the specific desired information, and the type of cells, we can use one of them.

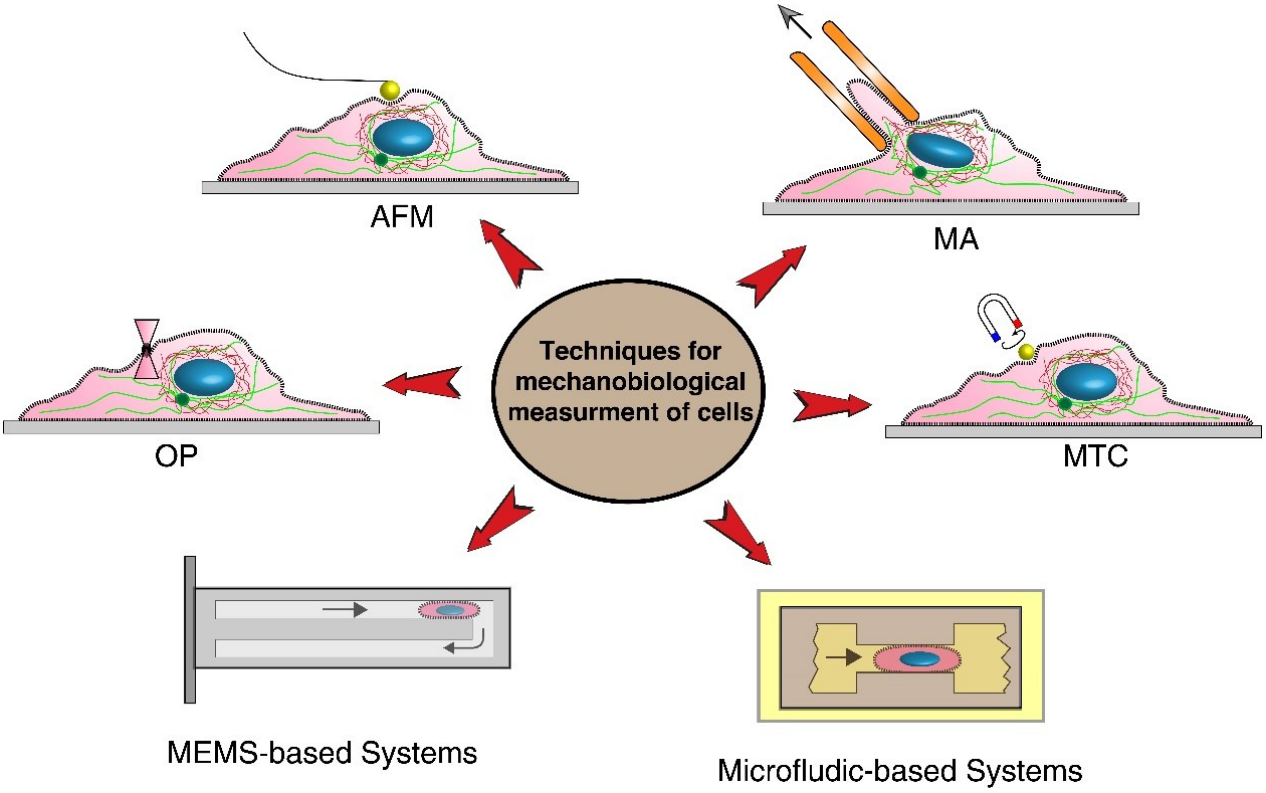

Figure 1-6. *Various tools for mechanical characterizations of living cells, AFM, OP (optical tweezer), MA (microaspiration), MTC (magnetic twisting cytometry), MEMS-based and microfluidic-based techniques*

1.1.2.2.A. Atomic Force Microscopy Method

Over the past three decades, AFM has been used as a key tool for the simultaneous morphological and mechanical characterization of living cells[52][72]. AFM method was introduced in 1986 as a tool for imaging and manipulating matter at molecular and cellular scales[78]. AFM can also be used in a liquid environment, and it has a flexible cantilever (several micrometers) at the end to probe the sample topography and measure forces between the tip and sample with piconewton sensitivity. AFM technique is not a high throughput method, but it has a simple principle of operation, allowing users to adjust this technique to measure the desired mechanobiological property. However, it has several intricacies that make the acquisition of quantitative data complex. To measure mechanical properties, the AFM tip is vertically indented into the cell until to pre-set loading force, and the applied force, which is proportional to the cantilever deflection, is recorded (**Figure 1-7**). The motion of the cantilever can be measured optically by a beam of laser, or through sensing elements built into the cantilever itself. Then, the AFM tip is controlled to return to its original position. During the approach-retract process, the deflection of the cantilever versus the vertical displacement of the AFM probe is recorded. The approach curve along theoretical models can be used to extract the cellular Young's modulus, while the retract curve can be used to quantify the adhesion force [72][79].

There are different contact models to extract the mechanical properties from the AFM-obtained curve. The most commonly used models for estimating the cellular Young's modulus include Hertz, Sneddon, Johnson-Kendall-Roberts (JKR), Derjaguin-Muller-Toporov (DMT), and Oliver-Pharr[52]. Each model can be used based on the different AFM tip geometries and sample properties. The Hertz model is the most frequently used model to approximate the contact between the AFM tip and the sample. Three assumptions are considered for using the Hertz model: the AFM tip is a perfect sphere, linear strain-stress relationship (maximum 30% indentation of sample thickness), the sample deformation is fully reversible. If these conditions are met, the Hertz model can be used to extract mechanical properties by defining the point of contact, which is not easy to determine, particularly for mammalian cells that have complex surface morphologies[52][72]. With the AFM technique, forces as small as 10^{-18} N can be measured.

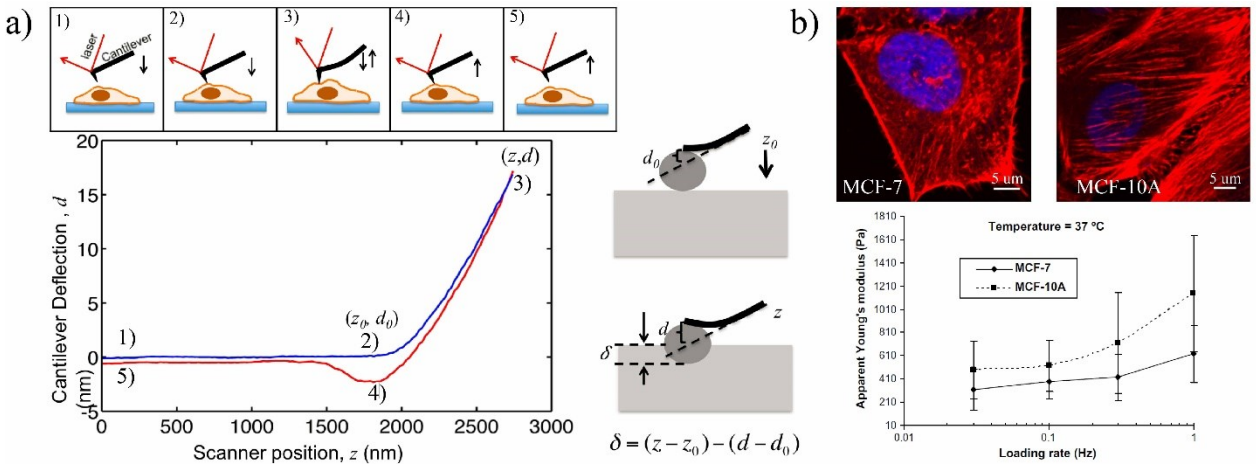

Figure 1-7. a) *AFM indentation and interpretation of the curve, 1) AFM above the cell surface, 2) AFM in contact with cell surface, 3) motion of AFM cantilever to contact the cell surface and, c) indent into cell until the set-point, 4) AFM tip detaching from the sample (AFM tip-cell adhesion), 5) returning to initial position*[80], ***b)*** *cell elasticity measurement of human breast cancer cells with AFM and visualization of actin filaments in both cell lines*[81].

1.1.2.2.B. MEMS- and Microfluidic-based Techniques

As earlier mentioned; however, classical methods provide high-resolution measurements, the single-cell analysis with classical methods is very time-consuming. MEMS-based approaches, including microfluidic techniques, can provide high- throughput alternatives that clinically can be used for deformability characterization of individual cells. With the aid of microfluidic-based systems, the biomechanical properties of thousands of cells can be characterized in a short time. Their resolutions might not be competitive with classical tools, so they are mostly focused on deformability-related parameters rather than elastic properties. In the following, few prominent techniques of them are discussed.

Researchers at Stanford University [82] developed a suspended MEMS resonator for characterizing mechanobiological properties of cancer cells by integrating a constriction channel to the device at the apex of a micro-cantilever. With measuring velocity and transit time of cells passing through the constriction channel, they evaluated the stiffness and friction of the cells. A MEMS resonator was proposed by *Corbin et al.* [83] to quantify the mechanobiological properties of human breast cancer cells (**Figure 1-8a**). They modeled the MEMS platform and the cells as a two degree of freedom system to estimate the mechanobiological properties of cells through the vibrational behavior of the system. They then studied the shift resonate frequency of the system after and before chemically fixing the adherent cells to predict their viscoelastic properties. MEMS

systems offer automated and rapid measurements; however, for mechanobiological measurement, they suffer from non-transparency and higher stiffness compared to living cells[84]

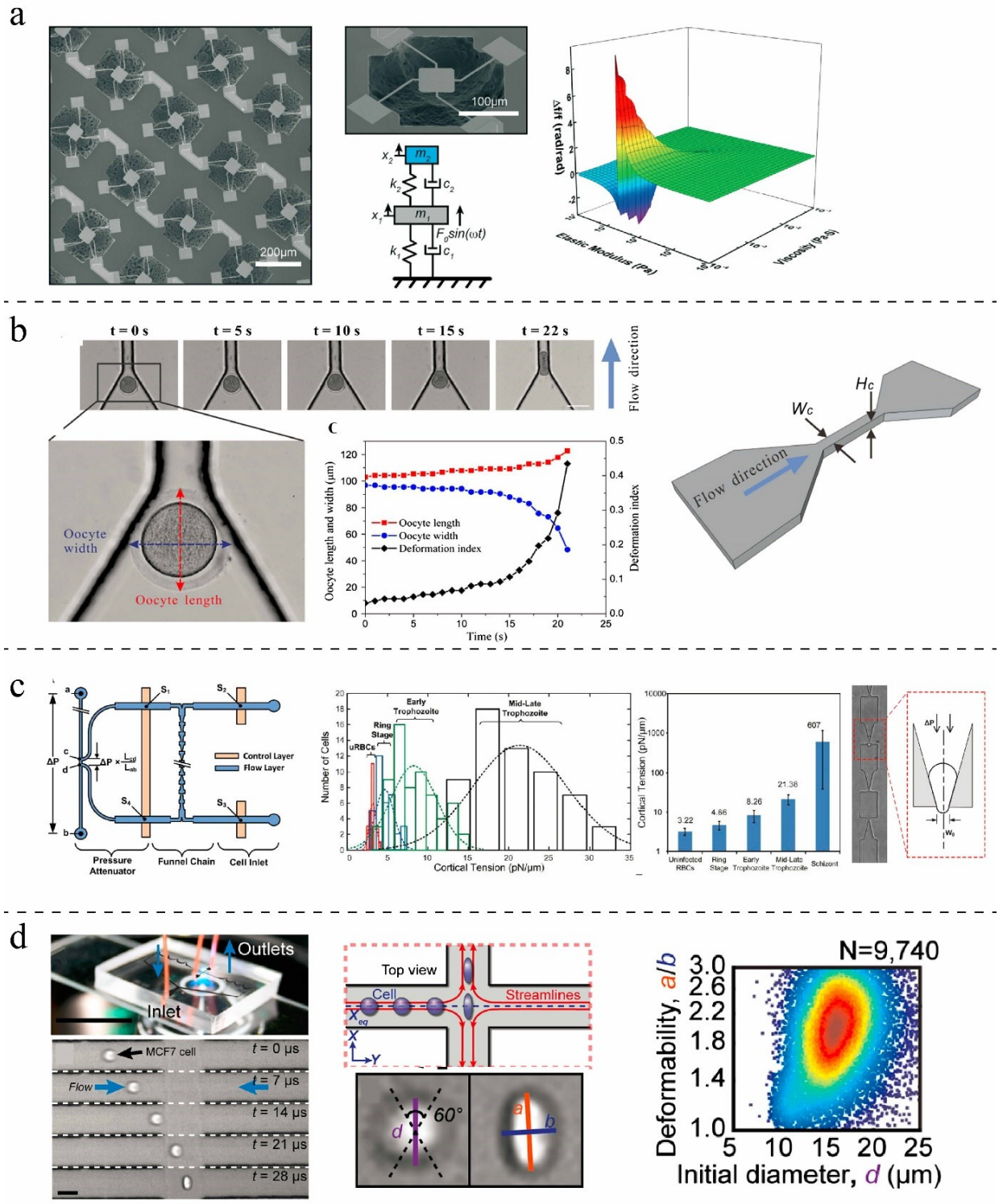

Figure 1-8. *Different microfluidic- and MEMS-based techniques for mechanobiological characterization of cells,* ***a)*** *Modeling cells as a two degree of freedom system and measuring their*

viscoelastic properties using a MEMS resonator[83]*,* ***b)*** *Constriction channels for induce mechanical deformation onto oocyte cells and measuring their deformations as they pass through the tight channel* [85]*.* ***c)*** *a microaspiration integrated into a constriction channel for quantifying the deformability properties of cells by measuring the threshold pressures* [86]*, d) hydrodynamic stretching of cells and high-throughput assay to measure the index of cells and investigate the deformability of cells*[87]

In contrary to Silicon-based systems, polymer-based micro-systems offer more advantages. The mechanical properties of cells are closer to the mechanical properties of these polymers, so their microenvironment *in vivo* can be mimicked better. Due to the optical transparency of the polymer, the behavior of living cells and their deformations can be monitored with light microscopy at the same time[88][89]. With the aid of microfluidic devices, fast mechanobiological assays can be performed using reduced quantities of samples. Microfluidic-based techniques can be classified based on the mechanical stimuli used to deform the cells.

Monitoring the movement of the cell as it passes through a constriction channel is one of the most straightforward techniques for studying the mechanobiological properties of living cells (**Figure 1-8b**). Under hydraulic pressure difference, target cells are squeezed by the wall of the channel, which is marginally smaller than the diameter of the cell. With the aid of the constriction channel, various parameters such as entry time, passage time, elongation and recovery time can be quantified. Clogging and channel blockage are the main limitations of these devices[88], [90], [91].

Deformation can be made with the aspiration technique in which the concept of conventional micropipette aspiration (MA) is mimicked for measuring the mechanobiological properties of the cell (**Figure 1-8c**). A cell is partially aspirated into a microfluidic channel and deformed through a series of funnel-shaped constrictions. Meanwhile, the elongation of the cell is measured by a microscope and camera to infer the rheological properties of living cells [86]. Living cells can also be exposed to the hydrodynamic forces and deformation by designing micro-channels in which various fluid stress stimuli are generated (**Figure 1-8d**). In contrast to the mechanical confinement-induced deformation, cells can be deformed by shear stress within micro-channels with a diameter higher than the cell diameter. The deformation index (DI) or stretch ratio is defined as the ratio of both axes of the cross-sectional area of the deformed cell and can be quantified by high-speed imaging. Using a high-speed imaging camera is one of the limitations of microfluidic-based fluid-induced deformation [82][83]. The optical stretcher is a popular method for the mechanobiological characterization of the suspended cells. This technique could be used to trap

and stretch single cells based on the laser-induced momentum transfer. The stretching forces can be affected by the size and type of cells, the refractive index, and laser power. Though optical stretching can measure the mechanobiological properties of cells, imposing forces are not large enough to promote significant deformability to simulate *in vivo* conditions encountered by migrating cancer cells. Furthermore, the effects of the laser beam on the mechanobiological properties of cells are unknown and need further studies [74], [93]. Electrical fields also can be implemented for mechanobiological characterization of cells. Whenever a single cell experiences an externally applied electrical field, it is swelled or expanded in size, a phenomenon known as electroporation. The electrical field increased the conductivity and permeability of the cell plasma membrane. The influx of small molecules through the open pores in the cell membrane causes swelling and expansion of cells. Swelling ratios (before and after establishing voltage) of cells can be recorded to evaluate the deformability of cells [84][86].

Table 1-1. *Comparison of different techniques for mechanobiological measurements of cells*

Techniques		Mechanical Stimuli	Important Parameters	Advantages*	Limitation*	Cell Type
Classical Techniques	Atomic Force Microscopy (AFM)	Cantilever micro indention	Tip deflection, Young's Modulus	High resolution, measurement, For both suspended and adherent cells, obtaining both structural and mechanical information [95][72]	Low throughput, the mechanical hitting of AFM tip may affect cells activities, the position of the probe, requiring high-resolution microscopes	MCF7 Osteoblast Human bladder [71]
	Micropipette (MP)	Negative force	Young's Modulus	A low-cost and well-established method	Limited spatial resolution. Low throughput, for suspended cells only	Human cartilage [73]
	Magnetic twisting cytometry(MTC)	Force is applied by magnetic beads	Stiffness and Young's Modulus	Induce little heat and photo damages compared to optical tweezer[96]	Resolution limitation, inducing non-uniform stress, The bead is localized randomly on cell, attachment angle affect the displacement	Melanoma [75]
	Optical Tweezers (OP)	Laser-induced surface force	Deformation index	Without physical contact,	Only for suspended cells, the damaging consequence of optical heating on cells	RBC [74]
	Parallel plate	Shear stress	Aspect ratio	homogeneity of the applied shear stress, simplicity	bulky devices, consuming a large amount of reagent, challenging to visualize the deformation	Epithelial ovarian cancer [97]

Techniques		Mechanical Stimuli	Important Parameters	Advantages*	Limitation*	Cell Type
Microfluidic-based Techniques	Fluid-induced deformation	Fluid shear stress	Deformation Index, size	High throughput, other chemical assays can be added, the process can be done continuously, deforming the cell without contacting, for both suspended and adhered cells	Expensive high-speed camera for image processing, bulky system	PBMCs [87]
	Constriction-induced deformation	Mechanical squeezing	Passage time, entry times, stiffness	Wide-ranging application in cell deformation, different geometry structure, Adjustable dimension for different cells	Clogging and channel blockage, effects of friction between cell and channel's wall, ignoring the effects of membrane rigidity and viscosity	K562 [98] MDA-MB-231[99]
	Aspiration-induced deformation	Negative pressure	Young's Modulus, cortical tension	Simple and straightforward method, a well-established mathematical model	Leaking problem, the rectangle-like cross-section of Microfluidic channels, Time consuming, requiring high vacuum pressure	Neutrophils [86]
	Electrical-induced deformation	Electroporation-induced swelling	Deformation Index, size of cells	Faster heat dissipation, better resolution Automation and parallelization of test with a reduced amount of samples	High energy consumption and high voltage	MCF-10A, MCF-7 [94]
MEMS Techniques	Suspended microcantilever	External actuator	Frequency of cantilever, passage time, transit time	All-inclusive systems, parallel analysis, better quality factor, automation	Fabrication is expensive, lack of transparency, higher stiffness compared cells, ,calibration process	Circulating tumor cells [100] Fibroblast [82]
	MEMS resonator	External actuator	Frequency of cantilever	High throughput,	Expensive fabrication, requiring external electrical system, only adherent cells	MCF7 [83]

*Information compiled from the references[56], [96], [101]

1.1.2.3. Impacts of Nanoparticles on the Cytoskeleton

Any changes in the cytoskeletal structure of cells can lead to the alternations of the mechanobiological properties of cells. In order to understand the effects of NPs on the mechanobiological properties of cells, we need to study the physiochemical interactions between NPs and the three main filamentous proteins: intermediate filament, actin-filament, and MT. In some studies, the disruption of the subcellular structure has been observed after the cellular uptake of NPs. Cytoskeleton is responsible for basic functions of cells such as a) to preserve the morphology of cells, b) to anchor organelle, c) to physically connect cells to the microenvironment, d) to produce internal forces for cells movement, e) to help cells for division, and f) endocytosis

[102], [103]. Therefore, any changes in the organization of the cytoskeleton might induce cellular dysfunction (see **Table 1-2**).

Table 1-2. *Cytoskeletal changes due to the NPs-protein interactions*

Author	Cell type	Methods	NPs type	Cytoskeleton changes
2007- Nadine Pernodet et al. [104]	Human dermal fibroblast	TEM, confocal imaging, migration assay	Gold NPs (13 nm)	Modification in actin networks. Impaired motility and adhesion.
2007-Patra et al. [105]	A549 (human lung cancer)	Confocal Microscopy	Gold nanoparticles	The morphology is changed, treated cells are rounded compared non-treated
2007-Pisanic et al. [106]	Rat pheochromocytoma (PC12M)	TEM, western blot, Fluorescent microscopy	Fe_2O_3 NPs	Reduction in the formation of actin microfilaments, they are less organized, diminish the ability for differentiation
2010- Huang X et al. [107]	A375 (Human malignant melanoma)	TEM, Confocal Microscopy, Western Blot	Silica NPs (MSNs)	The actin structure is disorganized and disrupted with NPs, cell migration in reduced
2012- Brian D. Hot et al. [108]	HeLa (cervical cancer)	Fluorescence imaging microscopy	Single wall Carbon nanotube (1±0.3 nm)	NPs caused cells to have shorter F-actins, the traction force is reduced, NPs did not affect G-actin and myosin II
2012- Yangzhe Wu et al. [109]	HAEC (Human Aortic Endothelial Cells)	AFM, fluorescent imaging	Diesel exhaust particles (DEPs)	Cells became degraded. Cellular cytoskeletal structures were impaired
2013- Choudhury. [110]	A549 (human lung cancer)	Raman, FTIR, TEM, Darkfield microscopy, UV-visible spectroscopy	Citrate-capped Gold NPs (20-60 nm)	Inhibiting the polarization of MT, MT structures are damaged, affecting the dynamic equilibrium
2013- Pi et al. [111]	MCF-7 (human breast cancer)	AFM, confocal microscopy	Selenium NPs	The organization of F-actin changed and they aggregated. Actin concentration reduced
2013- Yimei Wen et al. [112]	Acting and Tubulin proteins (cell-free system)	TEM, Hyperspectral Imaging,	Silver NPs	Inducing changes in the secondary structures. Silver NPs tend to bind actin vs. tubulin
2015- Iftekhar et al. [113] 5	Osteoblast cells	AFM, TEM, X-ray	Boron nitride NPs	They do not affect the morphology of cells
2015- Robert J et al. [114]	B35 neuroblastoma	Immunocytochemistry	Silver NPs	NPs induce F-actin inclusion, disrupting the actin function
2017- Mustafa R et al. [115]	HSC-3 (Human Tongue Squamous Carcinoma cells)	Western blot, DIC microscopy, scratch assay	Gold nanorods coated with PEG and REG	The cytoskeletal proteins rearranged. Cytoskeletal protrusions (filopodia and lamellipodia) reduced
2017- Yizhong Liu et al. [116]	Endothelial cells HUVEC	Fluorescent microscopy, Traction force microscopy,	Gold NPs-coated with PEG (20 nm)	The rearrangement of actin filament induced by NPs. Inhibition of Rock activity reduced the polymerization of actin. reducing the focal adhesion

Author	Cell type	Methods	NPs type	Cytoskeleton changes
2017-Larissa Fernanda et al. [117]	Human fibroblast CCD1072Sk	Immunofluorescence imaging, Cytofluorometry	Gold NPs and silver NPs	Impair the F-actin cytoskeletal reorganization. They lose cell polarization. (without losing their viability)
2018- Mohammad Ibrahim et al. [118]	SaOS-2 (Human Osteosarcoma cells)	Hyperspectral imaging, fluorescent imaging, western blot	TiO2 spherical NPs	The actin and microtubule cytoskeletal networks are disorganized.
2018-Qin et al. [119]	MDA-MB-231 (human breast cancer)	SEM, IF imaging, AFM, scratch assay	Fullerenol NPs	The concentration of actin reduced, the migration speed reduced, disturbing actin assembly

Most NPs are thought to penetrate cells through forming vesicles, and these membrane-bound vesicles transport NPs along MT to intracellular compartments. During this process, the NPs might have indirect interactions with cytoskeletal proteins, but it is not clear how they interact with those proteins while they are encapsulated inside lysosomes and endosomes. However, some evidence is showing that NPs can directly interact with the cytoskeletal proteins. It has been found that carbon nanomaterials can enter into the cytosol and directly interact with the subcellular structures of cells. This direct interaction may impose a negative effect on their biological functions[120], [121]. The findings of *Lundqvist et al.* [122] suggested a new domain of study, NPs-proteins interactions, by showing the presence of MT in the protein corona formed around the SiO2 NPs. *Furong et al.* [123] showed that single-wall carbon nanotubes could enter cells and directly alter cell morphology by disturbing the actin networks. They observed that these nanomaterials cause an irregular actin network in comparison to untreated cells. Various NPs parameters such as their shapes, concentrations, and incubation times are important when assessing the toxicity of nanomaterials in the cytoskeleton. The shape of the NPs can induce different effects on the cytoskeletal structure of cells. It has been shown that unlike silica NPs, nanorods silica with large aspect ratio can largely change the organization of actin filament particularly in the vicinity of the cell membrane, resulting in severe damages to the cytoskeletal structures[107]. *Holt et al.* [108], performed a sophisticated imaging analysis using compressed confocal microscopy images to study F-actin changes of HeLa cells loaded with extremely high level of nanocarbon tubes. They found that with carbon nanotube, the expression of G-actin remains intact; however, their ability to assemble into stable polymer is dramatically changed. Their results suggest that the shape of nanomaterials plays a determining role in the penetration ability of NPs. *Pisanic et al.* [106] studied

the effects of NPs concentrations on neuron cells. They found that, by increasing the concentration of metal oxide nanoparticles (Fe_2O_3), the density of actin filaments is reduced, preventing them from getting mature (less polymerization) under the stimulation of nerve growth factors.

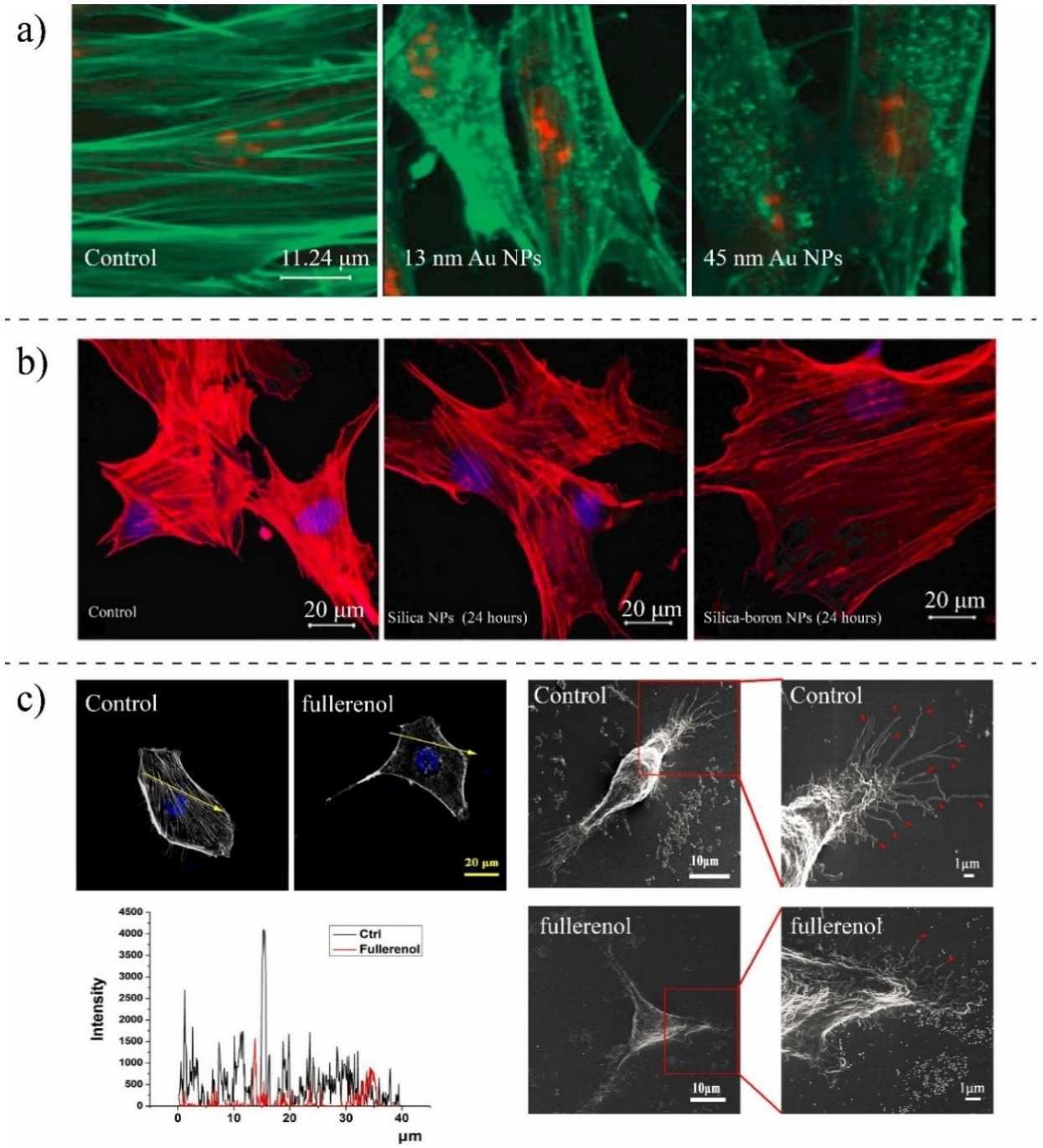

Figure 1-9. a) *Fluorescent imaging of human dermal fibroblasts stained for F-actin after three days of exposure to gold NPs. F-actins appeared to be in dotted format compared to control cells[25],* ***b)*** *mesenchymal stem cells treated with Silica (Si), and Silica-Boron (SiB): F-actin detected with red TRITC-phalloidin staining, and DNA stained with blue DAPI. Actins in control*

cells are packed longitudinally while they are arranged transversally in treated cells[124]*,* ***c)*** *SEM images of MDA-MB-231 cells treated with fullerenol NPs compared to control cells. Treated cells show shorter protrusions in comparison to control cells, and the concentration of actin fibers have reduced after uptake of NPs*[119].

NPs might induce morphological changes by altering the cytoskeletal structure. *Wu et al.* [109] showed that depending on the concentration and exposure time of particles, the cytoskeletal structure of human aortic endothelial cells[8] is impaired, after treating with diesel exhaust particles. Cytoskeleton fluorescence imaging has proved that the density of filamentous proteins is reduced by increasing the concentration and exposure time of NPs, inducing topographic changes in cell surface. *Patra et al.* [105] also observed that gold NPs cause cytoskeletal damage and induce profound morphological changes in human carcinoma cells (A549). *Subbiah et al.* [125] studied the morphological changes of A549, NIH3T3, and HS-5, and they found that silver NPs may induce changes in the topography of cell lines and they appear to be more rounded, compared to the untreated cells. *Xu F et al.* [126] demonstrated that silver NPs induce significant changes in the morphology and the cytoskeletal components of Rat cortical neurons.

In vitro alternations in MT and F-actin concentrations and cytoskeletal destabilization have been also observed in cells upon their interactions with nanomaterials. In a study that set out to determine the binding tendency of silver NPs to cytoskeletal structures of cells, *Wen et al.* [112] used imaging techniques to visualize the organization of actin and tubulin proteins after treating with silver NPs (size 30 nm). They observed that secondary structures of actins and tubules are changed due to the interaction with NPs, and alpha-helices of both proteins are decreased while their beta-sheets are increased. They also found that under electrostatic interactions, silver NPs tend to bind actin rather than tubules. In another study, *Tatsiana et al.* [25] showed that cellular uptake of gold NPs in human dermal fibroblasts is a function of size, concentration, and incubation time. Their findings revealed that the cellular uptake of gold NPs disrupts actin fibers of cells, and in contrast to the extended actin in control cells, in treated cells, actin filaments are broken and appeared as dotes (**Figure 1-9a**). However, no significant changes were found in actin or beta-tubulin protein levels. *Choudhury et al.* [110] studied the binding of nanosphere gold NPs to MT in the cell-free systems as well as in human lung carcinoma cells (A549) using Raman measurement, Fourier transform-infrared spectroscopy (FTIR), and other imaging techniques.

[8] endothelium refers to cells that line the interior surface of blood vessels and lymphatic vessels

Their findings showed that gold NPs depending on their size and concentration, might inhibit polarization of MT. They also observed that MT networks are damaged and shrunken upon interaction with gold NPs in comparison to control cells. The findings of *Prenodet et al.* [127] revealed that the density of F-actin in Human dermal fibroblasts is dramatically reduced, particularly in a layer adjacent to the substrate after incubation with citrate-capped gold NPs after six days, and consequently, cells showed less ability to migrate and proliferate. In contrary to non-treated cells, they showed that NPs-treated cells no longer have stressed F-actin. *Fernanda et al.* found [117] that silver and gold NPs can change the migration behavior of human fibroblast cells by degrading the concentration of F-actin. With the help of imaging techniques, they observed no change in the viability of cells after interaction with silver and gold NPs. However, NPs impair actin reorganization leading to decrease migration ability of cells. In a recent work done by *Qin et al.* [119], the effects of small size of fullerenol NPs were examined on metastasis behavior of invasive (MCF7) and highly invasive (MDA-MB-231) human breast cancer cells (**Figure 1-9c**). By staining the actin filaments, immunofluorescence imaging, and western blot analysis, they observed that the concentration of actin is altered and the cytoskeleton assembly is disrupted. It was also found that cytoskeleton reorganization changes the intracellular distribution of integrin, causing cells to lose their adhesion ability. They observed that treated cells have a fewer number of filopodia (filopodia are actin-rich protrusions that facilitate cancer cell motility and invasion, and actin bundles support the structure of filopodia[119]). Moreover, they found that fullerenol nanoparticles can significantly inhibit the migration of malignant cells when the concentration of NPs is increased.

Confocal imaging of the cytoskeleton of brain cells revealed that the level of β-tubulin and F-actin are remarkably decreased due to the internalization of silver NPs. *Ibrahim et al.* [128] used different techniques such as SEM, TEM, and immunofluorescence analysis to study the morphological changes of osteoblast-like cells under exposure of titanium-based orthopedic and dental implants nanoparticles (nano-Tio_2). It was observed that in response to nanoparticles, the actin and microtubule cytoskeletal networks are disrupted. In another study [129], the sub-lethal concentration of silver nanoparticles was used to investigate cytoskeletal changes in neural cells. They found that the percentage of AgNP-treated cells containing inclusions are doubled compared to control cells, indicating a significant disruption of actin filaments. *Liu et al.* [116] showed that NPs with size of 20 nm might alter the microfilament arrangement of endothelial cells. In this

study, five types of gold nanoparticles with different sizes and surface coatings were used to determine the viability and cytoskeletal change of endothelial cells. They found that gold NPs do not affect the viability of cells; however, the force balance between intracellular tension and paracellular forces are broken in 20 nm gold nanoparticles-treated cells, indicating morphological changes of cells. *Rasel et al.* [113] used different techniques to observe the morphology changes of osteoblast cells after treating them with boron nitride nanoparticles. They found that these particles do not have adverse effects on the viability and the metabolism of cells. *Nadine et al.* [104] found that citrate-gold NPs have profound effects on the cell morphology of human dermal fibroblasts, depending on their concentrations and exposure time. They observed that the density of actin filament is decreased in the presence of NPs by extending the exposure time, showing that the actin fibers are depolymerized due to cellular uptake of nanoparticles. *Ali et al*.[115] showed that gold nanorods interaction with oral squamous cell carcinoma (HSC-3) may change the cytoskeletal structure of cells, resulting in impeding the migration of metastatic cells (**Figure 1-10d**). Cytoskeleton protrusions were also observed after incubating cells with integrin-targeted gold nanorods.

In summary, in order to study the toxicity of nanomaterial due to the cellular uptake, the interaction of nanomaterial with the cellular structure of cells and cytoskeleton needs to be taken into account. Nanomaterial due to direct and indirect interactions with filamentous networks of cells may change the cytoskeletal organization, leading to alternation in cell mechanobiology.

1.1.2.4. Impacts of NPs on Cell Stiffness

The resistance of cells to the external forces can provide information regarding the health state of cells. The resistance of cells to the applied forces can be expressed by stiffness. This parameter shows the relationship between the stress and the applied strain and can be characterized by Young's modulus (E) of cells (unit in Pascals). Multiple studies have shown that cells can express different elasticities, depending on their diseased state[56][126]. In some diseases such as malaria[90], the level of stiffness may be increased. However, for other diseases such as cancer, several studies are showing that the stiffness of cancer cells is reduced compared to their normal counterparts[54], [130], [131]. In healthy cells, the cytoskeleton is well organized and the density of actin filaments, the main constituent of the cytoskeleton system, is higher, enabling cells to resist against external forces. In malignant cells, these organized structures cannot be observed, and the

density of filamentous proteins (stress fibers) is lowered, leading to a softer cellular structure[132]. The relationship between the cytoskeletal mechanical properties and the biological function of healthy and cancerous cells can provide a meaningful approach to evaluate the health state of cells[133]. Furthermore, many anti-cancer drugs are purposely designed to target the cytoskeletal structure[65]. For example, *Rotasch et al.* [134] showed that the pharmacological targeting of actin fibers could significantly affect cell mechanics. Therefore, mechanobiological measurements of cells can also provide a platform to assess the effectiveness of anti-cancer drugs which may be delivered through NPs, or NPs alone. As earlier mentioned, AFM is the most widely used technique for cell stiffness due to high-resolution imaging and quantitative measurements. Many researchers have used this tool to investigate the effect of NPs on cell stiffness (**Table 1-3**).

Table 1-3. *Effects of various NPs on the mechanobiological properties (stiffness) of cells*

Author	Year	Nanoparticles	Parameter	Cell Types	Techniques	Results
Buyukhatipoglu [135]	2010	Iron oxide	Young's Modulus	PAEC	AFM	The stiffness is increased
Yangzhe Wu[109]	2012	Diesel exhaust particle (DEP)	Young's Modulus	HAEC	AFM	Yonge modulus is reduced depending on the doses
Zhang et al. [136]	2012	Hematite particles ($\alpha - Fe_2O_3$)	Young's Modulus	k-12	AFM	The stiffness is increased.
Jinag Pi et al. [111]	2012	Selenium NPs	Young's Modulus	MCF-7 (human breast cancer)	AFM	Young's Modulus is reduced. Adhesion is reduced
Subbiah et al. [125]	2013	Hybrid NPs	Young's Modulus	A549 NIH3T3 HS-5	AFM	Stiffness is increased
Ogneva et al. [124]	2014	Silica-based NPs	Young's Modulus	Mesenchymal stem cells	AFM	Stiffness is increased
Rasel et al. [113]	2015	boron nitride nanoparticle (BN NP)	Young's Modulus	osteoblast cells	AFM	Elasticity is increased
Anna Pietuch et al. [137]	2015	Gold Nano rode and Spherical NPs	Stiffness	MDCK II cells	AFM	Stiffness varies depending on the Au concentration

Author	Year	Nanoparticles	Parameter	Cell Types	Techniques	Results
Babhosseini et al. [138]	2016	SphKIs with NPs	Deformability-related parameters (passage time and velocity)	MDA-MB-231	Microfluidic (Constriction channel)	Cells became softer
Moustafa Ali et al. [139]	2017	Gold Nanorods	Stiffness of nucleus	HEY A8	AFM	Stiffness increased and inhibited metastasis
Qin et al. [119]	2018	Fullerenol NPs	Young's modulus	MDA-MB-231, MCF7	AFM	Stiffness is decreased

NPs may increase the stiffness of cells through interactions with the different components of cells, which play central roles in cell mechanics. *Buyukhatipoglu et al*. [135] used AFM to estimate the stiffness of porcine aortic endothelial cells (PAEC) following uptake of bare iron oxide NPs. The result of their study showed that cells' length is increased after incubating PAEC with NPs and actin stress fibers are stretched across the cell body, causing a significant increase in stiffness of endothelial cells. Ogneva [124] showed that silica-based NPs may cause mesenchymal stem cells to have higher stiffness compared to control cells. The AFM measurements showed that the stiffness of the cells can be increased by 61% after interaction with NPs. They claimed that after NPs uptake, the content of F-actin is reduced and their structures are reorganized, altering their cell mechanics (**Figure 1-9b**). Subbaih [125] studied the effects of different hybrid NPs on different cell lines: A549, NIH3T3, and HS-5 using AFM measurements. The results revealed that, after treating cells with NPs, their mechanical properties are increased. *Anna Pietuch et al*.[137] revealed that gold nanosphere-treated MDCK II[9] cells display a concentration-dependent stiffness. Whit AFM measurements, they found that a higher concentration of CTAB[10] coated nanospheres gold (>3 µg/mL) can significantly increase the stiffness of cells whereas the low concentration (0.5 µg/mL) reduces the cell stiffness compared to non-treated cells. *Moustafa et al.* [139] carried out a study on the nucleus stiffness of ovarian cancer cells (HEY A8) and they proved that gold nanorods designed to target cell nucleus, can increase the stiffness of the cells while they can slow down the migration of cancer cells and suppress the metastatic ability of cells (**Figure 1-10b**). They observed that gold nanorods could enhance the expression of actin inner nuclear membrane lamin A/C protein.

[9] Madin-Darby canine kidney- is a subclone derived from the heterogenous parent line
[10] cetyltrimethylammonium bromide (CTAB)

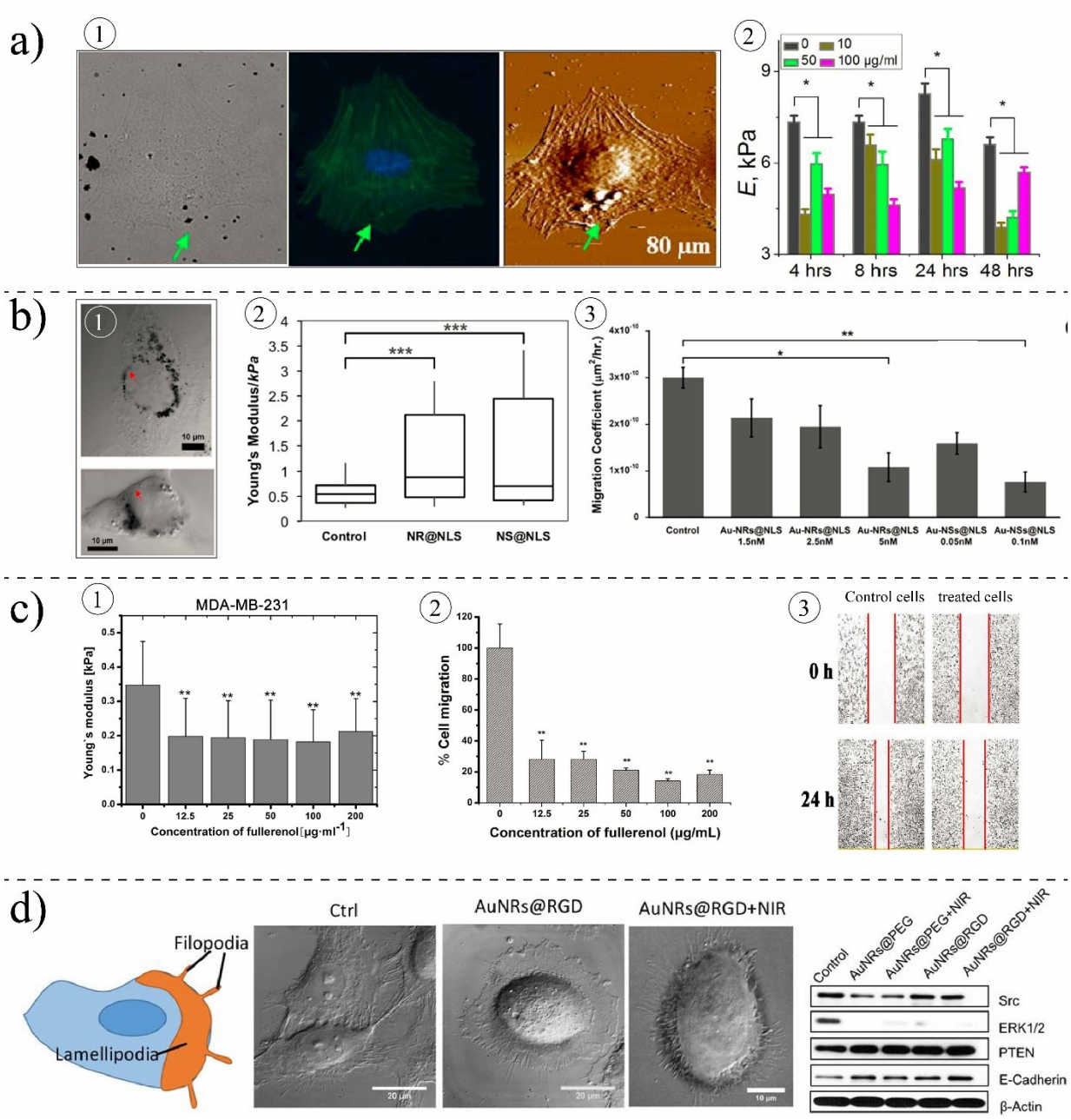

Figure 1-10. *Effects of NPs on cell mechanics,* ***a)*** *Effects of EDPs (diesel exhaust particles) on HAECs cells,* ***(a1)*** *bright field, fluorescent and AFM images of cells treated with NPs and their distribution in cells,* ***(a2)*** *elasticity (E) of treated cells compared to control cells after different exposure time and for different concentrations, (*, P<0.01)*[109], ***b)*** *Effects of gold nanospheres and nanorods on HEYA8 cell,* ***(b1)*** *TEM images of cells treated with NPs,* ***(b2)*** *treated cells are become stiffer compare to control cells,* ***(b3)*** *effects of NPs on migration ability of cells* [115], ***c)*** *effects of small fullerenol on human breast cancer cells,* ***(c1)*** *elasticity of MDA-MB-231 cells is reduced upon interaction with NPs,* ***(c2)*** *migration ability of cells is reduced,* ***(c3)*** *scratch assay measurement for treated cells and control cells*[119], ***d)*** *Effects of gold nanorodes on HSC, NPs could change the morphology of cells and reduce the movement ability of cells by changing the protein expression*[115].

On the other hand, some other works are showing that the mechanobiological properties of cells may be reduced due to the internalization of NPs in the cells. *Jiang Pi et al*. [111]observed that the internalization of selenium NPs could remarkably decrease Young's modulus of MCF-7 cells. Selenium NPs induced changes in the organization and regulation of cytoskeletal structures of cells by disrupting F-actin. *Babhosseini et al*.[138] designed a microfluidic device integrated with multiple constriction channels to study the mechanobiological changes after internalization of poly lactic-co-glycolic acid (PLGA) NPs coated with an anti-cancer drug (sphingosine kinase inhibitor). They observed that treated cells could pass through the constriction channel faster than the control cells, indicating a reduction in the stiffness of cells. It was also observed that, due to the internalization of NPs in cells, the concentration of actin filament is increased. Findings of *Yangzhe Wu et al*.[109] revealed a gradual down-regulation of cytoskeletal components of HAEC (Human Aortic Endothelial Cells) cells after exposure to diesel exhaust particles, causing them to have a softer body compared to non-treated cells (**Figure 1-10a**). In a recent work, *Qin et al.* [119] investigated the effects of small fullerenol NPs on the Young's Modulus of human metastatic breast cancer cells(**Figure 1-10c**). Their results revealed that NPs disorder the arrangement of actin fibers and cause them to become thinner compared to the strain, strong, and well-arranged fibers in control cells. The western blot measurement also showed a substantial reduction in the content of F-actin and G-actin. The effects of those changes also observed in Young's Modulus of cells. Their AFM measurements showed a significant decrease in Young's Modulus of MDA –MB-231 and MCF-10A after the internalization of fulleronal NPs.

1.1.2.5. Impacts of Nanoparticles on Cell Motility

Migration of cells plays a highly significant role in wound healing and cancer metastasis. For migration, cancer cells undergo epithelial-mesenchymal transition (EMT) by which epithelial cells lose their "epithelial phenotype" including lateral cell-cell adhesion and cell-matrix adhesions. Cells during EMT become migratory and invasive. The EMT can be reversed to return to the epithelial phenotype, called mesenchymal-epithelial transition (MET). Tumor cells that have undergone EMT can enter to a distant organ, but they need to revert back to the epithelial-like state (MET) in order to grow in the secondary site and form a solid tumor[140]. For migration, different steps are performed: a) cell body is polymerized to establish a front to rear polarity axis, b) protrusions of the cell membrane to form lamellipodia at the leading edge and (**Figure 1-10d**), c) cell body retraction. The cytoskeleton contributes to all these steps, and NP-cytoskeleton

interactions might alter the migratory ability of cells. By decreasing cell adhesion and altering the expression of cell migration-related proteins, NPs could change the migratory potential of cells. By reducing the cell adhesion, cells are not able to provide enough traction force to pull cells forward. For example, *Hou et al*.[141] showed that the adhesion of cells is reduced by treating cells with TiO2 NPs, slowing down the migration ability of cells. *Zhou et al*.[142] studied the effects of gold nanorods on three different cell lines, MDA-MB-231 (human breast cancer cells), PC3 (prostate cancer cells) and B16F10 (mouse melanoma cells). Their results revealed that rod-shaped gold NPs could effectively inhibit the migration and invasiveness of cells. Their investigations showed that NPs once are in cells can down-regulate the expression of energy-related proteins. They showed that the ATP productions are reduced (due to the inhibition of mitochondrial oxidative phosphorylation), and subsequently inhibits the assembly of F-actin, which is essential for cell migration. In another work, *Pan Y et al*.[143] showed that gold NPs (15 nm) could inhibit the endothelial growth factor of HUVEC[11] cells. Their wound-healing assays revealed that cell migration and tube forming are reduced after incubating cells with gold NPs. There are also few studies showing the reverse effects of NPs on cell migration. For instant, *Liu et al*. [134] observed an increase in the migration of human lung cancer cells treated with small gold particles (10 nm). Their results showed that gold NPs could notably facilitate the invasion of 95D cells. They showed that enhanced migration activity could be associated with increased expression of metalloproteinase 9. In a recent work, *Moustafa et al.* [115] showed that the shape of HSC cells is changed upon interaction with gold nanorods and cellular uptake of NPs reduces the migratory ability of cells through altering the concentration of migration-related proteins.

1.2. Thesis Motivation

Cancer is one of the most critical threats to human beings, and annually many people across the world are died due to cancer. There are more than 200 types of cancer, some of them are very aggressive, some are always fatal, and some are easily treated. In Canada, cancer is the leading cause of death and is responsible for almost 30% of all deaths, more than cardiovascular diseases. In 2017, on average, 221 Canadian died due to cancer every day, and based on the 2010 estimates, 49% of men and 45% of women are expected to get cancer during their lifetime. These alarming

[11] Human umbilical vein endothelial cell

statistics show the limitations of the existing therapeutic and diagnostic methods and emphasize the need for developing efficient and practical approaches for the control and treatment of cancer.

Recent advances in nanoscience and nanotechnology have contributed to the development of nanoscale materials as innovative tools to be used to optimize and revolutionize the conventional methods for cancer diagnosis and cancer therapy. What is the rationale behind using nanomaterials for cellular biology, particularly cancer? Small size and large surface area of nanomaterials have provided NPs with fundamental and structural properties that cannot be found in bulky materials or molecular and macroscopic agents. When these properties are linked with bio-targeting agents such as peptides, antibodies, and small molecules, they can be specifically used to target malignant tumors. As discussed earlier in the introduction section, in classical methods such as chemotherapy, drugs are delivered to both healthy and diseased cells, so it induces severe side effects. 99% of drugs in classical methods cannot reach the place of cancer[144]–[146]. Although there are a few non-NP successful systems like conjugated antibodies for targeted therapy to deliver compounds to specific locations, for example, for the treatment of human breast cancer cells[147], NPs may be desirable to use as carriers to have more control over drug targeting and release. In NP-based therapy, nanomedicines are designed to target only the desired places without inducing adverse side effects. Therefore, the non-target toxicity of anti-cancer drugs is substantially reduced, while the efficiency of the system is increased. Cancer treatment, with the help of nanotechnology, is an interdisciplinary field focused on biology, chemistry, engineering, medicine, and physic. Therefore, in NP-based therapy using nanotechnology, all these aspects have to be taken into account to design nanomedicines.

For cancer therapy, the interaction of NPs with biological systems, particularly with cells, has gained more attention. Studying the adoration and uptake of NPs by cells is a prerequisite for engineering nanomedicines[148], [149]. Moreover, a simple delivery of NPs to cells cannot provide the desired effects, and to develop an effective NP-based therapy system, we need to transport NPs to specific intracellular locations precisely. Hence, developing reliable and fast techniques for accurate localization of NPs within cells is also necessary to optimize nanomedicines for cancer therapy. NPs might cause negative or positive effects on cellular functions. For instance, they might enhance the proliferation or differentiation of cells, or they might be toxic to cells and, consequently, cause cell dysfunctions. So, besides the cellular uptake, biocompatibility, and localizations of NPs, we need to characterize NPs effects on cellular

behavior. There are different types of NPs to be used for cancer therapy. Gold nanoparticles have long been considered for cancer therapy due to their remarkable properties. Gold NPs exhibit unique physicochemical properties, including localized surface plasmon resonance (LSPR) and the ability to bind different molecular groups for surface modifications. The tunable LSPR properties of gold NPs allow diagnosing NPs at intracellular levels with a high resolution through optical measurements. These properties of gold NPs along with other benefits such as multi-functionalization, stable nature, and facile synthesis of gold NPs have made them suitable for cancer therapy and cancer management. Moreover, non-toxic and non- immunogenic nature of gold NPs provide them with additional benefits and enable them to penetrate and accumulate drugs at the diseased sites easily[150], [151].

Even though the NPs may provide favorable therapeutic effects on the cancerous cells, their intercellular, and structural effects on the cells are unknown[27], [58], [126]. Due to the nanosize and unique physicochemical properties, NPs are expected to interact with different compartments of cells such as cell membrane, cytoskeleton, and organelle, and those interactions might alter cellular functions and structures. One the other hand, it is well-documented that the genetic and epigenetic changes during the cancer progression alter the functional behavior of cells, and these changes are reflected in the mechanobiological properties of cells. Therefore, assessing the toxicity and uptake of NPs alone may not be sufficient criteria to design nanomedicines for cancer therapy. Depending on the physicochemical properties, NPs are expected to cause different levels of mechanobiological changes in cells. However, their exact effects on cell mechanics are unknown and were investigated only by a few studies. It is not clear how NP-treated cells with altered mechanobiological properties can be useful in the treatment and management of cancer. In the aim of clarifying those unknowns, in the current thesis, along with investigating uptake, biocompatibility, and localization of different gold NPs in cancer cells, we experimentally and computationally studied NPs effects on the mechanobiological properties and characterized their contributions to cancer migration. Understanding the biocompatibility of NPs as well as their effects in mechanobiology of cancer cells, take us one step closer to engineer/optimize nanomedicines for cancer treatment and management.

1.3. Thesis Scope and Objectives

This thesis presents the *in vitro* nano-bio-interaction investigation between different types of gold NPs and different cancer cell lines to engineer/design/optimize nanomedicines for cancer

treatment and cancer management. In this dissertation, in contrary to many other similar studies, we evaluated the effects of gold NPs in cancer cells in the context of cell mechanobiology to understand how NPs can be used to control the cancer progression by regulating the mechanobiological properties of cells. The scope of this study and the main objectives can be listed as follows:

1) Studying the *in vitro* cellular uptake of synthesized gold NPs (nanospheres and nanostars) in healthy and cancer cells and compare their behavior within cells versus ancient Indian medicine, *Swarna Bhasma,* under different NPs concentrations and incubation times.
2) Determining the localization of gold NPs in different intracellular regions and quantify NPs internalization degree using optical techniques including Hyperspectral and Raman imaging and compare two methods in terms of compatibility, speed, and resolution.
3) Characterizing cellular responses of cancer cells with different mechanobiological properties under external and internal forces through developing computational models to study the contribution of mechanobiological properties to phenomena involved in the adhesion and migration of cells
4) Studying how mechanobiological properties of cells such as bulk stiffness can influence the migratory capabilities and cancer progression and how their alterations could help for cancer therapy
5) Investigating the impacts of gold NPs with different nano-morphologies on mechanobiological properties and how gold NPs can be used to manage the migratory capability of cancer cells by regulating the mechanobiological properties of cells.

1.4. Thesis Organization

This thesis consists of ten chapters (**Table 1-4**), and this thesis is submitted in a manuscript-based format in which all chapters excluding the first chapter, second and last chapters are duplicated from the manuscripts which were accepted or submitted for publications in scientific journals.

Chapter 1: This chapter is the introduction of this thesis in which the background of nano-bio-interaction from two different aspects is discussed and reviewed. This thesis is submitted to the mechanical engineering department, so in this chapter, it has been tried to provide readers with

enough information regarding cells and their different components. However, readers for further information are referred to [60], [65], [68].

Chapter 2: In this chapter, the focus is given to the preparation of gold NPs, particularly chemically synthesized NPs and *Swarna Bhasma*. Important methods for the preparation of gold NPs including Turkevich and seed-mediated methods are discussed. Incineration methods for the preparation of metal-based Indian medicines are also discussed. Moreover, different nanotechnology techniques for the characterization of NPs are reviewed.

Chapter 3: The cellular uptake of citrate-capped gold NPs (nanospheres) in cancer cells is compared with *Swarna Bhasma* particles. Using different methods, the characterization of gold particles is discussed, while their effects in cancer cells under different concentrations and incubation times are presented.

Chapter 4: In this chapter, the interactions of two different shapes of gold NPs (nanospheres and nanostars) are studied in two different cancer cell lines (HeLa and HepG2) with surface-enhanced Raman spectroscopy. The effects of two different morphologies of nanoparticles on SERS are discussed to investigate the affinity of NPs to the different intracellular environment.

Chapter 5: In this chapter, Hyperspectral imaging (HSI) technique is offered to study, detect and localize gold NPs in two different cell lines (HepG2 and A549) by measuring the intracellular plasmonic shifts of gold NPs (with different morphologies) at the nanoscale level. In this chapter, it is discussed how the HSI technique can be used to characterize NPs in cells and develop nanomedicine for cancer therapy. Then, it is studied how nano-morphology affects the interaction of NPs with intracellular structures.

Chapter 6: In this chapter, the design, fabrication, and optimization of a microfluidic device for cell trapping is studied. With the aid of the numerical simulations, traps are designed to capture cells/particles using hydrodynamic forces. The geometric parameters are also tuned to increase the trapping efficiency of the system. This system can be used to gently trap cells at the desired place for optical and chemical characterization of cells.

Chapter 7: In this chapter, a fluid-structure interaction (FSI) model is developed to characterize cellular deformations of both healthy and cancer cells (human breast cancer cells) under different shear stresses. Healthy and cancerous cells due to their different mechanobiological properties,

respond differently to external forces. In this chapter, cellular deformations are separately calculated for the nucleus and cytoplasm of cells.

Chapter 8: In this chapter, an energy-dependent term, migratory index, is introduced to approximate the migration of cells depending on their bulk stiffness. By considering force transmission and cell deformation as two determining factors for cell migration, it is shown that invasive cells tend to regulate their mechanobiological properties in order to maximize their migratory capabilities. In this chapter, it is discussed why for most cell lines, cancerous counterparts are softer or stiffer compared to healthy cells.

Chapter 9: In this chapter, the AFM method is used to study the mechanobiological properties of NP-treated cancer cells (A549) compared to untreated cells. Two different morphologies of gold NPs are used to examine their potentials to change the cell stiffness as well as the migration of cancer cells. In this study, it is discussed how gold NPs by disrupting the organization of cells can change the cell mechanic. Then, it is discussed how these changes can regulate the migratory index and potentially suppress the metastatic ability of cells.

Chapter 10: in the final chapter, the summary of this thesis and conclusions are presented, and then suggestions for future works are mentioned.

***Table 1-4**. Organization of this thesis*

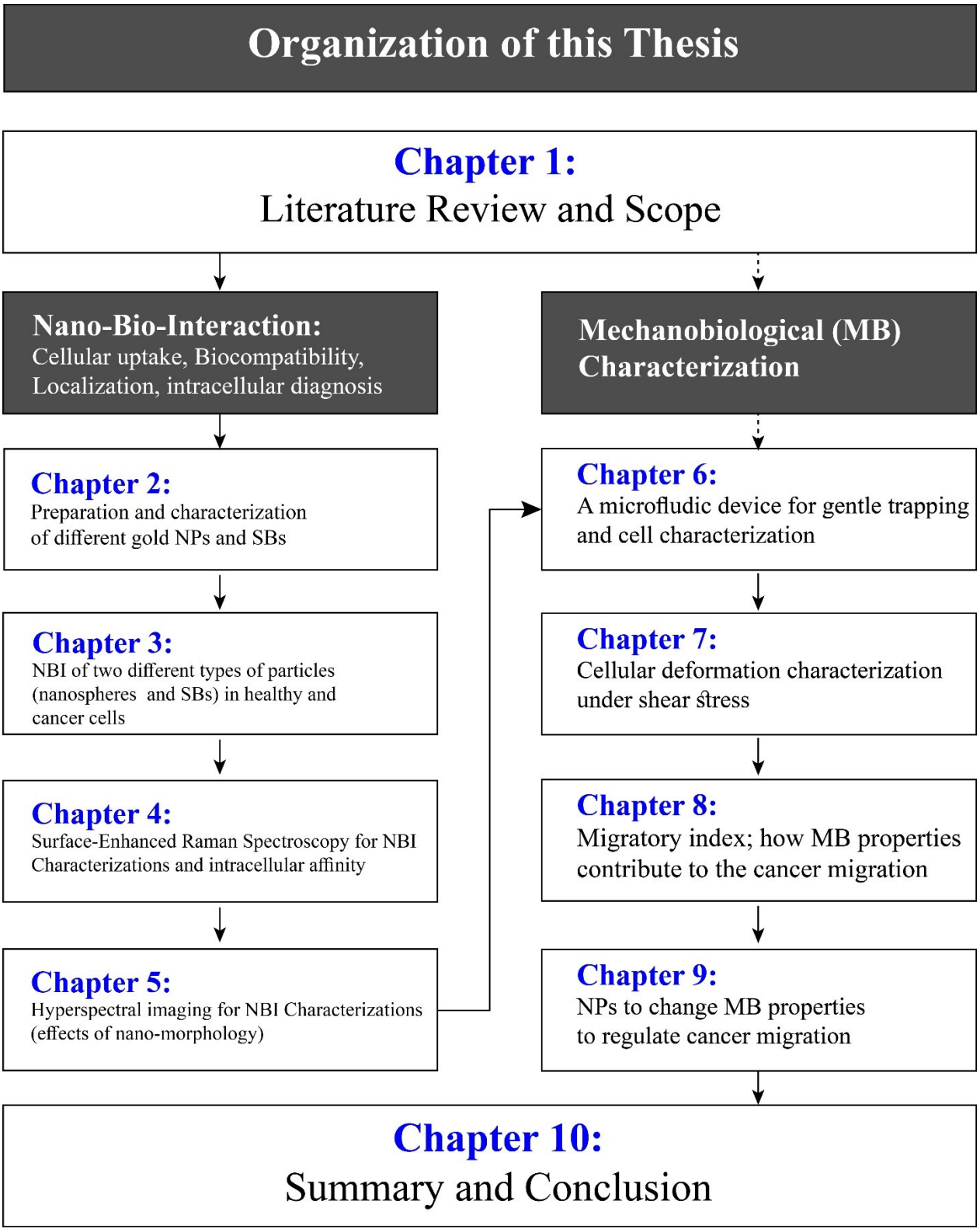

MB: Mechanobiological, SB: Swarna Bhasma, NBI: nano-bio-interaction, NP: nanoparticles

Chapter 2
Preparation and Characterization of Gold Particles

2.1. Introduction

Over the last few decades, nanoparticles research has received increasing attention. Metallic nanostructures possess a variety of physical and chemical properties. The properties of metal particles can be modified by changing their size, shape, surface, composition, and different preparation parameters. Among different metallic particles, gold nanoparticles are important components for their wide-ranging applications such as electronics, photonics, optoelectronics, chemical, and biomedical sensing. Gold particles, in contrast to bulk gold, offer unique opportunities to control their optical properties by modifying their physical properties. Because of this remarkable optical property, they have attracted considerable attractions for biomedical applications. They have been used widely for diagnostic and therapeutic applications based on their unique properties and the possibility of surface functionalization. Gold nanoparticles due to their ability for strong interaction with visible light, are considered suitable candidates for biological and biomedical detections. Gold nanoparticles can bind and accumulate at specific locations in biological cells or tissue, enabling visualization of that area under study. They can be detected with different microscopic techniques including optical microscopy, dark-field microscopy, photothermal microscopy, and confocal microscopy.

Different methods can be used to produce nanoparticles from various materials. Generally, there are two kinds of methods to prepare nanoparticles, “the top-down approach” in which nanoparticles are removed from bulk material using different techniques such as grinding, milling, and chemical methods. Using the top-down approach, a bulky quantity of nanoparticles can be made in a short time; however, this approach needs expensive tools that make their production hard. The second approach is the “bottom-up approach” or “chemical colloidal” in which nanoparticles are prepared from the atomic level (metallic ions). Different techniques such as chemical, electrochemical, photochemical, laser ablation and seed-mediated method are utilized to fabricate nanoparticles from metal ions precursor. Versatility, affordability, homogeneity, and easiness in technological implementation are the main advantages of the bottom-up approach. The “bottom-up” technique is also widely used to produce Nobel metals such as gold and silver.

2.2. Synthesis of Gold Particles

Interesting physicochemical properties of noble metal NPs, such as Gold and Silver, have made them good candidates in many different scientific and technological areas. Noble metal particles are widely prepared by chemical colloidal methods. Various methods are used to synthesize gold NPs. Some of the more commonly used methods ("bottom-up") are explained in the following part.

2.2.1. Turkavich Method (Spherical Gold Particles)

This method is one of the most commonly used techniques for preparing the spherical gold nanoparticles. This technique for the first time described by Turkevich in 1951[152], and then developed by Frens in 1972[153]. With the aid of this technique, gold particles can be synthesized in the size range of 10-20 nm. In this technique, gold particles with varying core sizes are prepared by reduction of chloroauric acid (Au^{+3}, HAuCl4) to gold atoms (Au^{0}) using different reducing agents such as citrate, amino acid, ascorbic acid or UV light. Sodium citrate is used as a reducing agent, and during this process, the color of the solution is changed from pale yellow to dark blue, purple, and ruby-red. The size of particles can also be stabilized using different capping or stabilizing agents. Using the same method, different sizes of particles in the range of 16-147 nm can be produced by controlling the ratio of reducing to stabilizing agents. Other parameters such as pH, temperature, and sodium citrate concentration can influence the generation of particle growth models. The role of monodisperse spherical gold nanoparticles is very important, and they are used as seeds for preparing anisotropic metals NPs, and their formation influences the final structure of the NPs.

2.2.2. Seed Mediated Methods

The seed-mediated technique is one of the most preferred approaches for the controlled synthesis of noble nanocrystals. With this reliable and versatile method, various types of anisotropic NPs can be synthesized, such as rod, stars, cubes, triangles, flowers, and so on. While the Turkevich method is used to generate spherical gold, during this process, the other shapes of particles can be seen. The seeding methodology controls the shape of particles through bypassing spontaneous nucleation or decoupling nucleation from crystal growth. The seed-mediated process includes two main steps. In the first step, seed nanoparticles are synthesized by reduction methods in the presence of stabilizing agents, then the growth of the seeds in growth solutions, including metal precursor, mild reducing agents, and shape-directing reagents. For metal reduction on the

surface of the seed nanoparticles, the activation energy is significantly lower than that for seeds nanoparticles in solutions. Therefore, the autocatalytic growth preferentially occurs on the surface of pre-existing seeds, causing further growth of metal nanocrystals[154], [155]. The size of nanoparticles can be controlled by the amount of seed nanoparticles, and external agents such as various molecules or ions can affect the formation of different shapes of nanoparticles[156]. Cetyltrimethylammonium bromide (CTAB) and cetylpyridinium chloride (CPC) are the two most commonly used cathodic surfactants to manipulate the shapes of nanoparticles. In comparison to other techniques, seed-mediated provides an efficient and versatile method in which nucleation and growth steps are properly separated. In fact, the nanocrystals growth conditions can be tuned while having no effects on the formation of seeds with specific size or structure.

2.2.2.1. Seed-Mediated Methods for Nanostar Particles

In comparison to spherical gold nanoparticles, branched gold nanoparticles (nanostars, nanorods, and nanoflowers) have attracted special interest due to their structural, optical and catalytic properties. For instance, due to their high electric field enhancement, particularly at their sharp edges and tips, they are very sensitive to local changes in the dielectric environment. These features have made them extremely attractive for surface-enhanced Raman scattering (SERS)-based detections. Among different branched particles, nanostars (or multi-branched) gold particles have received much attention. Gold nanostars contain a central core and multiple sharp arms which are protruded from their cores. The seed-mediated method is the most common technique for synthesis of gold nanostars. For the preparation of nanostars, using this method, the chloroauric acid is reduced by ascorbic acid on pre-synthesized seed nanoparticles at room temperature in the presence of surfactants[157]. These surfactants have preferential absorbance on the certain crystalline facets of the metal seeds, leading to the anisotropic growth process by changing the growth rates along specific crystallographic directions. The addition of silver nitride ($AgNO_3$) at different stages of nanocrystal growth influences the growth of the nanostar-shaped particles by providing a higher degree of control[158].

2.3. Ayurveda Gold Particles (Swarna Bhasma)

Ayurveda is an ancient holistic system of Indian medicine. The word of Ayurveda means the science of life. Bhasmas, meaning ash, are the metallic-based Ayurveda medicines which are obtained from incineration [159]. Different metals (gold, copper, silver, etc.), parts of plants, and

plant juices are used to prepare the metallic-based Ayurveda medicines. The Swarna (gold) has a unique place in the Ayurvedic system of medicine and prepared from elemental gold [160]. These metallic particles are utilized in various forms, such as raw gold, purified gold, and incinerated gold, which is called Swarna Bhasma. Swarna Bhasma (also called gold ash or Monatomic Gold) is used for the treatment of patients with various chronic disorders. In the Indian system of Medicine, it is believed that gold possesses various therapeutic values and they can be used for preventive and curative purposes. For instance, they can be used for cough, anemia, arthritis, nervous disease, rejuvenator, aphrodisiac, increasing the longevity of life, and combating the aging process in humans. They can also be used to boost the action and efficiency of various medicine and herbs. [161][162].

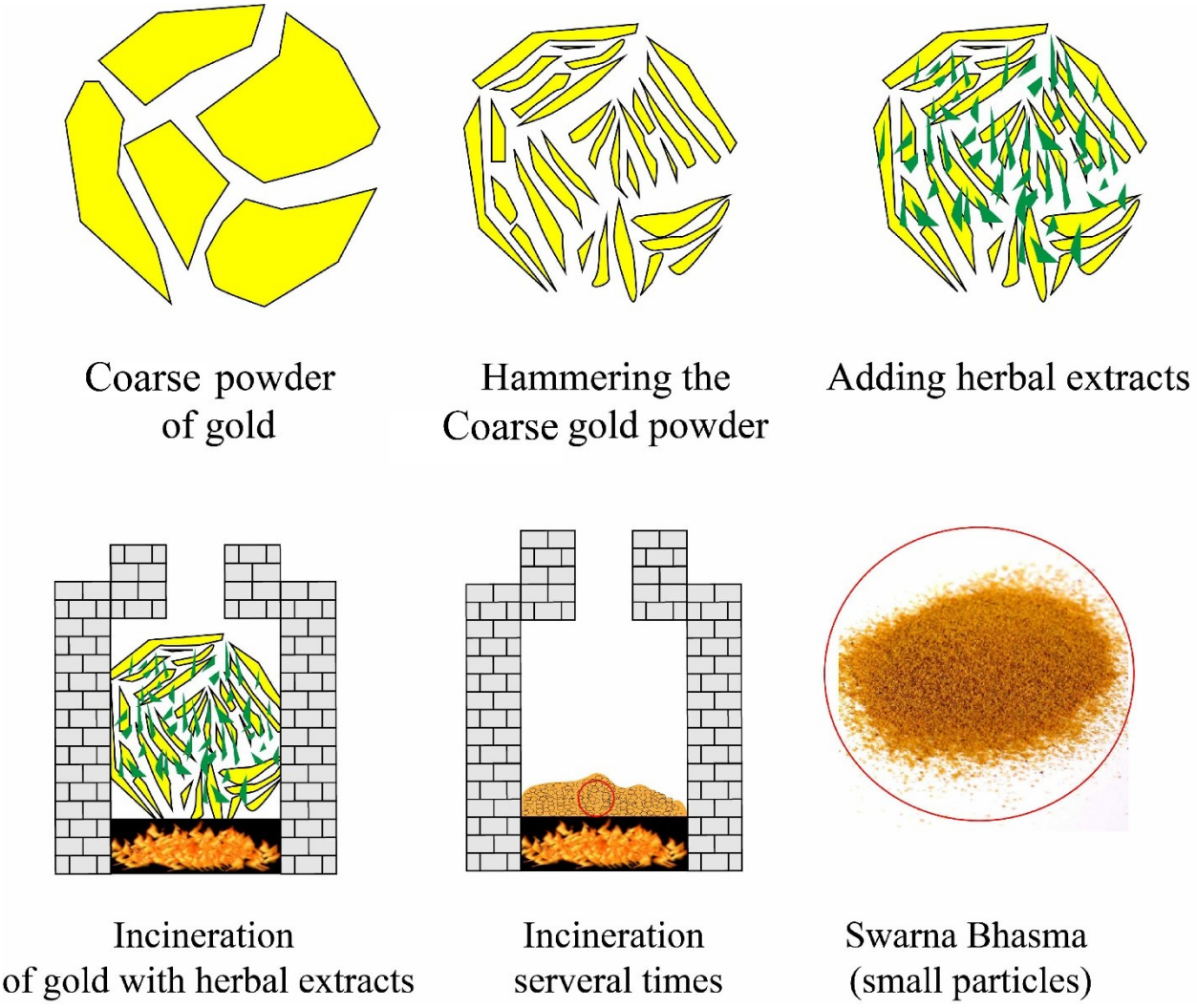

Figure 2-1. *Schematic showing the preparation of Swarna Bhasma (SB)*

2.3.1. Preparation of Swarna Bhasma

Among different forms of Ayurveda medicines, physicians mostly admired the incinerated particles. Bhasmas are very fine powders prepared by classical ayurvedic techniques such as calcination of minerals, metals, natural stones, or gems. During these processes, bulky golds are converted into therapeutic forms. The pharmaceutical preparation procedure is based on purification and incineration concept with herbal media. Based on the *Putapaka* method, three step procedures are required to prepare metal-based medicines: *Shodhana* (purification), *Bhavana* (wet grinding), and *Marana* (incineration/calcination)[163][164]. For the preparation of those nanomedicines, the metals, minerals, and gems are heated (at a high temperature until 1000ºC in earthen crucibles) and are cooled in particular liquid media for specified times. Then, in the wet grinding process, the materials are broken down by rubbing action between two surfaces, producing fine materials. They do these processes sometimes more than 100 times, and the physical and chemical properties of particles are changed compared to the parent metal. These processes are repeated many times in order to remove the toxic effects of the metal/minerals; however, after repeated incinerations, the size of gold particles is reduced more and more and particles are formed with size ranging from microns to nano[165]. Repetition in heating and cooling affects the compression tension equilibrium and brittleness, reducing the harness and particle size. During this method, compounds supplied from the inorganic part of plant materials are formed on the surface of particles.

2.3.2. Characterization of Swarna Bhasma

SBs can be used directly as medicine for various disorders. However, before using them, it is essential to characterize them in terms of size, metal content, chemical composition, and elemental gold[162]. Different methods such as X-Ray diffraction (XRD), energy dispersive spectroscopy, Inductively Coupled Plasma Atomic Absorption Spectroscopy (ICP-AES) and so on can be used to analyze the composition of particles. The physicochemical properties of SBs may vary depending on the geographical region and preparation methods. In work done by *Leslie et al*.[166], the SBs shown to contain 92% gold, and no mercury and organic compounds were found in the sample of SBs. The size of gold particles determined by XRD pattern showed that the gold crystallites lie in the range of 22-37 nm. *Thakur et al*., using XRD, reported that SBs contain more than 98% gold; however, other elements such as iron (Fe), copper (Cu) and Zinc (Zn) were detected

in trace elements. Using a laser particle size analyzer, they showed that the average size of SBs is less than 10 microns, and scanning electron microscopy (SEM) confirmed the globular and irregular shapes of particles. In one of our works[167], we characterized the size of SBs using DLS analysis, revealing that the mean diameter of particles is almost four micrometers while the size of crystallites is approximately 60 nm. The SBs particles are likely formed by aggregation of smaller particles. ICP-MS, XRD, and SEM-EDS analyses revealed that SBs contain only 56% gold which is a low value compared to similar samples characterized in other works. Other elements such as Mg, Ca, Fe and Si were found in the composition of SBs.

2.4. Optical Properties of Gold NPs

The free electrons in the gold and silver can travel through the materials. The mean free path in those two metals is almost 50 nm. Therefore, when size of particles is smaller than the mean free path, all interactions are expected to be with the surface. When metal particles are illuminated by light whose wavelength is larger than the size of particles, the metal's atoms conduction electrons oscillate collectively in resonance with the light frequency with respect to nanoparticles lattice. This collective oscillation is confined on the surface of metallic nanoparticles and called localized surface Plasmon resonance (LSPR). Due to the LSPR phenomenon, absorbance and scattering light occur with extraordinary efficiency in metallic nanoparticles. The LSPR band is determined by the dielectric properties of both the metal and surrounding medium, size, and shapes of particles. When the shape or size of the nanoparticles changes, the oscillation frequency of electrons is changed due to changes in the electric field density of the surface, providing different cross-sections for the optical properties.

The dielectric constant of the surrounding medium also alters the vibrational frequency as it affects the ability of the surface to accommodate the electron charge density of nanoparticles[168][169]. The effects of the capping materials are also very determining in shifting the plasmon resonance as they affect the surface of nanoparticles. This property of metallic particles is widely used for developing biosensors, as chemically bonding molecules induces changes in the LSPR band of particles by changing the electron density on the surface. Spherical gold particles possess LSPR band in the visible region; however, anisotropic nanoparticles show better optical properties compared to spherical particles.

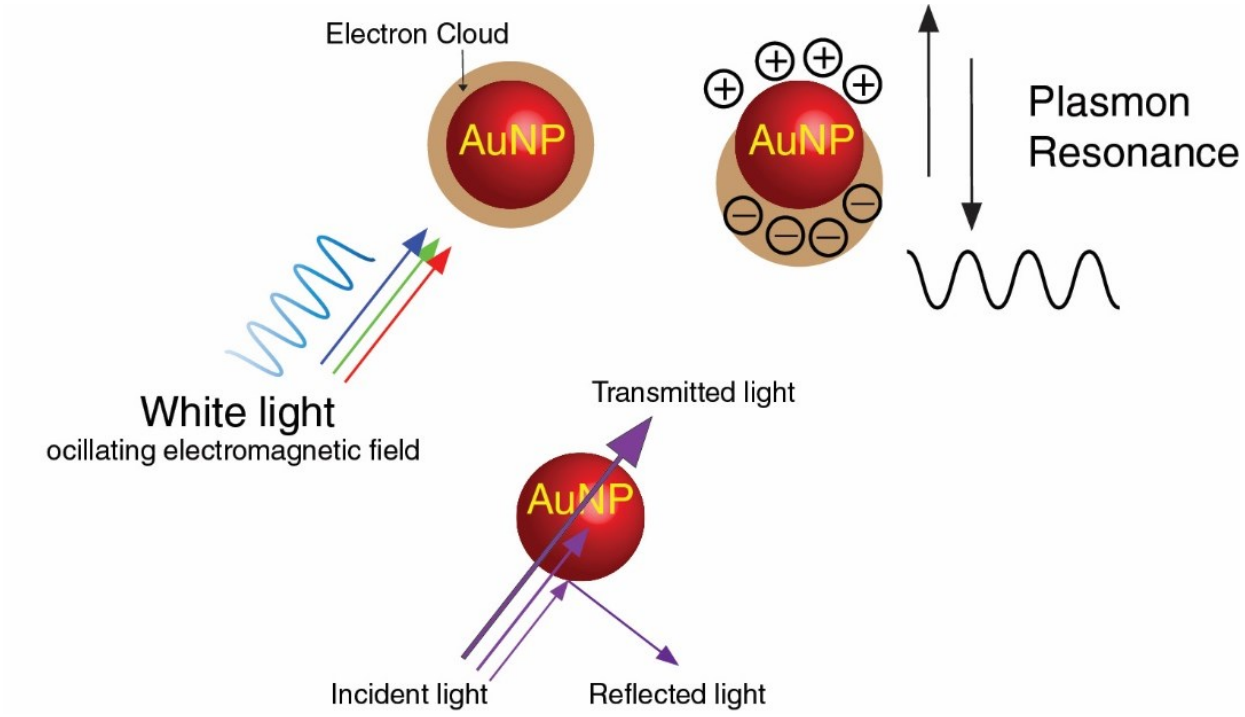

***Figure 2-2**. Schematic diagrams showing localized surface Plasmon resonance on the surface of gold nanoparticles*

2.5. Characterization of Nanoparticles

Before using particles, we need to characterize them. Particles have different properties such as size, shape, chemical composition, surface properties, charge properties, microstructure, concentration, and surface specification[170]. Depending upon the materials of interest, some of these properties can be important.

2.5.1. Inductively Coupled Plasma Mass Spectroscopy (ICP-MS)

Inductively coupled plasma mass spectroscopy is a sensitive method to detect metal and non-metals in liquid samples. With this technique, almost all elements in the periodic table can be detected. In this technique, samples are introduced into an argon plasma containing electrons and positively charged argon ions. ICP-MS cannot detect anions, so in the individual plasma atoms lose their electrons and become positively charged ions. Then, the positive ion beams enter a quadrupole mass analyzer in which the ions are separated based on their mass and charge ratio. Next, with a special mass detector, ions are characterized at higher and lower ranges. Due to the very high sensitivity of this system, this method is an ideal method for the elemental composition of metal-based engineered nanoparticles[171].

2.5.2. X-ray Diffraction (XRD)

XRD is one of the most used methods for the characterization of NPs. XRD provides information regarding the size, structure, nature of phase, and crystalline grain. The composition of the particles also can be determined with XRD by comparing the position and intensity of peaks with a reference pattern. In XRD, a beam of X-rays (electromagnetic radiation) is incident on the sample and the scattered beams are studied. These scattered beams might interface with each other (constructive interface), and this interface can be studied by Bragg's law to characterize the crystal or polycrystalline materials. The XRD technique can be compared with microscopic techniques; however, this is a time-consuming technique and require a large volume of samples.

2.5.3. Dynamic Light Scattering (DLS)

Dynamic light scattering (DLS), also called photon correlation spectroscopy, is a method to characterize the size of particles. In this method, the Brownian motion (BM) of particles is measured and correlated to the size of particles. Larger particles have slower BM, while smaller particles move rapidly. To estimate the size of particles, the intensity fluctuations of the scattered light are measured at very short time increments and are correlated to the BM of the NPs. If particles do not have any interaction with their adjacent particles, the light fluctuations can be correlated to the self-diffusion of particles, and the hydrodynamic diameter of particles can be calculated using the Stokes-Einstein relationship:

$$d_h = \frac{k_b T}{3\pi \eta D} \qquad 2\text{-}1$$

where d_h is the hydrodynamic diameter, D is the diffusion coefficient, T is the absolute temperature, k_b is Boltzmann constant, and η is the viscosity of the medium. The simple operation and rapid analysis time are the two main advantages of the DLS technique. The complicated data interpretation for samples that are not monodisperse is one of the drawbacks of the DLS system. Also, in the DLS technique, it is assumed that all particles are in spherical shapes[170].

2.5.4. Nanoparticle Tracking Analysis (NTA)

With the aid of NTA, particle size and size distribution can be determined. This technique also provides a real-time view of the nanoparticles in a solution. With this technique, the size of particles in the range of 10-1000 nm can be measured. To measure the size of particles, they need to be a suspension, and they are placed on an optically opaque background. A laser is then used to visualize

them directly through an optical microscope. The scattered light of particles is recorded with a light CCD camera, and the Brownian motion of particles is tracked, and their path is recorded. In the DLS technique, the intensity changes of scattered light are measured to calculate the diffusion coefficient of particles while in the NTA diffusion coefficient is calculated based on the movement of individual particles through taking successive optical images[172]. In this technique, the measurement is performed based on counting particles, and in contrast to the DLS methods (intensity weighted), the size distribution can be expressed in number[170].

2.5.5. Scanning Electron Microscopy (SEM)

Scanning electron microscope (SEM) is an electron microscope to provide images of samples' surfaces. To image a sample, a highly energetic focused electron beam is used to scan the surface of the sample, and then the detected signals are projected on a monitor to create an SEM image. As there is no directed path between electron beams and displayed images, the signals can be improved electrically. For conventional SEM instruments, the samples need to be conductive to prevent charging effects as a high vacuum condition is required. So, if they are not conductive, a thin layer of conductive materials such as gold and palladium is coated by low vacuum sputter coating or high vacuum evaporation[173]. Newer SEM system with field emersion guns (FEG) allows imaging uncoated or non-conductive samples at low acceleration voltage. The SEM system and its primary detection mode can provide a very high-resolution image of sample surfaces.

2.5.6. Energy Dispersive X-Ray Spectroscopy (EDS)

Energy Dispersive X-Ray Spectroscopy (EDS) is the second mode of SEM systems. This feature of SEM can be used to determine the elemental composition of the sample as well as their percentage in the analyzed sample[174]. EDS is a valuable tool to detect nanoparticles and characterize their elemental compositions. The EDS analysis is an elemental analysis method in which electron beams are bombarded on the sample, and the emitted x-rays are recorded to characterize the chemical compositions. In the EDS method, the electron beams excite the atoms on the surface of the sample, so specific wavelengths of X-rays are emitted. These wavelengths are characteristic of the atomic structures of the elements. With the aid of an energy dispersive detector, these emitted x-rays are analyzed. This procedure is called energy-dispersive x-ray spectroscopy and is useful for analyzing a very small amount of a specimen[175]. The x-ray generated by EDS can penetrate two microns in depth, so this technique is not limited only to the surface of

samples[176]. The EDS technique can be utilized to determine the composition of nanoparticles containing heavy metal ions at the surface of the sample. For instance, the presence of Au, Pd and Ag nanoparticles can be identified on the surface[177].

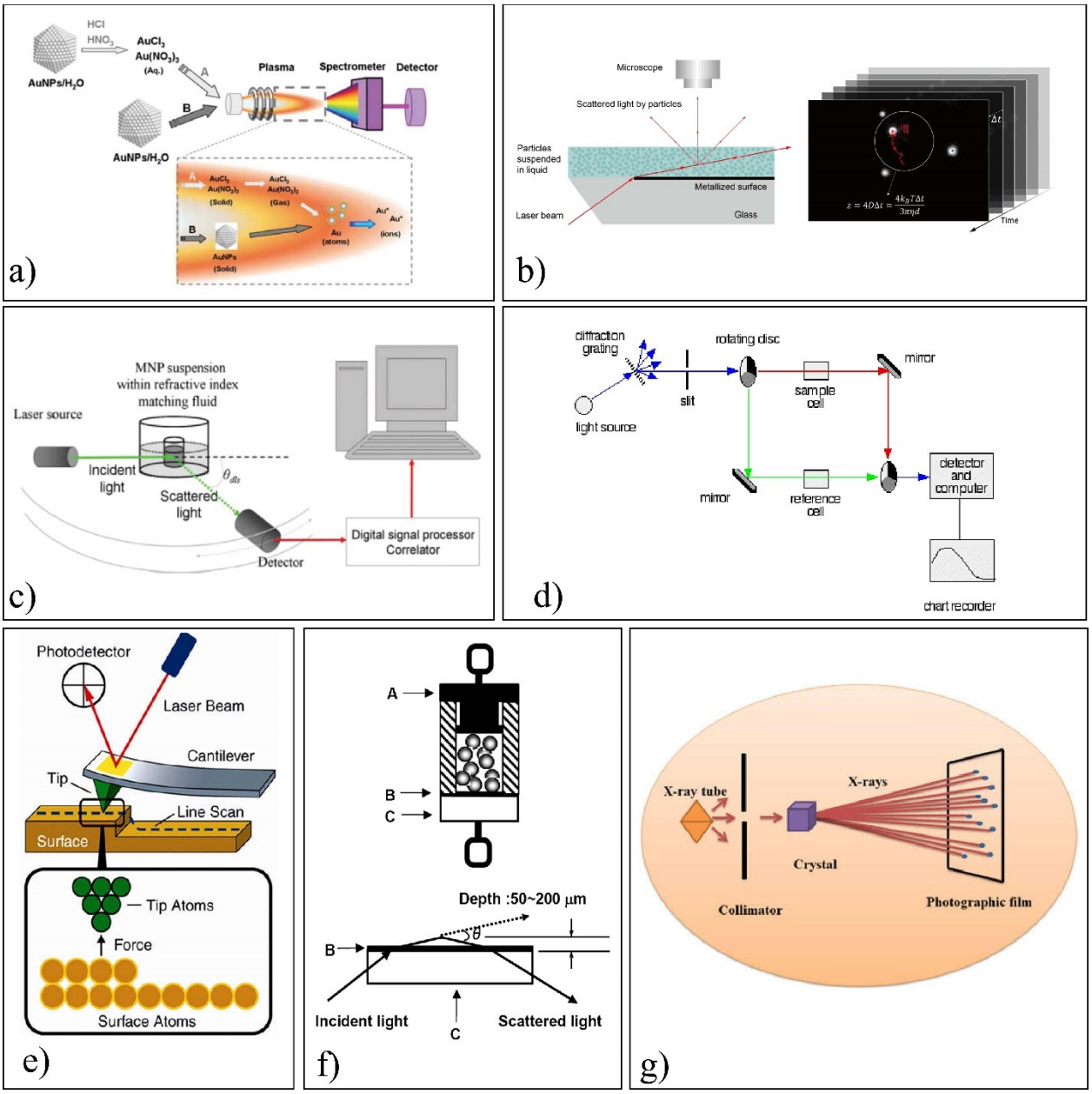

***Figure 2-3**. **a)** ICP-MS method for elemental composition of gold nanoparticles*[178], ***b)** schematic of NTS detection in which the particles are illuminated by a laser beam, and the scattered beams are recorded by a CCD camera attached to the microscope, and with a software, their trajectory is determined*[172]. ***c)** dynamic light scattering methods for particle size characterizations* [179], ***d)** (UV-VIS) spectroscopy system for optical characterization of particles, **e)** Atomic force microscopy for study the topography of particles by scanning the sample with a ting*

microcantilever[176]. ***f)*** *Electrophoretic light scattering (ELS) technique for measuring the zeta potential of particles,* ***g)*** *X-ray set-up for characterization of particles* [180]

2.5.7. Transmission Electron Microscopy (TEM)

In transmission electron microscopy, in contrast to SEM, a beam of electrons is transmitted through an ultrathin sample and interacts with the sample. A TEM image is created from transmitted electrons through the specimen and is recorded on a CCD camera. In TEM, electrons need to pass through the sample, so the samples have to be electron transparent (very thin<100 nm). The thickness of samples depends on the atomic number of sample and it can be increased by increasing the acceleration voltage. To study the morphology of particles, the sample can be thicker; however, for analytical measurements such as energy dispersive X-ray, much thinner samples are required. In TEM, the interaction between the electron beam and the crystalline samples is mostly based on the diffraction, and its intensity is changed by the orientation of planes of atoms in a crystal relative to the electron beam. The TEM technique is widely used for material characterizations and biological science. For TEM, not only the samples need to be thin, but they also have to withstand the high vacuum present inside the instrument. With the aid of TEM, the size of nanoparticles can be determined by imaging homogenously dispersed particles on the TEM grid. The size distribution of particles, then, can be derived by image processing tools[176].

2.5.8. Electrophoretic light scattering (ELS) for zeta potential

The ability of measuring the surface charge of particles and study how this may be changed upon their interaction with a complex biological environment is essential in developing nanoparticle-based drug delivery systems. The surface membrane of cells has a negative charge; thus the surface charge of particles can affect the cellular uptake ability of nanoparticles. Zeta potential is the charge between a solid surface and its surrounding medium. This potential is measured based on Millivolts. The ions distribution in the nearby region of particles is influenced by the net charge at the particle surface. So, a double electrical layer is created at the interface of particles and liquid. The first layer includes ions binding to the particle surface and the second one at the outer region of particles. The neighboring solution conditions (such as pH and temperature) affect the surface charge density of particles dispersed in the liquid. The surface charge of particles cannot be measured directly, so the zeta potential is measured and theoretically, it can be related to the surface charge of particles by solving the Poisson-Boltzmann equation. The zeta potential is defined as the electric potential between the double layers. Particles with zeta potential surface

between +30 and -30 millivolts are considered as unstable and prone to agglomeration. Electrophoretic light scattering (ELS) is mostly used to determine the zeta potentials of particles. With this technique, the electrophoretic mobility of particles dispersed in a liquid is measured to estimate the zeta potential. In this technique, colloidal particles are introduced into a chamber containing two electrodes. An electrical field is then applied to electrodes and particles travel with velocity toward the oppositely charged electrodes. The migration of particles are illuminated with a laser beam, and the velocity is estimated based on the frequency shift in the scattered light. The electrophoretic mobility (U_e) depends on the electric field strength as well as the particle's electric potential. This velocity is measured and correlated to the zeta potential by the Henry equation:

$$U_e = \frac{2\zeta\varepsilon}{3\eta} f(Ka) \qquad 2\text{-}2$$

where ε is the dielectric constant, η is the viscosity of the dispersing liquid, f (Ka) is Henry's function, ζ is the zeta potential of the particle, and Ue is the electrophoretic mobility[181][182].

2.5.9. Ultraviolet-Visible (UV-VIS) Spectroscopy

UV-visible spectrometers are used to measure the light absorbance in the UV-visible ranges from 190 to 800 nm. UV-VIS systems consist of a light source, a reference, and a detector. The reference beam in the spectrometer directly travels to the detector and the sample beam interact with the sample while its wavelength is changed continuously. The detector measure the sample beam intensities ratio (sample cell /reference cell) in order to determine at which wavelength the sample absorbed a large amount of ultraviolet light. The absorption of the visible and ultraviolet radiation excites electrons in atoms of the sample and their level of energy is changed from a low level to a higher level (empty orbital). With this technique, the surface Plasmon resonance peak of nanoparticles (mostly gold and silver) can be determined in UV absorption spectra. The magnitude, band position, bandwidth of Plasmon resonance are changed depending on the size, shape, and material composition of particles and dielectric medium. The peak position of metal nanoparticles (LSPR) is shifted to longer wavelengths by increasing particle size. Based on Mie's theory for spherical particles, only a single band is expected; however, for anisotropic particles, two or more peaks might appear in the spectra profiles.

Table 2-1. *Different techniques for characterization of particles*

Technique	Properties	Strengths (**S**) and limitations (**L**)
ICP-MS	Elemental compositions	**S:** a large liner limit, detecting isotope composition of elements **L:** spectral and non-spectral interfaces and high costs of measurements
Transmission Electron Microscopy (TEM)	Size, and morphology of particles (~1 nm), aggregation state	**S:** higher resolution compared to SEM, direct measurement of size and shape **L:** poor sampling, difficult preparation, and expensive method
Scanning Electron Microscopy (SEM)	Size and morphology of (~20 nm) particles and their dispersion in cells	**S:** Direct measurements of size and shape of particles **L:** only particles at the surface, requiring coating and dry samples, very expensive
Energy dispersive X-Ray spectroscopy (EDS)	Elemental compositions	**S:** high speed measurements, easy to use **L:** destructive technique, energy peak overlaps among different elements [183]
Nanoparticle Tracking Analysis (NTA)	Particle size and distribution (3-1000 nm)	**S:** having a lower concentration limit compare to DLS, capable of identifying two different particles in the same sample[184] **L:** NTA is slower in operation compared to DLS[184]
Dynamic Light Scattering (DLS)	Particle size and distribution	**S:** non-destructive methods, rapid and more reproducible, **L:** not good for polydisperse samples, assumption of spherical shapes
X-Ray Diffraction	Average particles size, structure of particles, crystalline, composition	**S:** well-established technique **L:** low intensity compared to electron diffraction
Electrophoretic light scattering (ELS)	Surface charge and zeta potential	**S:** Simultaneous measurement of many particles **L:** lack of precise and repeatable measurements
UV-Spectrometer	Particles size, LSPR band, concentration, agglomeration state	**S:** easy to use, good accuracy **L:** time-consuming initial set-up
Hyperspectral imaging (HSI)	Particle size, optical properties, location of particles	**S:** in addition to particles' characterization, their locations can be determined. **L:** time-consuming processing time and needs a big storage for storing data
Atomic Force Microscopy (AFM)	NP size and shape in 3D mode	**S:** providing 3D sample surface mapping, measurements in liquid **L:** time-consuming operation, overestimation of lateral dimensions [176]
Raman spectroscopy	Hydrodynamic size and size distribution with indirect analyses	**S:** simple sample preparation, surface-enhanced Raman spectroscopy (SERS) **L:** very weak signals, burning the samples[185]

2.5.10. Hyperspectral Imaging (HSI)

Hyperspectral imaging is a novel optical technique for the characterization of nanoparticles in biological environments. With this technique, particles can be detected in biological environments by studying their optical properties in nanoscale. HSI system consists of a visible-near-infrared (vis-NIR) spectrophotometer connected to a CCD camera. A halogen light source is used to illuminate the sample in the range of 400-1000 nm, and all spectral responses are collected in an HSI image. Each pixel of the scanned area (the image) provides spectral information of that point, allowing it to identify particles and localize them in biological environments. With HSI images, the presence, location, and aggregation level can be characterized. Storing a lot of hyperspectral data and processing them are the main disadvantages of this technique.

2.5.11. Raman Spectroscopy

The Raman spectroscopy can be used to study vibrational, rotational and low-frequency modes in a system. Monochromatic laser light is illuminated to a sample and the inelastic scattering is measured. The laser interacts with different molecular and structural components of the sample and the energy of the laser photons are shifted up or down. The shift provides information regarding phonon modes in the system. When light hits a molecule, it is excited from the ground state to a virtual energy state, generating Stokes Raman scattering. The Raman spectroscopy is used to determine the chemical bonds in molecules.

2.5.12. Atomic Force Microscopy (AFM)

This technique offers 3D images of surfaces at very high magnifications. The 3D image is created based on the interacting force between the surface of the sample and a very sensitive tiny cantilever with a sharp tip. This microcantilever is made of silicon or silicon nitride. When the cantilever scans the surface of the sample, it gets deflected and its deflection is measured by a laser beam. Non-contact based and contact-based are two main modes by which AFM can scan samples. For nanoparticle characterizations, the latter mode is commonly used and the scanning tip is kept 50-150 A° above the sample's surface. AFM topographic images are then created by scanning the tip above the surface.[173] The surface energy, elasticity of microcantilever and the tip curvature are some parameters affecting the final topological values. For AFM measurements, no surface modification such as coating is required. Due to the providing 3D images of samples, contrary to the SEM and the TEM, the height of nanoparticles can be characterized. AFM measurement is

time-consuming compared to the electron microscope. However, it is more compact and much less expensive[184].

In this chapter, different methods for the preparation of gold-based particles were reviewed. Moreover, different techniques for the characterization of nanoparticles were discussed. In the next chapter, these techniques are used to characterize the Swarna Bhasma and citrate-capped gold particles (nanospheres). Then, different imaging techniques are used to characterize them in human cells.

Chapter 3
Study the Cellular Entry of Swarna Bhasma and Chemically Synthesized Gold Particles in Human Cells

This chapter is based on the following two published papers (Paper 1 and parts of paper 2)

1) **Ahmad Sohrabi Kashani**, Kiran Kuruvinashetti, Daniel Beauet, Simona Badilescu, Alisa Piekny, and Muthukumaran Packirisamy. "Enhanced Internalization of Indian Ayurvedic Swarna Bhasma (Gold Nanopowder) for Effective Interaction with Human Cells." Journal of nanoscience and nanotechnology 18, no. 10 (2018): 6791-6798.
2) Beaudet, Daniel, Simona Badilescu, Kiran Kuruvinashetti, **Ahmad Sohrabi Kashani**, Dilan Jaunky, Sylvie Ouellette, Alisa Piekny, and Muthukumaran Packirisamy. "Comparative study on cellular entry of incinerated ancient gold particles (Swarna Bhasma) and chemically synthesized gold particles." Scientific reports 7, no. 1 (2017): 10678.

Gold nanoparticles (AuNPs) are used for a number of imaging and therapeutic applications in east and western part of the world. For thousands of years, the traditional Indian Ayurvedic approach to healing involves the use of incinerated gold ash, prepared with a variety of plant extracts and minerals depending on the region. Here, we describe the characterization of incinerated gold particles (Swarna Bhasma) in HeLa (human cells derived from cervical cancer) and HFF-1 (human foreskin fibroblast cells) in comparison to synthesized citrate-capped gold nanoparticles (nanospheres - AuNPs). We found that while individual SB crystallites are around 60 nm in size, they form large aggregates with a mean diameter of 4711.7 nm, some of which can enter cells. Fewer cells appeared to have SBs compared to AuNPs, although neither type of particle was toxic to cells. Imaging studies revealed that SBs were in vesicles, cytosol, or in the nucleus.

3.1. Introduction

Gold nanoparticles (AuNPs) are used for a number of imaging and therapeutic applications including diagnosis and treatment of cancers[186], [187]. Their physical and chemical properties are tunable, as they strongly depend on size, shape, aggregation state, and surface chemistry[188]. The use of AuNPs in modern medicine can be traced back to their use in the ancient traditional Indian Ayuverdic approach to healing[189]–[192]of many ailments. Ayuverdic (where Ayus means life principle, and veda refers to system of knowledge) is a philosophy, concerned with the protection of “ayus”, by combining healthy living with therapeutic measures. Medicinal preparations typically consist of mixtures of plant- and animal-derived products, minerals and other

metals [190], [193], [194]. Gold derived Ayuverdic medicine is called Swarna Bhasma (gold ash)[191] [164], [195], [196], and testing their localization, entry and impact on human cells in comparison to chemically synthesized AuNPs will be the focus of this study.

Swarna Bhasma gold ash is prepared through a process called Putapaka, which involves heating and quenching gold with various plant extracts. Gold is hammered into a ribbon from a coarse powder, then ground with various herbal extracts and incinerated at high temperature ($\sim 1000\,^{\circ}C$) in earthen crucibles. During the incineration phase, which is repeated several times, the size of gold particles is reduced more and more with each cycle, via mechanical comminution[164], [197]. It is important to note that by this top-down approach, the gradual reduction in size of the gold particles brings them increasingly closer to colloidal AuNPs. The gold ash, Swarna Bhasma (SB), prepared according to Ayuverda texts will be called Incinerated Gold Particles for this study.

Several comparisons have been made between SBs and colloidal AuNPs, which are chemically synthesized through the reduction of gold salts by various natural or chemical reducing agents[198]. Chemically synthesized AuNPs can be made with different surfactants and stabilizing groups, and their size can vary from 1 to 100 nm. Spectroscopic measurements of SBs revealed that they are comprised of individual particles. SBs appear as a red-brown powder and consist of nanoparticles in the range of 50–70 nm, which aggregate to form agglomerates of 2–25 μm in size [197][14][15]. The composition and size of SBs from different pharmaceutical companies is variable. They contain a range of compounds and elements, including heavy metals[199], derived from herbal extracts typically used for medicinal purposes. The presence of heavy metals has been associated with possible contamination of the soil, where the plants are grown, or from the crucibles used for the long calcination processes. Thus, the size, composition, and morphology of AuNPs and SBs are different. However, given that both are used in medical applications, it is crucial to understand how they interact with, and impact, the core physiological functions of human cells[187][198][200].

Several studies have explored the entry mechanisms and cytotoxicity of colloidal AuNPs with different surface moieties, size and morphology *in vitro*, with variable outcomes. In general, small spherical particles (e.g. $<2\ nm$) were reported to cause cytotoxicity in different mammalian cell lines, when compared to rod-shaped particles, although their toxicity varied depending on the surface coating (cationic vs anionic) and the cell line[198][201]. It is assumed that most AuNPs

less than 50 nm in size enter cells via receptor-mediated endocytosis in a clathrin-dependent manner[201][202]. However, evidence suggests that they also enter cells via caveolin-mediated endocytosis or micropinocytosis[203]–[205] depending on their size, shape, surface coating, and if they form aggregates[187], [206]–[209]. Also, they could enter via these different pathways depending on the cell type and/or receptors expressed at their surface[208], [209]. It may also be desirable to target AuNPs to the cytosol or other subcellular locations inside the cell, such as the nucleus or mitochondria. However, to do this, they must escape from the endomembrane system, since particles are initially contained in vesicles, regardless of the mechanism of entry[210]. Surface functionalization could promote their escape from lysosomes into the cytosol, as in the case of encapsulation of AuNPs in a cationic core-shell polymer colloid that expands upon acidification in the lysosome causing rupture[211], while larger aggregates could mechanically disrupt vesicle membranes. There are reports of using protein tags with specific amino acid sequences known to mediate transport into the nucleus[212] or mitochondria[213], [214]. Again, it is not clear how these tags have accessibility to the protein complexes that recognize them when the particles are retained in vesicles, particularly when they are in lysosomes or autophagosomes. However, once they are in the cytosol, the tags could become accessible to mediate transport. In addition, very small particles may not require tags to pass through the nuclear pores, or outer mitochondrial membrane.

This paper presents a comparative study of AuNPs and SBs in their (i) localization, (ii) physiological impact and (iii) entry in cancerous and non-cancerous human cells, which are crucial to understand for their design and therapeutic use. We found that SBs contain a large variety of elements, some of which are present at significant concentrations (e.g. Mg and Ca). While individual SB crystallites are 60 nm in size, they form large aggregates with a mean diameter of 4711.7 nm. In order to assess the toxicity of SBs and AuNPs to human cells, the interaction with both healthy (HFF-1) and cancerous cells (HeLa) was studied through a number of imaging techniques. It was observed that the viability of HeLa and HFF-1 cells after treating them with gold ash (Swarna Bhasma) particles, does not change, even by increasing the concentration or the incubation time. Imaging revealed that while some SBs were in membrane-bound vesicles or vacuoles, others were in the cytosol and nuclei of cells, while AuNPs accumulated primarily in the endomembrane system. Mechanically disrupting SBs (broken particles) into smaller 100–200 nm particles increased their accumulation in cells where they localized to the endomembrane system

similar to AuNPs. Interestingly, larger SBs accumulated in the nuclei of HeLa cells after nuclear envelope breakdown during cell division. Further studies revealed that SBs enter cells by more than one mechanism. These studies show that SBs are large, inert aggregates, which could be explored for use as carriers.

3.2. Material and Methods

3.2.1. Swarna Bhasma (SB)

Indian gold ash (Thanga Parpam, Siddha Medicine) was purchased as a powder from Jaya Indian Medicine Pharmaceutical Pvt. Ltd., Maduravoyal, Chennai, Tamilnadu, India. In all experiments, gold ash particles hereafter referred to as incinerated gold particles (SBs), was suspended in deionized water. Samples of re-suspended SBs were cast on glass slides and dried at room temperature to collect SEM (Scanning Electrical Microscopy) images, using a Hitachi S 3400N. Dynamic Light Scattering (DLS) experiments were performed by Dynalene Lab Services on the re-suspended SBs, using a Nicomb 380 instrument to characterize their size. 7700× Agilent ICP-MS (Inductively-Coupled Plasma Mass Spectroscopy) was used to measure the elemental composition of the SBs. Briefly, aqua regia (3HCl:1HNO3) heated at 110 °C for 3 hours was used to digest the sample. After cooling, the sample was filtered through a 0:2 µm PTFE filter, before the measurements were performed.

3.2.2. Synthesis of Citrate-capped Gold Nanoparticles (nanospheres)

Citrate-capped spherical AuNPs were prepared by the reduction of chloroauric acid with sodium citrate using the Turkevich method[215], [216]. Briefly, 75 ml of chloroauric acid solution containing 45 µg/ml gold was heated, and 5 ml of 1% sodium citrate was added to the boiling solution. After the solution turned purple, it was boiled for another 15 minutes, then left to cool to room temperature.

3.2.3. Mechanical Disruption of Swarna Bhasma

Breaking SBs into smaller particles and dispersing them in the de-ionized water, was done in two steps: (1) using an Omni mixer Homogenizer (600 W power) for 20–25 minutes at variable speeds, and (2) using ultrasonic waves with the Branson 200 Ultrasonic cleaner at 40 kHz 8–10 times for five minutes each time (**Figure 3-1**).

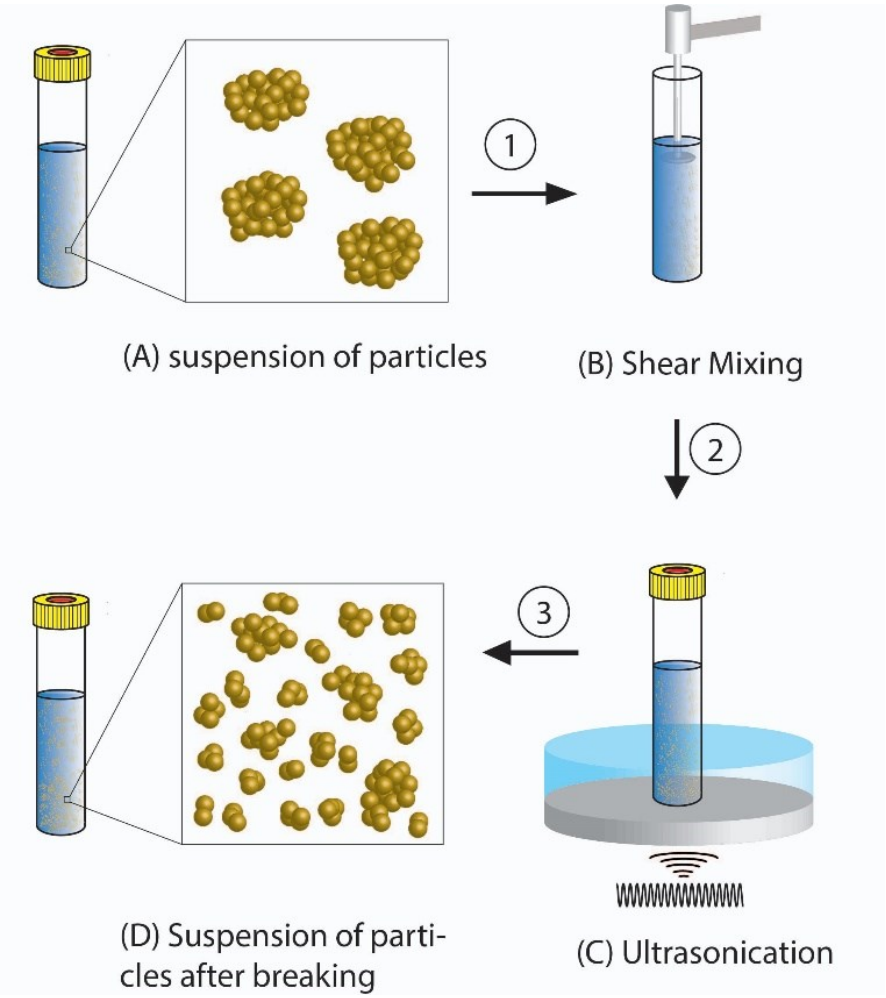

Figure 3-1. *A Schematic diagram illustrating the process of mechanical disruption of SBs. First, SBs, suspended in deionized water, are dispersed, using a shear mixer (step 1). Next, the sample tube, containing SBs and DI water, is placed in an ultrasound bath, to break larger particles into smaller particles (Step 2), (a) Suspension of SBs, (b) Shear mixing the large particles in DI water, (c) Sonication to reduce the size of large particles, (d) Particles, after breaking*

3.2.4. Cell Preparation

HFF-1 (human foreskin fibroblast) and HeLa (human cervix adenocarcinoma) cells were cultured in Dulbecco's modified Eagle's Medium (DMEM; Wisent), supplemented with 10 or 15% Fetal Bovine Serum (FBS) 100 U penicillin and 0.1 mg/ml streptomycin, and 2 mM L-glutamine. Cells were incubated in a humidified chamber at 37 °C and passaged when they were 75–100% confluent. To prepare slides for imaging, cells were plated on acid-washed coverslips in 6-well dishes at 40% confluency prior incubation with SBs.

3.2.5. Cell Fixation for Microscopy and Imaging

Cells were fixed and stained for immunofluorescence. DAPI (4,6-diamidino-2-phenylindole, Sigma-Aldrich) was used to visualize DNA and 1:250 mouse anti-tubulin antibodies (DM1A, Sigma-Aldrich) and anti-mouse Alexa 488 secondary antibodies (at 1:400 dilution) were used for staining microtubules. Cells plated on coverslips were washed with pre-warmed PBS, and then fixed in ice-cold 10% w/v TCA in water. Afterwards, cells were washed three times with TBST buffer (150 mM NaCl, 50 mM Tris pH 7.4, 0.5% Triton X-100), after which DAPI was added at 1:1000 dilution (1 mg/ml stock) for five minutes. Cells were washed twice with TBST, then once with 0.1 M Tris pH 9, after which, one drop of mounting media (4% n-propyl gallate in 50% w/v glycerol, 50 mM Tris pH 9) was added to each coverslip. A Leica DMI6000B epifluorescence microscope was used to image the fixed cells with the 63×/1.4 PL APO oil immersion objective (pixel size 0.102 m). Z-stacks of 0.5 m were acquired with a Hamamatsu OrcaR2 camera and Volocity software (PerkinElmer) using a piezo Z stage (MadCityLabs). All images were exported as TIFFs, and Image J (NIH) was used to convert them into maximum intensity z-stack projections.

For SEM measurements, cells were fixed with TCA as described above, but instead of washing with TBST, cells were dehydrated with a series of ethanol solutions. Cells were incubated with 50% v/v ethanol in water for 15 minutes, then in 60%, 70%, 80%, 90% and 100% ethanol, each time, for 15 minutes. The coverslips were added face up to glass slides and left to dry in a fume hood overnight. After sputtering the coverslips with gold, cells were imaged by SEM using the Hitachi S 3400N, with the voltage of 15 kV and a vacuum of 50 Pa.

Hyperspectral microscopy was performed using the CytoViva hyperspectral imaging system with enhanced dark-field optical illumination (CytoViva, Inc) on AuNPs or SBs in HeLa cells. Using the 60x/1.4 or 100x/1.4 oil objectives, dark-field images were collected at oblique angles, and the reflective fluorescence was measured for selected pixels, using a spectrophotometer integrated CCD, with a spectral range of 400–1000 nm and spectral resolution of 2.8 nm

3.3. Results

3.3.1. Physicochemical Characterization of SBs and AuNPs

SB particles of varying shapes and sizes were compared. Particle aggregation occurs during the incineration steps, which are carried out for long periods of time at high temperatures. Consistent with previous studies, DLS measurements showed that SBs have a wide size

distribution, with an average of 4711.7 nm (**Figure 3-2c**). **Figure 3-2a** and **c** show SEM images for larger (unbroken) versus smaller SB particles, after mechanical disruption. The large, unbroken particles shown in **Figure 3-2a** appeared to be non-uniform in size and shape, while the broken particles were smaller in size (150– 300 nm) and more uniform in shape (**Figure 3-2b**). Due to the different preparation processes, the compositions of the Swarna Bhasma particles may be slightly different. For this reason, the elemental composition of the SBs used in this study was quantified *in vitro*, using ICP-MS and SEM-EDS.

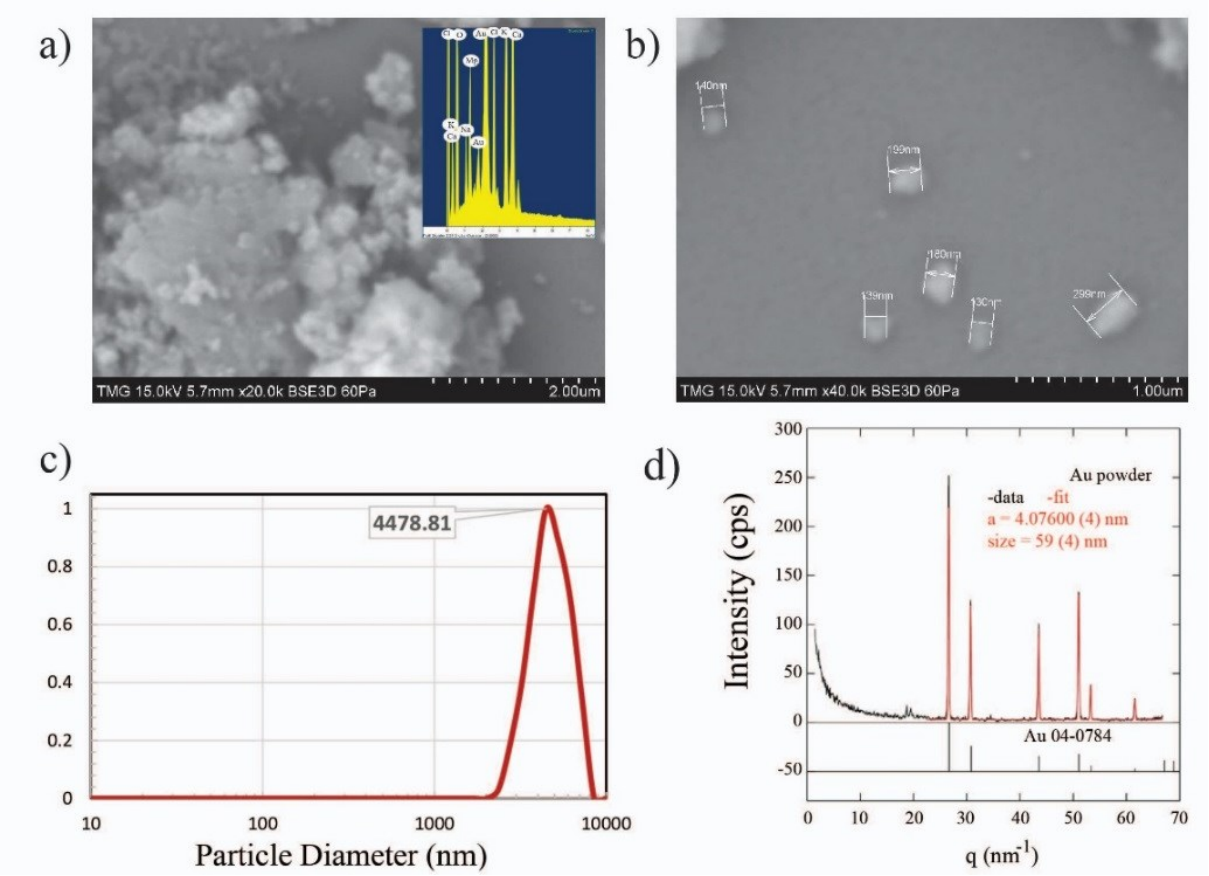

Figure 3-2. a) *A SEM image of unbroken SBs showing the size of the aggregates and EDS-SEM (inset) indicating the elemental composition of particles,* ***b)*** *SEM image of the aggregates after mechanical disruption of the particles and their sizes,* ***c)*** *a graph showing the average size of Swarna Bhasma by DLS measurements,* ***d)*** *a graph shows the XRD pattern of SBs in comparison to Au, and the size of individual particles is indicated.*

As shown in **Table 3-1** and **Figure 3-2a** (inset)**,** gold was found to be the most abundant element in SBs. Interestingly, this value was low in comparison to other samples that have been characterized. ICP-MS revealed that the particles contained other elements, some of which were

present at higher concentrations, such as Mg, Ca, Fe, and Si (0.29–1.9%), while others (Mn, Ni, As) were found in trace amounts (**Table 3-1**). This was consistent with EDS-SEM results, which showed that the concentration of gold appeared to vary depending on the area used for analysis, with significant peaks corresponding to elements including Mg, Ca, Fe, and Si (**Figure 3-2a**). Additional components in the SBs are likely oxygen and carbon caused by oxidation during the incineration process. The presence of oxygen in Bhasmas was revealed by X-ray fluorescence spectroscopy.

Table 3-1. *The elemental composition of SBs determined by ICP-MS*

Elements	Concentration %
Gold (Au)	56.88
Mg	1.8
Ca	1.4
Fe	0.29
Si	0.29
Trace Elements	
Mn	0.037
Ni	0.02
As	0.15

We characterized the synthesized gold nanoparticles (AuNPs) to compare their physicochemical properties with SB particles. The average diameter of the colloidal AuNPs was calculated to be 32 nm. The elemental composition of colloidal AuNPs as determined by ICP-MS and EDS revealed that gold was the most abundant element as expected (**Table 3-2**; **Figure 3-3c**). Imaging AuNP by SEM showed that they are spherical in shape and may vary in size between 100–200 nm (**Figure 3-3b**).

Table 3-2. *The elemental composition of synthesized AuNPs determined by ICP-MS.*

Elements	Concentration (ppm)
Gold (Au)	89.6
Mg	0.273
Ca	1.16
Na	20.9
Si	2.69

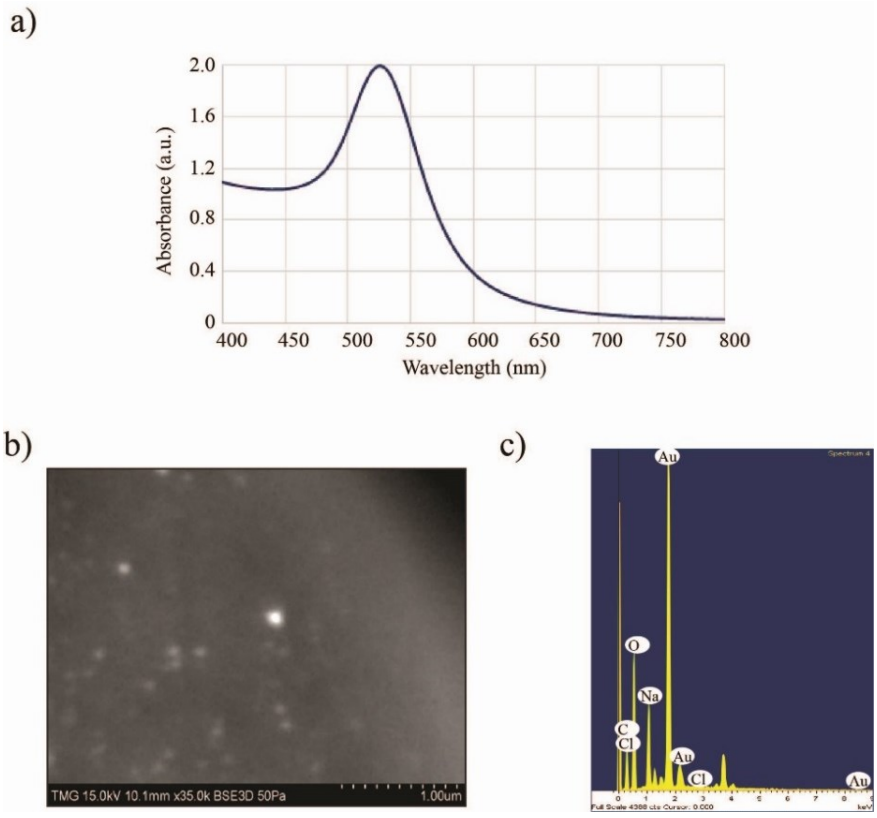

***Figure 3-3**. **a)** The graph shows the LSPR band corresponding to colloidal gold, **b, c)** AuNPs were imaged by SEM, **b)** and by EDS-SEM, **c)**, which shows the shape and size of the particles, and the elemental composition, respectively.*

3.3.2. Characterizations of SBs versus AuNPs in Human Cells

Since SBs have not been studied in human cells, their toxicity and subcellular location were characterized in comparison to AuNPs. Two well-characterized human cell lines were chosen for this study, namely HeLa cells, derived from human cervical adenocarcinoma, and HFF-1 (human foreskin fibroblasts) cells, which are non-cancerous. HeLa and HFF-1 cells were treated with AuNPs and SB particles for 4 days. After, the cells were fixed and stained for tubulin, which is the core component of microtubules that controls cell architecture, and DAPI to visualize chromatin (**Figure 3-4**). The bright-field and fluorescence microscopy images in **Figure 3-4** revealed that AuNPs accumulate in the endomembrane system surrounding the nucleus, which includes the Golgi and endosomes. High levels of AuNPs accumulated in cells and appeared to be non-toxic, as no cell death was observed up to a week after treatment. . Fewer cells had SBs, and their distribution was more varied in comparison to the AuNPs. While some of the particles appeared to be in the endomembrane system surrounding the nucleus, others were in vacuoles, cytosol, or in

the nucleus as seen in **Figure 3-4a**. Interestingly, some of the larger aggregates disrupted the microtubule networks, which appeared to 'bend' around them (**Figure 3-4b**). Similar to the AuNPs, the SBs appeared to be non-toxic, as no cell death was observed up to a week after treatment.

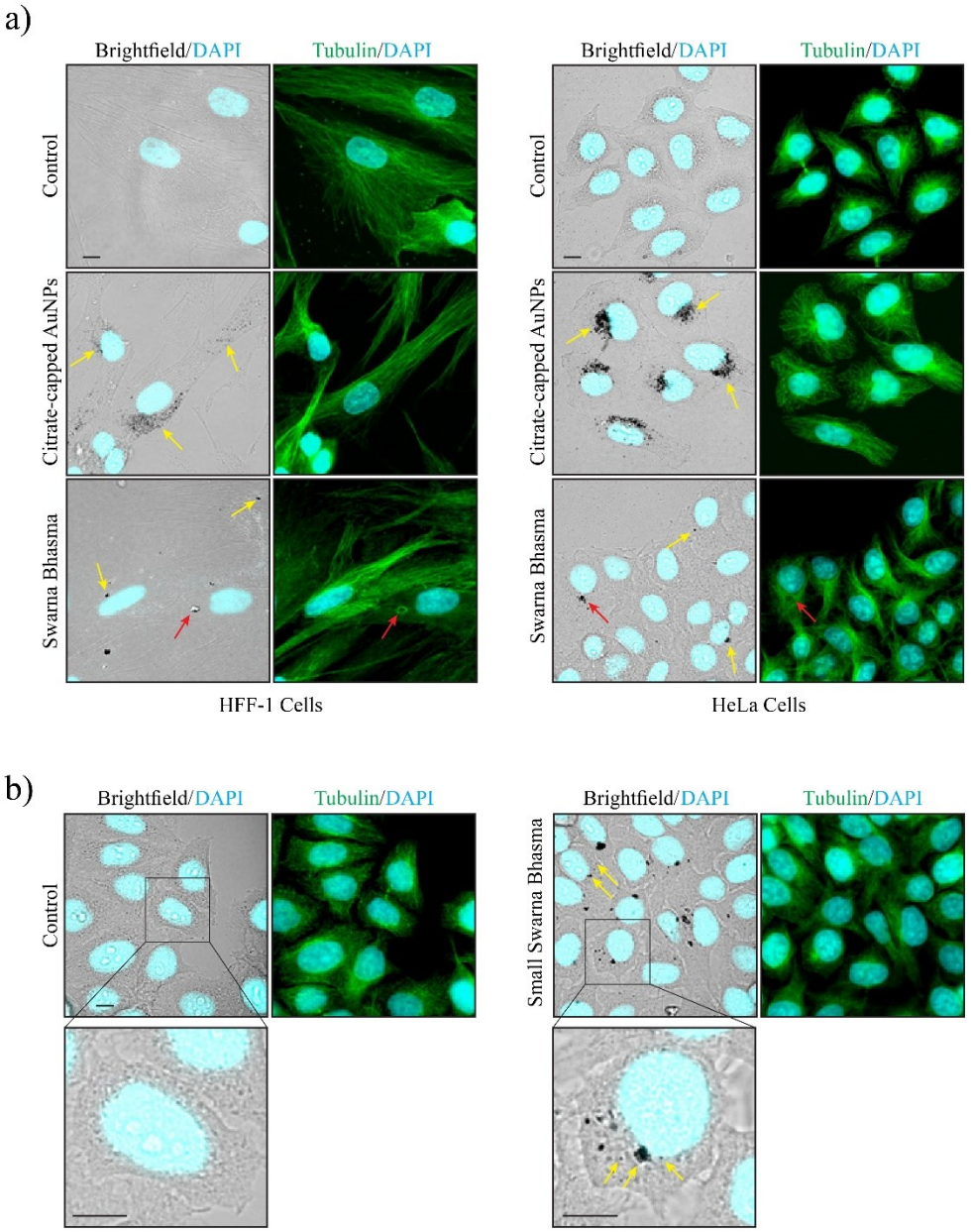

Figure 3-4. a) *Bright-field and fluorescence images of HFF-1 and HeLa cells co-stained for DAPI (to stain DNA; blue) and tubulin (to stain microtubules; green) show the location of AuNPs and SBs (yellow arrows). The red arrows point to microtubules that have been displaced around a particle.* ***b)*** *Bright-field and fluorescence images of HeLa cells co-stained for DAPI (blue) and tubulin (green) show the location of mechanically disrupted SBs (small; yellow arrows). The scale bars are 10μm.*

3.3.3. Effects of Dosages (SBs) and Incubation Times on Human Cells

HeLa cells were treated with 10 µg of SBs, then fixed and stained for imaging by the light microscopy, after 24 and 72 hours (different incubation time). HeLa cells divide once every 24 hours, and the two time points (24 and 72) represent one and three population doubling times, respectively. **Figure 3-5** shows that there was an increase in the number of cells, after three population-doubling times, and SBs were visible in HeLa cells at both incubation times (black arrows). These data suggest that SBs are not toxic to HeLa cells. Also, the particles appeared to be distributed randomly in the cells. It is seen that the number of cells containing particles decreased as the cell number increased, suggesting that, due to multiple rounds of division, they were distributed between the cells. To test the effect of the SB dosages on the cell viability, HFF-1 cells were treated with 5, 20 or 60 µg of SBs to reach the final doses, as indicated. Approximately 24 hours after treatment, cells were fixed and stained for imaging by the light microscopy (**Figure 3-6**). It can be seen that, when the dose increased, a higher proportion of cells contained SBs (black arrows; **Figure 3-6**). The cytoskeletal integrity of the cells remained intact as shown by tubulin staining. Collectively, the data suggest that SBs are not toxic to HFF-1 cells, even at high concentrations when most of the cells appeared to contain particles.

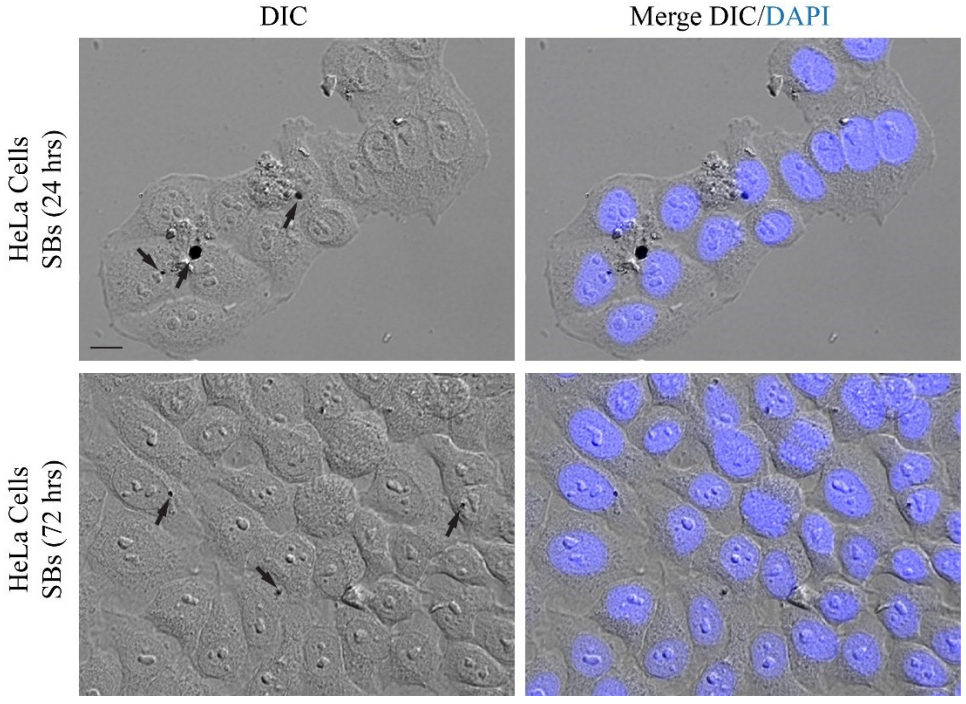

***Figure 3-5**. SBs are not toxic to HeLa cells. DIC (Differential interference contrast), merged DIC, and DAPI to stain DNA (blue; right) show fixed HeLa cells 24 and 72 hours, after treatment with*

10 µg SBs. Black arrows point to SB aggregates, which appear in random subcellular locations, including the cytosol and the nucleus

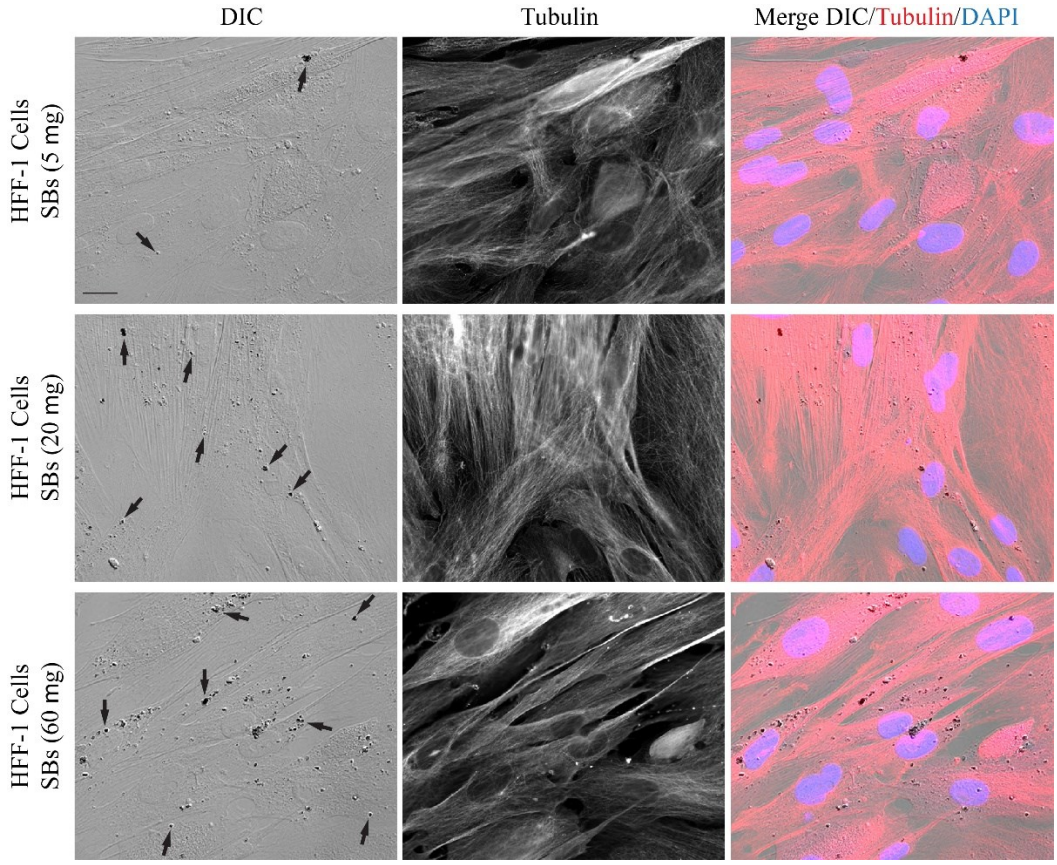

***Figure 3-6**. SBs are not toxic to HFF-1 cells. DIC , tubulin (middle), and merged overlays with DIC, tubulin (red) and DAPI (blue; right) show HFF-1 cells after increased dosing (20, 40 and 60 µg) with SBs (black arrows) as indicated. After a total of 60 µg of SBs were added to the cells, each cell contains SBs and their integrity is maintained.*

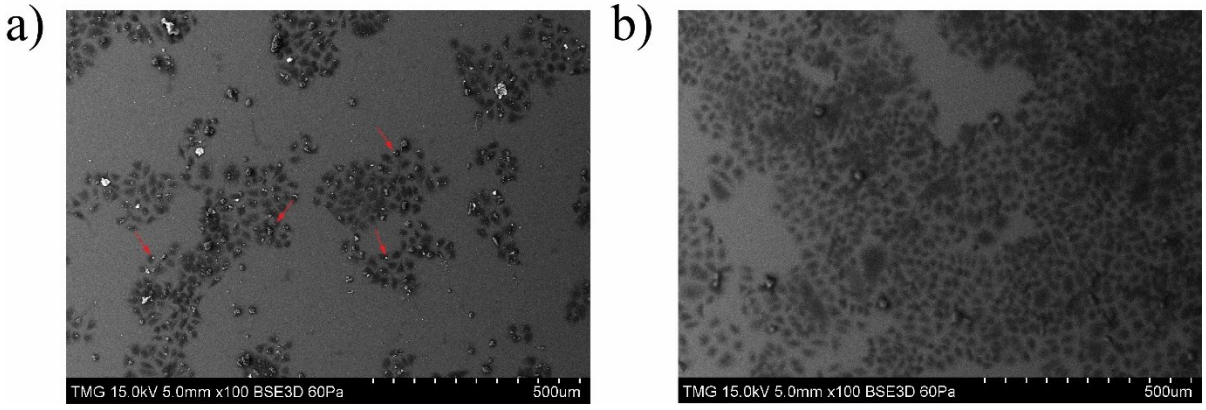

***Figure 3-7**. Broken SBs easily accumulate in HeLa cells. **a)** SEM images of HeLa cells incubated with 20 µg of broken SBs, **b)** control HeLa cells (not treated with particles).*

To characterize the distribution and localization of SBs in human cells, SEM was used to take images of SBs in HeLa cells before (unbroken) and after the mechanical disruption (broken). **Figure 3-7** illustrates how the broken SBs (a), versus untreated control cells (b), were distributed in HeLa cells, by showing a large area of cells after treatment with 20 µg SBs. While some aggregates were visible outside of the cells, a large number of cells contained SBs. **Figure 3-8 a**, **b** shows the SEM image of the broken and unbroken SB particles, respectively. In **Figure 3-8a**, several aggregates can be seen outside of the cells, and only a few particles inside the cell. However, **Figure 3-8b** and **c** show that, after mechanical disruption of particles, more particles are visible in random subcellular locations, including near the nucleoli (in the nucleus), and in the cytosol. The distribution and localization of broken particles within the cells suggest that breaking the large aggregates of SB into smaller agglomerates through mechanical disruption enhances their uptake into HeLa cells.

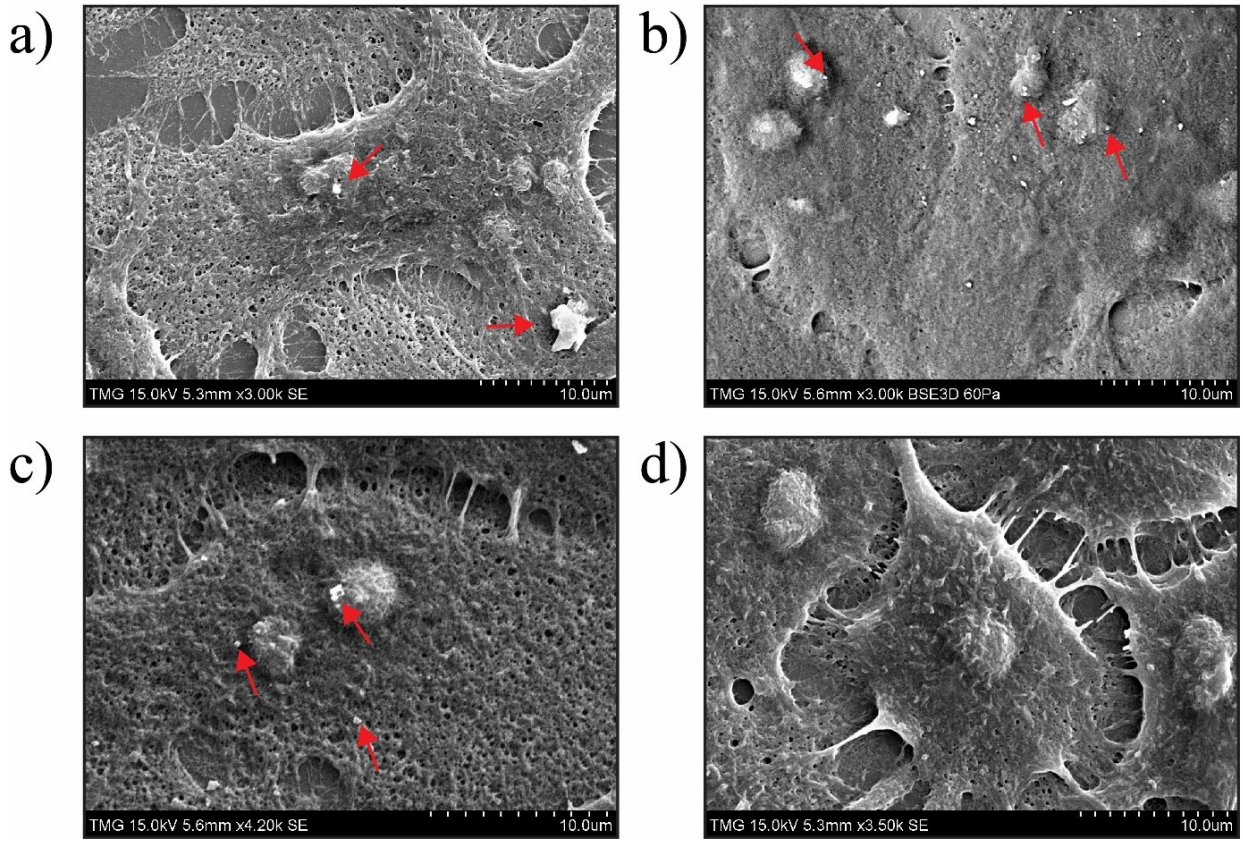

***Figure 3-8**. SBs localize randomly in HeLa cells. **a)** SEM image of HeLa cells treated with unbroken Swarna Bhasma, **b,** and **c)** SEM image of HeLa cells treated with broken SBs, **d)** control HeLa cells (not treated with particles). Red arrows indicate aggregates and particles.*

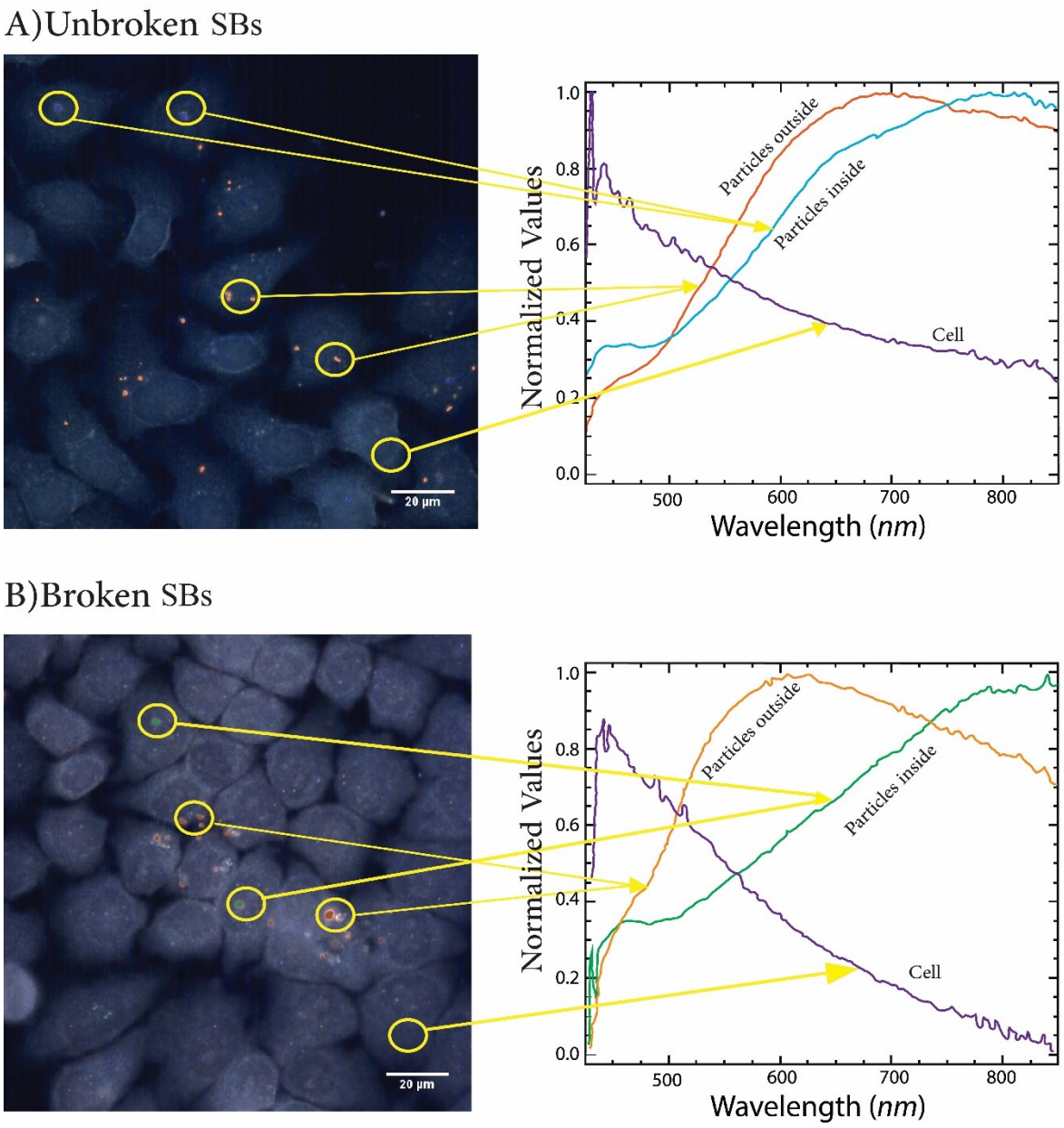

Figure 3-9. *Broken and unbroken SBs have different spectral properties in different subcellular locations in HeLa cells.* ***a)*** *Enhanced dark-field hyperspectral images of HeLa cells with unbroken SBs and their corresponding spectral profiles. The arrows point to SBs in the cytosol (orange graph) and nuclei (blue graph) of cells.* ***b)*** *Enhanced dark-field hyperspectral images of HeLa cells incubated with broken SBs and their corresponding spectral profiles. The arrows point to SBs in the cytosol (orange graph) and nuclei (green graph) of cells. Purple spectral profiles on each graph show the spectra of HeLa cells corresponding to the indicated areas. Graphs show wavelengths on the x-axis (in nm) and the normalized lamp spectrum on the y-axis. The scale bars for the images are 20 µm.*

3.3.4. Characterization of SBs in HeLa Cells by Hyperspectral Imaging

To further characterize SBs in HeLa cells, enhanced dark-field hyperspectral images were taken of unbroken and broken SBs. CytoViva technology distinguishes the spectral response coming from aggregates or particles of different sizes. Unbroken SBs in the cytosol results in an Au plasmon band around 700 nm, while SBs, localized inside the nucleus absorb at a longer wavelength (800 nm; **Figure 3-9** and **Figure 3-10**). Interestingly, broken SBs in the cytosol have a plasmon band around 600 nm, while those in the nucleus show a band around 800 nm (**Figure 3-9b** and **Figure 3-10**). The shift toward the Near-Infrared region of the spectrum for the unbroken SBs in the cytosol likely is due to their size. The difference between SBs in the cytosol versus nucleus may reflect different molecular interactions in different subcellular components. These results show that dark-field hyperspectral technology is a powerful method for the characterization of gold particles in cells, by providing invaluable information on inter-particle interactions as well as on possible influences of different components of the cells.

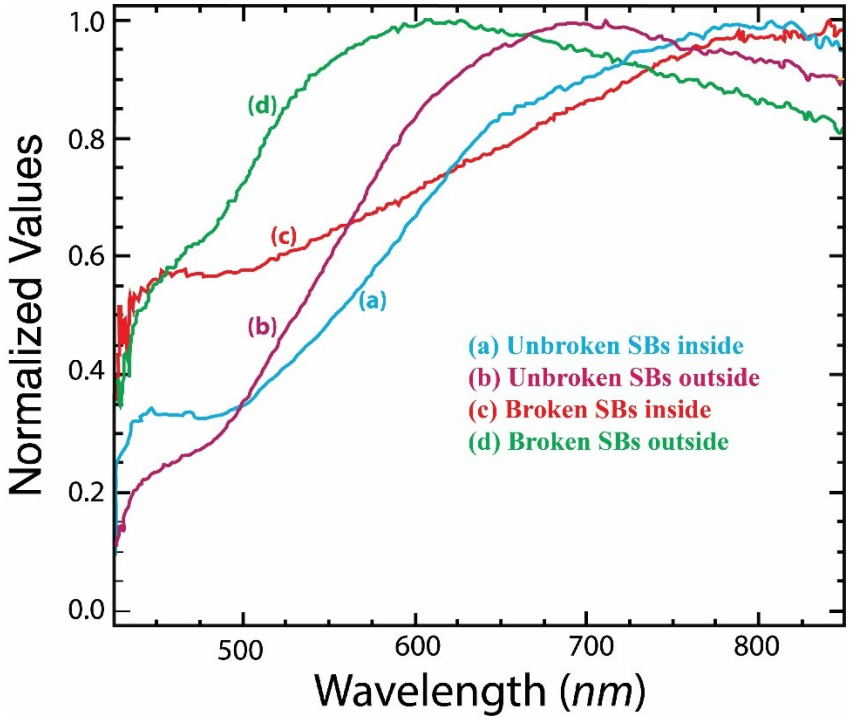

Figure 3-10. *Broken and unbroken SBs have different spectral properties in different subcellular locations in HeLa cells. A comparison of the spectral profiles of SBs is shown for unbroken (a and b) and broken aggregates (c and d). The graphs show wavelengths on the x-axis (in nm) and the normalized lamp spectrum on the y-axis.*

3.3.5. Nuclear localization of SBs

The nuclear localization of SBs was also investigated. Through functionalization, AuNPs can escape from lysosomes into the cytosol, where they could gain access to organelles such as mitochondria or the nucleus[210][213][214][211]. Although anti-cancer drugs like Doxorubicin can enter the nucleus without requiring a carrier, it may be desirable to use a carrier to have more control over drug targeting and/or release[217], [218]. AuNPs can be further modified so that after their escape into the cytosol, they can be selectively targeted to the nucleus[214]. However, particles in the cytosol could also randomly incorporate into the nucleus during division. As cells enter mitosis to divide, their nuclear envelope breaks down, and nuclear components mix with the cytosol until they are re-packaged during telophase. SBs were observed in the nucleus of a small proportion of HeLa cells. To determine if SBs can be sequestered in the nucleus by chance during cell division, DIC microscopy was used to image dividing HeLa cells containing citrate-capped AuNPs or SBs (**Figure 3-11**). During mitosis, AuNPs remained closer to the cell poles as indicated by the yellow arrows in **Figure 3-11**. This is consistent with their retention in vesicles of the endomembrane system, which remain near the centrosomes during mitosis. The distribution and movement of SBs were random, as some particles remained close to the condensed chromatin, while others moved to opposite sides of the cell as shown in **Figure 3-11**. Therefore, this data suggests that SBs are randomly sequestered in the nucleus during nuclear envelope reformation after cell division rather than being selectively targeted.

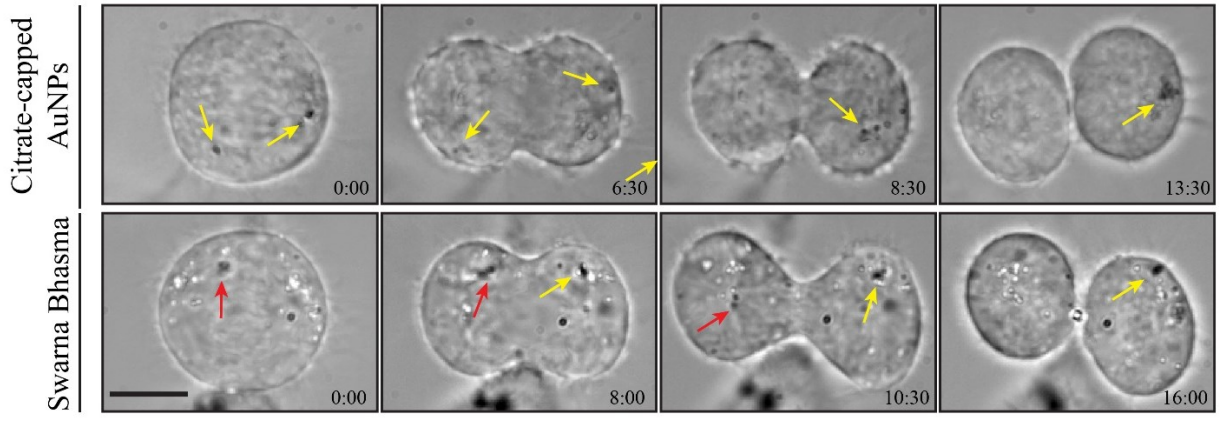

Figure 3-11. *Time-lapse images show dividing HeLa cells treated with citrate-capped AuNPs (top panel) or SBs (bottom panel). Yellow arrows indicate AuNPs or SBs that segregate to the poles of*

the cell, while red arrows point to SBs that stay near the chromatin and are likely incorporated into the nucleus. The scale bars are 10 μm.

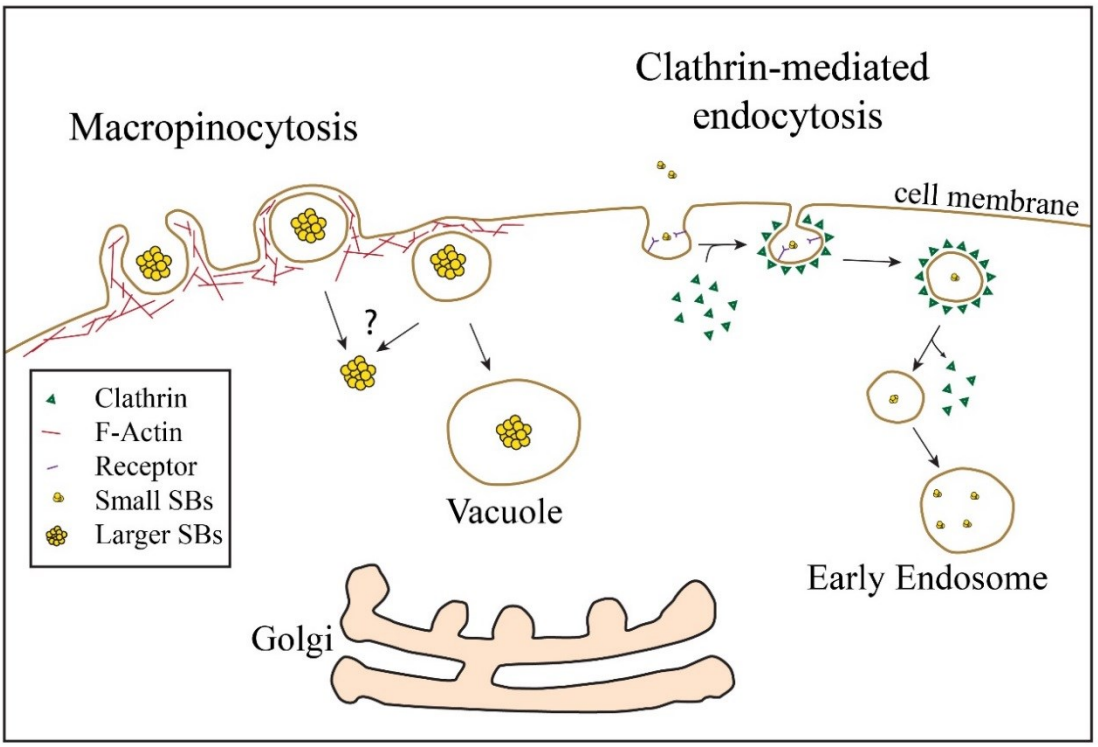

Figure 3-12. *A schematic illustrating various ways through which larger and smaller SBs can enter human cells. Unbroken and broken SBs accumulate in random locations in HeLa and HFF-1 cells, such as the cytosol and nucleus.*

3.3.6. Entry Mechanism of SBs

SBs differ from AuNPs in their physical properties and subcellular localization, and likely also vary in the mechanism by which they enter cells. Previous reports showed that AuNPs enter human cells via clathrin-dependent receptor-mediated endocytosis, where they remain in the endomembrane system[201][207][209]. A schematic of the possible entry mechanisms of SBs is shown in

Figure 3-12. A schematic illustrating various ways through which larger and smaller SBs can enter human cells. Unbroken and broken SBs accumulate in random locations in HeLa and HFF-1 cells, such as the cytosol and nucleus.. Both unbroken and broken particles accumulate in the endomembrane system, cytosol, and nucleus within HeLa and HFF-1 cells. Although not shown here, larger particles may enter cells via macropinocytosis, where they could gain access to the cytosol via disruption of vacuoles. Once in the cytosol, they could accumulate in the nucleus during

cell division, after nuclear envelope breakdown. Smaller particles may enter cells via clathrin-mediated endocytosis, where they accumulate in endosomes.

3.4. Conclusions

This study describes the toxicity, subcellular distribution and entry mechanism of Swarna Bhasma Incinerated Gold Particles, SBs, in human cells. This is the first study, to our knowledge, that has characterized SBs in human cells. SBs are large irregular-shaped particles formed from 60 nm crystallites that are not toxic to HeLa or HFF-1 cells. As shown in

Figure 3-12. A schematic illustrating various ways through which larger and smaller SBs can enter human cells. Unbroken and broken SBs accumulate in random locations in HeLa and HFF-1 cells, such as the cytosol and nucleus., small SBs likely enter HeLa cells via receptor-mediated endocytosis, where they accumulate in vesicles, within the endomembrane system, similar to AuNPs. However, large SBs may enter cells by macropinocytosis and accumulate in vacuoles. Vesicles that are part of the endomembrane system, display restricted patterns of movement, which mirrors that of the microtubule tracks they traffic along. Since microtubules emanate from the centrosomes, the vesicles tend to accumulate in the endomembrane system that hugs the nucleus, where the centrosomes are located. In support of this, vesicles containing AuNPs showed these types of movements. However, while some vesicles with SBs showed these types of movements, others were more random. In addition, SBs were observed in the cytosol and nucleus in some cells, suggesting that they had escaped from vesicles or vacuoles.

The localization of SBs in the nucleus occurs during cell division. As eukaryotic cells enter mitosis, their nuclear envelope breaks down exposing chromatin to the cytosol, and the nuclear envelope re-assembles as chromosomes finish segregating during telophase. Particles that are in the cytosol are randomly located, and could get sequestered in one of the daughter nuclei as they reform. We propose that this may be a mechanism by which cytosolic particles gain access to the nucleus, which is often overlooked in the literature. Another interesting question is how SBs gain access to the cytosol when they all presumably enter via membrane-bound vesicles. As outlined above, SBs enter HeLa cells by receptor-mediated endocytosis and macropinocytosis, where they accumulate in membrane-bound vesicles or vacuoles, respectively. These membranous networks protect cells from foreign material and molecules. Large particles could cause membranes to break via mechanical disruption, or impede fission/fusion of the vesicles during remodeling of the membranous networks. Alternatively, SBs may contain elements or compounds that promote

rupture of lysosomes or vacuoles. Once SBs gain access to the cytosol, they could be sequestered in the nucleus during division.

The composition of SBs varies between manufacturers even for those from a similar region. It is not clear how their composition impacts their entry, location or toxicity at the cellular level, or medicinal properties at the organismal level. It would be interesting to compare different SBs, as well as study their impact on different cell types than those studied here. For example, large particles may more successfully enter phagocytic cells (e.g. macrophages) causing an increase in the proportion of cells with SBs in comparison to HFF-1 or HeLa cells. SBs are typically administered by oral ingestion, and another question is how these particles are able to pass through the epithelial cells lining the digestive tract to enter the body, or if they enter the body at all and their medicinal properties are attributed to how they act as carriers for beneficial molecules from plant extracts. It would be interesting to explore the compounds and elements that are typically coupled with SBs to determine which ones confer medicinal properties. Some compounds could be small and amphipathic, permitting them to pass freely through the cell membranes. Given that SBs are inert, large particles, they could be further explored for use as carriers, imaging and/or temperature control for diagnostics or treatments.

In this chapter, the behavior of two different types of gold particles (Swarna Bhasma, nanospheres) was studied within human cells under different conditions (incubation time and particles concentration). In the next chapter, in order to study the effects of NPs shape on their interactions with intracellular environments, two different shapes of particles (nanostars and nanospheres) are used to characterize them in two different cell lines through Raman spectroscopy.

Chapter 4
Nano-Morphology on the Interaction of Gold Nanoparticles with the Human Intracellular Environment

This chapter is based on the following submitted manuscript:

- **Ahmad Sohrabi Kashani**, Simona Badilescu, Alisa Piekny, and Muthukumaran Packirisamy, "Nano-Morphology on the interaction of gold nanoparticles with the human intracellular environment" submitted to *ACS Applied Nano Materials,* January 2020

Gold nanoparticles have potential applications for the diagnosis and treatment of diseases due to their optical, sensing, and biological properties. Gold nanoparticles can be used as nanocarriers for the delivery of therapeutic agents, or as nanoprobes to detect and monitor intracellular events. Studying their localization and properties in cells is an essential step toward developing nanoparticle products for *in vivo* use. Raman spectroscopy is a powerful and non-invasive method that we used to investigate how two different morphologies of gold particles; nanostars, and nanospheres interact with HeLa (cervical cancer) and HepG2 (liver cancer) cells. Gold nanoparticles with branched structures are more effective in enhancing the Raman spectra for cell-relevant bands compared to nanospheres. Moreover, we observed a higher level of Raman enhancement of nanostars and nanospheres in HeLa cells compared to HepG2 cells, suggesting HeLa could uptake a higher level of both types under a same condition. We also used scanning electron microscopy and light microscopy to study the distribution of both types of nanoparticles in cells. Our results highlight the importance of morphology in mediating changes in affinity of gold nanoparticles to different chemical structures in cells, which is important for developing nanomedicines for cancer therapy.

4.1. Introduction

Cancer is one of the greatest threats to public health, and the early detection and treatment of cancer play a significant role in increasing the chances of survival[27]. Recently, nanomaterials like gold are being explored for potential biomedical applications in the diagnosis and treatment of cancer, as bioimaging, nano-sensors, and drug delivery systems[219][220]. The use of gold nanoparticles in medicine is developing rapidly due to their tunable size, easy preparation and functionalization, optical properties, inertness in biological environments and excellent

biocompatibility. In some cases, these gold nanoparticles can be conjugated with specific moieties to be directed to specific subcellular organelles to help cure them. Gold nanoparticles' physicochemical properties such as size, morphology, and surface modification are critical parameters for their delivery to precise locations within cells[221][187]. Despite many advancements in this area, a better understanding of how the properties of nanoparticles change in cells, and how they influence the intracellular environment is necessary to develop effective and practical nanoparticle-based drug delivery systems. The physicochemical properties of nanoparticles, such as size[222], shape[41], surface charge[223], and surface coating[48] may affect how they interact with cells and their behaviors in a biological environment. The morphology of nanoparticles plays a significant role in cellular uptake and intracellular distribution. In recent decades, gold nanoparticles with different shapes such as spheres[224], triangles[41], rods[115], cubes[225], wires[226], and stars[39] have been prepared and investigated for drug delivery applications. However, only a few studies have investigated the toxicity and internalization of asymmetric particles such as gold nanostars. A star-shaped nanoparticle includes a core and a number of sharp branches protruding from it. Because of their localized surface plasmon resonance (LSPR) properties and surface-enhanced Raman spectroscopy activity, nanostars make excellent platforms for diagnostic and therapeutic applications[227]–[229] Understanding the precise localization/distribution of nanoparticles in cells, and how their physicochemical properties such as size and morphology affect how they interact with the intracellular environment is necessary to develop their use as nanomedicines [31][230].

Surface-enhanced Raman spectroscopy (SERS) is invaluable for studying cell-nanoparticle interactions by providing label-free, highly sensitive, and non-invasive measurements. Using this method, different molecular structures in the intracellular environment can be detected by measuring the inelastic scattering of the incident laser light. Using SERS, the vibrational fingerprint and low-frequency modes of moieties located in the close vicinity of the nanostructured noble metal and even at a very low concentration (picomolar and even femtomolar) can be measured by enhancing the inelastic light scattering. Due to the LSPR excitation of nanoparticles by incident light, the local electromagnetic field is magnified by 10, resulting in the enhancement of Raman scattering. The enhancement of spectra due to the interactions between components of the cell and nanoparticles can also be measured [231]. Thus, the SERS technique has received considerable attention in the analysis of cells and drug delivery systems[232]. In contrast to the other methods,

SERS can detect the distribution of particles in cells and how they interact with the local environment [27][233], which is necessary for the development of nanomedicines, particularly when they are required to be in a specific region in cells. *Zhu et al*.[234] used SERS mapping and transmission electron microscopy (TEM) to investigate the interaction and distribution of spherical gold nanoparticles in human breast cancer cells (MDA-MB-231). They observed that the maximum Raman signal occurs near the cytoplasm, supporting the affinity of gold nanoparticles to phenylalanine. *Huang et al.* [235]implemented the SERS method to distinguish normal liver cells from cancerous ones (hepatoma) by incubating cells with gold nanoparticles of different sizes. They showed that the relative ratios of the intensities of Raman peaks could be used to differentiate cancer cells from non-cancer cells. Using Raman/SERS spectroscopy and Raman mapping, *Leopold et al*. [236] studied the cellular and subcellular localization of polyethylene glycol (PEG) functionalized gold nanoparticles in human alveolar adenocarcinoma cells (A549). By performing a full Raman mapping of A549, they showed that the gold nanoparticles were enriched in the cytoplasm near the nucleus, suggesting their potential use for intracellular sensing. *Shah et al*.[233] used 2D-array Raman spectra of human prostate cancer cells to determine the dynamic uptake and localization of gold nanoparticles coated with PEG at different time points. The toxicity and localization of other types of nanoparticles in cells have also been studied with Raman Spectroscopy. *Lopis et al*.[237] performed Raman measurements on different regions of cells to study the distribution of three different nanoparticles: aluminum oxide, cerium dioxide nanoparticles, and carbon nanotubes in human liver cancer cells. They observed that the nanoparticles were distributed in the cytoplasm. *Doreny et al*.[238] employed Raman spectroscopy to detect the localization of polystyrene particles in A549 cell lines. They fixed the cells to carry out Raman mapping on whole cells. They showed that this technique could also be used to measure changes in the subcellular environment, which could indicate different responses to the nanoparticles. *Knief et al*. [239] used Raman spectroscopy to examine the toxicity of carbon nanotubes in human lung cancer cells (A549). They found that there was a correlation between changes in the spectra and toxicity with increased time of exposure.

In the present work, we used SERS to study two different morphologies of gold nanoparticles: nanostars and nanospheres in HeLa and HepG2 cells. The nanoparticles were monitored for internalization, localization, and Raman enhancement. First, we characterized the physical properties of both shapes of gold nanoparticles by microscopic and optical methods.

Confocal Raman Spectroscopy was then used to study the two types of gold nanoparticles in cells. By acquiring Raman spectra from the different regions of cells, including the periphery, cytosol and nucleus, it was possible to detect their precise locations. Furthermore, we performed Raman scanning on the entire cell to determine the affinity of gold particles for different chemical moieties in the intracellular environment. These studies were coupled with classical microscopy techniques to verify the distribution of both morphologies of gold nanoparticles in HeLa and HepG2 cells. We found that nanostars vs. nanospheres are more effective in SERS enhancement in both cell lines while the enhancement degree was higher in HeLa cells compared to HepG2. The SERS measurements revealed a different shape-dependent affinity of NPs in intracellular environments. Besides, SEM and hyperspectral images showed both types of NPs localized mainly at the pre-nuclear region, and Raman scanning supported this pattern by showing a higher SERS at those regions. These results highlight the importance of nano-morphology in designing nanomedicines for cancer therapy.

4.2. Materials and Methods

4.2.1. Synthesis of Gold Nanoparticles

The Turkevich method [240]was utilized for the preparation of nanosphere-shaped gold particles. Gold chloroauric acid was reduced with a sodium citrate solution to synthesize the particles. 50 ml of $HAuCl_4$ solution containing 40 µg/ml of gold was heated to the boiling point, and 5 ml of a 2% sodium citrate solution was added. The solution was then heated for 15 minutes, and its color turned to purple. A seed-mediated method was used to prepare nanostars. To synthesize nanostars, 10 ml 0.25 mM gold precursor ($HAuCl_43H_2O$), 10 µL of 1M hydrochloric acid, and 100 µL of freshly prepared seed solution were mixed in an Erlenmeyer flask and stirred for 5 minutes. Next, 50 µl of 100 mM ascorbic acid and 100 µL of silver nitrate were added simultaneously and further stirred for 30 s[241]. The color of the solution turned from light pink to blue.

4.2.2. Cell Preparation and Fixation

HepG2 (human hepatocellular carcinoma) and HeLa (human cervical adenocarcinoma) cells were used in this study. Cells were cultured in Dulbecco's Modified Eagle's Medium (DMEM; Wisent), supplemented with 10 or 15% Fetal Bovine Serum (FBS), 100 U penicillin and 0.1 mg/ml streptomycin, and 2 mM L-glutamine. The cells were incubated in a humidified chamber

at 37°C and passaged when they were 75-100% confluent. To prepare slides for imaging, cells were plated on acid-washed coverslips in 6-well dishes. We used 10% TCA (trichloracetic acid) to fix the cells for immunofluorescence imaging, and they were immune-stained with antibodies to tubulin (DM1a; Sigma) and myosin (MYIIB Sigma) and anti-mouse and anti-rabbit Alexa-488 and 568 (Thermofisher) secondary antibodies as previously described [167]. An epifluorescence Leica microscope (DM1600B) with 63x oil immersion objective, a Hamamatsu Orca R2 camera and Volocity software was used to image fixed cells. ImageJ also was used for image analysis.

4.2.3. SEM and Laser Confocal Microscopy

For SEM measurements, the cells were fixed with 10% trichloroacetic acid (TCA) and washed with TBST (see reference [13] for details). A series of ethanol solutions was used to dehydrate the cells. They were incubated with 50% v/v ethanol in water for 15 minutes, then in 60%, 70%, 80%, 90% and 100% ethanol, respectively, each for 15 minutes. The coverslips were added face up to glass slides and left to dry in a fume hood overnight. Before SEM imaging, we sputtered the top surface of the coverslips with gold and palladium, and then we imaged slides with a Hitachi S 3400N SEM system. Using traditionally prepared slides, a laser confocal microscope (LEXT OLS 400 3D) with 405 nm short-wavelength and 100X objective was used for 3D surface imaging of samples and measuring the dimensions of cells. This system, in contrast to SEM, could provide a non-contact measurement to determine the height information of the samples.

4.2.4. Size and Zeta Potential Measurements

Zetasizer Nano ZS90 (Malvern Instruments Ltd., Worcestershire, UK) was used to characterize the size distribution of both types of particles based on the dynamic laser scattering (DLS). A Helium-Neon laser with 4mW at 633 nm was employed at 25°C for our measurements. 1 ml of each sample of particles was placed into disposable square cuvettes (scratch-free) for the measurements. We set the dispersant refractive index of water (1.33) for our measurements and for each data point, we averaged ten scans. Furthermore, Zeta Plus electrophoresis system (Brookhaven Instrument Corp.) was used to characterize the zeta potential of two types of NPs under the ambient temperature. The data was collected based on the phase-light scattering, in which a laser light illuminates the particles in the presence of an electric field[242]. Then, the phase shift was used to determine the electrophoretic mobility. For our measurements, the temperature and the

PH measurement were set 25°C and 7.4 respectively. We averaged ten data points and reported their average in this study.

4.2.5. Hyperspectral Imaging

We used a hyperspectral imaging system (CytoViva, Auburn) with 60X and 100X oil immersion objectives to collect high-resolution dark-field images of samples and measure the spectral profiles of cells and gold particles in cells with a spectrophotometer-integrated CCD in the visible and near-infrared range (400 – 1000nm). For hyperspectral imaging, the samples were fixed as described in **Sec. 4.2.2** but without staining. Hyperspectral imaging provides a novel approach to detect the presence of nanoparticles in cells and determine their localization and interaction with the local environment[27][230]. ENVI.4.8 software was used to analyze the region of interest (ROI) of cells and the hyperspectral absorption signals.

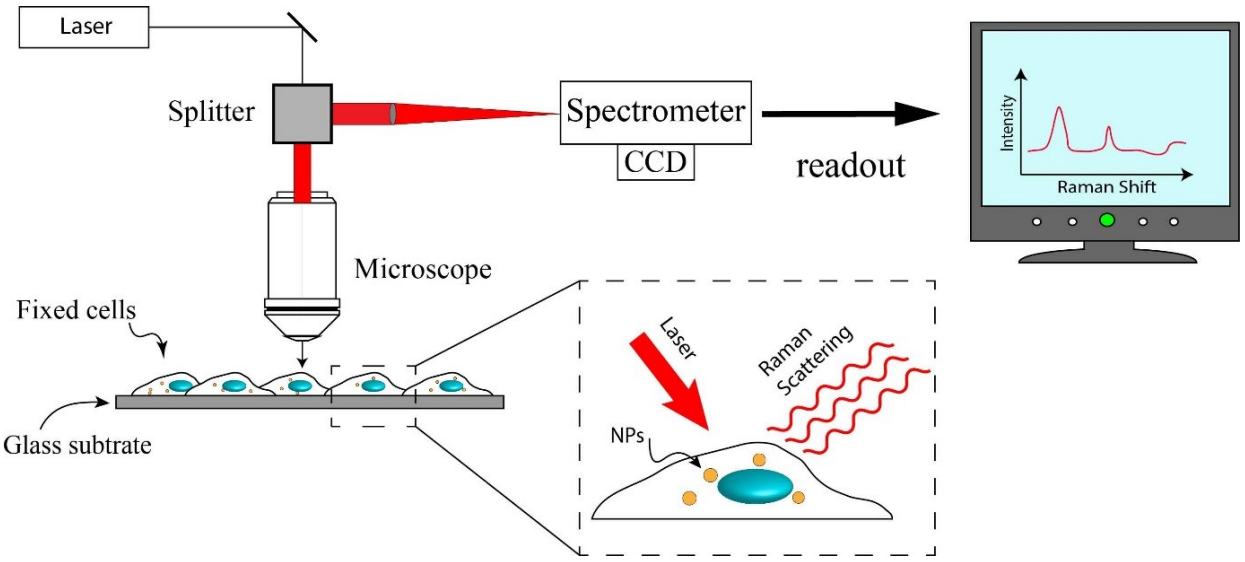

Figure 4-1. *Schematic setup of the confocal Raman spectrometer for probing the fixed cells on a glass substrate (CCD: Charge Coupled Device)*

4.2.6. Raman Spectroscopy Measurement

Raman measurements of the fixed cells on a cover glass were performed with a confocal Raman system (Renishaw inViva) coupled with an optical microscope (Leica) (**Figure 4-1**). Before acquiring measurements, the spectrometer was calibrated with a silicon sample at the static spectrum. We used a 532 nm laser (with the power of 5mW at the sample) to excite our samples, and single spectra were collected using 50X and 100X objectives, in both static and extended

modes for 1~2 acquisitions at 30s laser exposure over a range of 300~3200 1/cm. For each profile, we collected four Raman spectra from different regions of the cell (cytoplasm, nucleus, and periphery) to calculate an average intensity for each position. The adaptive method (Spectragryph) was used to correct the spectra and remove background noise and autofluorescence. Moreover, we applied a Savitysky-Golay smoothing-derivative with interval (5) and polynomial order of (6) to smooth the spectra. For line mapping, we excited with the 532 laser and collected Raman spectra along a line and for 24~28 points with two acquisitions per point for 10s. The Spectragryph package and WiRE software were used for post-acquisition data processing.

4.3. Results and Discussion

4.3.1. Characterization of Gold Nanoparticles

The morphology and size of the synthesized gold nanostars and sphere-shaped nanoparticles were characterized using SEM and DLS methods. **Figure 4-2a** shows the SEM image of gold nanostars immobilized on a glass substrate, illustrating their size and structure. **Figure 4-2a** shows their tendency to form aggregates in solution, or when deposited on a solid substrate. As can be seen in this figure, the synthesized nanostars have approximately 10 short spikes. **Figure 4-2b** shows the result of the DLS analyses of the colloidal solution of nanostars. The mean outer diameter of nanostars was ~104 nm, and the size of their aggregates was up to 2319 nm. **Figure 4-2c** shows the plasmon band of nanostars at 611 nm, confirming the presence of short branches. The characterization of spherical gold nanoparticles was described in detail in our previous work[167]. **Figure 4-2d** shows an SEM image of nanospheres in cells. Although the average size of nanospheres was in the range of 18 nm (**Figure 4-2e**), they might aggregate in cells and form clusters of 50-150 nm. We also characterized nanospheres with UV-vis spectroscopy (**Figure 4-2f**) with a plasmon band at 521, in agreement with the average size measured by DLS. The Zeta potential measurements of both nanostars and nanospheres showed that they have negative surface charges and that nanospheres have a more negative surface. Nanostars and nanospheres have -30±1 mV and -53±6 mV surface potentials, respectively.

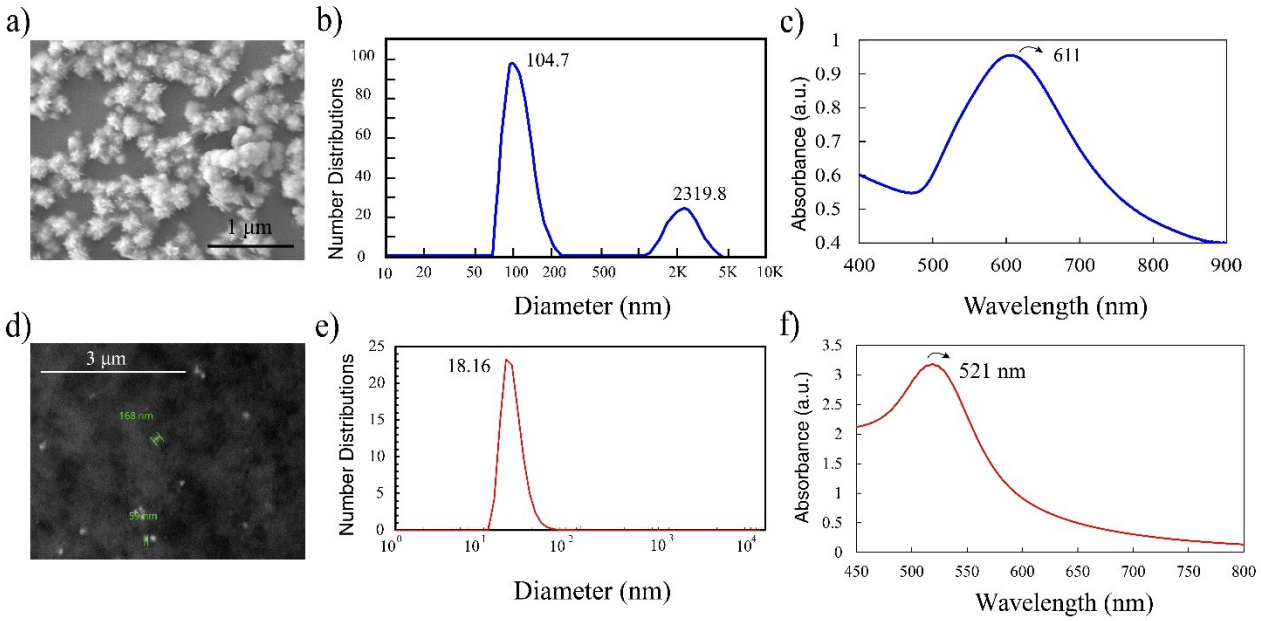

Figure 4-2. a) *SEM image of nanostars dehydrated on a glass substrate,* ***b)*** *Size distribution of nanostars (average diameter) measured by DLS,* ***c)*** *Nanostars LSPR band,* ***d)*** *An SEM image of spherical particles in HepG2 cells and theirs average sizes,* ***e)*** *DLS analysis of colloidal spherical particles, showing their average diameter,* ***f)*** *LSPR band corresponding to spherical particles*

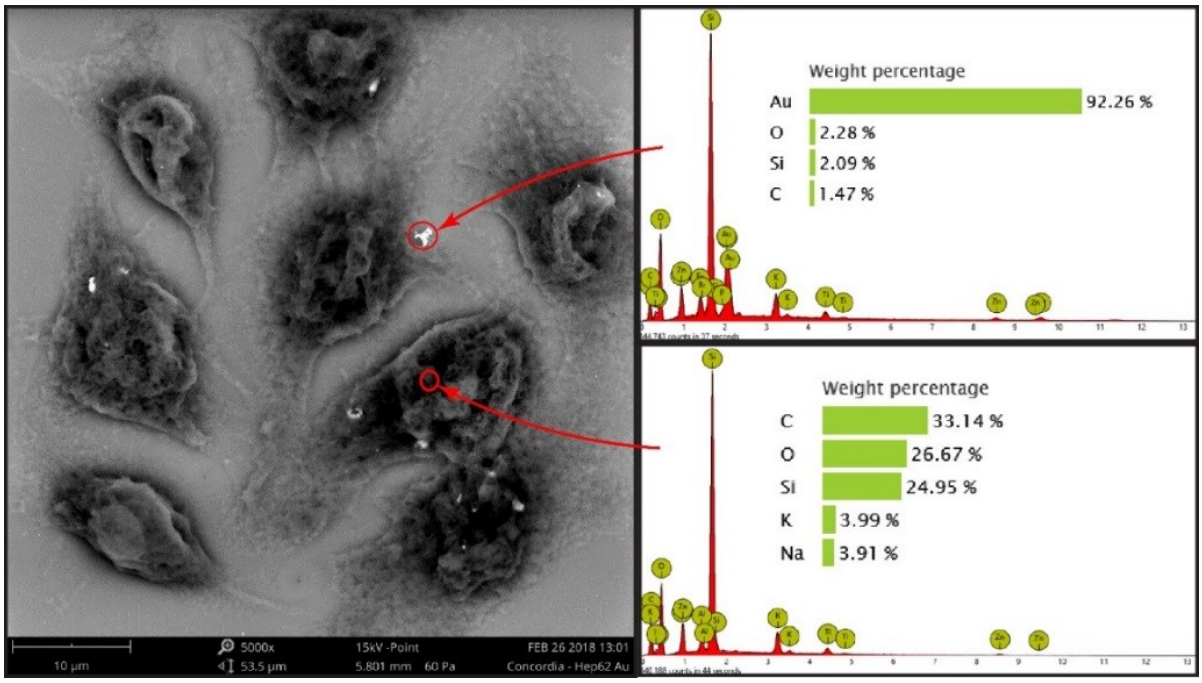

Figure 4-3. *SEM image of gold nanospheres, showing the corresponding EDS analysis of gold (top) in comparison to HepG2 cell (bottom).*

SEM-EDS (Scanning Electron Microscopy-Energy Dispersive Spectroscopy) analysis also was used to characterize the elemental composition of gold nanoparticles. The EDS analysis of gold aggregates (nanospheres) in HepG2 cells is shown in **Figure 4-3**. The EDS spectrum revealed that more than 90% of the nanoparticles in cells is gold, with elements such as Oxygen, Silicon, and Carbon also present in lower quantities. The EDS analysis of HepG2 also showed that Carbon is the most abundant element in cells, as expected.

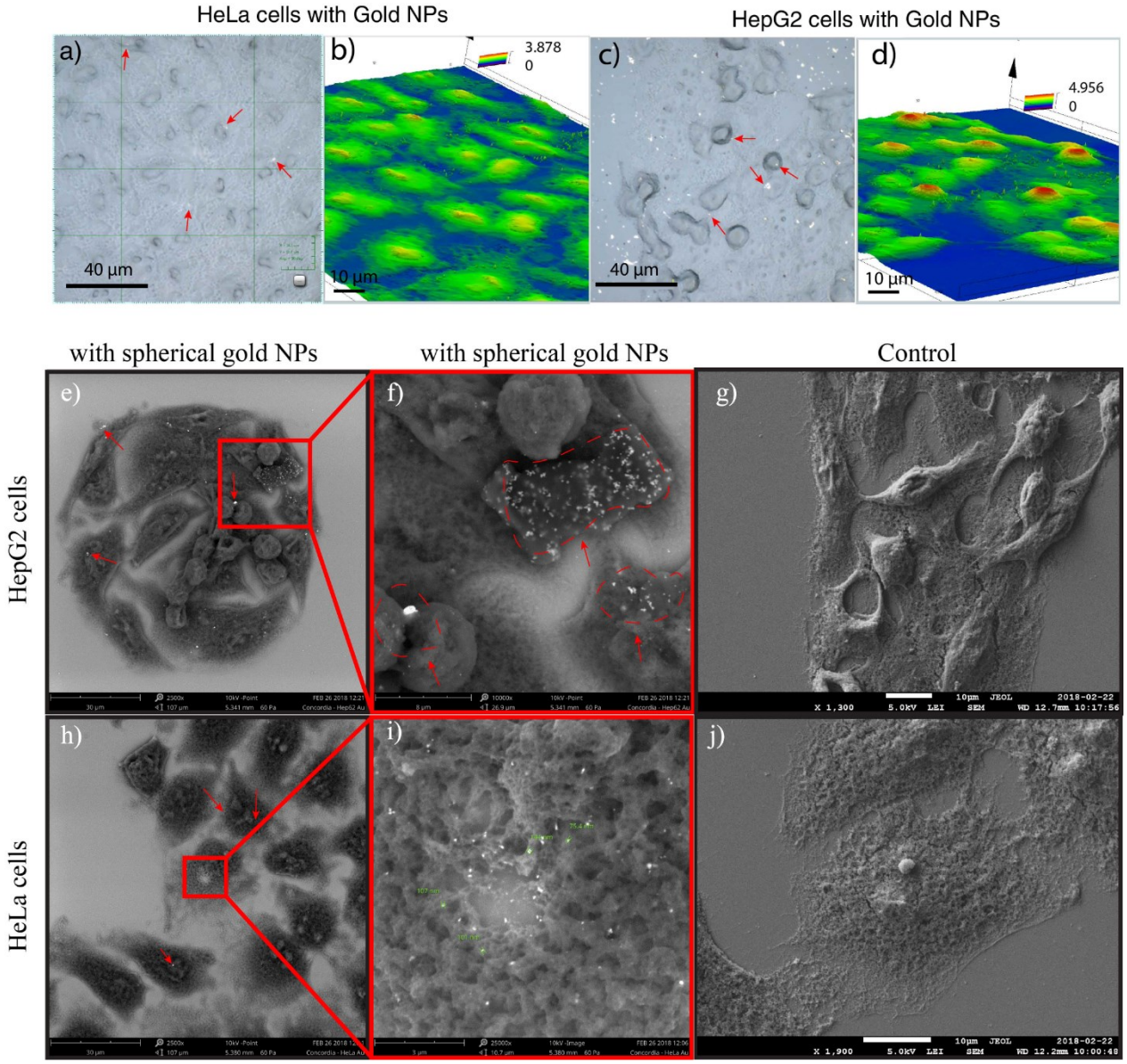

***Figure 4-4**. **a-d)** 2D images of HeLa and HepG2 cells and their corresponding 3D illustrations after treating with nanostars showing the height of cells (red arrows show the gold particles/aggregates- scale bar is 40 µm), **e-g)** SEM images of HepG2 cells and **h-j)**HeLa cells treated with nanospheres, compared to untreated cells (the samples were not coated).*

4.3.2. Characterization of Gold Nanoparticles in Cells using SEM

Due to their small size, high-resolution imaging techniques are required to visualize nanoparticles in cells. Limitations of conventional light microscopy do not allow us to distinguish individual nanoparticles in cells. Therefore, SEM was employed to observe morphological changes and study the distribution of nanoparticles in cells. **Figure 4-4** (**a- d**) show images of HeLa and HepG2 cells with gold nanoparticles, along with 3D illustrations showing the dimension and height of the cells. As expected, HepG2 cells are more 'round' compared to HeLa cells, which are more 'flat'. **Figure 4-4** (**e-j**) show SEM images of both HeLa and HepG2 cells incubated with 8 µg of nanospheres, in comparison to untreated cells. At higher magnification, individual nanoparticles can be seen localized in the cytosol and near the nucleus of cells ("**f**" and "**i**"). A few particles can also be seen in the nucleus, particularly in HeLa cells (**Figure 4-4i**). No significant morphological changes in the cells were observed when compared with the control cells. It should be noted that the preparation and quality of a biological sample may influence the resolution of the SEM images. Coating with a thin layer of metal can enhance their resolution. However, as gold particles are at the nanoscale, the coating may hinder the details of individual nanoparticles in cells. **Figure 4-5** compares the quality and the resolution of SEM images for both coated and uncoated samples. As shown in this figure, the individual or smaller aggregates of nanoparticles are visible in cells but the structural details of the cells are challenging to see. To the contrary, in **Figure 4-5b**, the cellular structure and the border of the cells is clear, but a coating layer has hindered the visualization of nanoparticles in cells.

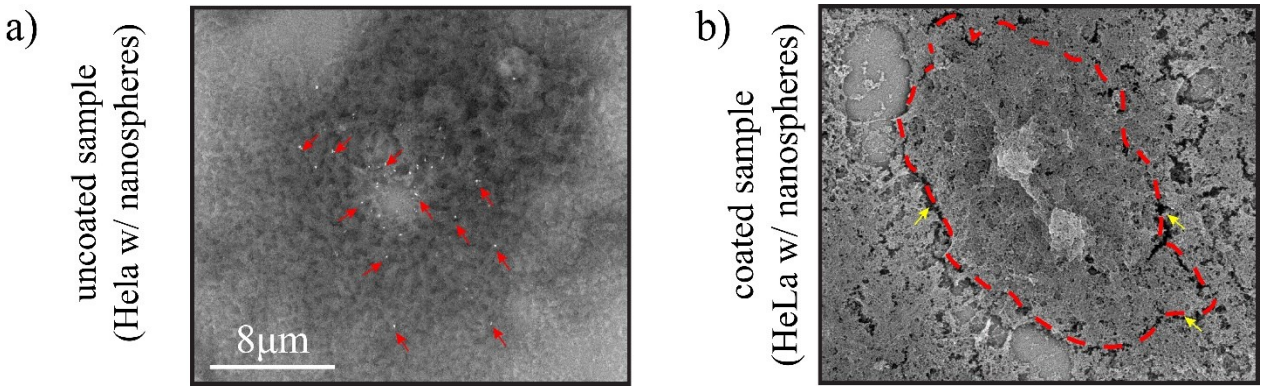

***Figure 4-5**. SEM images of coated and uncoated samples. **a)** Uncoated sample (red arrows point very small aggregates of nanoparticles in HeLa cells, **b)** coated sample with a thin layer of gold (yellow arrows show the border of a single HeLa cell)*

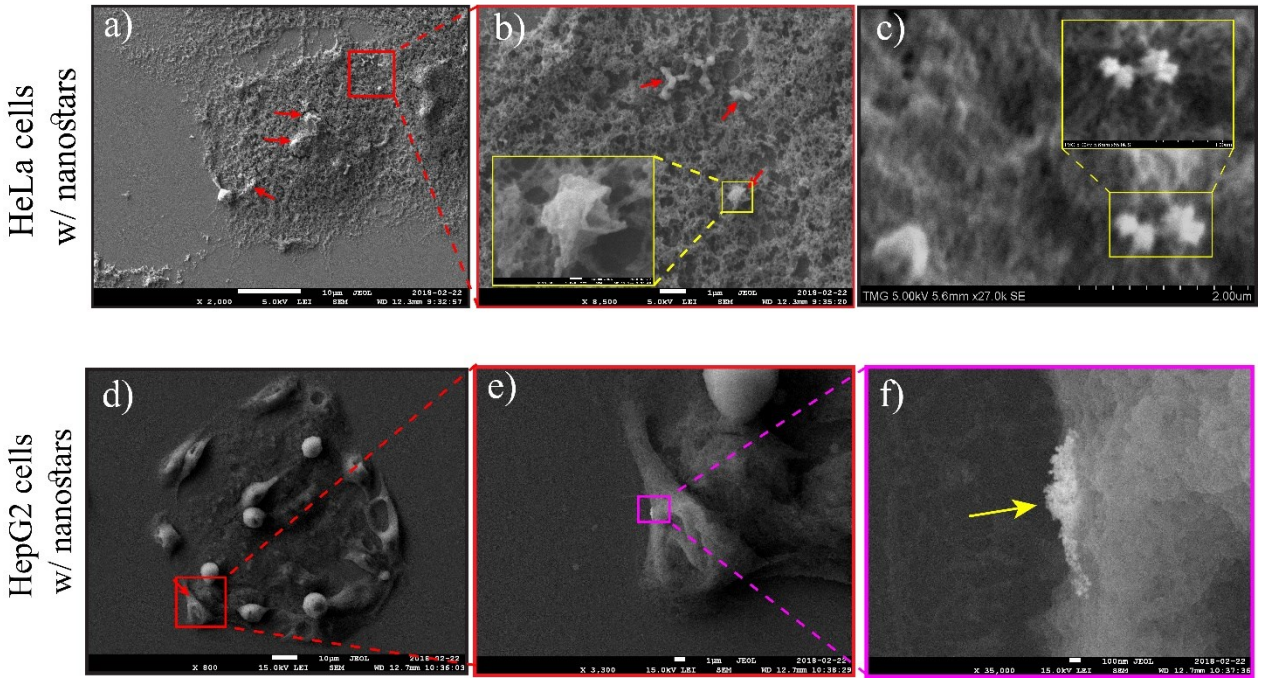

Figure 4-6. *SEM images of HeLa and HepG2 cell lines treated with nanostars, showing their distribution in cells.* ***a)*** *SEM image of a HeLa cell, showing nanoparticles in different regions of the cell (red arrows),* ***b)*** *a higher magnification of the shown area,* ***c)*** *Individual nanostars in HeLa cell,* ***d)*** *A lower magnification image of HepG2 cell treated with nanostars,* ***e)*** *a higher magnification image of a single HepG2 cell,* ***f)*** *nanostars aggregate attached to the periphery of the HepG2 cell.*

The distribution of nanostars in HeLa and HepG2 is shown in **Figure 4-6**. Nanostars, similar to nanospheres, accumulate in the cytosol and near the nucleus of HeLa cells. However, SEM images show that nanostars form larger aggregates in HeLa cells, and only a few smaller aggregates or individual particles (**Figure 4-6c**) can be seen in cells. **Figure 4-6e** shows an SEM image of larger clusters of nanostars at the periphery of HepG2 cells. Due to the challenges in obtaining sufficient contrast to visualize nanoparticles, they were hardly visible in HepG2. A backscattered electron detector (BSD) was used to provide better contrast [243]. With this setup, elements are differentiated based on their atomic mass numbers. An aggregate of nanostars is shown at the outer periphery of a HepG2 cell at higher magnification (**Figure 4-6f**). A morphological transformation of the branched gold nanoparticles to spherical ones can be observed in **Figure 4-6b** and **f**. However, a few nanostars without morphological changes were visible in cells (**Figure 4-6c**).

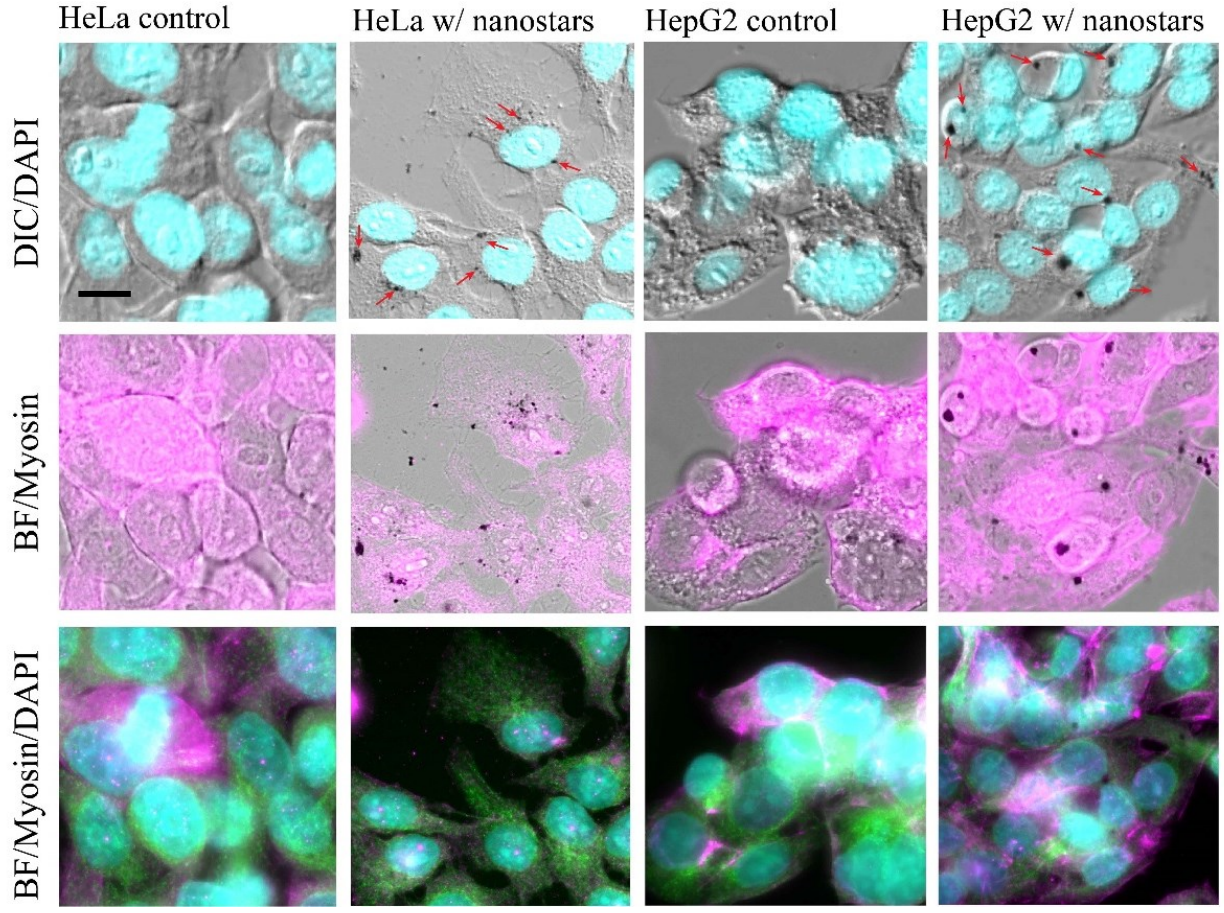

Figure 4-7. *Immunofluorescence images of cells incubated with nanostars and stained for DNA (cyan), Microtubules (green) and Myosin (magenta). Red arrows show the nanostars inside the HeLa and HepG2 cells and at the periphery of the nucleus. Larger clusters of nanostars can be seen in HepG2 cells and at the periphery, and random distribution of nanostars can be seen in HeLa cells (BF: Bright field, Scale bar is 20 µm)*

4.3.3. Immunofluorescence Imaging of Nanoparticles in Cells

We also used immunofluorescence imaging (IF) to visualize the distribution of nanostars (8 µg) inside HeLa and HepG2 cells. Cells were stained for myosin, DAPI (to visualize DNA), and tubulin. Clusters of nanostars can be seen in random locations in the cytosol as well as near the nucleus. As seen in **Figure 4-7**, smaller clusters of nanostars with more random distributions were visible in HeLa cells compared to HepG2 cells, which had larger clusters located in large vacuoles near the nucleus. These results are in agreement with SEM images, where the larger aggregates of nanostars tended to be in large vesicles in HepG2 cells. It is not clear why the nanostars would cluster and localize differently in the two cell types, but this could be indicative of their different morphology and genetic backgrounds.

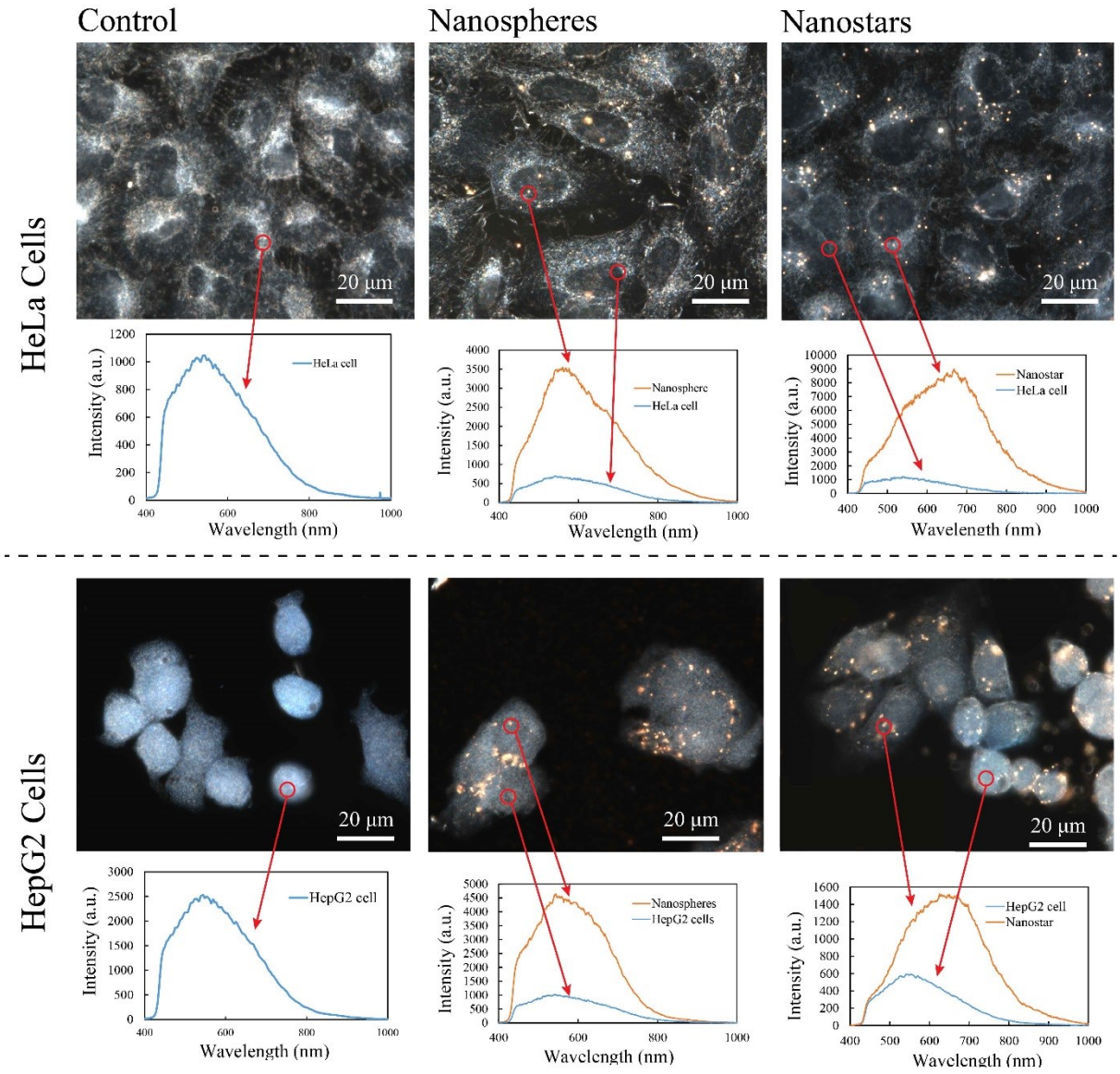

Figure 4-8. *Dark-field images of both treated cell lines versus control cells and the corresponding spectral profile (it should be noted that spectra were not normalized with respect to the Halogen light)*

4.3.4. Dark-Field and Hyperspectral Imaging of Nanoparticles in Cells

To further characterize nanostars and nanospheres in cells, they were imaged at 100x magnification with an enhanced dark-field microscope, and spectra of 400-1000 nm were collected simultaneously using a coupled hyperspectral system [27][230]. The signal-to-noise ratio is improved up to 10-fold using this imaging system compared to standard dark-field systems. **Figure 4-8** shows nanostars and nanospheres in HeLa and HepG2 cells compared to control cells. Due to the light scattering of gold nanoparticles, they appear bright in the dark-field images. The

small bright dots in **Figure 4-8** are clusters of nanostars and nanospheres in cells. The mean spectra of both cells and particles are plotted in **Figure 4-8** (bottom panels). As shown in **Figure 4-8**, the absorbance spectra in regions where no nanoparticles are seen are very broad, while gold nanoparticles have more intense near-infrared spectral signatures of 540 –750 nm depending on their morphology, location, and aggregation. **Figure 4-8** shows aggregates of nanostars and nanospheres predominantly in the cytosol of HeLa and HepG2 cells. Similar to our observations with other microscopy methods, the dark-field images in **Figure 4-8** show that HeLa cells accumulate more particles, and in the form of small aggregates compared to HepG2 cells, where there are fewer larger aggregates distributed more randomly. The plasmonic band corresponding to small clusters of nanospheres is at 550 – 600 nm, while it is 650 – 700 nm for small clusters of nanostars. While not shown here, the large cluster of both particles peaked between 700– 750 nm, showing that some nanostars might transform into sphere-shaped particles as they aggregate and/or in cells. Nanostructures with sharp tips such as gold nanostars display poor stability, and as observed in the SEM images, some of them may undergo morphological changes as they aggregate and with the biological environment. These changes can be seen in the corresponding LSPR blueshifts.

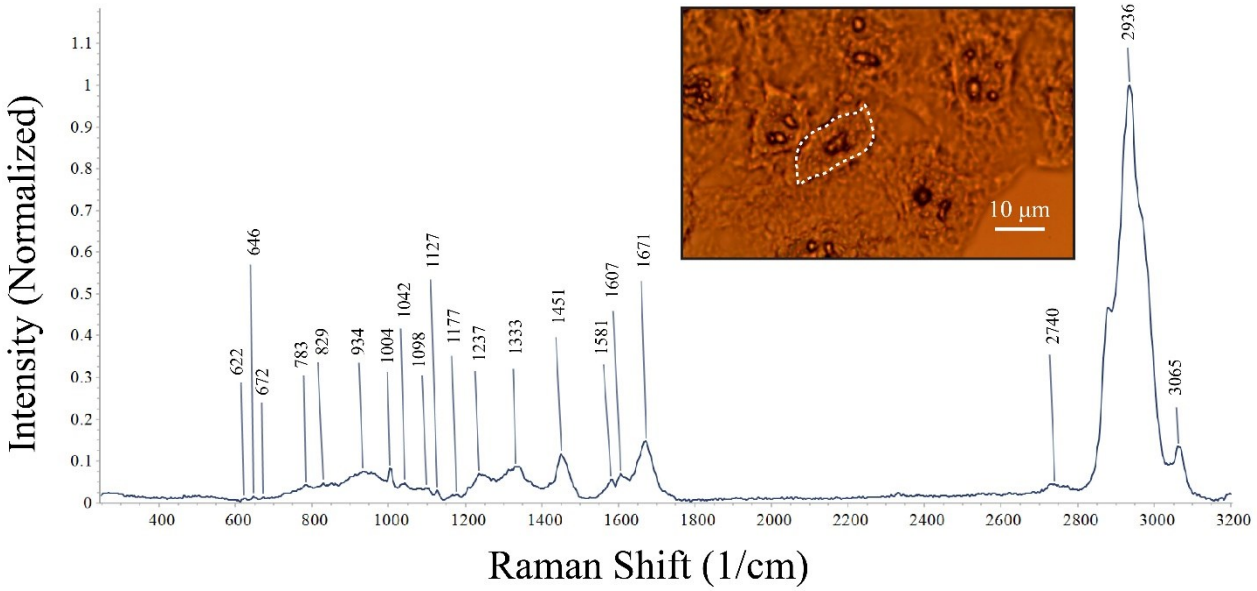

Figure 4-9. *A typical Raman spectrum of fixed HeLa cells (the cell on which the Raman measurement was performed shown in inset)*

4.3.5. Micro Raman Spectroscopy of Fixed Cells

To further characterize the two types of nanoparticles in cells, we studied changes in the Raman peaks of cells. First, Raman measurements were performed on fixed non-treated HeLa cells. The Raman shifts and their corresponding intensities in the 300-3100 1/cm spectral region are shown in **Figure 4-9**, and the main peaks with their chemical assignments are listed in **Table 4-1**. These show some of the different chemical bonds or structures typically found in cells, reflecting a myriad of key components such as proteins, lipids and/or nucleic acids. We observed some variations from cell to cell, likely, due to the differences in cell cycle stage, health, or due to methodologies used such as fixation.

***Table 4-1**. Raman peaks of HeLa cells and their assignments*

Peak positions (1/cm)	Assignment
622-623	Phenylalanine (Protein)[244]
645-646	Tyrosine (Protein)[244]
672	C-S stretching [245]
728-829	Adenine [246]
783	Nucleotide ring breathing [245]
828	Tyrosine (DNA) [245]
855	Tyrosine vibration [246]
934-937	C-C skeletal vibration [247]
1003-1006	Phenylalanine (Proteins) [248]
1095-1098	C-C stretching (Lipids), C-N stretching (Proteins), nucleic acid O-P-O (DNA) [248]
1174-1177	Tyrosine and phenylalanine [13]
1237-1240	Amide III- nucleic acid O-P-O[248]

Peak positions (1/cm)	Assignment
1333-1338	Protein – Adenine and guanine [13]
1451	Ch2/Ch3 bending (Protein) Ch2 Scissoring (Lipids)[227]
1576-1582	Protein [13]
1603-1606	Phenylalanine, Tyrosine [247]
1671-1672	Random coil of amide I (Protein) C-C stretching (Lipids)[227]
2854	Ch2 stretching (Proteins and Lipids) [227]
2934-2936	Ch3 stretching (Proteins and Lipids)[227]

Figure 4-10a shows a comparison of the average Raman spectra of Hela cells with nanostars and nanospheres to control cells in the range of 300-1800 1/cm. We observed an increase in intensity in the range of 900-1800 1/cm. In control cells, the resolution and intensity of peaks below 1000 1/cm were very low; however, in the presence of gold nanoparticles, SERS enhancement revealed bands with higher intensity. This enhancement was due to the LSPR properties of gold particles, which increases the Raman vibration intensity. **Figure 4-10a** illustrates that nanostars enhanced the Raman spectra more than those from nanospheres. We also compared the enhancement factor of each peak for both types of nanoparticles compared to non-treated cells in **Figure 4-10b.** In a few spectra, gold nanospheres are more effective (or almost the same) than nanostars in enhancing the Raman signals. For instant, for peak 825 1/cm corresponding to Tyrosine (as shown in **Figure 4-10b**), nanospheres could enhance the Raman signal approximately 1.5 times higher than nanostars. It should be noted that different parameters may affect the enhancement, such as morphology, size, internalization level, and aggregation of the nanoparticles [249]. For instance, a larger enhancement takes place for chemical structures that are in close vicinity of the sharp edges of noble nanoparticles [10]. This behavior could explain why nanostars, which have sharper structures at their branches, enhance the Raman signals more than nanospheres. In addition to their morphology, the different interactions of nanoparticles with subcellular components also could impact the Raman signal.

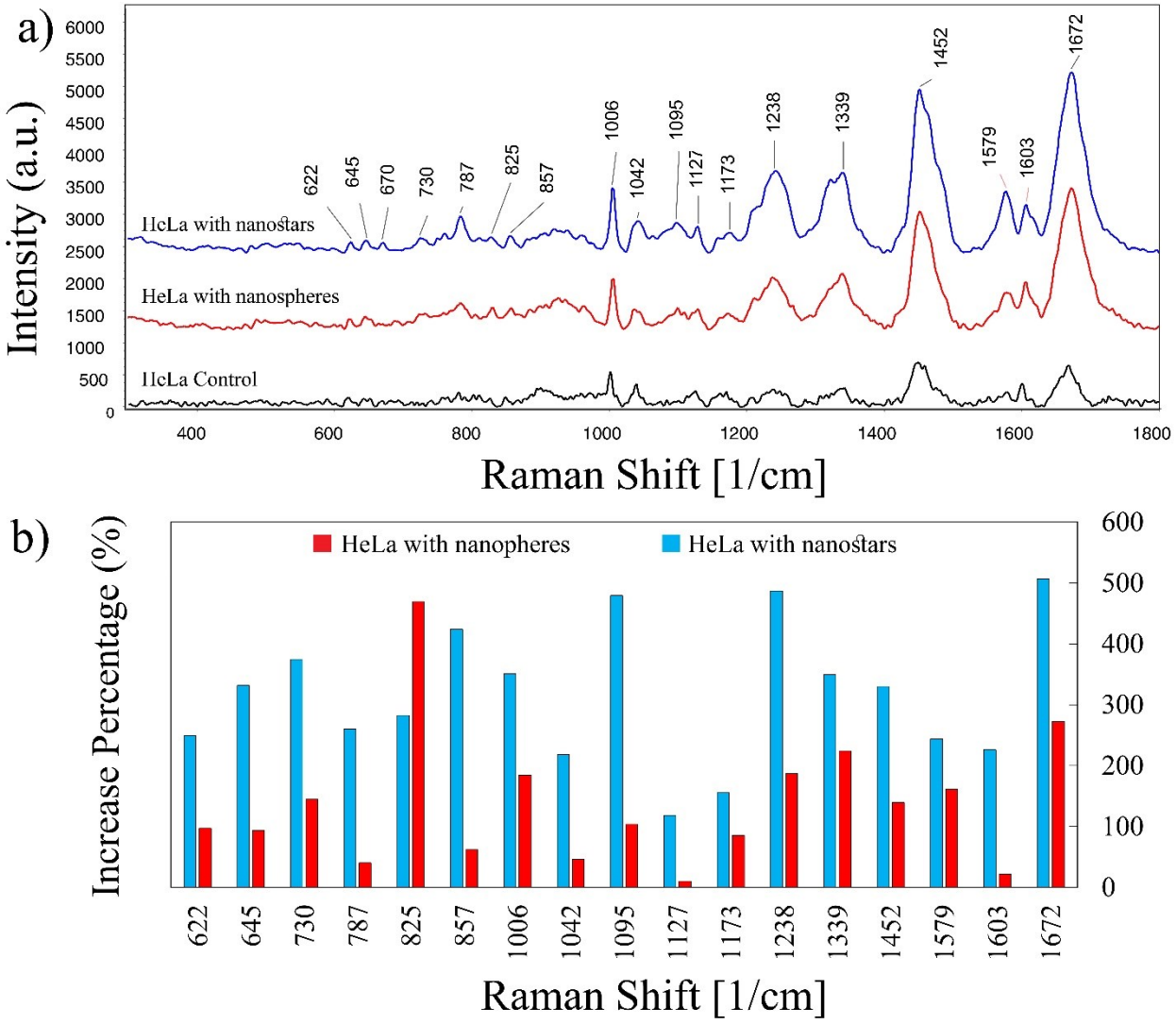

***Figure 4-10**. **a)** Raman spectra of HeLa cells treated with both shapes of nanoparticles and control cells, **b)** SERS enhancement due to gold nanostars and gold nanospheres in HeLa cells (compared to control cells) (Enhancement (%) = $100(I_{treated} - I_{control})/I_{control}$, $I_{treated}$ is the Raman intensity of cells with particles, and I(control) is the Raman intensity of untreated cells with respect to baseline. (The enhancement factor shows the enhancement percentage in bands compared to the same bands in non-treated cells.)*

The Raman signals of HepG2 cells with nanostars and nanospheres are shown in **Figure 4-11a**, in comparison to the control cells. The SERS spectra were collected from the cytosol of cells, then averaged and plotted. Similar to HeLa cells, the Raman intensity is enhanced due to the gold nanoparticles. Similar to HeLa cells, nanostars more effectively increased the intensity of Raman signals compared to nanospheres. However, **Figure 4-11b** shows that both types of nanoparticles were less effective at enhancing the spectra in HepG2 compared to HeLa cells. This supports our

prior observations that more nanoparticles accumulate, and/or are in different states of aggregation in HeLa cells [250]. Aggregates may produce inter-particle local field hotspots between nanoparticles and the metal surface [250]. Since nanostars displayed a higher level of aggregation, they likely enhance the Raman signals more than nanospheres in both cell lines. As discussed earlier, gold nanoparticles enhance the spectra reflecting the different molecules or groups that would be in their close proximity, and the extent of this enhancement can be used to provide information on their location and number.

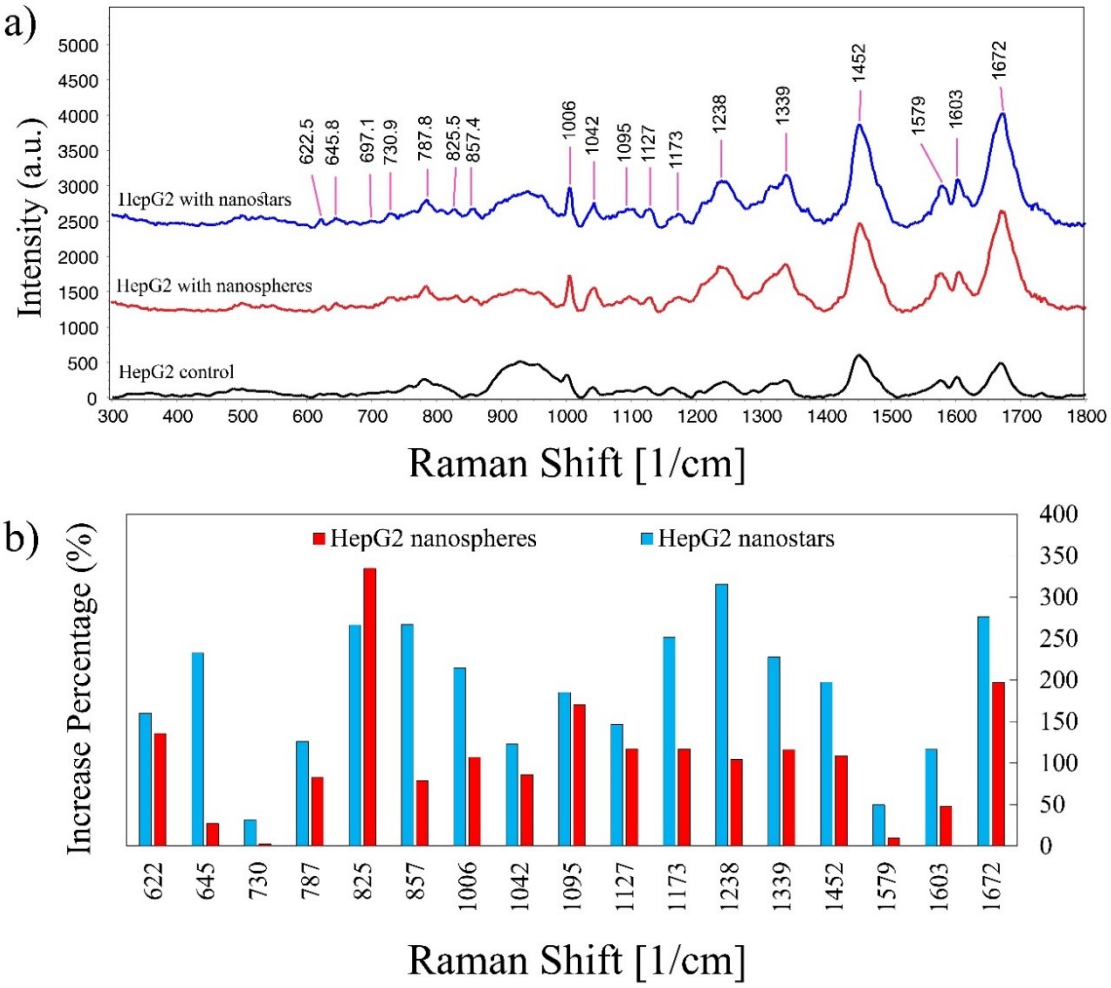

***Figure 4-11**. **a)** Raman spectra of HepG2 cells treated with Au nanostars and Au nanospheres compared to Raman spectrum of control HepG2 (particles in the Cytosol), **b)** Enhancement percentages of Raman signals of HepG2 cells treated with gold nanospheres and gold nanostars*

Figure 4-10b and **Figure 4-11b** show the percentage increase of Raman signals in both HeLa and HepG2 cell lines. In HeLa cells, enhancement of the 622, 645, 1042, 1095, and 1606 1/cm bands

with nanostars was stronger than with nanospheres, while the peak at 825 1/cm with nanospheres was stronger than nanostars. In HepG2 cells, similar to HeLa cells, enhancement of the 645, and 1063 1/cm bands with nanostars was stronger than nanospheres, and for 645, 1042, and 1095 1/cm bands, the enhancements was similar for nanostars and nanospheres. In HepG2, similar to HeLa cells, we observed a stronger peak at 825 1/cm with nanospheres vs. nanostars. For both cell lines and with both types of nanoparticles, the 1238 and 1672 cm^{-1} bands increased the most, likely because of the strong affinity of the negatively charged gold nanoparticles to positive charges on amide groups in proteins, or with other positively charged moieties in lipids. However, for nanospheres, the maximum enhancement for both cells was at 825 1/cm, corresponding to tyrosine. While it is not clear why they enhance this molecular structure, it likely reflects a preferential interaction in the local environment. However, the morphology of the different particles also could reflect this change. We also measured Raman signals within different regions of the cell. **Figure 4-12** compares the Raman intensities in the cytoplasm and nucleus in HeLa and HepG2 cells. The spectra corresponding to the nucleus had higher intensities in comparison to those taken from the cytoplasm. This likely reflects the enrichment of nucleic acids as well as associated proteins.

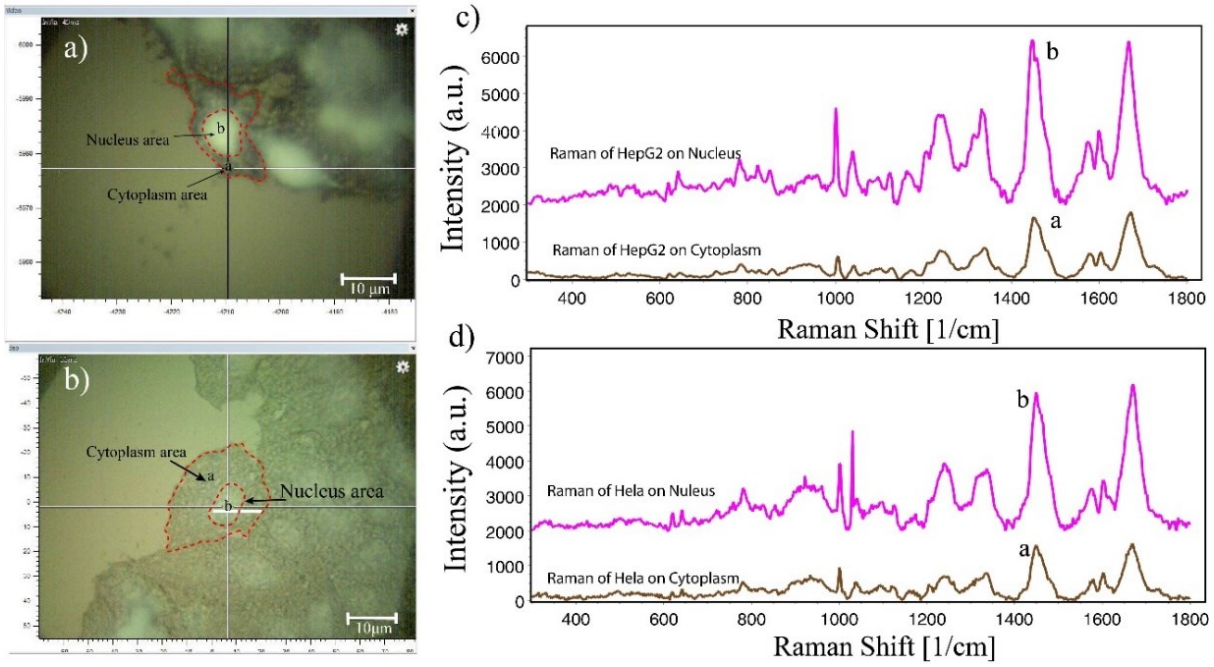

***Figure 4-12**. Raman signals of both HeLa and HepG2 cells at different regions (cytoplasm and nucleus) showing a higher concentration of nucleic acids and proteins in the nucleus. **a, c**) HepG2 with nanostars, **b, d**) HeLa cells with nanostars*

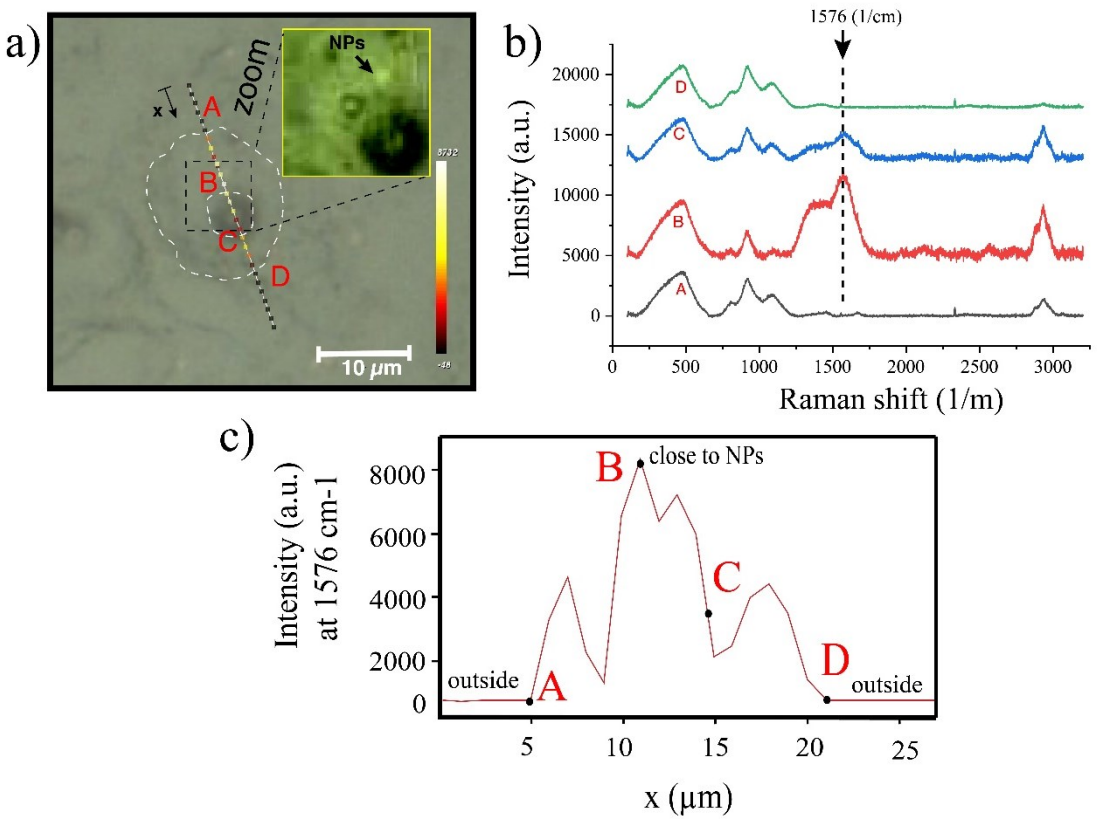

Figure 4-13 *Raman mapping along the indicated line for HeLa cells, treated with nanostars (exposure time: 10 sec).* ***a)*** *Microscopic image of an individual HeLa cell (the border, the cells, and the nucleus are shown with dashed white line) and Raman line mapping (the legend shows the intensity of signals). An arrow in the zoomed area points to an aggregation of nanostars.,* ***b)*** *Raman signals of the HeLa cells in different regions in the cells (A, B, C, and D),* ***c)*** *The intensity of Raman spectra along the line at 1576 1/cm band.*

4.3.6. Raman Mapping of Cells Incubated with Nanostars

As shown in the previous section, nanostars enhance the majority of Raman signals compared to nanospheres. A likely explanation for this could be the increased surface area due to their branched morphology. We also measured the Raman signals across a specific region of a HeLa cell with nanostars, as shown in **Figure 4-13** to verify the localization of nanostars in cells . We scanned 25 points at the indicated region and recorded the signals for each pixel. The optical image of the cell is shown in **Figure 4-13a**, and nanostar aggregates are visible in the enlarged area. The line mapping was chosen to pass through the particles, and signals (100 – 3200 1/cm) were collected along this line at 1 μm intervals. To avoid bleaching the samples, the exposure time and number of acquisitions were reduced (see the methods section). **Figure 4-13b** shows the Raman signal profiles along the line, and **Figure 4-13c** shows the Raman signals at 1576 1/cm

(protein) for the indicated points; A – periphery, B – cytosol near nucleus, C – cytosol, and D – periphery. As expected, the most intense signal corresponded to the location of the gold nanostars in the cytosol. The maximum Raman enhancement at "B" point confirms the presence, accumulation, and location of nanostars in the cytoplasm, at the periphery of the nucleus. As earlier was shown, the higher intensities at the nucleus regions come from the enrichment of nucleic acids and proteins.

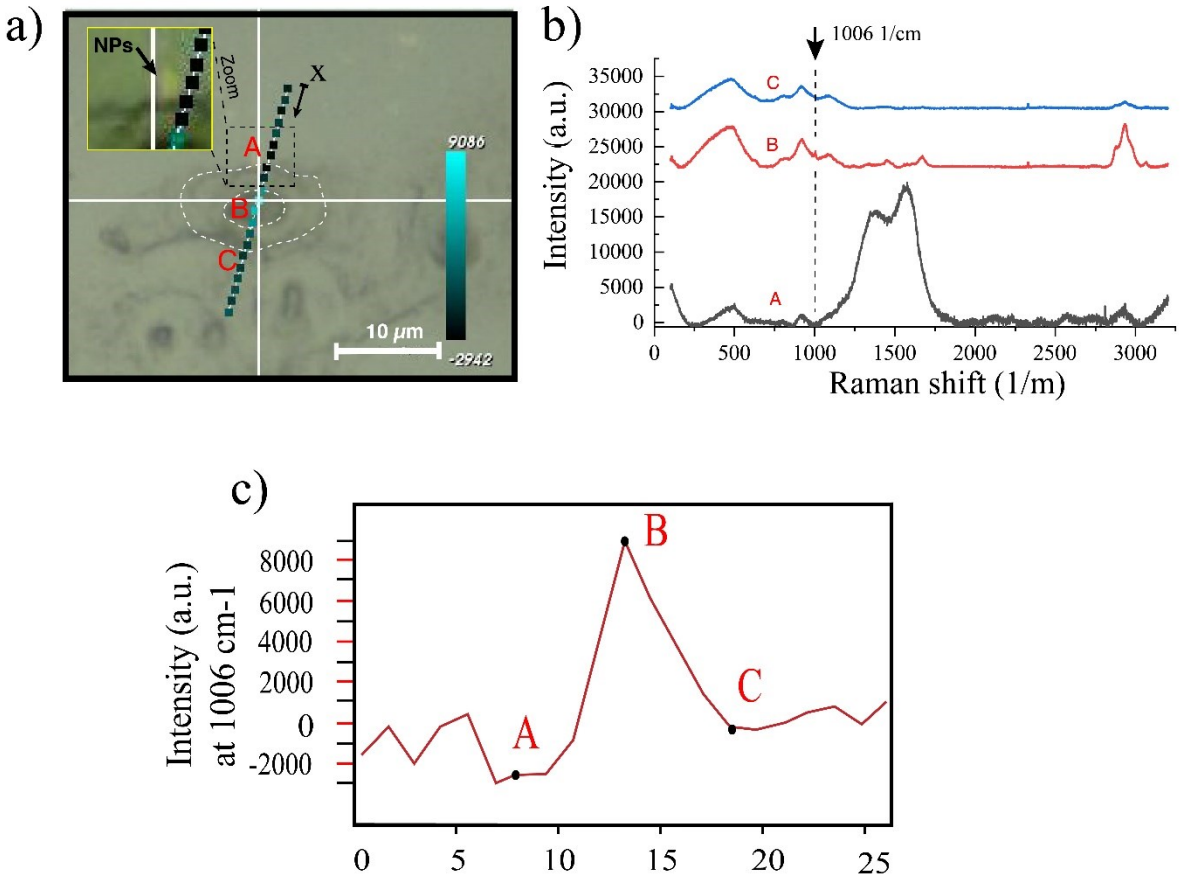

Figure 4-14. *Raman mapping along the indicated line for a single HepG2 cell, treated with nanostars. (Exposure time for mapping: 10 sec.).* ***a)*** *Optical image of a single cell (the border of the cell and nucleus are shown with dashed lines, and the legend shows the intensity of the Raman signals).* ***c)*** *Raman responses from different positions in the cell (A, B, and C),* ***b)*** *Raman intensity changes of the 1006 1/cm band along the line for 26 spots (A, B, and C: Raman signals at the shown points).*

Raman signals were also measured along a line in HepG2 cells with nanostars (**Figure 4-14a**). Raman signals were collected similar to HeLa cells. As shown in the enlarged area, an aggregate of nanostars is located just outside of the cell (**Figure 4-14a**). The Raman profiles from different

positions at the periphery and inside the cell are shown in **Figure 4-14b**. Several bands were visible in the region inside the cell that were not present at the periphery, and likely reflect proteins, lipids and nucleic acids typically found within cells. By increasing x, the intensity of the 1005 1/cm band is increased until it reaches its maximum value in the nucleus region which then decreased at the periphery of the cell (**Figure 4-14c**). Similar to HeLa cells, the SERS enhancement can be seen between 1200 - 1800 1/cm where the nanostars had accumulated. This enhancement is in agreement with the SERS spectra of nanostar aggregates in aqueous solution [227].

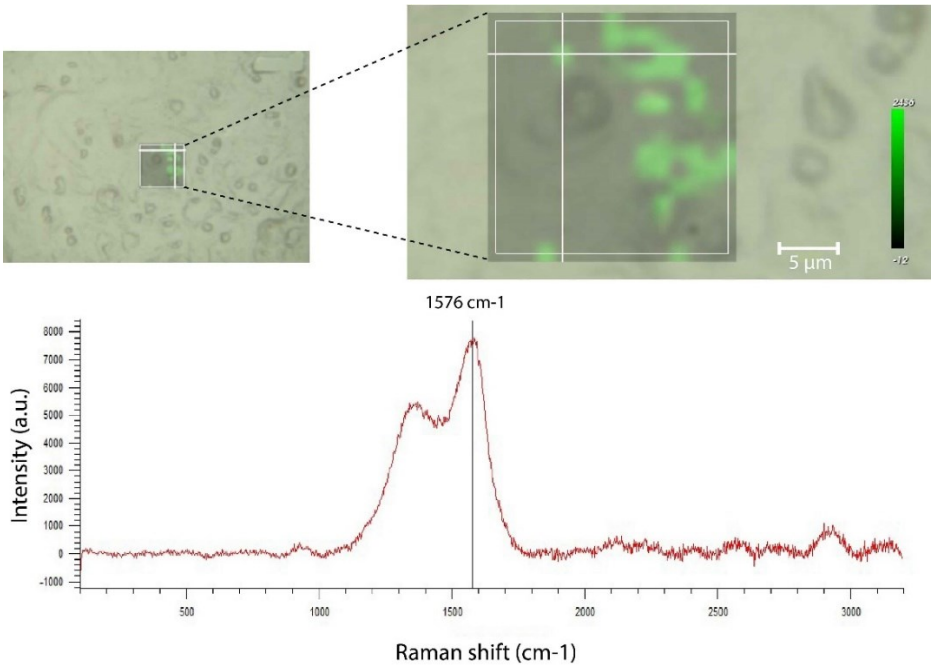

***Figure 4-15**. Raman mapping of HeLa cells with nanostars excited by green laser with respect to 1576 1/cm peak and the corresponding Raman spectrum.*

A full scan was also performed on a single HeLa cell and is shown in **Figure 4-15**. The whole cell and surrounding area were scanned at 1.5 µm intervals (in order to avoid bleaching, the exposure time again reduced to 5 seconds for each acquisition). The 1576 1/cm band was enhanced as displayed in **Figure 4-15**. While due to the low-resolution scanning, NPs aggregates are not visible in the cells, the SERS enhancement is likely due to the presence of gold nanoparticles in the cell.

4.4. Conclusions

It is crucial to improve our understanding of cell-nanoparticle interactions at the molecular level to improve nanoparticles for use in medical applications. Raman spectroscopy provides a

powerful technique to study the structural features of chemical structures in cells by measuring their vibrational features. In the present work, the interaction of gold nanostars and nanospheres with HeLa and HepG2 cells was studied by investigating SERS signals and by conventional imaging techniques. Raman measurements of cells revealed that both nanostars and nanospheres can enhance the sensitivity of Raman measurements particularly for bands corresponding to proteins and lipids. However, their effects may be different, depending on the morphology of particles and the type of cell. The results suggest that nanostars aggregate more easily in solution and in cells, especially HepG2 cells, and as a result, fewer cells tended to accumulate these particles where they were found more randomly distributed. Nanospheres accumulated to a greater extent and had less aggregation in both HepG2 and HeLa cells, although HepG2 cells tended to take up fewer particles compared to HeLa cells. While both types of nanoparticles increased the local Raman spectra, nanostars increased the signals more than nanospheres for the majority of the spectra. However, the enhancement by nanostars was much stronger in HeLa cells compared to HepG2 cells, likely reflecting the observation that HepG2 cells accumulate fewer particles.

Furthermore, it was observed that gold particles do not have similar SERS enhancement effects for different Raman bands, indicating that different types of nanoparticles have different affinities for different chemical structures. In particular, enhancement of a band at 825 1/cm for nanospheres likely reflects their interaction with a specific subset of proteins compared to nanostars, which showed greater enhancement with many other chemical structures that could reflect different proteins or lipids. This information should be taken into account when designing nanoparticles for cancer therapy applications to understand how the local environment could affect the efficiency of nanoparticle accumulation, aggregation, and morphology.

In this chapter, we studied how nano-morphology affects the interaction of particles with different intracellular environments through SERS. To study the NBI, we also need to localize them within cells. In the next chapter, a new technique is offered to localize particles in different regions of cells through hyperspectral imaging. Besides, it is discussed how this system can be used to characterize nano-morphology in cancer cells. Two different systems were compared in [27].

Chapter 5
Using Intracellular Plasmonics to Characterize Nano-Morphology in Human Cells

This chapter is based on the following submitted manuscript:

- **Ahmad Sohrabi Kashani**, Alisa Piekny and Muthukumaran Packirisamy, "Using intracellular plasmonic to characterize nano-morphology in Human cells" (submitted to *Nature microsystems and nanoengineering Journal*, December 2019)

Determining the characteristics and localization of nanoparticles inside cells is crucial for the design of nanomedicines for cancer therapy. Hyperspectral imaging is a fast, straightforward, reliable, and accurate method for single-cell analysis to study nanoparticles in cells. With a hyperspectral image, we can collect spectral information from thousands of pixels in a short time. In this work, we examined different gold particles with different physicochemical properties in cells. We used hyperspectral imaging to detect, characterize and localize three types of gold particles (with different morphologies): nanospheres, nanostars and Swarna Bhasma (SB), an Indian Ayurvedic/Sidha medicine, in A549 (human non-small cell lung cancer) and HepG2 (human hepatocellular carcinoma) cells. Dark-field imaging, spectral and spatial measurements revealed that nanospheres are more uniformly distributed and provide more accurate information on their intracellular microenvironment compared to the other particles. Intracellular detection is based on the shift measurement in the wavelength of the localized surface plasmon resonance band during the interaction of nanoparticles with their surrounding medium. The trend in plasmonic shifts for all three types of particles in cells is similar in exhibiting broader and longer bands. However, the intracellular plasmon changed depending on the size and the morphology of nanoparticles. This highlights that this approach can be used to accurately characterize particles in cells. Our results also suggest the potential of this technique to be used for subcellular sensing through plasmonic shifts.

5.1. Introduction

Nanoparticles (NPs) with different physicochemical properties are being developed for a wide range of biomedical applications. Due to their small size and tunable properties, they are being explored for use in cancer diagnostics and treatment. NPs can be used as carriers to deliver drugs with improved efficiency compared to conventional methods. For example, with NPs

delivery system, the release of drugs can be optimized under controllable conditions. Lack of selectivity and negative effects on healthy tissues/cells are the main drawbacks of the classical methods[251][252][31]. NPs provide an advanced approach to develop therapeutic techniques in which NPs with unique physicochemical properties, nanomedicines, are designed to transport drugs to a specific place in the body or even in the cells. Before exploring their clinical use, it is essential to thoroughly evaluate NPs in cells to understand their toxicity, distribution, and how they impact the intracellular environment and vice versa [149][253]. Detection and intracellular localization are critical in the development of nanomedicines, and at the same time extremely challenging because of the sensitivity and resolution limits of the current techniques. To understand nanomedicines-based treatment efficiency, we need to advance our ability to visualize NPs uptake and identify/characterize NPs in the subcellular level[254]–[256].

Various microscopic and spectroscopic techniques have been developed for the subcellular detection and visualization of NPs. Scanning electron microscopy (SEM) and transmitting electron microscopy (TEM) have high resolution and permit the visualization of NPs at the subcellular level. For example, *Shapero et al*. [257] used TEM to visualize silica particles in A549 cells, and they found that these NPs are localized in the lysosomes, and not in the nucleus. Despite the advantages of TEM, this technique is costly and needs a complicated sample preparation that can impact the cellular structure [258]. Sample preparation for SEM technique is simple; however, this technique can only be used to image the surface of cells. Light microscopy can be used to visualize NPs and their surrounding environment; however, only clusters of particles can be visualized [253]. Recently *Chen et al*. [259] developed a super-resolution fluorescence imaging technique with a spatial resolution of 10 nm, well below the light diffraction limit. They used this technique to detect silica nanoparticles (MSNs) in HeLa cells, which they visualized in lysosomes and mitochondria. However, this method has limitations as it requires the addition of fluorescent tags onto NPs, which is restricted by their functionalization, and requires a system capable of imaging with super-resolution.

Raman spectroscopy (RS) and infrared absorption (IR) also have been used for the detection and localization of NPs at the subcellular level. The low spatial resolution of the IR technique has limited the application of this technique for intracellular diagnosis. However, Raman Spectroscopy is a powerful technique that can differentiate chemical structures in cells based on their unique vibrational modes. Once a sample is illuminated by a laser, the emissions are shifted by the

vibrational properties of molecules due to the inelastic scattering[260][27][258]. Raman shifts can be measured for molecular diagnosis and quantify their concentration. Noble NPs, such as gold, can enhance the intensity of Raman spectra in the vicinity of molecules, which is called surface-enhanced Raman spectroscopy (SERS). With Raman mapping and SERS effects, the localization/distribution of NPs in the subcellular level can be determined by Raman mapping over the entire cells. *Shah et al.* [234] studied the localization of gold NPs in human prostate cancer cells by confocal Raman scanning at a single-cell level. They showed that this technique could facilitate the measurements of a variety of gold NPs in different cell types and in different subcellular locations. The difficulty in interpreting the SERS spectra, as well as the time-consuming operation for the Raman scanning, are two main limitations of Raman techniques[261][262].

Recently, our group monitored the intracellular location of NPs using plasmon properties [230]. For this technique, hyperspectral images (HSI) in combination with dark-field imaging (DK), are utilized to characterize different subcellular components and determine the locations of NPs. Over the past few years, hyperspectral imaging techniques have received considerable attention for single-cell analysis [263]–[267]. Both spectral and spatial information of NPs can be simultaneously recorded with hyperspectral imaging, providing a novel platform for the intracellular characterization of NPs. The entire spectrum can be acquired at each point in the HSI image, and in contrast to the SERS method [268][269], no complex interpretation is required. Using the HSI technique, the high-resolution spectral information of thousands of pixels can be recorded in less than one hour. Using our technique, the localized surface plasmon resonance (LSPR) of gold and silver can be studied at the nanoscale to detect their location and monitor their micro-environment in cells. The LSPR properties of NPs depend on their physicochemical properties such as size, morphology, functionalization, and the surrounding medium. The hyperspectral technique provides information on changes in these properties as well as their intracellular localization. In contrast to SERS, NPs can be characterized in cells much more rapidly using an advanced label-free method while their internalization can be studied by measuring the unique spectral signatures.

Here, in the current paper, we used hyperspectral imaging to study the interactions of three different types of gold NPs: nanospheres, nanostars, and Swarna Bhasma, an Indian Ayurvedic/Sidha medicine, in A549 (human non-small cell lung cancer) and HepG2 (human hepatocellular carcinoma) cells. SBs are large gold-derived particles prepared as Ayurvedic/Sidha medicine and are variable in composition and shape [270][167]. As described earlier, the LSPR of

gold particles is sensitive to the surrounding medium, and we measured changes in plasmonic shifts to determine the location and characteristics of particles in cells (**Figure 5-1**). Besides, with this system, we could confirm the presence of NPs in cells by considering their unique spectral signatures. Our findings showed that the distribution of each type of gold particles is different. A greater accumulation of nanospheres was observed in cells compared to the other particles, and they exhibited a greater plasmonic shift with more sensitivity to their neighboring medium. This study revealed that the intracellular plasmon depends on the size and morphology of particles. By improving our understanding of their properties in cells, this information will help advance the development of NPs for medical applications.

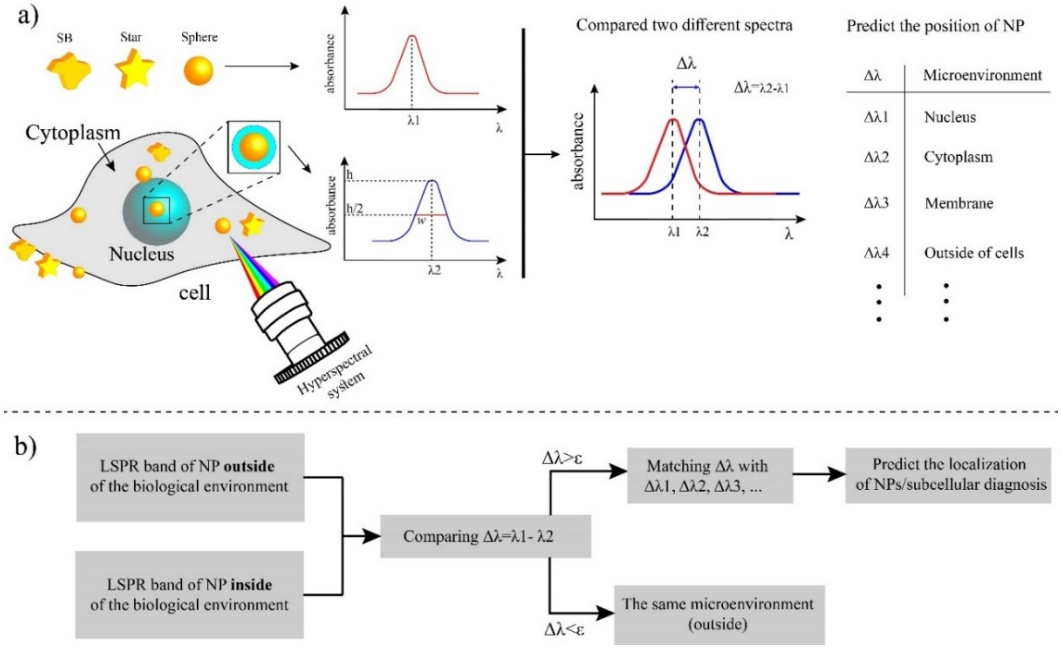

Figure 5-1. a) *A schematic showing how the detection/localization of NPs (with different morphologies) is determined within cells by the hyperspectral technique when their surrounding microenvironments are changed.* ***b)*** *The concept of the using hyperspectral images for subcellular detection/localization (ε shows small and negligible differences in LSPR band),*

5.2. Materials and Methods

5.2.1. Synthesis of Gold Nanostars and Nanospheres

Turkevich method[216], the most commonly used technique for preparing the spherical particles, was used to synthesize the nanospheres by reducing gold chloroauric acid to gold atoms. Briefly, we boiled 80 ml of HAuCl4.3H2O solution containing 40 µg/mL, and then added 5 ml of 1% sodium citrate. We then heated the solution for 15 minutes, and the solution changed from pale yellow to purple and then ruby-red. For the preparation of nanostars, a seed-mediated approach

was utilized. 10 ml of the 0.25 mM of gold solution was mixed with 10 µL of 1M HCL and 100 µL of pre-synthesized seed solution. Ascorbic acid and silver nitrate then were simultaneously added to the solution and stirred for a few minutes. Then, the solution became blue.

5.2.2. Swarna Bhasma

Swarna Bhasmas are Indian gold-based particles that are prepared by the incineration of gold in the presence of herbal extracts. The incineration process is performed many times until their size reaches down to the size of the chemically synthesized particles. SB particles were purchased from Jaya Indian Medicine Pharmaceutical Pvt Ltd, Maduravoyal, Chennai, Tamilnadu, India in powder format, and they were suspended in deionized water.

5.2.3. Hyperspectral Imaging System and Processing Data

A hyperspectral imaging system (CytoViva, Aruban, AL, USA) was used to capture HSI images of fixed NP-treated cancer cells on glass coverslips. This system provides a high-resolution dark-field-based optical microscope combined with a photo-spectrometer for spectral characterization and spectral mapping at the nanoscale. The spectrophotometer is connected to CCD (charged-coupled device) camera attached to a microscope to take images of the sample (**Figure 5-2**). This method is a label-free technique and does not need any labels. This system with a halogen light source permits the capturing of visible to near-infrared (VNIR) spectra in the range of 400 – 1000 nm, with a resolution of 2.8 nm within each pixel of the scanned field-of-view. Each pixel of an HSI image is ~25 nm using the 100X objective. Gold particles are brighter in HSI images, and they can be characterized by studying their spectral information. The LSPR properties of gold particles in the biological environment can be measured to identify them and determine their spatial distributions in cells without destroying the sample[271].

In order to capture HSI images, the condenser was adjusted until it touches the cover glass in the presence of the oil, and an oil-immersion objective (60X or 100X) was then used to focus on the desired area. Before taking HSI images, the sample was imaged with the dark-field optical system. Before collecting the spectral information of the same area, the exposure time for each spectral area was set to 0.15~0.25s, and the intensity was adjusted to a value between 1000-5000 units to make sure that spectral signals do not exceed the maximum limitation. The desired area was scanned in 700 × 700 pixel resolution. We then used ENVI 4.8 (Exelis Visual Information Solutions, Boulder, CO, USA) software for processing the collected spectral data. We chose the

desired regions of interest (ROI), and the mean spectral data was collected for approximately 70~100 pixels. A spectral library (SPL) was created from the ROI, and their spectra were filtered against the control cells to obtain the spectral data of gold NPs (F-SPL). Furthermore, the filtered spectral data were calibrated with respect to the halogen source light spectra. This process is necessary when two peaks from a sample and the lamp halogen, are overlapped, causing not to analyze HSI images accurately. Finally, the spectral intensities were normalized between 0 and 1 to compare the LSPR band. The spectral mapping was performed using spectral angle mapper (SAM) algorithm to scan the HSI images and find pixels whose spectral profile is matched with the corrected F-SPL with a threshold value of 0.1. In this algorithm, the intensity of the spectra does not affect the SAM analysis. The possibility of ignoring the intensity of signals is an advantage of the SAM as any variation in spectral intensity does not affect the results. The smaller difference shows a better match with the reference spectrum. Using ImageJ, we also used dark-field images and hyperspectral images to count the number of particles inside cells by considering their average sizes. The student t-test was used in order to compare statistical data, and differences were considered significant at $p<0.05$.

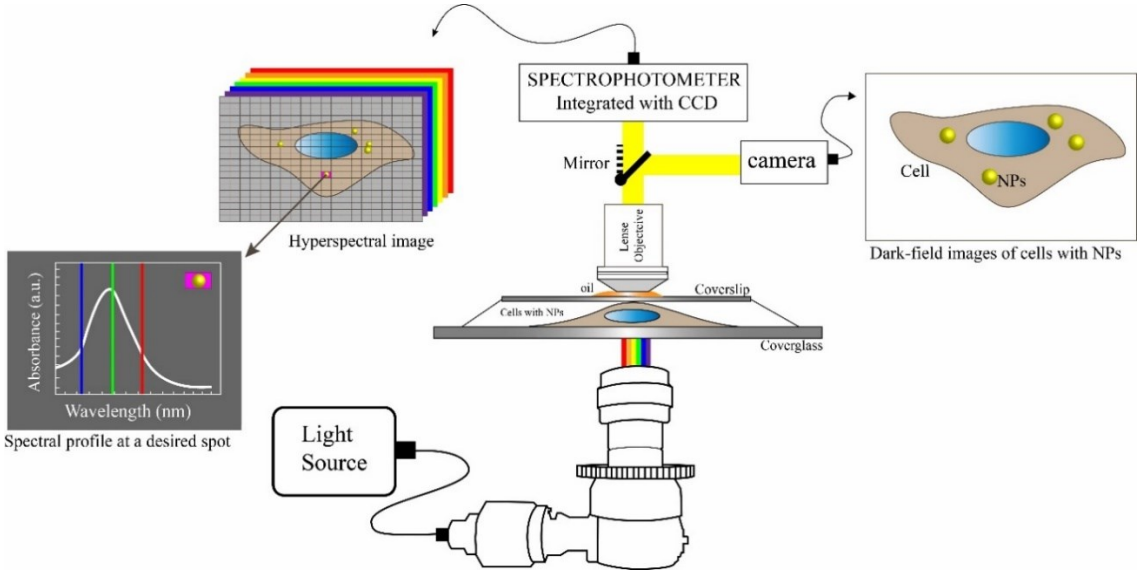

Figure 5-2. *A schematic showing the hyperspectral imaging instrument coupled with a Dark-field imaging system to study the interaction of nanomaterials with cells*

5.2.4. Cells Culture

A549 (human non-small cell lung carcinoma) and HepG2 (human hepatocellular carcinoma) cells were used to characterize gold NPs in cells. A549 cells and HepG2 cells were

cultured in F-12 medium and Dulbecco's Modified Eagle Medium, respectively. Media was supplemented with 10 % (v/v) fetal bovine serum (FBS; ThermoFisher Scientific), 2 mM glutamine, 100 µg/ml streptomycin, and 100 units/ml Penicillin (Wisent). Cells were kept in an incubator at 37°C with 5% CO_2. Cells were passaged at 70% confluency.

5.2.5. Cell Fixation

Cells were plated on acid-washed glass coverslips in 6-well dishes to 40% confluency, then particles were added for 24-48 hours. Cells were fixed in fresh, ice-cold 10% w/v TCA and washed with TBST as previously described, before placing the coverslip on a slide and sealing[167].

5.2.6. Size and Zeta Potential Measurements of Particles

We used Zetasizer Nano ZS90 (Malvern Instruments Ltd., Worcestershire, UK) along with dynamic light scattering (DLS) analysis to measure the average size of all gold particles. The system is equipped with a red laser (633nm) with power of 4mW, and a detection angle of 90°. The hydrodynamic size of particles was measured in deionized water based on the Brownian motion. Due to the different sizes of particles, the light is scattered with different intensities. We added 12 µL of each suspension to a disposable square corvette (scratch-free). For each gold sample, we made ten DLS measurements with a fixed run time of 20s. The average particle sizes reported in this study. Furthermore, we used Zeta Plus electrophoresis instrument (Brookhaven Instrument Corp.) to determine the surface charge of gold particles. For our measurements, we set temperature and PH 25°C and 7.4 respectively. For each sample, we analyzed the sample 10 times and the average was reported as the surface charge of each type of particle.

5.3. Results and Discussions

5.3.1. Characterization of Gold Particles

The physicochemical properties of three different types of gold particles were characterized by DLS, SEM, and potential Zeta analyzers before using them in cells. DLS showed that the hydrodynamic diameter of nanospheres is smaller compared to the other particles, with an average size of 14 nm (**Figure 5-3a**). Nanostars, as shown in **Figure 5-3b**, tended to aggregate when dried on glass coverslips, and the size of the individual nanostars varied between 50 to 100 nm with an average size of 65 nm. SB particles were significantly larger compared to nanostars and nanospheres. The crystal size of SBs was around 70 nm[167], while the average size of the

aggregates was up to 700 nm (**Figure 5-3c**). With the use of electrophoretic light scattering (ELS), we measured the surface charge of particles based on the Poisson-Boltzmann equation[272]. All particles displayed a negative potential; however, their levels were different. Synthesized particles showed negative charges due to the presence of citrate at their surface membrane. During the reduction process, both nanostars and nanospheres are decorated with citrates, which are the main source of the negative charge. Nanospheres were more negative compared to nanostars, suggesting that they are more stable. Zeta potential measurements showed that the surface of SBs was coated with negative ions, but was less negative compared to the other particles. The elemental composition of SBs was reported in our previous studies [167] [270]. Gold is the main element in SBs; however, they also contain other elements such as Mg, Ca, Fe, and Si.

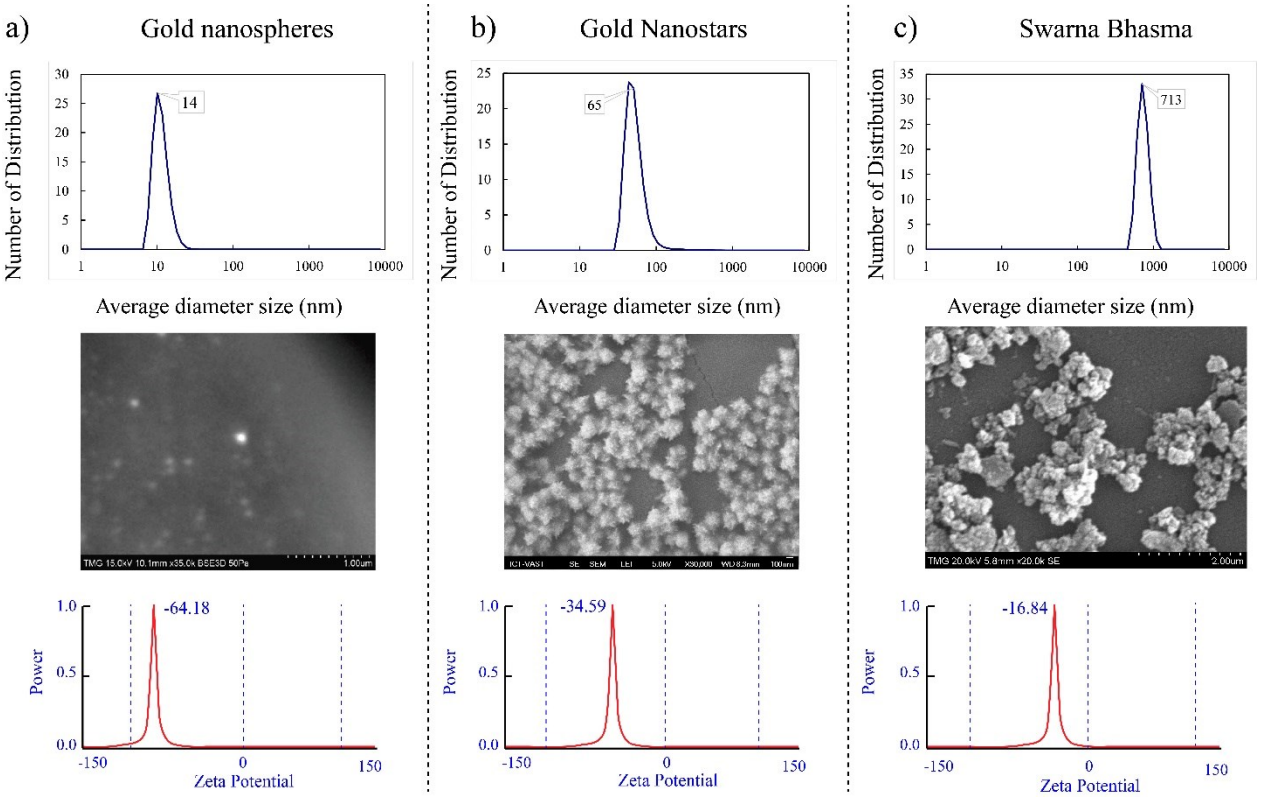

Figure 5-3. ***a)*** *Average size of nanospheres, SEM image of nanospheres, and their zeta potential measurements,* ***b)*** *the average size of nanostars, SEM of nanostars aggregates, and their surface charge,* ***c)*** *Size distribution of SB particles suspended in deionized water, SEM of SBs, and their zeta potential measurements*

5.3.2. Hyperspectral Imaging for Characterization of Particles

The particles were further characterized by hyperspectral imaging. Particles were dried on glass coverslips and sealed, and their z-profile spectra were measured at nanoscale. Depending on

their size, particles have different colors. The LSPR properties for the three different gold particles in this study are shown in **Figure 5-4**.

SBs and nanostars are larger, with longer wavelength LSPR bands. Nanospheres are smaller and more consistent in size, with LSPR bands of 540 nm for individual particles, and between 650~750 nm for aggregates (**Figure 5-4a**). Nanostars had two different peaks, one strong peak reflecting their spherical core and another weak peak corresponding to the branches (**Figure 5-4b**). The band at 750 nm (particle #1) belongs to branches, which becomes stronger when they get longer. The weaker signals confirm that branches are short, as shown in the SEM images. SB particles do not have any specific shape, and their LSPR bands are broader compared to the other particles. Smaller SBs have a band at 650~850 nm while larger SB particles have a broader band at 900~950 nm, as expected for bulky gold materials (**Figure 5-1c**).

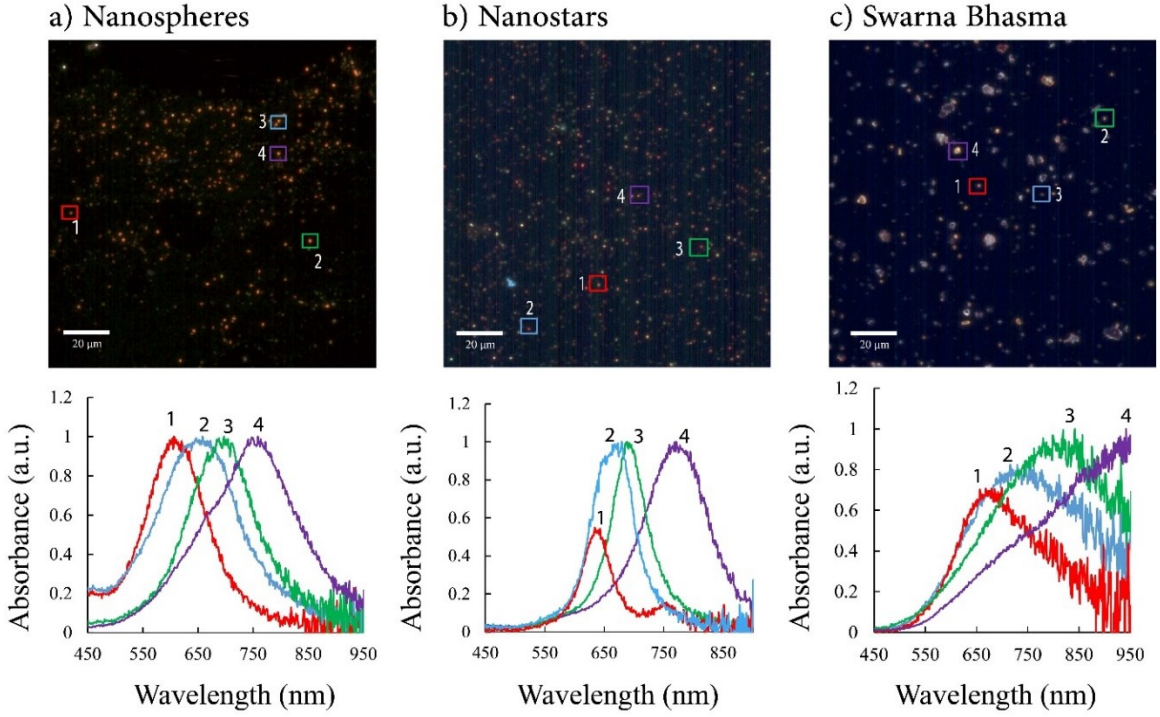

Figure 5-4. *Hyperspectral images (on top) of three different types of gold particles and their corresponding LSPR bands (on bottom),* ***a)*** *Nanospheres,* ***b)*** *Nanostars,* ***c)*** *Swarna Bhasma (Scale bar is 20 µm)*

5.3.3. Enhanced Dark-filed Images for Visualization of Particles in Cells

Next, we characterized the particles in A549 and HepG2 cells. Cells were fixed after 24 hours of treatment, and dark-field (DK) imaging was utilized to image the particles in cells with high resolution. Using this system, the noise-to-signal ratio is up to ten times lower compared to

other optical instruments, providing enhanced images of nanomaterials in nanoscale[30][273][274]. In this system, the oblique angle of source illumination is adjusted such that, it precisely focuses on the sample and bypasses the objective. This provides high contrast (very intense scatter from the sample and very dark background) to detect particles in cells.

Figure 5-5 shows images of cells with the different gold particles compared to non-treated cells. Due to the dark background, the gold particles are bright and easy to visualize. A549 and HepG2 cells had more nanospheres than nanostars or SBs. As shown in the DK images, nanospheres were localized mostly in the perinuclear regions. A549 cells appeared to have more nanospheres compared to HepG2 cells. Nanostars were more randomly distributed in the cytosol in HeLa and HepG2 cells, while cells had much fewer SBs. These larger particles may be more challenging for cells to uptake [167]. Therefore, in contrast to nanospheres and nanostars, SB particles were not found in all cells, and they were more randomly distributed similar to nanostars.

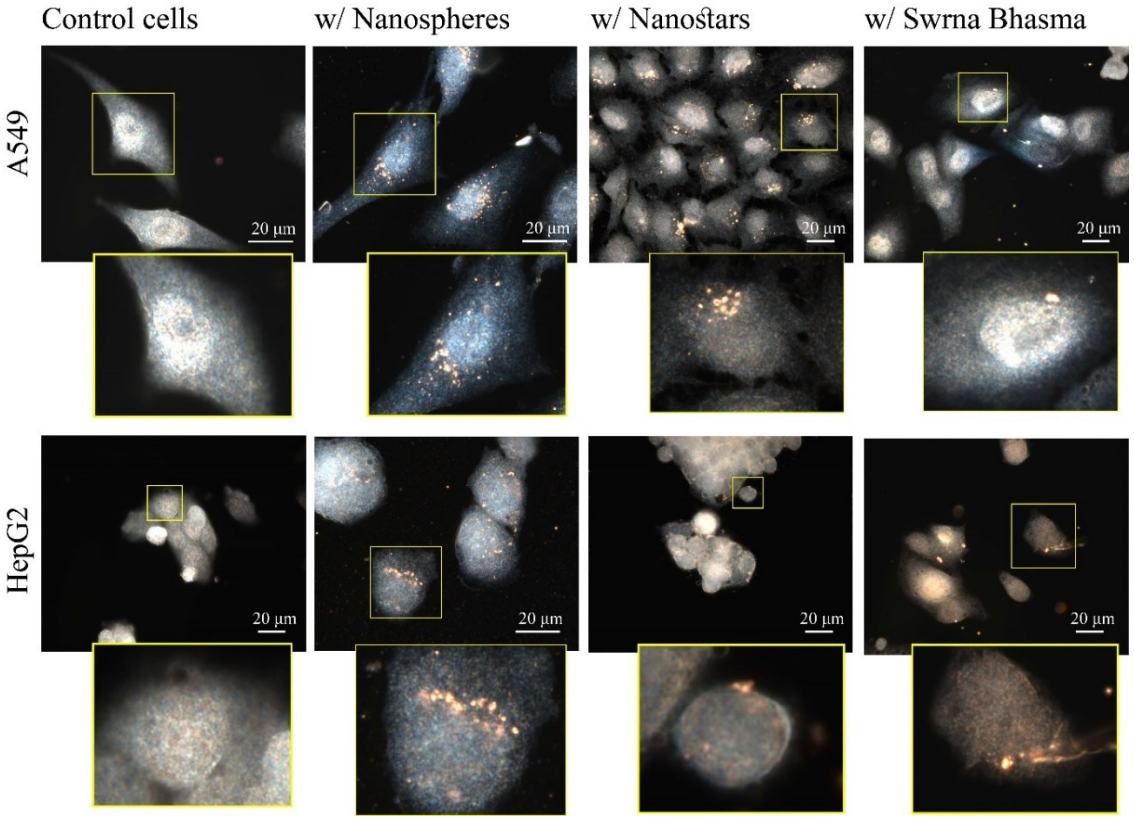

Figure 5-5*.Dark-field images of cancer cells treated with three different particles. Few SBs entered into cells, while nanospheres were found more in cells (Scale bar is 20 µm).*

5.3.4. Particle Detection with Hyperspectral Methods

As discussed earlier, HSIs can be used to detect particles such as gold NPs in cells. In **Figure 5-6a**, and **b** typical HSI images of A549 and HepG2 cells are shown. **Figure 5-6** shows the absorbance spectra of different regions of the cell including the cytoplasm (red) and nucleus (orange). The absorbance intensity of the nucleus was higher compared to the cytoplasm. The nucleus is more electron-dense compared to the cytosol and likely absorbs more light. In **Figure 5-6**, the green profile shows the absorbance of the particle/aggregate in cells. Gold particles, due to their specific LSPR properties, display unique spectral information depending on their size and morphology, as well as their surrounding microenvironment. The band position of NPs in cells and how it changes can be used to detect them in the subcellular level. A large peak is seen between 600 – 700 nm. The cytoplasm and nucleus have peaks in the range of 500 – 600 nm, which comes from the halogen light (shown in **Figure 5-6** – inset). We normalized the HSI profiles to obtain more precise spectral responses. The normalized data are plotted in **Figure 5-6** (right panels). After correction, the spectra from the nucleus and cytoplasm are flat, and the gold particle/aggregate peak is at 700 nm. The corrected spectral information allows for the detection of particles in cells and to characterize their properties in cells.

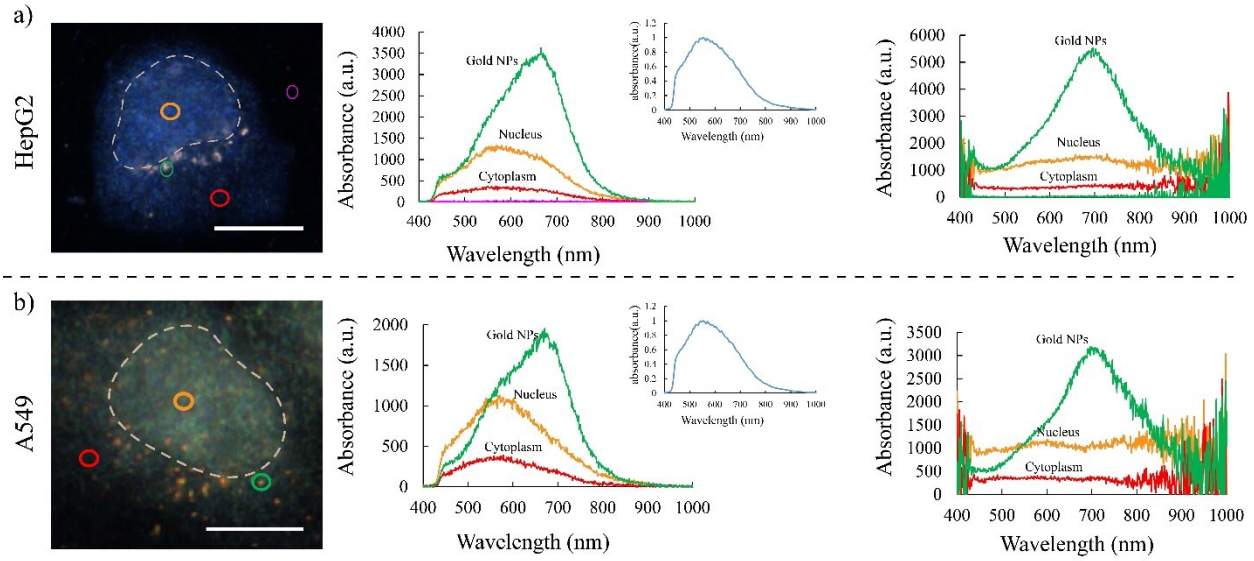

Figure 5-6. *Spectral responses of different regions of cells (nucleus, and cytoplasm), gold NPs (nanospheres) in HepG2 cells (top), gold NPs in A549 cells (bottom) and corrected responses after normalizing data with respect to the halogen lamp spectrum (Scale bar is 20 µm).*

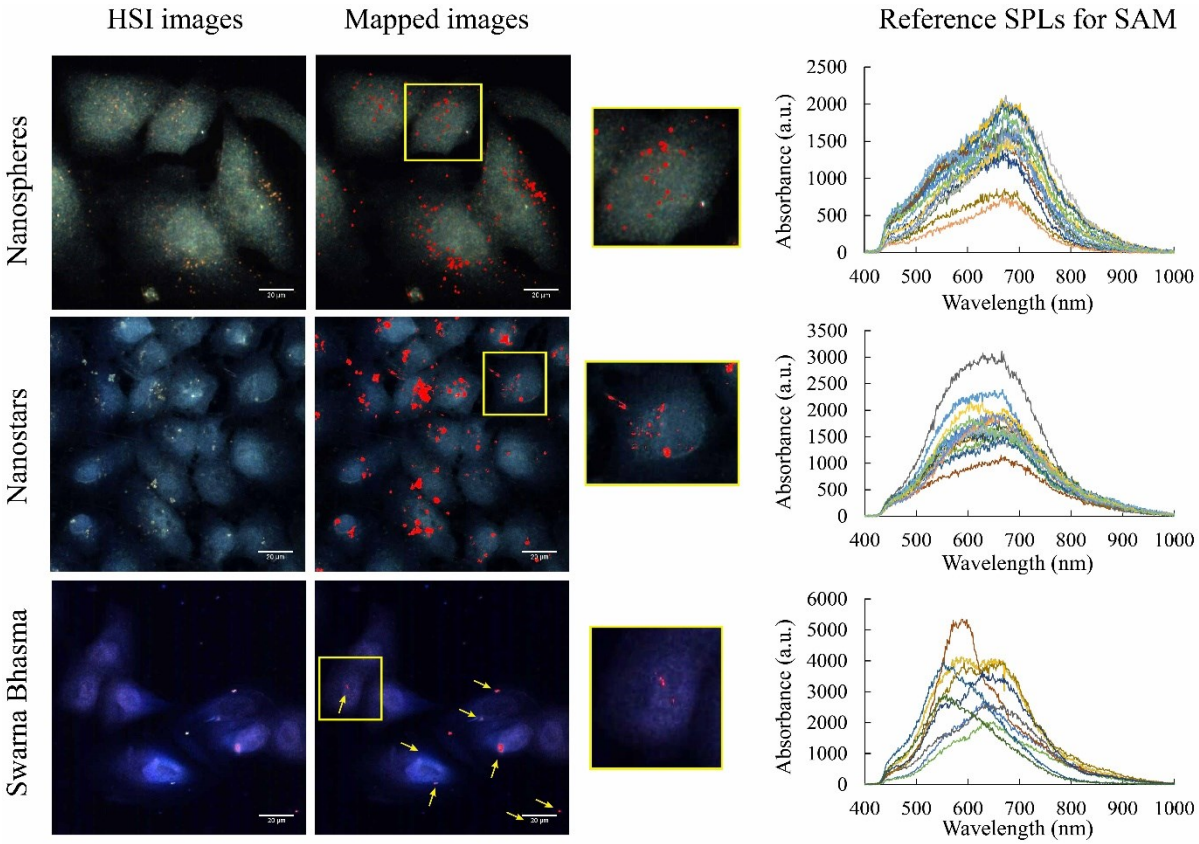

Figure 5-7*. Spectrally mapped gold particles in A549 cells with the SAM algorithm against the SPL (right panel) to localize particles in different regions of cells (Scale bar is 20 µm).*

5.3.5. Particle Mapping in Hyperspectral Images

Different particles in cells might not be detected visually with HSI images. Scanning through the spectral data of an HSI image can be utilized to distinguish pixels that match our desired spectra. The spectral angle mapper algorithm was used to spectrally scan HSI images. Before performing SAM analysis, a spectral reference was defined for gold particles. An ROI of gold particles within cells was chosen for, and their spectral data was converted to create a spectral library for mapping analysis. This SPL included both spectra from particles and cells, so it was filtered against the spectral information from cells without particles; the spectral information of control cells (without particles) was subtracted from the SPL of cells with gold NPs. The filtered SPL (F-SPL) was used to classify the different pixels in the HSI images. With SAM, the spectral similarity is measured between two spectra. With this algorithm, each spectrum was assumed to be a vector (with a direction and length), and the angle between the vector at each pixel and the F-SPL vector (gold particles) was calculated and compared to the user-definable threshold (0.1). The

SAM algorithm is a tool to detect pixels whose bands are similar to gold NPs, enabling to diagnose particles that are not visible in HSI images. This technique can be used to determine the distribution/localization of particles within cells. Due to the lack of resolution of HSI images compared to DK images, spectral measurements were used to detect the particles. **Figure 5-7** shows the mapping of three different particles in A549 cells with respect to SPL shown on the right panel. With the SAM algorithm, the particles are labeled in red after mapping to show their distribution in cells. Nanospheres were enriched at perinuclear regions, although could be seen in various regions of the cell including the nucleus. Zooming into a single cell, the mapped image shows nanospheres in the nucleus, although they were not visible in the original HSI image. Nanostars were more aggregated and localized more randomly compared to nanospheres, with only a few in the nucleus. SB particles are larger, and the mapped image does not provide further information on their distribution in cells. As can be seen in the right panel, their spectra varied more, likely due to their inconsistent morphology.

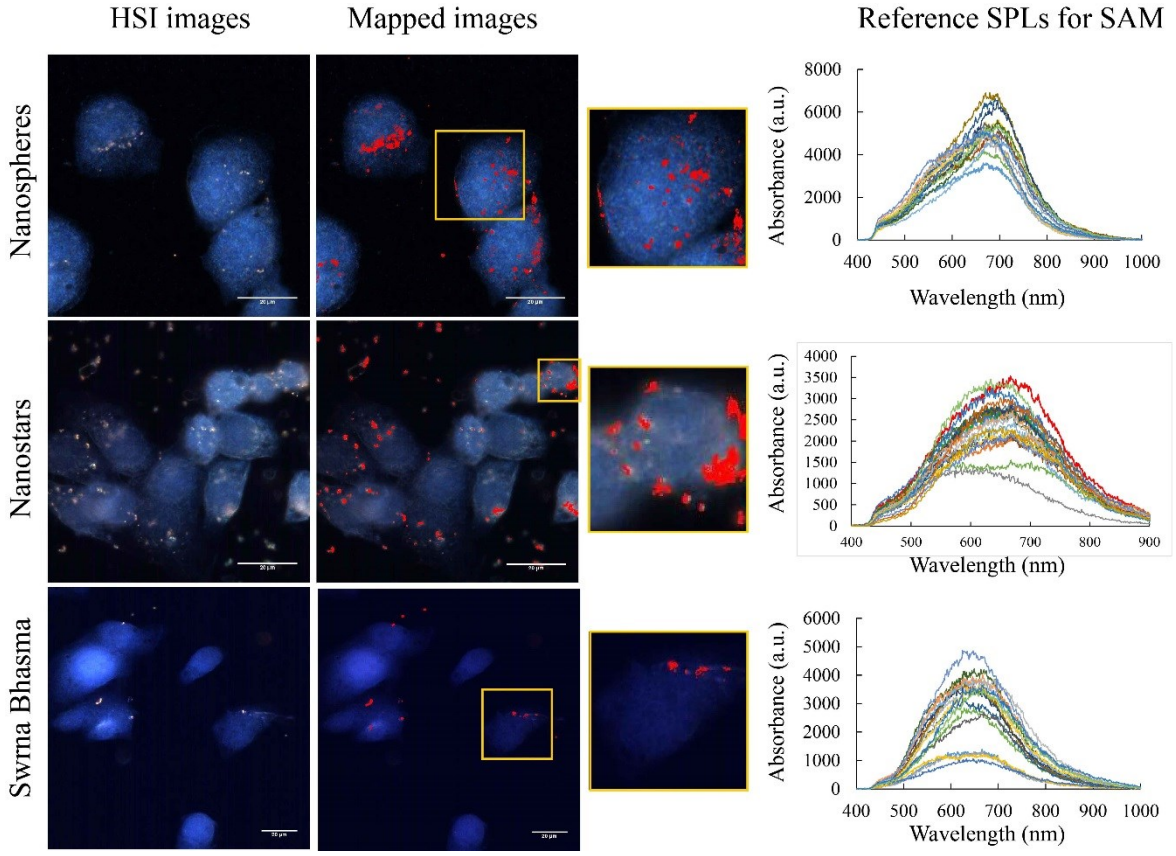

***Figure 5-8**. Spectrally mapped gold particles in HepG2 cells with SAM algorithm against the SPL (right panel-without normalization to the halogen lamp) to localize particles at various regions of cells (Scale bar is 20 µm).*

Similar mapping was performed on HepG2 cells, as shown in **Figure 5-8**. The distribution patterns of the three different types of gold particles in HepG2 cells was similar to A549. HepG2 cells had more nanospheres and nanostars compared to SB particles. However, HepG2 appeared to have fewer nanospheres and nanostars than A549 cells. There is no significant change in SBs between the two cell lines, and only small aggregates were in cells, with larger particles on the membrane surface. We observed a few individual/aggregates of nanospheres in the HepG2 nucleus and their level of internalization was less compared to A549 cells.

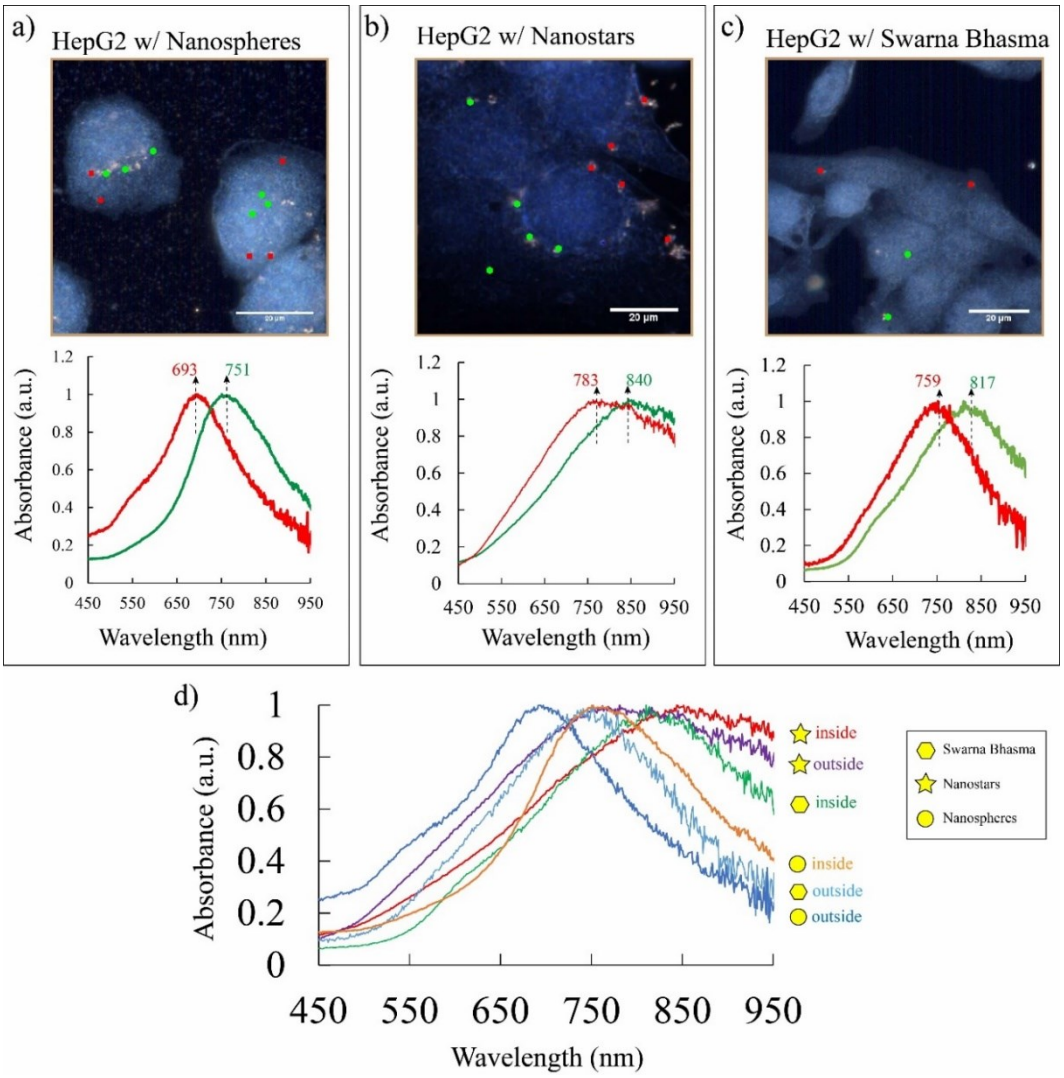

***Figure 5-9**. Spectral responses of gold particles at different regions of cells. **a)** HepG2 cells with sphered-shaped particles showing a band shifted from 693 to 751 nm for outside (at the periphery of cells) and inside (cytoplasm) particles, **b)** HepG2 cells with nanostars, inside aggregates (cytoplasm) showed a shifted band from 783nm to 840, **c**) HepG2 cells with SBs particles and the plasmonic shift from 759 nm to 817nm (Scale bar is 20 µm).*

5.3.6. NPs Spectral Responses for Intracellular Diagnosis

LSPR of gold NPs is influenced by size, morphology, and the local microenvironment. The LSPR scattering maximum wavelength is sensitive to the microenvironment and its optical properties, such as dielectric constant or refractive index. So any change in the local environment of gold NPs can cause a shift in the LSPR band (plasmonic shift). This change can be quantified through the following equation [275][276]:

$$\Delta\lambda_{max} = m\Delta n\left[1 - e^{-\frac{2d_d}{l_d}}\right]e^{-\frac{2d_a}{l_d}} \qquad 5\text{-}1$$

where $\Delta\lambda_{max}$ is the maximum expected plasmonic shift, m is the bulk refractive index of the NPs, Δn is the refractive index change induced by the absorbance, d_d is the thickness of the dielectric layer, l_d is the characteristic electromagnetic-field-decay, and d_a is the thickness of the absorbed analyte. This equation shows that the plasmonic shift is directly proportional to changes in the dielectric constant of the local environment. By increasing the dielectric layer thickness, the last term is increased, causing a higher shift in the LSPR band.

The shift in the LSPR band of gold NPs in cells enables us to detect and sense small changes in the environment adjacent to particles and confirm their presence in cells. Different regions in cells exhibit different microenvironments, which affect the optical responses of biomolecules or particles in their vicinity[277]. These effects are reflected in the LSPR responses. In **Figure 5-9a**, **b**, and **c**, the LSPR bands of three different particles in HepG2 cells are illustrated. Gold particles were marked with different colors in different regions of cells (edge/outside of cells in red, cytosol in green), and their corresponding spectra were compared below. As shown in **Figure 5-9a,** gold nanospheres outside or in the periphery of cells exhibited peaks at ~693 nm. Nanospheres inside cells had a shifted spectra of 751 nm. This shift is likely due to their interactions with components of the cell, such as proteins and/or lipids. Once particles enter into cells, they interact with different subcellular compartments, so the surface/local environment surrounding particles is dramatically changed, leading to an alteration in the optical properties of their local regions. The effects of these changes can be reflected in the spectral responses. For gold nanospheres, a shift can be seen for gold nanospheres situated in HepG2 cells compared to the outside gold nanospheres (**Figure 5-9a**). The peak for outside particles is sharper, while for inside particles, it becomes broader likely due

to changes in their surfaces. Spectra are also influenced by the size and aggregation of particles. The size of nanospheres is more consistent than the other two types, and their plasmonic shifts can be solely correlated to their intracellular interactions. However, for SBs and nanostars, the effects of size and degree of aggregation should be taken into account in interpreting their plasmonic shifts. For nanostars, the bands shifted from 760 – 790 nm to 830 – 860 for particles localized at the periphery and inside cells, respectively (**Figure 5-9b**). SBs particles are larger, and only a few smaller particles were inside the cells. Their bands shifted similar to the nanospheres; however, they were more broad (**Figure 5-9c**). Due to the irregular morphology and the inconsistent size of SBs, their LSPR changes may be also associated with their size and morphology.

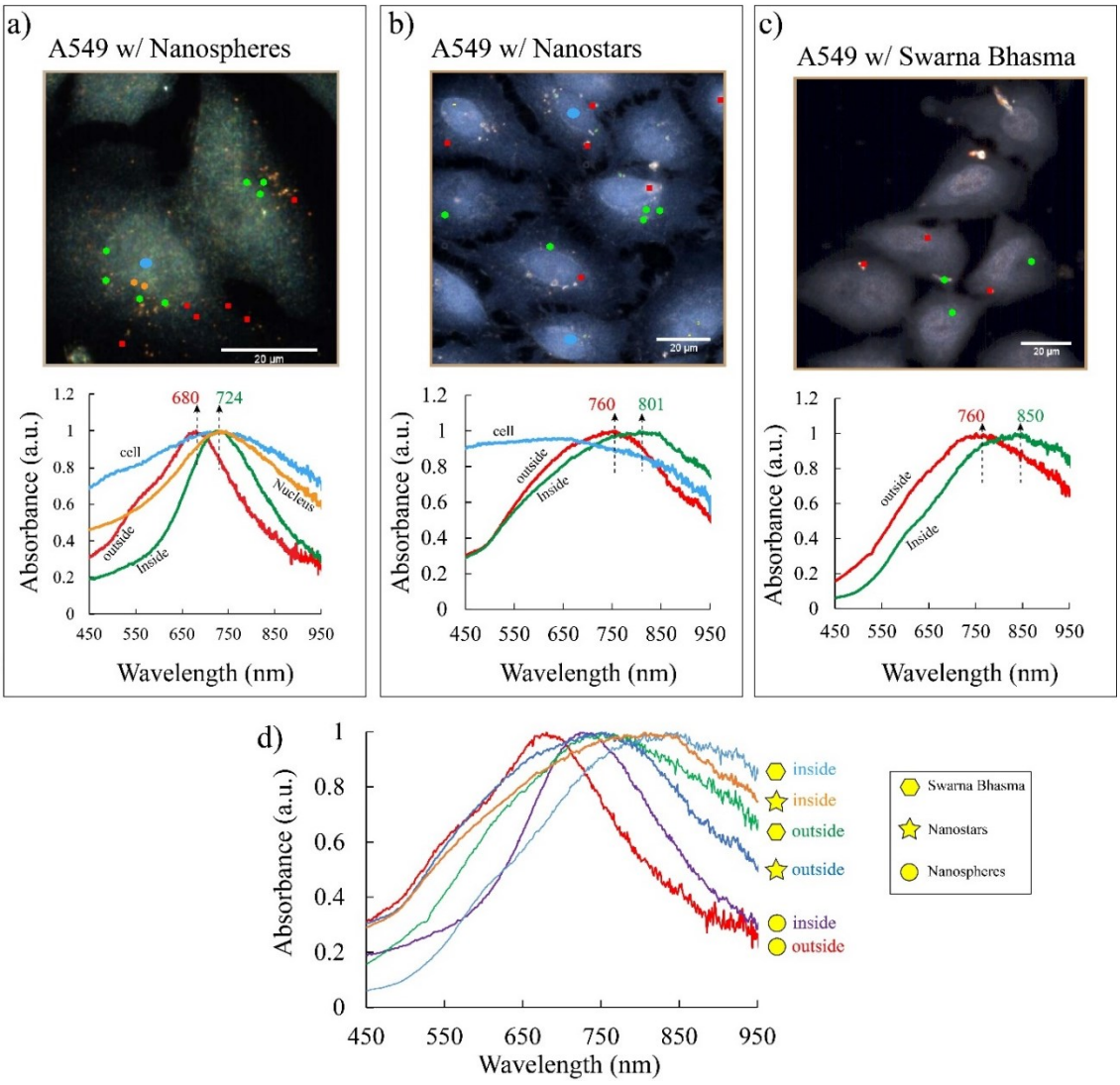

***Figure 5-10**. HSI images of A549 cells with three different gold particles, **a)** nanospheres, **b)** nanostars, and **c)** Swarna Bhasma, and their spectral responses corresponding to the different*

locations of cells, at the periphery (of cells) or edge of cells (on cells surface) and inside of cells mostly at the perinuclear regions (Scale bar is 20 µm).

A similar comparison was made for A549 cells with the three different types of particles to characterize their interactions with subcellular components. Since the nuclear region was more clear on these images, particles in the nucleus also were measured (orange). For gold nanospheres, the peak shifted to the right from 680 nm to 724 nm when particles were outside/periphery of cells compared to the cytosol (**Figure 5-10a**). The peak of particles in the nucleus was similar to the cytosol but was broader (full width at half maximum). LSPR of NPs with relatively small size is more sensitive [278]to the surrounding region/surface, so they can reflect changes in their surface better. So, the smaller size of nanospheres allows them to sense their surrounding changes better, and they appeared to be more sensitive to any changes in their local environment. Another noticeable change in spectral responses was the peak broadness. For nanospheres, the broadness was increased by 10~15% for nanospheres situated in the cells compared to nanospheres localized at the periphery of cells (**Figure 5-10a**). The broadness change (%) was determined by measuring the increase or decrease in the LSPR peak width (at half maximum) of NPs inside cells compared to the NPs outside or in the periphery of cells. In contrary to nanostars and SBs, a few nanospheres were also found in the nucleus of A549, and as shown in **Figure 5-10a**, their plasmonic bands were shifted while they became broader compared to the NPs in cytosol. There are some studies, showing that cytoplasm of cells has ten times higher dielectric constants compared to the cells membrane[279][277], and in another study [280] the dielectric constant of the nucleus was found to be four times higher compared to the cytoplasm. Besides the different interactions of NPs with subcellular compartments, the differences in dielectric constants could be another reason for the plasmonic shifts between particles situated in the periphery and particles in the cytoplasm or near to the nucleus. Nanostars tend to aggregate, and their peaks were broader compared to nanospheres, and their peaks shifted from 760 nm to 800 nm for particles/aggregates outside compared to inside cells (**Figure 5-10b**). SBs are larger, and only a few of them were found inside cells where they randomly localize in the cytosol. The mean band for particles inside cells shifted from 760 (outside) to 850 nm (inside), and the peaks were broad likely reflecting their non-uniform morphologies (**Figure 5-10c**).

Table 5-1. *Effects of the surrounding medium and morphology of NPs on intracellular plasmonics*

Cell line		Nanospheres	Nanostars	Swarna Bhasma
		Sphere-shaped	Branched-shaped	Non-uniform- shaped
HepG2 cells	Plasmonic shift ($\Delta\lambda$)*	$\sim 44\ nm$	$\sim 39\ nm$	$\sim 90\ nm$
	Broadness change (Δw)**	$+13.6\%$	-8.9%	$+19.1\%$
	Q-factor*** (inside cells)	4.55	2.68	4.45
A549 Cells	Plasmonic shift	$\sim 58\ nm$	$\sim 37\ nm$	$\sim 58\ nm$
	Broadness change	$+9.1\%$	$+19.6\%$	$+4.3\%$
	Q-factor	4.72	2.46	3.82

*$\Delta\lambda = \lambda_{inside\ cytoplasm} - \lambda_{periphery\ of\ cells}$

**$\Delta w = 100 \times \frac{w_{inside\ cytoplasm} - w_{periphery\ of\ cells}}{w_{periphery\ of\ cells}}$ (w: full width at the half maximum)

***$Q = \frac{\lambda}{w}$ (λ: peak frequency, w: full width at the half maximum)

The plasmonic shift for different cells and particles are reported in **Table 5-1**. The plasmonic shift shows the differences in LSPR band at the periphery of cells and LSPR band in the cytoplasm (at the periphery of the nucleus). The plasmonic shift takes place for all three types of particles between 44-90 nm depending on the type of cells, the morphology of particles, and their subcellular location. The data in **Table 5-1** indicates that nanospheres displayed a more consistent behavior in terms of peak broadness and the plasmonic shift, while two other particles exhibited different peak broadness in the different cells, likely due to the non-identical shapes of SBs and the different aggregation levels of nanostars. The spectra profiles of nanostars revealed that they were aggregated at the periphery and inside the cells. Therefore, nanostar plasmonic shifts from outside (periphery of cells) to inside cells (cytoplasm) can reflect both particle-particle interactions and particle-subcellular interactions. The results also indicated that the plasmonic shifts are stronger for SB particles whose size is larger compared to other particles. It seems that higher shifts in SBs originate mostly from the induced changes between particles rather than interactions with the

subcellular systems. Among these three particles, nanospheres are better candidates to reveal information on the local environment due to their effective interactions with their surrounding medium. Any shifts in these bands can be correlated to the different subcellular regions of cells with better accuracy compared to two other particles. Besides, nanospheres offer higher quality factors (Q-factor) in comparison to two other morphologies of particles (**Table 5-1**). The quality factor was calculated as the ratio between LSPR peak (nm) and the width at the half maximum(nm)[281]. The Quality factor shows the energy losses for the coherent motion of the electron, and depends on size, morphology, and surrounding medium of NPs. For surrounding medium-sensing, resonances with higher quality factors are desirable (narrow widths)[282]–[284]. Moreover, our results showed that SBs particles and nanostars have limitations to reach different subcellular regions of cells. However, nanospheres due to their smaller sizes were found in different subcellular regions in cells, enabling them to be used for subcellular diagnosis through intracellular plasmonics.

5.3.7. Particles Distribution in Cells

It was observed that particles after entering into cells were localized in three different regions, at the periphery or distance from the nucleus, at the perinuclear region, and inside the nucleus. Discrete nanospheres can be identified in different parts of cells, while nanostars aggregated either inside cells or at their periphery. SB particles are much larger, and the size of their aggregates might reach to microns, and their internalization level was not high. In order to estimate the number of particles in cells, the occupied area of particles in cells was measured, and by considering the average size of particles, they were counted in cells. At least 150 cells were considered for each particle type, and their distributions were quantified in three different (**Figure 5-11e**) regions and plotted in **Figure 5-11**.

The average number of nanospheres per cell was higher for both cell lines compared to two other types of particles, and A549 cells had almost two times more nanospheres, but it should be noted that A549 cells are larger in comparison to HepG2 cells, and they can accommodate more particles. There is no significant difference between the particle numbers of two other particles in two cell lines. In contrary to the nanostars and nanospheres, the uptake of SBs particles in cells was very low, and their distributions in different regions are random. It is evident that particles mostly localized in the cells and at the periphery of the nucleus (**Figure 5-11d**). This pattern can be seen

in both cell lines. SB particles were few (with smaller size) in cells and did not follow a specific distribution pattern in cells.

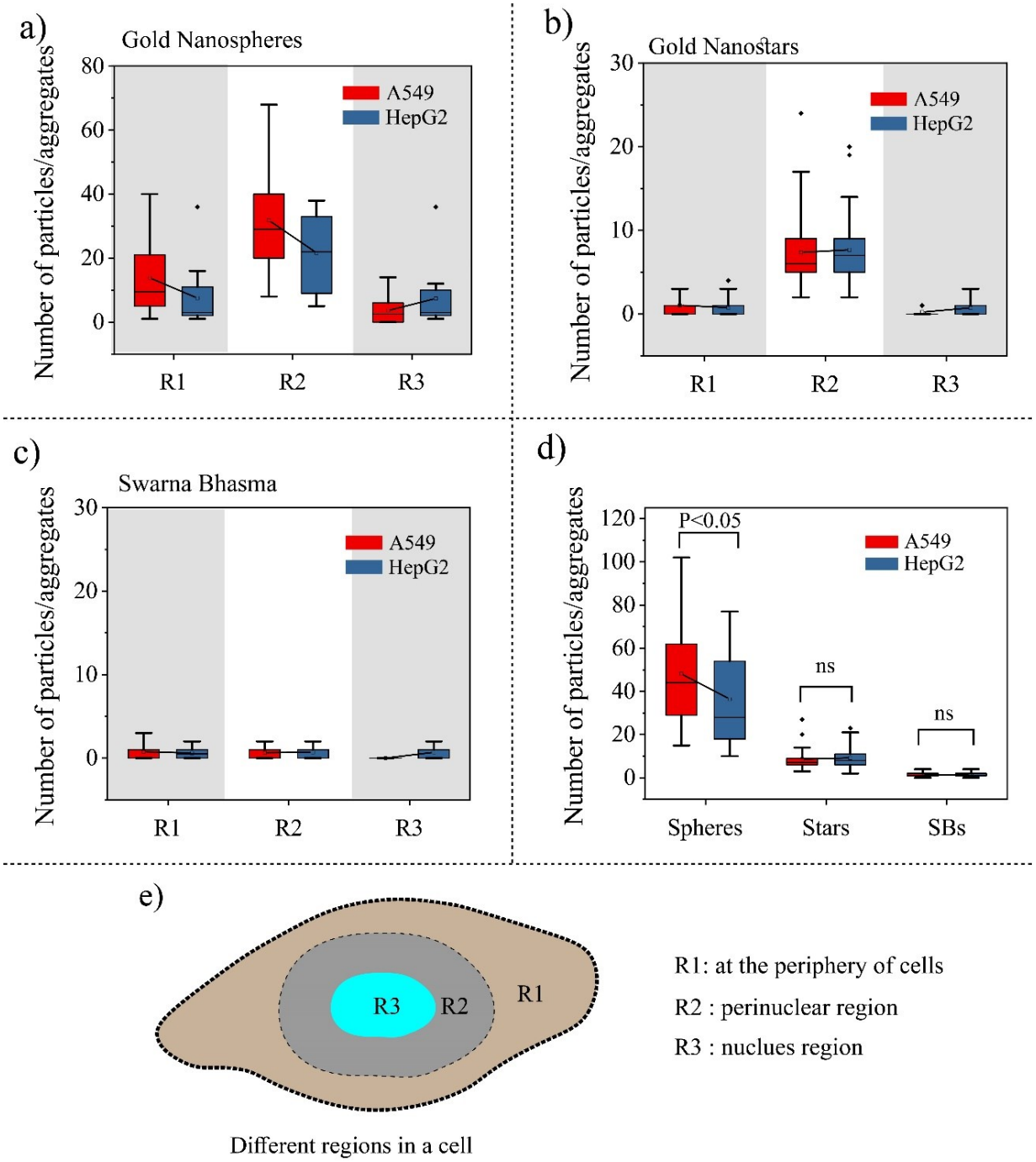

Figure 5-11. *Distribution of particles in cells.* ***a)*** *nanospheres particles distribution in different region of cells,* ***b)*** *gold nanostars distribution in different regions of cells, c) SBs particle distributions in cells,* ***d)*** *total number of particles in two cells,* ***e)*** *different regions in cells (R1: far from the nucleus and at the cell periphery, R2: perinuclear area, and R3: nucleus)*

5.4. Conclusions and Outlook

In NPs-based cancer therapy, precise subcellular detections/distributions of NPs are crucial to design effective nanomedicines. Although the detection of NPs in biological environment has been accomplished using electron microscopy, yet newer, cheaper, more advanced and faster methodologies provide opportunities. Highly sensitive optical properties of gold NPs have provided a novel and non-invasive platform to develop LSPR-based methods to diagnose NPs in subcellular levels. In the current work, this idea was verified by using three different gold particles (with different morphologies), and we showed that how hyperspectral imaging and spectral measurements at nanoscale enable us to localize particles in different subcellular regions and understand their interactions with subcellular compartments. Intracellular diagnosis with hyperspectral imaging allows not only to confirm the presence of particles in cells but also their nanoscale spectral measurements provide information on their surrounding medium. Inside the cell, there are various microenvironments and gold particles localized in these regions exhibit different plasmonic shifts depending on the optical properties of their surrounding regions as well as their physicochemical properties. Our results revealed that particles could sense their intracellular environment. We examined particle responses at different subcellular regions, at the periphery of cells, at the perinuclear and inside nucleus. Our measurements showed that particles depending on their interactions with their local environment have different intracellular plasmonic responses. During these interactions, the surrounding medium of particles is changed, affecting the LSPR properties of NPs. Stability and consistency in both morphology and size of particles are two important factors for intracellular detection. Due to the inconsistency and irregular shape of SBs and the strong tendency of nanostars to aggregates, the plasmonic shift in their responses cannot be purely correlated to modifications in their surrounding medium and how they interact with subcellular compartments. The effects of particle-particle interactions and different morphologies of particles are also reflected in the plasmonic shift. Among three particles, nanospheres distributed more uniformly within cells and they appeared to reflect the effects of their surrounding environment better as they showed a more consistent behavior in cells. Furthermore, the distribution of particles showed that nanospheres are capable of navigating to different subcellular regions in cells while two other particles had limited access to different subcellular regions. Designing proper NPs with specific physicochemical properties will play a critical role in subcellular diagnosis with hyperspectral imaging. The unique spectral signature of gold NPs and

plasmonic shifts of NPs can be used to make a comprehensive library for different subcellular regions of cells. This library can be used to detect NPs in subcellular levels, predict their localizations in cells and study how they interact with their subcellular compartments.

So far, we used different imaging and optical techniques to characterize the NPs in cells. After these initial steps, in the next chapters, the focus is given to the mechanobiology of cells, and how NBI affects the mechanobiological properties. In order to characterize the mechanobiology of cells, we need to capture cells at desired sites. In chapter 6, a new microfluidic is offered to trap cells/particles at specific trapping sites.

Chapter 6
Efficient Low Shear Flow-based Trapping of Biological Entities

This chapter is based on the following published paper:

- **Ahmad Sohrabi Kashani** and Muthukumaran Packirisamy. "Efficient Low Shear Flow-based Trapping of Biological Entities." Scientific reports 9, no. 1 (2019): 5511.

Capturing cells or biological entities is an important and challenging step toward *in-vitro* studies of cells under a precisely controlled microscale environment. In this work, we have developed a compact and efficient microdevice for on-chip trapping of micro-sized particles. This hydrodynamics-based trapping system allows the isolation of polystyrene micro-particles with a shorter time while inducing a less hydrodynamic deformation and stress on the particles or cells both after and before trapping. A numerical simulation was carried out to design a hydrodynamic trapping mechanism and optimize the geometric and fluidic parameters affecting the trapping efficiency of the microfluidic network. By using the finite element analysis, the velocity field, pressure field, and hydrodynamic force on the micro particles were studied. Finally, a PDMS microfluidic device was fabricated to test the device's ability to trap polystyrene microspheres. Computational fluid analysis and experimental testing showed a high trapping efficiency that is more than 90%. This microfluidic device can be used to trap cells to study the dynamic interaction of nanoparticles and single cancer cells. For example, to study the cellular uptake of cells using optical measurements or to study the effects of cellular uptake on the cellular deformation and elasticity of cells.

6.1. Introduction

In recent years, the use of microfluidics and microfabrication has been adopted in various areas of engineering and science. Microfluidics is an important technology suitable for numerous applications in biomedical, drug delivery, cellular analysis, diagnosis, cancer detection, and biotechnology [292], [286]. One of the most exciting advancements in the application of microfluidics has happened in the biological and biomedical areas. Reduced sample volume, short-time analysis, control of spatiotemporal chemical composition, precise and predictable fluid flow regime (laminar flow), portability and integration with sensors actuators, controllers and

automation systems have made microfluidic devices an attractive miniaturized platform for biological and biomedical applications [91], [287].

Capturing and trapping of cells is the first critical step in single-cell studies and can be defined as the development of technologies for the immobilization of cells at a precise location for further analysis. At the same time, a fluid flow needs to be applied to provide the cells with nutrients and other media influencing the behavior of the cells. Isolation of single cells from the surrounding environment and their analysis have important implications for diagnostic and therapy. For example, capturing circulating cancer cells in peripheral blood is beneficial for detecting cancer at early stages and estimating the risk of metastatic relapse [288]–[290]. Before the advancement of microfluidics, conventional strategies such as sample tubes and pipettes were used to manipulate the biological particles at the microscale. The lack of sufficient precision, high-throughput, online monitoring, time and reagent consuming have limited their application in single-cell analysis. Many microfluidic-based technologies have been developed to control the spatio-temporal of the environment of cells. Based on the types of forces used in manipulation of the cells on the chip, they are classified into different categories: optical [291], electrical [292], magnetic[293], acoustic[294] and hydrodynamic manipulations [295]. Hydrodynamic trapping of cells offers a low-cost, simple, efficient and high-throughput arraying of the cell without controlling or using other equipment such as lasers, electrodes, magnets, and ultrasound transducers. In this technique, the sample and the medium are introduced by flow channels providing conditions for the observation of the responses of the cells to the environmental changes [296], [297]. Depending on whether the target particles are in contact with a support surface, the hydrodynamic trapping systems are classified into two main methods: contact-based methods [298] in which the fluid flow is implemented to physically confine the cells against microfabricated obstacles or walls, and contact-less methods [299] which are based on micro eddies, micro-vortices and stagnation flow. Due to some limitations of contact-less trapping techniques such as low efficiency and low-throughput, most of the efforts have been directed toward the implementation of the contact-based methods to capture and manipulate individual cells. Two concepts have been used for the contact-based trapping technique: 1) Path with the least flow resistance[300] where single cells are directed into the trap sites possessing much smaller hydrodynamic resistance compared to the bypass or the main path, and after filling the trap site, the subsequent cell is redirected to another path having the least flow resistance, 2) Di Carlo[301] method, in which micro-sieve arrays are designed to trap

single cells from a suspension of flow. This method suffers from a relatively low-efficient single-cell trapping compared to the first concept and most of the samples are lost during the trapping process. In order to optimize the efficiency of hydrodynamic single-cell capturing systems, the geometric parameters, as well as the fluid flow factors, should be taken into account.

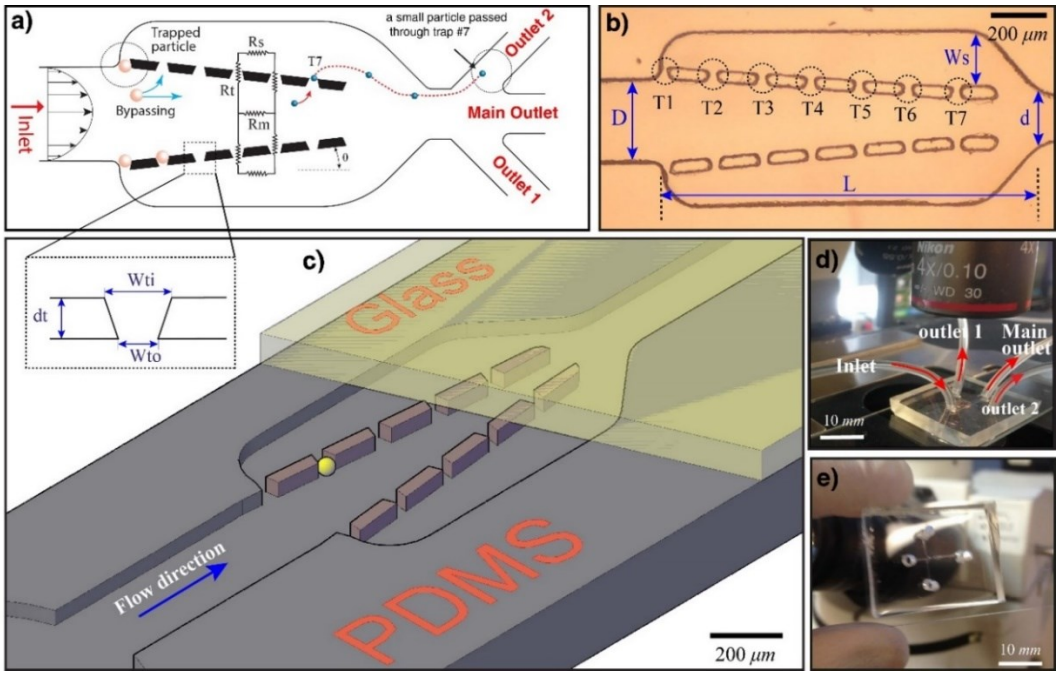

***Figure 6-1**. **a)** Schematic illustrating the working concept of the system and the fluidic resistances of the main channel (R_m), side channels (R_s) and trap sites (R_t) and the dimensions of the trap: inlet of the trap width (W_{ti}), outlet of the trap width (W_{to}), depth of each site (d_t), **b)** micrograph of the microfluidic showing the geometric parameters of the main channel and side channels (D: inlet of the main channel, d: outlet of the main channel, L: length of the main channel, and W_s: maximum width of the side channel), **c)** a 3D illustration of the trapping device, **d)** the PDMS microfluidic device and the inlet and outlet connections, **e)** A photograph of the fabricated chip*

Here, we developed a lab-on-a-chip system using the contact-based hydrodynamic trapping method to immobilize single cells by positioning a series of micro-sieves on the main channel sidewalls. In this system, the combination of the two above-mentioned concepts is implemented to design an efficient trapping microfluidic device. In our design, similarly to Di Carlo design, micro-sieves are used, but on the sidewalls, to capture individual cells or particles while at the same time the concept of "path with the least resistance " is utilized to tune the geometric parameters of the main and the side channels in order to enhance capturing efficiency of the device. The network includes two side channels and a main convergence channel designed to direct the streamlines toward the trapping sites. In contrast to Tan and Takeuchi [300] and other works, a channel with

inclined walls is designed to increase the hydrodynamic resistance of the main channel, enabling to navigate single cells into the trapping sites. With the proposed design, the trapping device can be more compact as the main channel does not need to be extended to generate a higher flow resistance than trap sites. Compared with the previous studies using the similar concept, this design offers a fast loading time while less mechanical deformation and stress are introduced onto the target cells both before and after trapping. In this work, first, we used a computational fluid dynamic simulation analysis by COMSOL Multiphysics to optimize the geometric parameters of the channels and trap sites, and predict the fluid flow pattern inside the channels, considering the dimensions of the target biological particles. Finally, polystyrene beads were used in order to demonstrate the feasibility and the working mechanism of the fabricated device to simulate the capture of single cells.

6.2. Conceptual Design of the Device

The illustration of the trapping system is shown in **Figure 6-1**. The microfluidic arrangement is composed of a main channel, trap sites and two side channels connected to the main channel at the outlet. The trapping sites are shaped in trapezoid grooves, having the outlet opening smaller than target particles, to capture the particles. The concept of this design is to keep the flow resistance of the empty sites low compared to the main channel in order to direct the particles into the trap sites through optimizing the geometry of the traps and the main channel. The design contains many hydrodynamic trap sites placed between the side and the main channels. The main objective of the design is to reduce the number of unoccupied sites and maximize the trapping efficiency of each trap and let the extra cells or particles to be drained by the outlet of the main channel in order to avoid blocking the main channel. Also, the main and side channels need to be designed such that each trap achieves not more than a single particle/cell while they experience less hydrodynamic stress. Each entering particle from the inlet of the main channel can be either transported by medium to one of the trap sites or can be drained by the outlet of the main channel. Assuming laminar flow inside the microfluidic channel (without gravitational, inertial forces) and when there are no interactions between particles and microfluidic walls, each particle follows the streamlines, and the efficiency of trapping can be characterized by the flow rate through trap sites[302]. When the particles' Reynolds number is very low (<1), particles follow the flow streamlines. Microparticles/cells are in microscale and the inertial effects which cause particles to travel across streamlines are very small compared to the viscous force, and they tend to follow

streamlines[303]. The flow rate through each path can be determined by the corresponding hydrodynamic resistance. In fact, more flow can be passed through the path with a lower hydrodynamic resistance. The hydrodynamic resistance of the empty trap sites, main channel, and the flow parameters (input and output conditions) of the network need to be controlled to manage the trapping efficiency of the device and the fluid pressure difference between the main and side channel. In order to increase the efficiency of trapping, either the hydrodynamic resistance of the main channel has to be increased or the hydrodynamic resistance of the trapping path has to be reduced. The dimension of trap sites depends on the size of target cells, and the dimension of trap sites needs to be small enough to not allow the target cells to pass through them. Due to the size constraints of the traps, only limited changes on the dimensions of the trap sites can be performed. As a result, to optimize the trapping efficiency of the system and to maximize the flow rate in the traps, one has to manipulate the geometrical parameters of the other paths such as the main and the side channels. The hydrodynamic resistance of a channel with an arbitrary cross-section can be obtained from the following relationship [304]:

$$R = \frac{\Delta P}{Q} = 16\pi^2 \eta \int_0^L \frac{I_p(x)}{A(x)^2} dx + \rho Q \left(\frac{1}{A_2^2} - \frac{1}{A_1^2}\right) \qquad 6\text{-}1$$

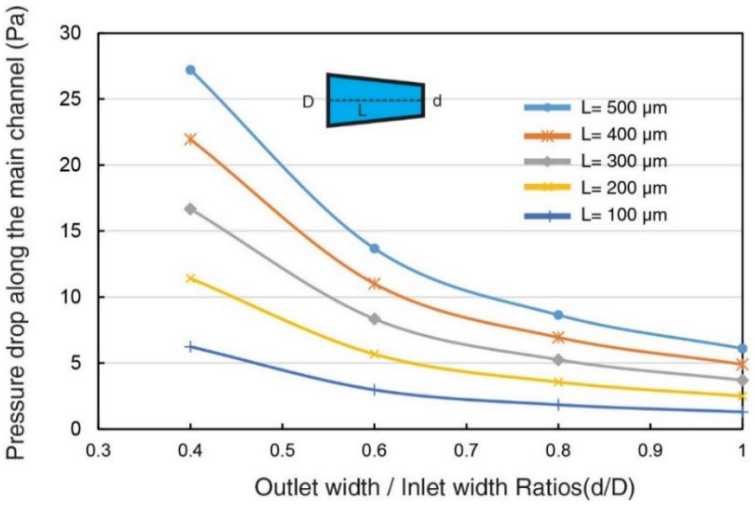

***Figure 6-2**. Pressure differences along a channel with different lengths and d/D ratios (The inlet velocity: 2.8 mm/s, D: inlet width of the main channel, d: outlet width of the main channel)*

where A_1 and A_2 are the microchannel cross-section area of the inlet and outlet of the channel, L the length of microchannel, Q the flow rate inside the channel, ΔP the pressure difference along

the microchannel, η is dynamic viscosity of fluid, and I_p is the specific polar momentum of inertia. From this equation, it is obvious that the fluidic resistance of a certain channel is not only a function of its geometry but also is proportional to the flow rate inside the channel. For a constant cross-sectional area channel, the area of inlet and outlet are same, so that the last term of Equation 6-1 can be canceled and the hydrodynamic resistance of the straight channel becomes purely the function of geometry such as length, height, and width[305]. Increasing the fluidic resistance along the main channel is one of the simple ways to increase the trapping efficiency of the system[306]. In order to increase the hydrodynamic resistance of the system, the straight main channel can be replaced by a rectangular micro-channel cross-section with a linear wall profile, allowing to enhance the pressure gradient between the main and side channels. Using a converging micro-channel, the last term in **Equation 6-1** increases due to the reduced area at the outlet, producing a greater hydrodynamic resistance at the main path. Without changing the angle of sidewalls and only by increasing the length of the main channel, the hydrodynamic resistance of the main channel can also be increased to provide a positive pressure gradient toward trap sites. (According to the Darcy-Weisbach and for the Hagen- Poiseulle flow, the flow resistance is directly proportional to the length of the channel and the longer is the main channel, the larger will be the flow resistance). However, with the aid of a converging channel not only the microsystem can be more compact, but the particle loading time can be faster as well. **Figure 6-2** shows pressure difference along a converging channel for different lengths of the channel and the different ratio of outlet to inlet width of the main channel (d/D). The length of a straight channel with the equivalent flow resistance is presented in **Table 6-1**. For instance, for designing a straight channel with a flow resistance as same as a converging channel with $d/D = 0.4$, and $L = 100\ \mu m$, the length has to be extended 5.2 times compared to the length of converging channel ($L_{eq} = 5.2 \times 100 = 520\ \mu m$)

Table 6-1. *The ratio of an equivalent straight channel length to the converging channel length (L_{eq}/L) for different d/D and L to produce the similar flow resistance*

Channel length(L)	d/D=1	d/D=0.8	d/D=0.6	d/D=0.4
100 µm	1	1.53	2.48	5.2
200 µm	1	1.49	2.37	4.76
300 µm	1	1.46	2.32	4.63
400 µm	1	1.45	2.30	4.58
500 µm	1	1.44	2.28	4.54

6.3. Materials and methods

6.3.1. Computational Analysis

A 3D finite element analysis (FEA) was performed to estimate the velocity field and pressure gradient within the microfluidic device. Incompressible Naiver-Stokes and continuity equations were employed to characterize fluid flow parameters inside the micro channels [307].

$$\rho \frac{\partial u}{\partial t} - \nabla.(-pI + \eta(\nabla u + (\nabla u)^T) + \rho(u.\nabla).u = F \quad 6\text{-}2$$

$$\nabla.(u) = 0 \quad 6\text{-}3$$

where ρ is the density of the fluid, p is the fluid pressure, u is the velocity field within the channel, I is unit diagonal matrix, η is dynamic viscosity of fluid, and F is the volume force on the fluid that can be ignored for a pressure-driven fluid flow in the absence of the other volume force. COMSOL Multiphysics® 5.2 was employed to solve the governing equations and determine the optimal geometrical parameters of the initial design in order to have an efficient hydrodynamic trapping system. In this model, a constant velocity was considered as the inlet boundary condition, and a uniform zero gauge pressure was set at the outlet of the main channel. The no-slip condition was applied to all the other surfaces. The suspended particles were considered as spheres, and the interaction between them was assumed to be negligible by considering the relatively low concentration of particles inside the channel. The trajectories of the particles entering the main channel were characterized using numerical simulation to assess the trapping efficiency of the device, for a rigid particle moving through a fluid, the equation of motion is defined by the following equation [308].

$$m_p \frac{du_r}{dt} = F_D - F_e - Fb \quad 6\text{-}4$$

where m_p is the mass of particle, $u_r = u - u_p$ is the relative particle velocity to the fluid velocity, u_p is the particle velocity, F_e is external force and F_b is the buoyancy force. The gravitational force (including the buoyancy) is considered to be negligible, and no external force is applied on particles. The drag force acting on the particles can be obtained from the following equation [309]

$$F_D = \frac{C_D u_r^2 \rho A_p}{2} \quad 6\text{-}5$$

where C_D is the drag coefficient, A_p is the projected area of the particle in the plane perpendicular to the flow direction. The drag coefficient is a function of particle Reynolds number defined as:

$$Re_p = \frac{\rho|u - u_p|d_p}{\mu} \quad 6\text{-}6$$

where d_p is the diameter of particles. For creeping motion (Stokes flow) when $Re_p < 1$, the inertia force is negligible, and the viscous force is the predominant force [310], [311], the particles follow the fluid streamlines [302]. Considering the maximum velocity of particles in trap sites, the particle's Reynold number for the inlet velocity of 2.8 mm/s is less than 0.1, and remains less than unity, for the inlet velocity of 28 mm/s, confirming that for this range, particles indeed follow the streamlines with good accuracy.

6.3.2. PDMS Chip Fabrication

Conventional soft lithography was used to fabricate the PDMS microfluidic chips. AutoCAD was used to draw the design layouts, which were printed onto the masks (Fineline Imaging, Colorado Spring, USA). Photolithography was used to fabricate the master molds on silicon wafers. The negative photoresist (SU-8 2030) was spin-coated at 1900 rpm for 30s on a 4" silicon wafer to obtain a layer with 70 μm thickness. Before exposing it to the UV, the photoresist was baked at 65℃ for 3 min and 95℃ for 6 min. The transparent mask was then used to pattern the design using a mask aligner and UV light for 20 s and post-baked at 65℃ for 2 min. and at 95℃ for 7 min. In the final step, the SU-8 layer was developed for 5 min using SU-developer to obtain the mold, and finally, it was dried with an N2 gun. Before casting the PDMS, the surface of the mold was salinized in vapor phase for removing the cured PDMS easily. A mixture of pre-polymer and curing agent with a weight ratio of 10:1 was degasified in a vacuum desiccator to remove the bubbles. The PDMS was then poured onto the mold and placed on at 80℃ oven for 2 hours. Then, the PDMS layer was peeled off the mold, and the inlet/outlet were punched by a 1mm punch. Finally, with the aid of oxygen plasma bonding, the PDMS chip was bonded to a glass slide to seal the channels.

6.3.3. Bead Preparation

Polystyrene particles (Microspheres- Nanospheres, Cold Spring, USA) with a diameter of 50 μm were dispersed in 0.05% Tween 20 in Phosphate buffered saline (PBS) in order to have a

solution with a concentration of 50 particles/µl. The suspension was sonicated to ascertain a good dispersion.

6.3.4. Experimental Setup

The microfluidic chip consists of one inlet for injecting the medium and the particles suspension and three outlets, two from the side channels and one from the main channel. A 2 ml syringe with 23G needle was connected to the inlet of the fabricated device through a polytetrafluoroethylene (PTFE) tube with size of $0.59\,mm\,ID \times 0.25\,mm$ thickness. Before using the microfluidic chip for operation, the PDMS surfaces were incubated for 30 min with tween 20 (10 % in PBS) in order to prevent the polystyrene particles from binding to the channel surfaces. Tween 20 can effectively disrupt the hydrophobic interaction between the particles and the PDMS surfaces [312]. The inlet tube was then connected to the syringe pump (KD Scientific Legate 110) for loading the suspended microparticles into the device at a specific flow. The trapping process was next observed under a microscope (Nikon Eclipse 80i). A digital camera (Infinity) coupled to the inverted microscope was used to capture photographs and videos.

6.4. Results and Discussion

6.4.1. Simulation Results

The fluid flow in the design shown in **Figure 6-1** was simulated to understand the flow characteristics and to optimize the parameters affecting the trapping performance of the individual trap sites. The amount of flow passing each trap determines the trapping efficiency for various geometric configurations of the main and the side channels. By increasing the hydrodynamic resistance of the main channel, particles and cells have more chances to be trapped by side traps. The higher pressure gradient across side traps causes more flow through each trap resulting in a higher probability of trapping. The dimensions of each trap site were chosen in accordance with the diameter of the cells or particles. The inlet and outlet openings of each trap were set close to the particle diameter (1.2 and 0.8 times of the particle diameter, respectively), and the height of the microfluidic channels was set at 1.4 times the diameter, allowing particles to move freely within the microfluidic network. The width of the main inlet channel was selected large enough to let particles enter the trapping area without accumulation. The different features of the trap sites, the main channel and side channels for the three various designs are shown in **Table 6-2**.

***Table 6-2**. The geometric parameters of microfluidic network and trap sites (unit in μm)*

Parameters	d/D	d	W_s	W_{ti}	W_{to}	d_t	θ
Design 1	1	350	150	60	40	40	0
Design 2	0.7	250	220	60	40	40	2.2°
Design 3	0.48	168	240	60	40	40	4.4°

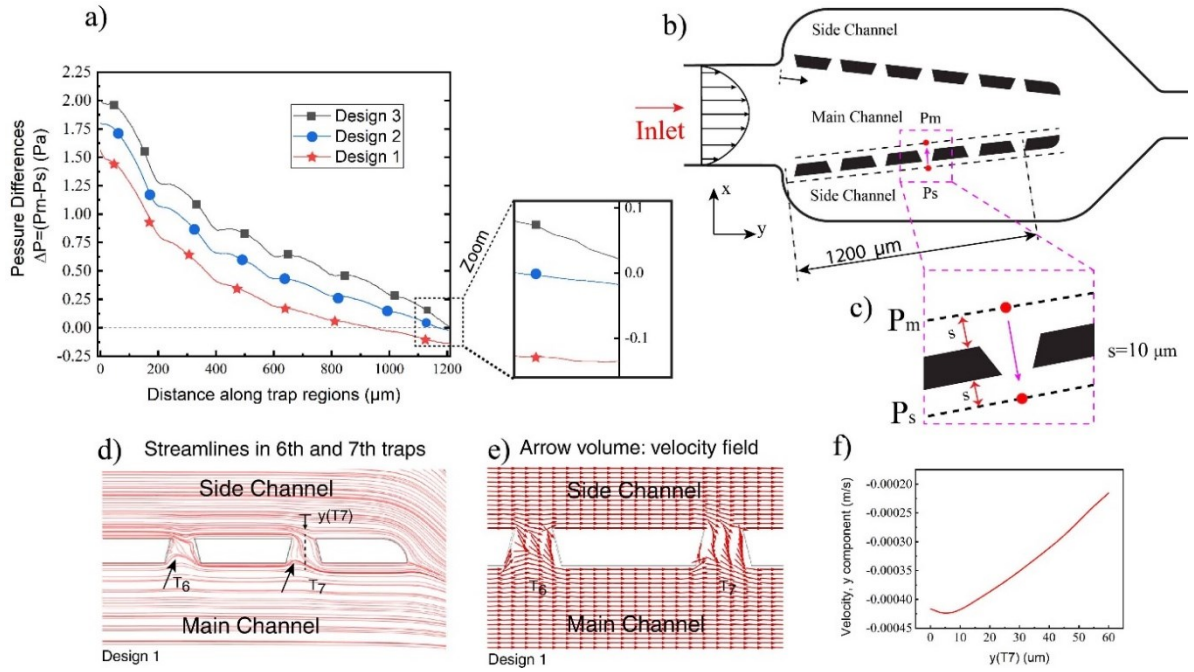

***Figure 6-3**. **a)** Pressure difference ($\Delta P = Pm - Ps$) between the main channel (P_m) and side channels (P_s) for three different designs, **b**, **c)** schematic of main and side channels and traps and the coordinate for measuring Pm and Ps., **d)** streamlines within trap 6 and 7 in Design 1 showing the flow direction from side channels to the main channel. Two arrows in 6th and 7th show that the flow is trying to enter the trap, but the gradient pressure is not strong enough to change the direction, **e)** velocity field (normalized arrows) within 6th and 7th trap sites showing the flow direction in the traps, **f)** velocity profile (v: in y-direction) along a line passing through the last trap*

The set parameters were used to model the microfluidic in COMSOL Multiphysics and characterize the velocity contours and the pressure distribution within the microfluidic device. The pressure difference values between the main and side channels were computed for three different sidewall angles and plotted in **Figure 6-3a**. This figure illustrates the pressure differences between the main channel P_m and the side channels P_s for three different angles under a constant inlet velocity (2.8 mm/s). It is evident that when inlet and outlet cross-sections are similar, for a straight channel and

Design 1 ($\theta = 0$), the pressure differences between the main channel and side channels is small and maybe even a negative value (for trap 6 and 7), meaning that the flow may be reversed from the side channels into the main channel. **Figure 6-3c**, and **d** present the flow streamlines and velocity field (normalized arrows) respectively within 6th and 7th traps, confirming that the flow is directed from side channels to the main channel. As two arrows show in **Figure 6-3d**, the flow is trying to enter traps, but the gradient pressure is not strong enough to navigate flow completely to traps and they re-enter the main channel. By increasing the sidewall angle ($\theta = 4.4°$), the pressure differences between the main and side channels are increased to remain positive for all trap sites, providing a flow direction toward the traps. For example, the pressure difference increases from 1.5 Pa to 2 Pa for the first trap (Design 3,$\theta = 4.4°$). As can be seen in **Figure 6-3**, using the third design, the maximum positive pressure gradient between the main and the side channels can be reached. It can be observed that the effect of the stepped sidewall is noticeable in the middle of the channel, while its effect is less pronounced on the first and last trap sites. Mesh distribution, as shown in **Figure 6-4a,** was generated in order to simulate the fluid flow in the microfluidic channels. Pressure and velocity profiles for Design 3 are shown in **Figure 6-4 b** and **c**, clearly indicating the pressure difference along the main channel. However, its values remain high compared to the side channels at the same positions. The pressure distribution shows that for all traps, there is a positive pressure gradient from the main channel to the side channel, directing the suspended particles to the trapping sites.

In order to characterize the effects of sidewall angle on the trapping efficiency of the system, flow passing through each trap site were calculated for three different designs using the geometric parameters shown in **Table 6-2** and considering water with a dynamic viscosity of 0.001 Pa.s and density of 998 kg/m^3 as the working fluid. **Table 6-3** indicates the proportion of flow at each trap to the total flow entering the main channel from the inlet. The calculated values confirm the lower ratio at the seventh trap site, meaning that a low flow can pass through the last traps, and as a result, the chance of cells to be captured by this trap is relatively low. Moreover, for the third design, these ratios are larger compared to the two first designs. For Design 1 and 2, the passing flow rate for the last trap is negative (showing the reversed flow from side channel to the main channel), while for Design 3 this value becomes positive (flow from the main channel to the side channels). It can be seen that more than 62 % of the entering flow rate is drained by the outlet for Design 1, and its value is reduced to 44 % for Design 3.

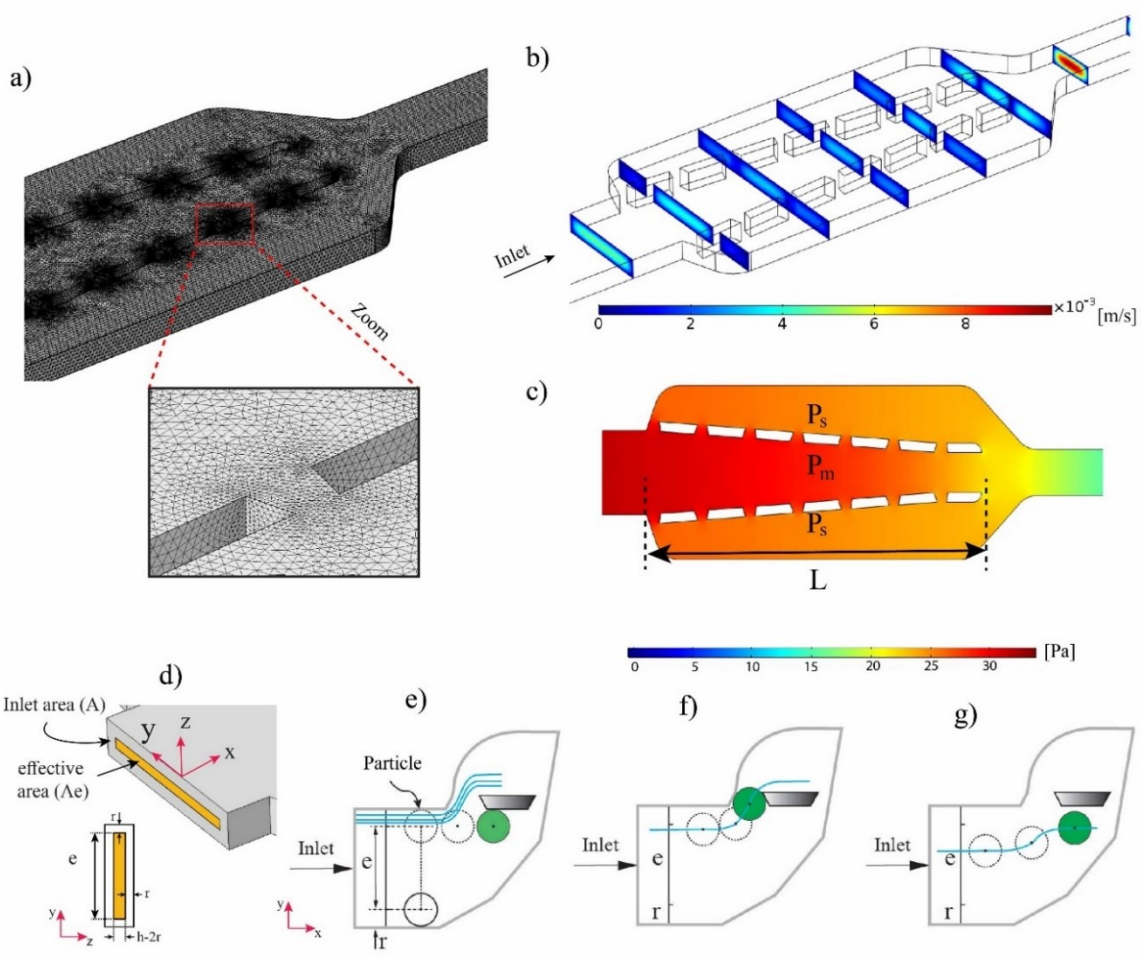

Figure 6-4. *Laminar flow simulation within the microfluidic network with Design 3 with inlet velocity of 2.8 mm/s,* ***a)*** *mesh distribution in the model and traps: 1456469 tetrahedral elements were created to generate the mesh,* ***b)*** *velocity contour (m/s),* ***c)*** *pressure contour (Pa),* ***d)*** *A schematic of the effective area A_e= (h-2r) (D-2r),* ***e)*** *streamlines within different regions of the inlet and their potential to navigate cells/particles into the trap sites. This diagram shows that streamlines flowing through the first trap cannot capture the very close particle to the sidewall.* ***f)*** *A close streamline to the sidewall passing through the center of mass and can direct the particle into the first trap site.* ***g)*** *although the streamline passes through the center of mass, it is not able to direct the particle into the first trap site. (The blue lines show the flow streamlines inside the main microchannel, h: height of the channel, e: effective entrance width, r: radius of the target particle or cell)*

The concept of using a converging channel to enhance the trapping capability of the microfluidic traps is confirmed with the derived flow rate ratios. The narrower outlet opening increases the hydrodynamic resistance of the microchannel; however, the choice of a very narrow outlet is limited because of the possible clogging within the channel. In order to have a continuous flow inside the main channel without clogging, the dimensions of the outlet should be carefully

determined. Experiencing less stress by the trapped particle/cell due to the hydrodynamic forces is another determining factor for designing the outlet width. By increasing the angle (θ) , the fluidic resistance of the main channel is increased, and more stress will be applied on the trapped particles/cells due to the higher pressure in the main channel. Due to these reasons, we limited the minimum outlet width of the main channel, such that only three particles could pass easily through the outer channel at the same time to prevent the accumulation of particles.

As was mentioned earlier, the flow behavior inside the microchannel is laminar, so in order to trap particles into the designed sites, two conditions need to be met. First, at least one of the streamlines has to pass through the center of mass of the entering particle, which is supposed to be captured. Second, the streamline passing the center of the particle has to pass through one of the trap sites. Even though some streamlines very close to the sidewall of the inlet channel can pass through trap sites, they have no impact on particles since they cannot pass the particle center due to the physical limitation of the particle [302][313]. In fact, the streamlines at a distance less than the radius of particles from channel wall (both in z and y directions) are not able to deliver cells into trap sites since these streamlines do not pass through the center of cells. This concept and the various possible conditions for streamlines and the injecting particles are clearly shown in **Figure 6-4(d-g)**. By considering the two above conditions and size of the target particles, more precisely, the trapping probability T_e for each trap (i) can be defined as the fraction of flow at the effective area which can pass through the traps. Effective area is a portion of the inlet area (A) where the passing streamlines are able to deliver particles into traps $A_e = (D - 2r)(h - 2r)$.

$$T_e = \frac{Flow\ rate\ passing\ through\ i_{th} trap\ coming\ from\ the\ effective\ area}{Total\ inlet\ flow\ at\ the\ effective\ area\ (A_e)}$$

Table 6-3. *Flow rate ratios for the three different designs (%)*

Ratio	Q_1/Q_{in}	Q_2/Q_{in}	Q_3/Q_{in}	Q_4/Q_{in}	Q_5/Q_{in}	Q_6/Q_{in}	Q_7/Q_{in}	Q_{out}/Q_{in}
Design 1 ($\theta = 0$)	9.29	5.07	2.53	1.18	0.40	-0.21(*)	-0.92(*)	62.86
Design 2 ($\theta = 2.4°$)	9.63	6.83	4.15	2.63	1.59	0.55	-1(*)	49.24
Design 3 (($\theta =$ 4.4°)	10.41	8.06	5.40	3.87	2.74	1.45	0.13	44.8

Q_i: Flow rate at i_{th} site, Q_{out}: Flow rate at the outlet, Q_{in}: Flow rate at the inlet
*: flow is directed from side channel to the main channel.

Flow rate at each trap is a mix of two flow rates coming from the effective and ineffective areas. In order to estimate the efficiency of a specific trap, the portion of flow rate from the effective area which enters into the trap needs to be determined. Because of the laminar flow, the flow rate corresponding to a certain section can be predicted by counting the number of streamlines passing through the section of interest. Since the particles entering in a laminar flow follow the streamline paths, the probability of a trap site can be approximated by measuring the ratio of the passed particles at the trap site to the total number of arriving particles at the effective entrance of the main channel. For this purpose, with the aid of the particle tracing module of COMSOL Multiphysics, a uniformly distributed number of particles representing the streamlines were released across the effective region (A_e) of the main channel inlet, and their trajectories were then simulated. It was assumed that particles do not affect the fluid flow in channel. By monitoring the trajectory of each particle or cell, the efficiency of each site for trapping was evaluated by counting the particles flowing through it and comparing to the total number of the released particles. **Figure 6-5a** shows the probability of trapping for each trap using the mentioned concept. Due to the geometric symmetry of the design, the chance of trapping is identical for both trapping series on the right and left sides of the main channel ($Te_{1\sim7}\,(right) = Te_{1\sim7}\,(left)$), and due to this reason the probability was calculated only for one trapping series. From this figure, it is clear that the trapping probability for each trap is almost proportional to its relative flow (**Table 6-3**). However, the results show that by considering the size of particles, the trapping efficiency for the second trap is higher compared to the first site. The differences between two values arise from the fact that for calculating the relative flow rate, the total inlet flow was considered while trapping probabilities were measured based on the total flow rate passing only through the effective area. Probability and relative flow rate for each trap have the same trend, and by increasing the hydrodynamic resistance of the main channel both the probability and the relative flow rate are increased. For estimating the trapping efficiency, it was assumed that there are no particles in the channel. Once a trap is filled, the trapping efficiency of the rest traps is changed due to the different fluidic resistance in main channel and traps site. The effects of trapping progress on the probability of each site are shown in **Figure 6-5b**. For measuring the probability values, it was assumed that trapping is occurring sequentially. When a trap is filled by a particle, its fluidic resistance is increased, allowing other traps to receive the subsequent particles with a higher probability. Based on the results, the average trapping probability for all traps is 13.93 %, with a standard deviation of 3.6, showing a fairly

uniform trapping process. In order to determine the effects of different inlet velocity on the trapping performance of the system, the trapping probability for each trap site of the Design 3 was calculated by carrying out a similar simulation. When the inlet velocity was increased from 0.2 to 2 mm/s the difference between trapping efficiencies was negligible.

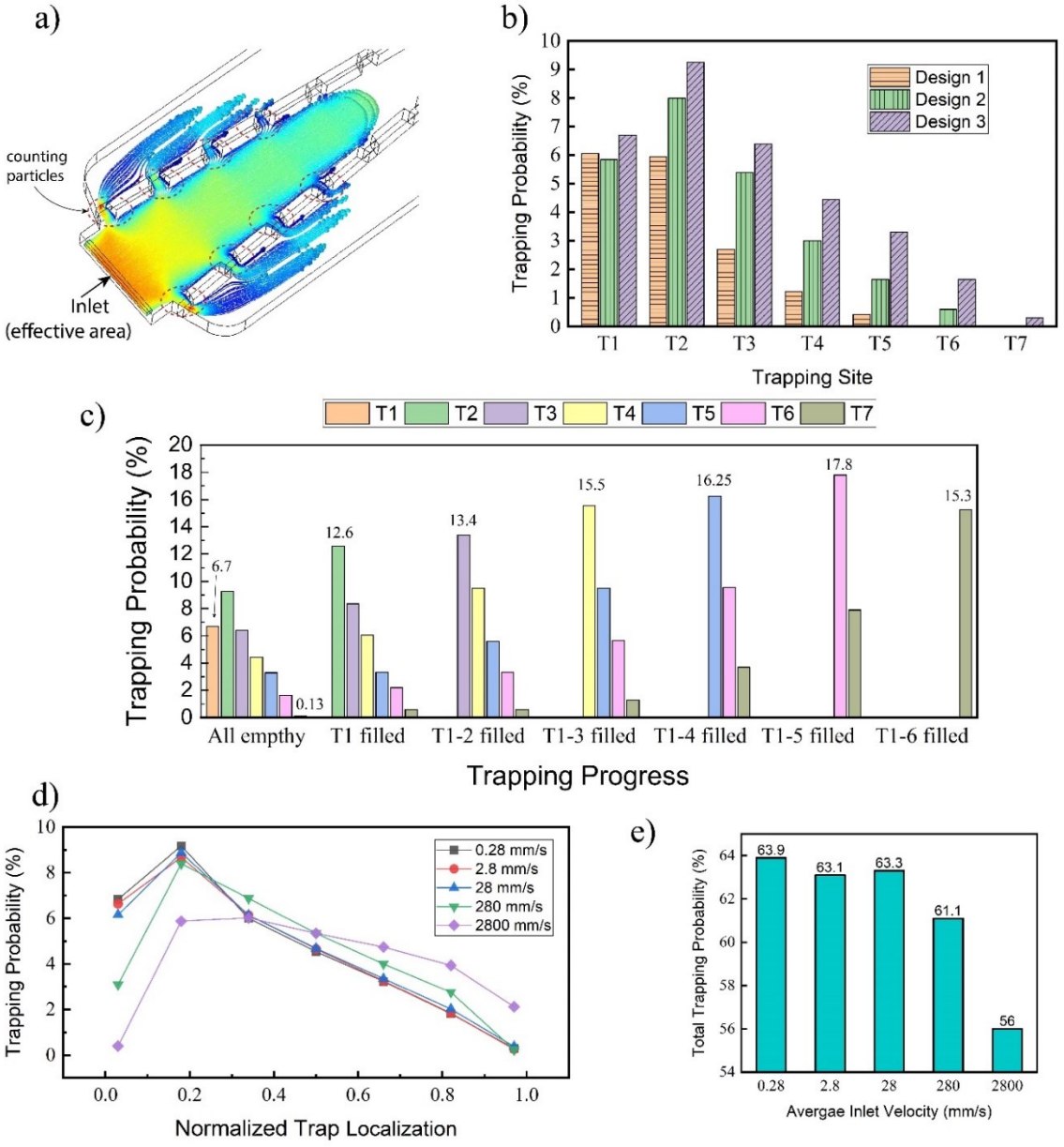

Figure 6-5. *a) Particles are released at the effective area and the number of particles passing each trap is counted to estimate the trapping efficiency (contour color shows the velocity magnitude of particles),* ***b)*** *trapping probability of each trap site for three different designs (inlet velocity: 2.8 mm/s),* ***c)*** *trapping probability of each site during the trapping process (inlet velocity: 2.8 mm/s), when a trap site (T_i) is filled, its trapping probability is considered zero),* ***d)*** *changing the trapping*

efficiency versus the normalized trap location (x/L) by increasing the inlet velocity (velocity in mm/s, x: trap location is shown in ***Figure 6-3****, L=length of the converging channel),* ***e)*** *total trapping probability with respect to the inlet velocity. (*$total\ trapping = 2\sum_0^7 T_{ei}$*)*

By increasing one order more of the inlet velocity, the trapping efficiency appeared to be decreased at the first position, but the efficiency did not change significantly at the other positions. By increasing the inlet velocity to 280 and 2800 mm/s, the trapping probability at the first and second positions decreased significantly while the trapping probability values at the 5th and 6th were increased as shown in **Figure 6-5c**. However, the total trapping efficiency of the system was reduced to 61.1% and 56% showing 2% and 9% drops, respectively compared to the other inlet flow values (**Figure 6-5d**). According to Equation **6-1**, by increasing the flow rate, the hydrodynamic resistances of both the main channel and the trap sites are increased, and the results show that at a higher flow rate, the equivalent hydrodynamic resistance of the trap sites is increased faster in comparison to the hydrodynamic resistance of the main channel, therefore, reducing the total trapping efficiency. It can be seen that the device can operate at a wide range of inlet velocity without fluctuations.

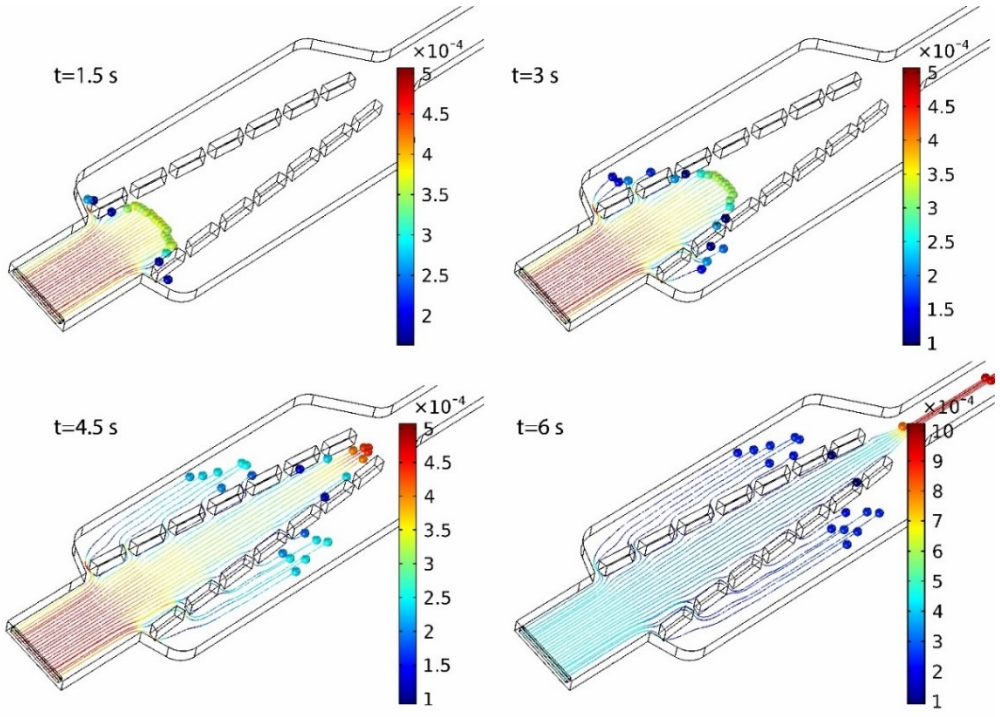

Figure 6-6. *Trajectories of particles entering the main channel of the microfluidic device at different times. The particle tracing simulation was performed to predict the probability of trapping of each site. It should be noted that the particles in the simulation are virtual, so they are not*

stopped at the entrance of the trap sites. (Inlet velocity: 0.28 mm/s, the contour color shows the velocity magnitude in m/s)

Figure 6-6 demonstrates the time-dependent particle tracing simulation. A certain amount of the particles was released uniformly at the entrance of the main channel (only effective area) and their trajectories were observed through finite element simulation. As can be seen in this figure the particles have different velocities depending on their initial position at the inlet of the rectangular channel. In the middle of the channel, particles possess larger velocities and their velocities slow down as they arrive closer to the channel walls. Depending on the position of the particles, they can be, either trapped by one of the trap sites or drained by the outlet of the main channel.

6.4.2. Mechanical Stress Analysis

The fluid-induced stress can alter the functional behavior of both the healthy and cancerous cells such as proliferation, transport, differentiation or even cell death [314]–[316], therefore it is crucial to provide proper experimental conditions with reduced hydrodynamic stresses to avoid their undesired effects (mechanical damages and decreased cellular viabilities) on cells. When the cells or particles are far from the trap sites, they are subjected to a relatively low stress. After trapping, the particles/cells have to undergo much more mechanical forces due to the larger fluid pressure on their surfaces and their contacts with the traps. An additional FEM analysis was carried out considering a polystyrene single particle (microsphere with diameter 50 μm) sitting in the trapping site in order to characterize the mechanical stresses experiencing at the trap position. A fluid-structure interaction (FSI) analysis (details described in [315]) was created using the COMSOL Multiphysics to estimate the hydrodynamic stress acting at fluid-particle interface and characterize deformation of the trapped single particles/cells due to the pressure difference across the cell. By assuming an incompressible and Newtonian fluid, the stress tensor acting at the interface of particle and fluid can be determined by the following formula[317]:

$$\sigma_{ij} = -p\delta_{ij} + \mu(\frac{\partial v_i}{\partial x_j} + \frac{\partial v_j}{\partial x_i}) \qquad 6\text{-}7$$

where σ_{ij} is stress, δ_{ij} is the Kronecker delta, v_i is the fluid velocity in "i" direction, and P is fluid pressure. Equivalent elastic strain (EQS) can also be used to quantify the deformation of cells/particles under hydrodynamic force[315] In order to measure the mechanical stress and the

hydrodynamic deformation, it was assumed that all traps are closed by particles, and the pressure and deformation on a cell trapped in the second site (having the maximum trapping probability based on **Figure 6-5b**) was calculated by considering the physical and mechanical properties of polystyrene particles: density (1050 kg/m^2), Elasticity (3 MPa) and Poisson ratio (0.33) and water as the working fluid. For FSI simulation, the contact points are also assumed to be fixed and no displacement happens in contact points of particles and trap walls, and on the boundary of particle and fluid, the velocity of fluid equals the rate of change for displacement of solid domain (particle). Similar to the computational section, for FSI simulation, the inlet velocity and outlet pressure were set 2.8 mm/s and zero respectively and no slip conditions were applied for all walls.

The FSI results (**Figure 6-7a**) show that with the aid of this design a low stress and deformation are applied to the trapped particle/cell compared to similar designs, suggesting that cells can be gently trapped by this micro device without experiencing a high stress. Considering the same boundary conditions, the same analysis was carried out to compare the applied stress and deformation by two other microsystems [318], [319], and the results are shown in **Figure 6-7b**, **c**. The Von Mises stress was computed from stress tensor of the particle to estimate the reaction stress to fluid forces on the particle including contact points between trap walls and particles (**Figure 6-7**, right panel). It is evident that our design offered relatively gentle trapping in comparison to the other two devices, under the same conditions while is able to manipulate cells with high efficiency. In our design, the maximum reaction stress is 12.9 Pa at the particle-trap wall points and is smaller in comparison to two other models. This figure also shows the total stress distribution around the trapped particles (red arrows) for our design and two previously reported works, showing that smaller total stresses are distributed around particles in our design compared to two others. The maximum stress and average equivalent elastic strain (EQS) [315][317]were also calculated and plotted in **Figure 6-7**e, d respectively. The average equivalent elastic strains for each device was computed by averaging EQS over the total surface of the trapped particles. EQSs show that, under the same conditions, the deformation-induced by hydrodynamic forces is less in our design in comparison to the two other devices.

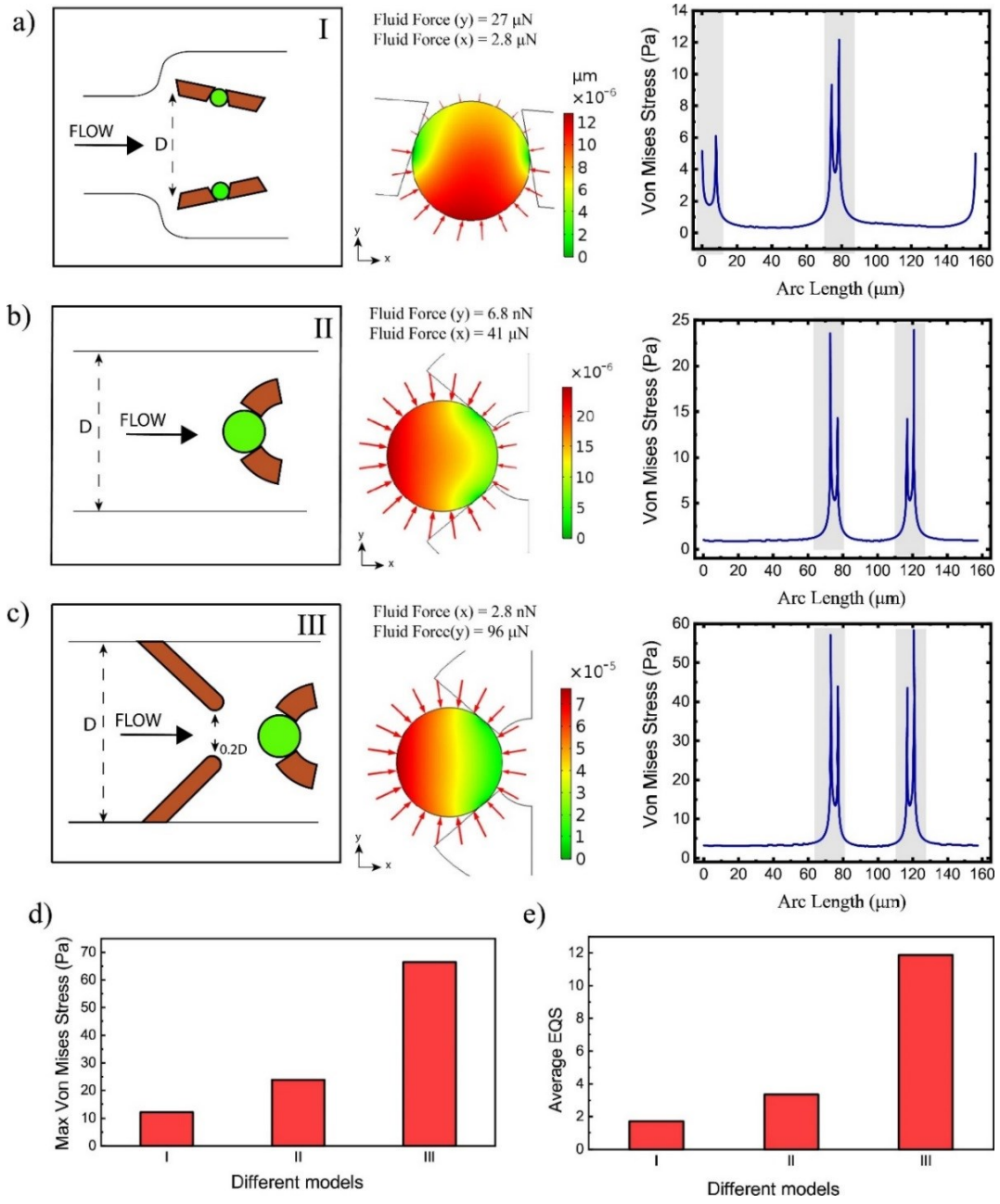

Figure 6-7*. Total displacement (µm) contour due to the hydrodynamic forces, total stress on the trapped particle walls (red arrows), fluid forces in x and y directions (by integrating total fluid stress on the whole perimeter of the trapped particles) and Von Mises stress along the perimeter of the trapped particle and the contact parts between particles and trap walls are highlighted:* ***a)*** *in our Design (max. stress:* $12.15\ N/m^2$*),* ***b)*** *in the design in* [318] *(max. stress:* $23.91\ N/m^2$*),* ***c)*** *in the design presented in* [319]*(max. stress:* $62.41\ N/m^2$ *),* ***d)*** *Max Von Mises stress (at the contact point between particles and trap walls),* ***e)*** *average equivalent strain over the trapped particles for different models. (Inlet velocity: 2.8 mm/ s, the contour color on the micro particles shows the magnitude of the total displacement, and the red arrows show the distribution of total hydrodynamic stress around the particles and their scale factors are not identical, scale factors are 20, 5 and 1.5 for models I, II and III respectively)*

Two types of fluid force are acting on the particle wall at the boundary of the fluid domain: normal forces due to hydrodynamic pressure and tangential force due to shearing effects. Under the same boundary conditions, the shear stress and normal pressure applying on the wall of trapped particles for our model and two other models are plotted in **Figure 6-8**. As can be seen in this figure, the normal pressure on the particles wall is much more for all three models compared to the experienced shear stress due to the fluid flow. In our design less normal pressure (P_{max}: 0.95 Pa) is applied to the trapped particle while in models II and III, the trapped particles experience 2.6 and 9.2 Pa normal pressure respectively. In the current model, the maximum shear stress on the trapped particle is slightly smaller than the second model while is much smaller than the third model. The total force applied by only fluid flow on the trapped particles is reported in **Figure 6-7** in both x and y directions, and compared to other models, in our design less total stress is applied to the particle wall.

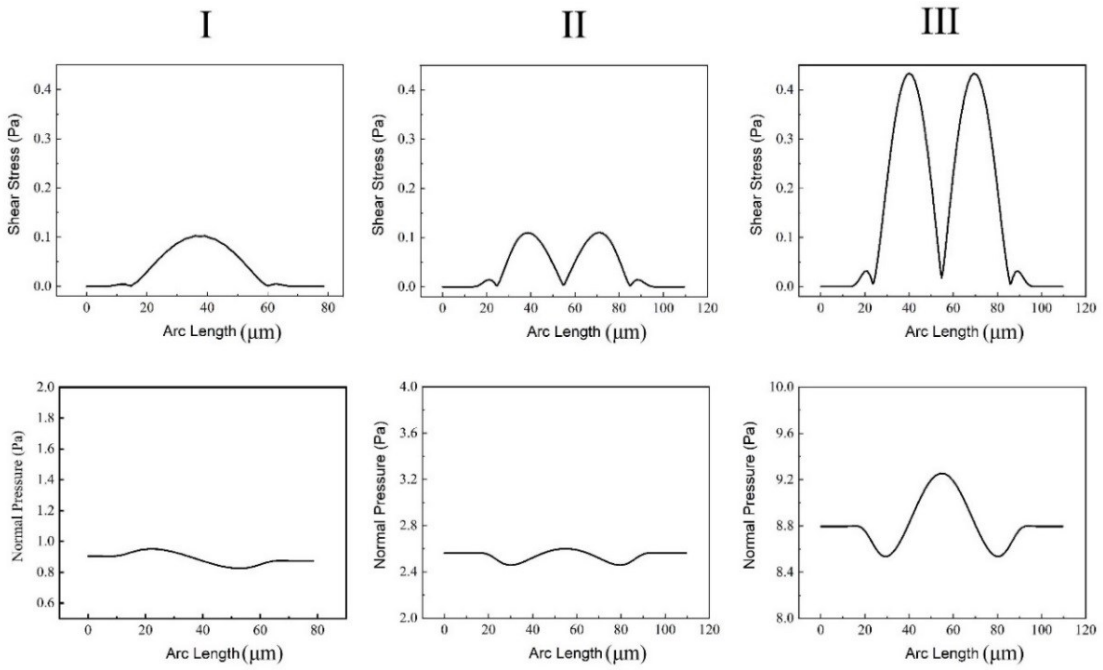

Figure 6-8. *Shear stress and pressure stress applying on the trapped particles in the current design (I) compared to other designs (II and III) under the same boundary conditions (inlet flow rate: 2 mm/s and the outlet pressure set zero).*

So far, the design parameters of the microfluidic device were optimized, and the trapping performance of the microsystem was analyzed using simulation. The optimal parameters were used for the following experiments and further analysis.

6.4.3. Experimental Results

After optimizing the geometrical parameters of the microfluidic circuit, the optimized microfluidic device with different sidewall angles was used to test the trapping performance of the microsystem using microbeads with a diameter of 50 μm. Under the flow with very low Reynolds number (Re ≤1), it is expected that particles move on the streamlines in agreement with the simulation results. Although the trapping efficiency is not influenced by the inlet flow rate (based on the numerical simulation), the microparticles were loaded with a relatively low flow rate into the channel to observe the motion of the particles (<10 μl/s). In order to avoid clogging inside the microfluidic channel and monitor trajectories of particles, they were injected at a low concentrations and it was found that microbeads are distributed non-uniformly at the entrance of the main channel and non-sequential trapping was observed during micro particles loading. In the simulation section, the fully developed fluid flow at the entrance section was used to estimate the efficiency of the system. The entrance length (the distance before the fluid flow becomes fully developed) can be obtained from $L_e=0.006Re.D_h$, where Re is Reynolds number and Dh, is the hydraulic diameter of the channel [315][320]. By considering the hydraulic diameter of the entrance channel and calculating the Reynolds number, the entrance length is very small. The distance of channel before the inlet section is much longer than L_e, confirming that in our experiment, at the entrance section always the fluid flow is fully developed. Three different designs were tested to observe their ability to trap particles and characterize their efficiency. It was observed that the main channel convergence affects significantly the efficiency of single particle trapping. **Figure 6-9** shows the optical images of the trapped particles for both Design 1 and Design 3 under the same conditions after 15 min of operation, confirming the feasibility of the microdevice for trapping single cell/particle. As it can be seen from the microscopic images, more particles were captured by the trap sites using Design 3 compared to Design 1. By repeating the injecting process of particles using new and empty microfluidic devices, it was observed that more than 90 % of Design 3's traps achieve single-particle trapping. Furthermore, by reversing the infusion of the medium, the device was shown to be capable to release most of the trapped particles.

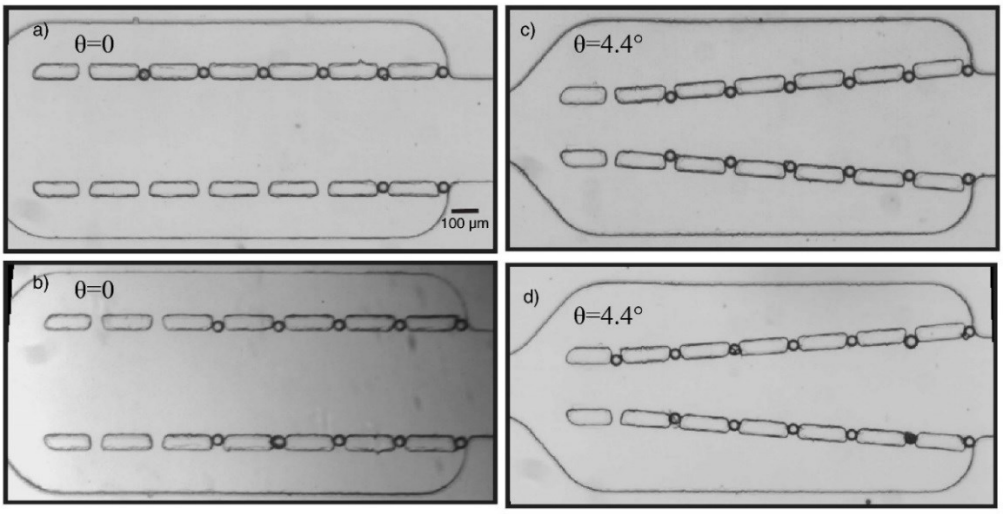

Figure 6-9. *Shear stress and pressure stress applying on the trapped particles in the current design (I) compared to other designs (II and III) under the same boundary conditions (inlet flow rate: 2 mm/s and the outlet pressure set zero).*

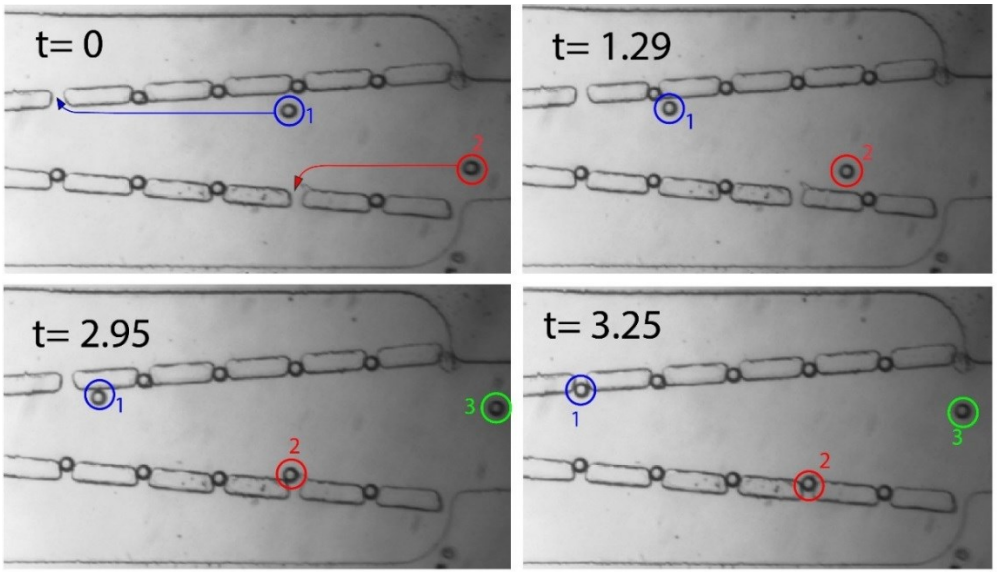

Figure 6-10. *Time-dependent motion of particle within the microchannel under a very low flow rate to observe their motions. Particle 1 due to its initial position is flown toward a trap on its right side while particle 2 is flown toward a trap site on its left side because of its initial position. (Fluid is flowing from right to left)*

Figure 6-10 illustrates the time-dependent position of two particles (1 and 2) under a fairly low inlet velocity. As mentioned earlier, the particles may navigate to one of the trap sites depending on their starting positions in the entrance cross-section of the main channel. As it can be seen from

the figure, some of the trap sites have already been filled with particles, and the extra hydrodynamic resistance induced by the immobilized particles diverge the flow streams and the motion of the subsequent micro-particles entering to the system toward the other vacant trapping sites. Particle 1 moves toward the empty trap site on the top while particle 2 is directed toward the empty site on the bottom side channel and finally they are trapped. The simulation results showed that by decreasing the outlet width, more flow can pass through all trap sites, but micro-bead clogging occurs during the injecting process, inducing significantly more stress on the immobilized particles. It was observed that in the case of Design 3, micro-bead clogging does not occur as extra micro particles can be drained easily by the outlet. Due to the low flow rate at sites close to the outlet, their chances to direct particles toward trap sites is very low.

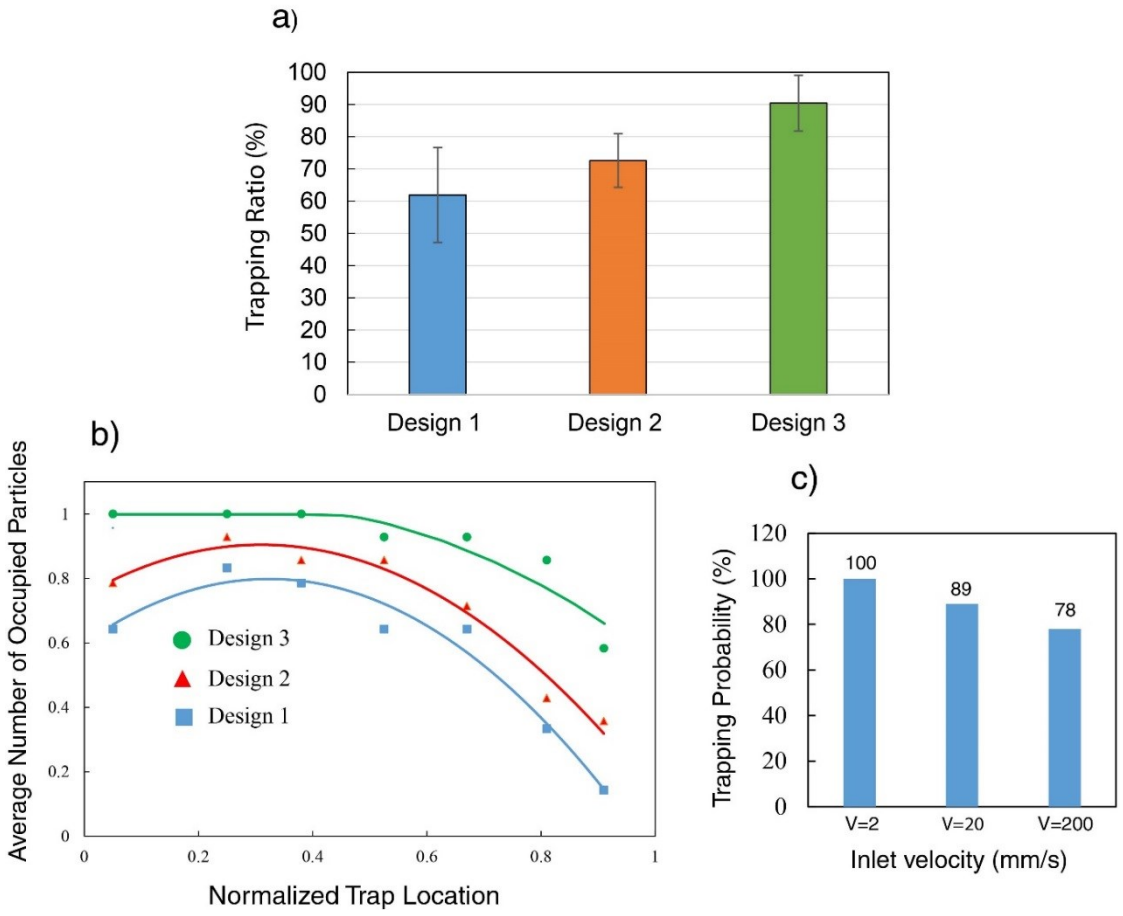

***Figure 6-11**. **a)** Trapping probability of each design with error bar under the same conditions, **b)** Trapping efficiency versus normalized trap location (x/L) for different designs (solid lines show the curved trends, L: length of the converging channel, x: trap location), **c)** trapping efficiency for the first trap (Design 3) by increasing the inlet velocity*

To assess and quantify the trapping efficiency of each microfluidic system, the ratio of the number of trapped particles to the total number of sites was calculated. For each device, the experiment was done at least six times and the average value was calculated as the trapping efficiency. In order to ascertain that similar conditions exist for all experiments, a new device, free of particles, was used. To characterize the trapping efficiency of each device, spherical 50 μm polystyrene micro particles were injected through the syringe pump at the velocity of 2 mm/s then the highest number of occupied traps was recorded. **Figure 6-11**a shows the trapping efficiency of three different microfluidic systems. The results show that the trapping efficiency of the system with identical inlet and outlet openings is about 60% and this value can be increased up to 90% by tuning the convergence of the main channel. In agreement with the numerical analysis, it was observed that trap sites close to the outlet remain empty even after 15 min of operation due to the low rate of flow. However, in Design 3, the gradient pressure at the sites is improved and particles will be captured with a higher probability. Moreover, to quantify the trapping ability of each trap, the average number of particles trapped in different traps were recorded (this value is 1 for a site location when the trap is filled by particles, and zero when is remained empty during the experiment). The experimental trapping efficiency of each trap location is presented in **Figure 6-11b**. For Design 1 and 2, in agreement with the finite element analysis, it was observed that the average trapping efficiencies for traps T_6 and T_7 are almost low, confirming their low flow rate ratio values, and the efficiency is decreasing from T_1 to T_7. However, for Design 3 the average trapping is higher compared to the other designs and more uniform. The average trapping for first, second and third trap locations is almost similar for Design 1 and Design 2, and it reaches to maximum for Design 3. For the fifths, sixth and seventh trap locations, the average trapping is significantly improved from Design 1 to Design 3. For the 7th trap location, the average trapping is increased by almost 50% which is in good agreement with numerical simulation indicated in **Figure 6-6**. In order to observe the effects of the inlet velocity on the trapping, the trapping efficiency for the first trap (Design3) was experimentally measured by increasing the inlet velocity to 20 mm/s and 200 mm/s. We observed that by increasing the velocity, the efficiency of the first trap is slightly reduced by 11% and by increasing velocity to a higher velocity (200 mm/s), the efficiency of the first trap reached 78% (**Figure 6-11c**) and its trend is in agreement with simulation results. It was observed that by increasing the inlet velocity, the traps located at the middle part of the main channel (T2-4) are filled at an earlier time compared to the first trap.

6.5. Conclusions

In this study, a microfluidic platform was developed to capture single particles using a hydrodynamic-based approach and the fluidic resistance concept. A series of trap sites were located on both sides of the main channel to accommodate single particles by controlling hydrodynamic forces. In our design in order to increase the hydrodynamic resistance of the main channel and direct suspended particles or cells into the trap sites, inclined sidewalls were designed instead of extending the main channel length, resulting in a more compact configuration. Numerical simulations were performed to tune geometric parameters and optimize the trapping ability of the microsystem through estimating the trapping efficiency of the device. With the aid of this microsystem, single particles can be trapped rapidly, with an efficiency of 90%. Moreover, the numerical simulation revealed that single particles can be trapped at the trapping positions without experiencing a high level of stress in comparison to similar devices, suggesting a proper configuration for capturing delicate single cells. This system can be further developed for particle sorting by accurately designing and controlling the width of three outlets to allow all the small particles to be directed into two side outlets after passing through trap sites.

In this chapter, we introduced a microfluidic device for gentle trapping of cells. This device can be used for further characterization of cells and study the dynamic interaction of gold nanoparticles and cells. In the next chapter, it is discussed how mechanobiological properties of both healthy and cancerous cells affect the deformation of cells under hydrodynamic forces, and how forces are transmitted within cell bodies.

Chapter 7
Cellular Deformation Characterization of Human Breast Cancer Cells under Hydrodynamic Forces

This chapter is based on the following published paper:

- **Ahmad Sohrabi Kashani**., and Muthukumaran Packirisamy, 2017. Cellular deformation characterization of human breast cancer cells under hydrodynamic forces. *AIMS Biophysics*, *4*, pp.400-414.

Understanding how cells sense mechanical forces and how respond biologically to them is an interesting and quickly-progressing area. Cells within their microenvironment are subjected to various physical forces such as mechanical loads and shear stress. Cells respond and adjust to these forces by mechanotransduction mechanism in which deformation and mechanical forces are converted into biomechanical signals. To quantify mechanotransduction (or mechanosensing) responses and to correctly interpret the behavior of cells under *in vitro* stimulation, magnitude and distribution of the stresses on the cell membrane should be characterized. In this study, a 2D Finite Element Model is introduced to simulate the deformation of individual benign cells (MCF10A) and malignant (MCF7) human breast cancer cells under hydrodynamic forces. A fluid-structure interaction method is implemented to model fluid flow and the single adherent cells inside a microchannel to study the nature of mechanical forces (viscous and pressure) and to determine their contribution to the deformation of cells. Due to the different mechanical properties, cells respond differently to the forces exerted by the fluid flow. It was found that the maximum stress and strain take place at the interface of the adherent cell and channel wall. Also, under the same boundary conditions, nucleus and cytoplasm of an individual malignant cell undergo more deformation comparing a single benign cell. Furthermore, it was observed that both two cell lines experience much more stress when their attached area to the substrate is reduced

7.1. Introduction

Living cells, the basic unit of our body, have specific biomechanical, bioelectrical, and biochemical properties, allowing them to adapt themselves with their dynamic microenvironment. With the aid of these biophysical properties, cells are able to preserve their biological functions [57][54][56]. In a human body, living cells are constantly subjected to diverse types of biomechanical stimuli, particularly, fluid dynamic stimuli such as shear and hydrostatic stress.

Cells in the human body either are directly exposed to flowing flows or are under a load of interstitial fluid flow arising from the movement of fluid through extracellular matrix of tissue. For example, in the blood vessels, cells such as leukocyte, and epithelial cells are in direct contact with fluid flow and shear stress. However, other types of cells such as bone cells, fibroblasts, muscle cells, human breast cells, and articular chondrocytes experience fluid flowing due to the deformation of tissues [321]–[323]. The shear flow-induced mechanical stress has significant effects on cellular functions of both healthy and cancerous cells, such as cell proliferation, transport, gene expression, and apoptosis. For instant, mechanical forces caused by blood flow can affect remodeling and function of vascular endothelial cells, or shear flow can alter viability and proliferation of cancer cells [324][314]. Mechanotransduction is a mechanism by which cells are able to sense and respond to such bio-mechanical environments by changing their morphology of membrane or their rigidities. With the help of this mechanism, cells convert deformation caused by mechanical forces into biological signals in order to adjust themselves to the changes. The reaction of cells in the form of morphological and functional responses not only helps cells to maintain their physiological functions but also plays a significant role in the development and progression of diseases such as cancer and metastasis[316][58]. How cells respond to the mechanical stress is conditional to both specific molecular sensors, and their internal mechanical properties. Mechanical properties of single living cells change in accordance with their healthy level. For example, many studies have substantiated that metastasis cancer cells are less stiff comparing to normal or benign cells [325][326]. Due to different mechanical properties of normal and cancerous cells, they respond differently to the fluid flows in the body. So, further research on such different cellular responses of healthy and unhealthy cells could provide a possible method for diagnosis of diseases.

Due to the difficulty of controlling hydrodynamic conditions under *in vivo* studies, isolated cultured cells under well-defined conditions need to be studied to investigate the responses of cells to the hydrodynamic stimuli. Owing to the complex geometry of cells, complex boundary conditions, and inhomogeneous nature of cells, with cell experimentations alone, the response of single cells to fluid flow cannot be interpreted clearly [56]. Computational models not only enable us to interpret the experimental results but also provide us an ability to predict the response of cells to their biomechanical environment. Many experimental and computational analyses have been made to understand how living cells respond to the fluid flow inside a human body. *McGarry et*

al. [327] computationally and experimentally studied the deformation of bone cells under shear stress using solid mechanic model. *Aleksey Ni et al*. [328] developed a 2D model to study the motion and deformation of a single red blood cell (RBC) under different flow conditions in a micro-capillary filled with plasma alcohol using finite element method (FEM). *Michael C et al.* [329] applied a computational method to estimate heterogeneous displacement and stress-strain field in sheared and focally adherent endothelial cells. Moreover, it has been substantiated that surface tension can affect the mechanical responses of the biological cells [330], and its effect has been studied computationally. For instant, *Ding et al.* [331]used FEM to study the effects of surface tension on the mechanical responses of the living cells. They showed that by considering the surface tension effects, the elastic moduli of living cells can be interpreted with higher accuracy when they are probed by Atomic Force Microscopy (AFM).

In this study, we developed a fluid-structure interaction model in order to characterize the deformation of adherent benign human breast cancer cell (MCF 10A) and malignant human breast cancer cell (MCF7) under the action of hydrodynamic fluid flow (it should be noted that neither cell lines are normal, and both cell lines have different origins and are from different disease). Cells experience different stress, strain and deformation when they are subjected to hydrodynamic forces with respect to their mechanical properties. It is well-known that elastic properties of cancerous and normal are different, and cancerous cells are softer comparing their counterpart [58]. Therefore, when they are subjected to hydrodynamic stimuli, they exhibit different deformations. To the best of our knowledge, cellular deformation comparison between cancerous and healthy cells exposing to hydrodynamic stimuli have not been studied computationally. This study is presented to compare deformations and responses of both cell lines under the same conditions. This study not only could help us to fully understand mechanotransduction mechanisms of healthy and cancerous cells, but also enable us to characterize the behavior of human breast cells in various healthy levels under *in vitro* mechanical stimuli.

7.2. Materials and Methods

7.2.1. Fluid-Structure Interaction Model

The main objective of this project is to characterize fluid flow parameters within a microchannel and quantify mechanical stresses acting on the healthy and cancerous cells due to the hydrodynamic forces. With the aid of this numerical study, the cellular deformation of normal and

cancerous human breast cancer cells is also computed under the applied fluid flow regime. A schematic of the channel under the investigation in this computational study and the adherent cells are shown in **Figure 7-1**. The channel includes two parallel plates, and the target cell is attached on the bottom plate. This parallel-plate flow chamber is used to incite the attached cells by creating a pressure gradient across the microchannel [332]. Fluid flow within the channel imposes both shear and normal mechanical stresses at the interface of cell surfaces and surrounding fluid flow. Cellular deformations and the presence of cells themselves affect fluid flow within the channel. The interaction of cells and surrounding fluid flow either can be weakly coupled in a one-way method or strongly coupled in a two-way method [333]. In the one-way method, it is assumed that the deformation of cells is relatively low, so the effects of changes in the solid domain on the fluid domain are ignorable. However, in the two-way coupling, the fluid flow parameters are influenced by changes in the solid domain or deformation of cells.

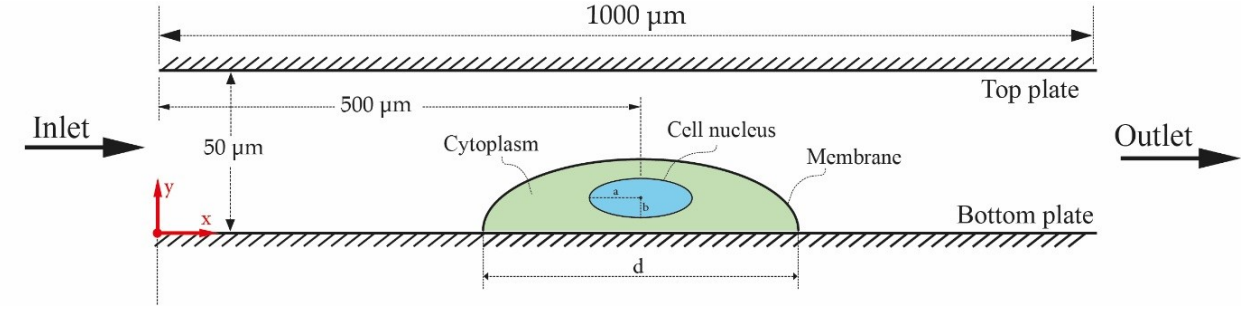

Figure 7-1. *Schematic of an adherent cell within a channel (d: diameter of the cell)*

7.2.2. Case Study and Governing Equations

The system includes a main microchannel with one inlet, one outlet and an adherent cell on the bottom plate of the main channel. A 2D numerical analysis is carried out in order to estimate the flow parameters within the main microchannel as well as characterize deformation of cells under various inlet flow rates. The strongly coupled method is used to numerically solve the interactions between the surrounding fluid and the cell domain. The fluid flow in the microfluidic system is assumed to be Newtonian, laminar, viscous and incompressible flow. The motion of incompressible Newtonian flow is expressed by Navier-Stokes and continuity equations as follows [307]:

$$\rho\frac{\partial u}{\partial t} - \nabla.(-pI + \eta(\nabla u + (\nabla u)^T) + \rho(u.\nabla).u) = F \qquad 7\text{-}1$$

$$\nabla.(u) = 0 \tag{7-2}$$

where ρ is the density of fluid, p is the fluid pressure, u is the velocity field inside the microchannel, t the time, ∇() the divergence operator, I is unit diagonal matrix, η the fluid dynamic viscosity and F is the affecting force on the fluid. For a fluid flow without gravitation and other volume forces, the volume of body force can be neglected (F=0). The total hydrodynamic loads acting on the surface of cells are defined as forces per area as follow [334]:

$$F^T = -n.(pI + \eta(\nabla u + (\nabla u)^T) \tag{7-3}$$

where n is the outward normal unit vector of the boundary, u is the velocity field on the surface of cells pointing out from fluid. F^T is the fluid loading including pressure and viscous forces. The first term in Equation 7-3 is the pressure gradient which is extracted from the fluidic simulation results. The second term is the viscous component of the force which is a function of velocity and dynamic viscosity of the fluid. On the fluid-cell interface, the fluid velocity equals the rate of change of the cell, and this interface is considered as no-slip wall for the fluid domain. In order to have laminar fully developed flow at the local area of the adherent cell, the test section in our simulation was designed to be longer than expected hydrodynamic entry length. Entry length correlating with Reynold number (Re) can be obtained by $L_e=0.006Re.D$. Reynold number within microchannel region for all flow regime is defined as follow:

$$Re = \frac{\rho v D}{\eta} \tag{7-4}$$

where v is the mean velocity, D is the hydraulic diameter of the channel, and η is dynamic viscosity of the fluid.

7.2.3. Material Properties

In the present work, the cell is modeled as an oblate-shape body having cytoplasm and nucleus, and the cell is separated from the surrounding environment by a membrane. An ellipsoidal shape is assumed for the nucleus of the cells to estimate their behavior and deformation. Both cytoplasm and nucleus of the cell are modeled as hyperelastic material, and it is assumed that the adherent cell has isotropic and homogeneous material properties. **Table 7-1** shows dimensions and material properties of human breast cell lines which were used in the finite element modeling[326][335][336]. As mentioned above, the mechanical properties of the two cells lines are different, and Young's Modulus of MCF7 is smaller comparing benign human breast cells.

Hence, these differences were taken into account in our simulation by using different values for both cells. Young's Modulus values available in the literature for MCF10A and MCF7 vary from 0.25 the kPa to 0.7 kPa, and from 0.15 kPa to 0.47 kPa respectively; 0.47 kPa and 0.7 kPa were chosen for MCF10A and MCF7 cells, respectively as the maximum values to perform simulation. Nucleus stiffness is greater than cytoplasm region, and based on the information available in the literature, the stiffness of nucleus was considered ten times greater than the stiffness of cytoplasm[337][338]. The fluid medium is assumed to be an incompressible Newtonian fluid having properties as same as water. Dynamic viscosity of 0.001 pa.s and density of 997 kg/m^3 were used as the properties of water in our analysis, and no-slip condition was considered for both top and bottom plates.

Table 7-1. *Dimensions and material properties of human breast cell lines*

Parameters	MCF7	MCF10A
Average diameter (μm)	d=14	d=14
Nucleus size-ellipsoidal shape(μm) [326][336]	a=3.2, b=1 (*)	a=2.8, b=1
Height of profile(μm) [326]	3.15	3.3
Elasticity of cytoplasm (kPa) [338]	0.47	0.7
Elasticity of Nucleus (kPa) [337][338]	4. 7	7.0
Density of Cytoplasm (gr/cm^3)[338]	1.05	1.05
Density of Nucleus (gr/cm^3) [338]	1.3	1.3
Poisson's ratio [335][338]	0.49	0.49

(*) a: half of major diameter. b: half of minor diameter

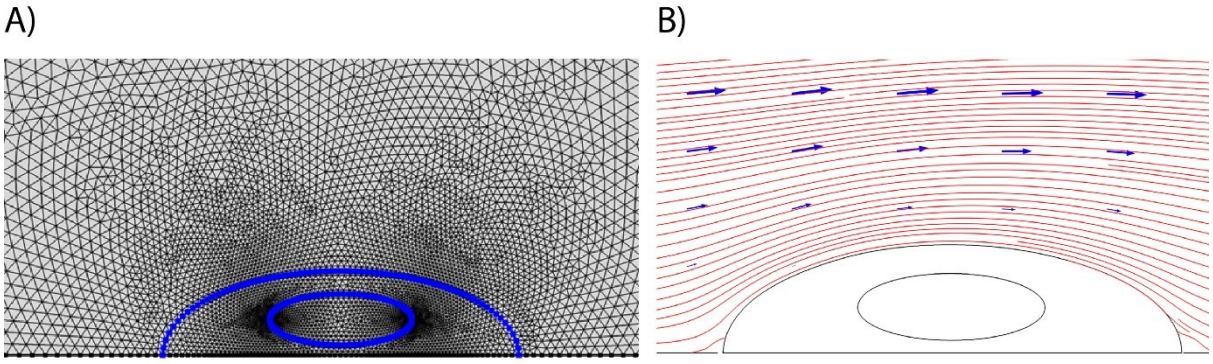

Figure 7-2*.(A) Mesh network and elements sizes for system of an adherent cell (MCF10A) and fluid flow; (B) Stream lines around the cell (arrows illustrates the direction and magnitude of velocity within the channel).*

7.2.4. Numerical Simulation

In order to solve the governing equation as well as modeling microchannel, cell and fluid flow within microchannel, commercial software for finite element analysis known as COMOSL Multiphysics 5.2 was used. To have a fully coupled solver, a 2D model with moving mesh modules was utilized to model the interaction between fluid and the cell. The fluid flow domain changes considerably by deformation of the solid domain (cell), so in order to couple the solid and fluid domain together, a direct two-way coupling formulation was implemented. Simulation with different velocities and boundary conditions were performed to induce various external shear stresses on the surface of the cell, and to distinguish the different behaviors of normal and cancerous cells. An iterative, segregated solution method was used to carry out all simulations. In order to obtain a converged solution, the variables were solved repeatedly and sequentially. Mesh element of the system including cell and surrounding fluid flow is shown in **Figure 7-2A**. The size of elements inside the cell and at the interface of cell and fluid flow is smaller than other parts of the domain to have reasonable accuracy for very small changes. **Figure 7-2B** presents streamlines and magnitude of velocity neighboring the cells. From this figure, it is evident that streamlines closing to the cells are influenced by the body of the attached cells.

7.3. Results and Discussion

Using the design in **Figure 7-1**, dimensions and material properties shown in **Table 7-1**, fluid flow were simulated within the microchannel to characterize flow parameters. Before deriving the results, a mesh independence test was performed to choose an appropriate mesh size in accordance with the size of the channel and the adherent cell. The pressure along the length of microchannel at the local area of the cells was computed by decreasing mesh size and increasing degree of freedom. Properties of various mesh element sizes used in the simulation are shown in **Table 7-2**. This process performed until reaching ignorable differences between the results for two successive mesh size. The pressure along microchannel is plotted in **Figure 7-3** under various mesh elements sizes. Based on the result, the difference between mesh 3 and 4 is very small, so in order to have efficient computation, the mesh 3 was used for the following simulation.

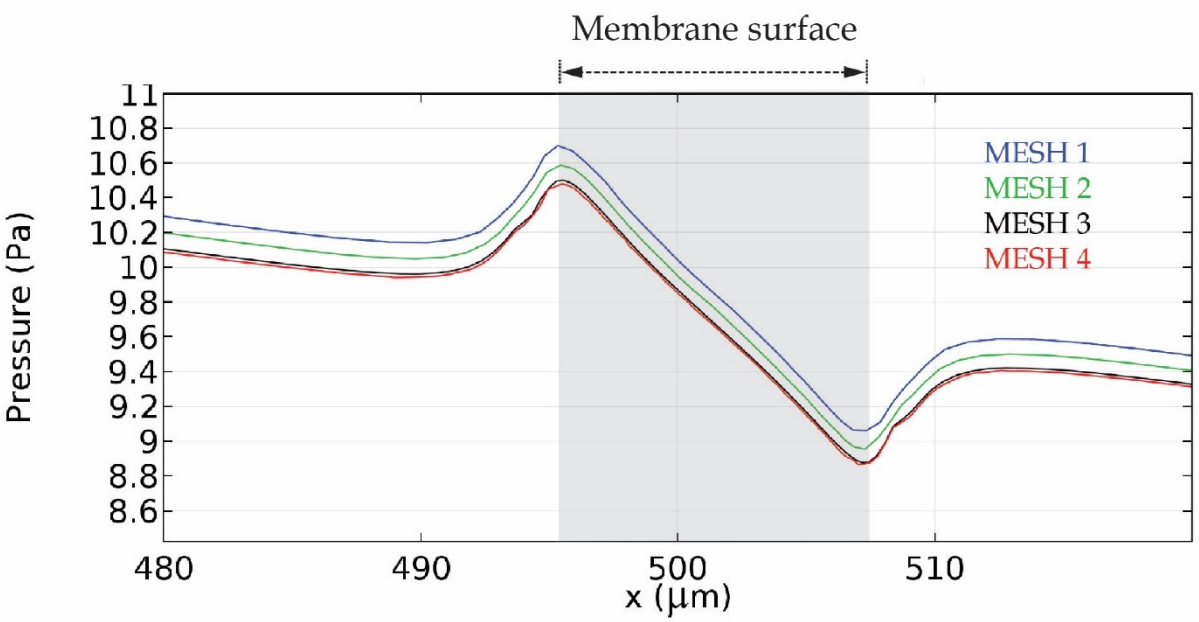

Figure 7-3. *Pressure along the length of bottom wall and membrane surface of an adherent cell under various mesh sizes*

Table 7-2*. Properties of elements in various mesh types*

Mesh number	Maximum element size	Minimum element size	Grow rate	Curvature factor	Resolution of curvature	Number of elements
Mesh 1	37	0.125	1.26	0.3	1	1604
Mesh 2	20	0.075	1.2	0.26	1	2413
Mesh 3	5	0.02	1.12	0.24	1	10822
Mesh 4	3	0.01	1.08	0.2	1	21359

Figure 7-4 compares pressure fields within the microchannel for two different conditions: when the channel is free (without cell), and when it is occupied by either MCF7 or MCF10A cell lines. This figure clearly demonstrates the effect of solid domain (the adherent cell) on the pressure field at the zone of a single cell. For the free channel, pressure along the length of the channel is linearly decreased, while for a channel with the cell, a variation in pressure near the cell is observable. Similarly, any changes at the boundary of the cell such as membrane deformation can alter flow parameters such as velocity and pressure within the channel. The deformable structure of the cell deforms when it is subjected to a pressure, and as a return, this deformation changes the flow field.

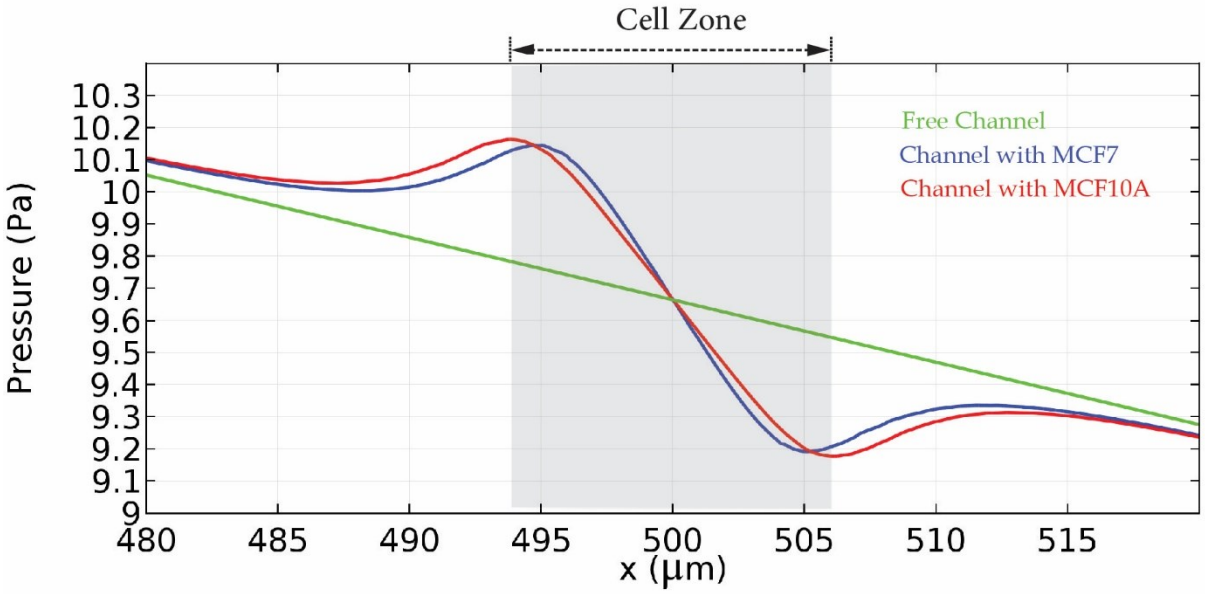

***Figure 7-4**. Pressure along channel for three various conditions: free channel, channel with cancer cell and channel with healthy cell.*

Figure 7-5 indicates the contour of Von Mises stresses for two different cell lines and corresponding shear stress along the channel and in the vicinity of cells. As mentioned in Section 2.2 and Equation 7-3, forces acting on the membrane of the cells include both viscous and pressure forces. For a steady, laminar and fully developed flow between two infinite stationary plates, the shear stress within flow field can be obtained using the following expression [307]:

$$\tau_{xy} = \frac{6\eta U_{ave}}{h}\left\{1 - \frac{2y}{h}\right\} \qquad 7\text{-}5$$

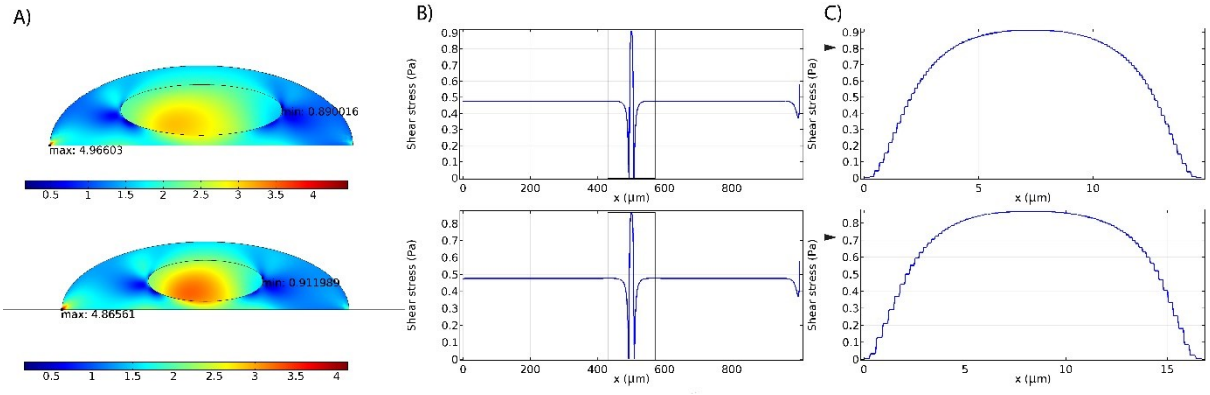

***Figure 7-5.** Von Mises stresses **(A)** over two cell types and corresponding shear stress along length of the channel; **(B)** and membrane surface; **(C)** of the adherent cells under inlet average velocity of 4 mm/s*

where η is the dynamic viscosity of the fluid, U_{ave} presents average velocity, *h* is height of channel, and y is the distance from the bottom plate. For an inlet average velocity of 4 mm/s, imposing shear stress on the wall of the bottom plate (y=0) of the system is τ_0 = 0.48 Pa using Equation (7-5. **Figure 7-5** shows that shear stress on the bottom wall is constant along the channel and is matched with the analytical solution (using Equation **7-5**) except in the inlet, outlet of the channel and the local area of cell. In the vicinity of the cell, the shear stress on the membrane of the cell is significantly increased due to the existence of the cells. The results indicate that the shear stresses on the membrane of the cells are almost two times greater than shear stress on the wall. From the contours, it is evident that maximum stress takes place at the interface of the cell and substrate, the minimum stress is at the interface of cytoplasm and nucleus. Since the cancerous cells are softer, cytoplasm and nucleus of them undergo more deformation under same hydrodynamic loading compared to MCF10A cell lines. The effect of hydrodynamic load on the nucleus of MCF10A is less in comparison to MCF7, it means that greater force is transferred from the membrane of MCF7 to its nucleus.

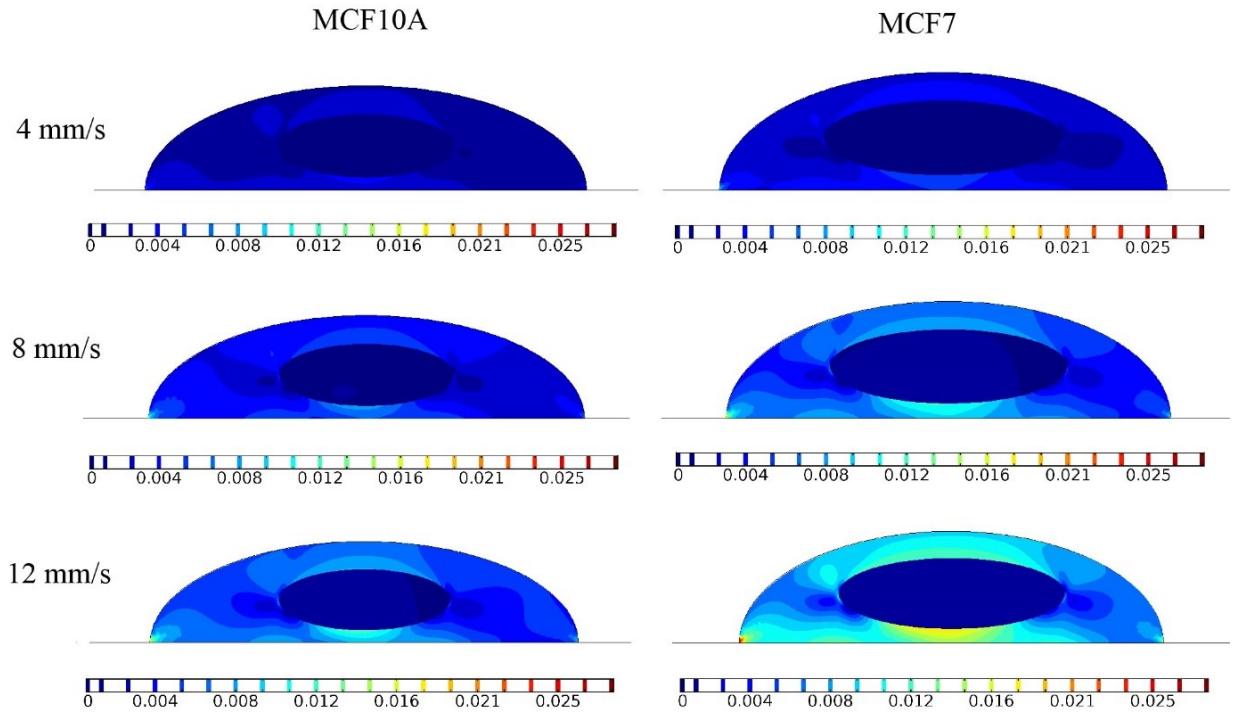

***Figure 7-6**. Distribution of equivalent elastic strain (EQS) for both MCF10A and MCF7 under various average inlet velocities: 4 mm/s,8 mm/s4 mm/s,8 mm/s and 12 mm/s*

To study the effect of fluid flow on the cell lines and quantify their deformation, cellular deformation of the cells under various inlet velocities were computed using equivalent elastic strain (EQS). Von Mises equation can be used to define EQS for elastic material as follows[339][340]:

$$EQS = \frac{1}{\sqrt{2}(1+v)}\left[\left(\varepsilon_{xx}-\varepsilon_{yy}\right)^2+(\varepsilon_{xx}-\varepsilon_{zz})^2+\left(\varepsilon_{yy}-\varepsilon_{zz}\right)^2\right]^{0.5} \quad 7\text{-}6$$

where v is Poisson's ratio, ε_{xx}, ε_{yy} and ε_{zz} are principal strains in direction of x, y and z respectively. **Figure 7-6** shows contours of equivalent elastic strains for the two cell lines when they are subjected to various hydrodynamic forces due to different average inlet velocities. It was assumed that the cell is completely attached to the bottom plate so that no displacement happens at substrate-cell interface. It can be seen in this figure that greater values of EQS occur in regions between substrate-cell interface and nucleus of each cell type. As was observed from **Figure 7-5**, cells experience the maximum value of shear stress at the top of the membrane, and hence the EQS values are greater comparing other parts of the cell at these regions. Moreover, these results show the effect of hydrodynamic force on the deformation of the nucleus under various inlet velocities. Even though nucleus of cells is stiffer, by increasing the inlet velocity, more deformation is experienced by nucleus of each cell line. As expected, the nucleus of MCF7 lines is deformed much more at the same inlet velocity when compared to MCF10A lines due to its lower stiffness. It means that nucleus of malignant cells senses more deformation under same mechanical forces within channel. To characterize the deformation values for cytoplasm and nucleus of the two cell types, the average equivalent elastic strain (AEQS) for nucleus and cytoplasm of each cell lines were computed by averaging EQS over nucleus and cytoplasm surfaces of the both cells. The average equivalent elastic strains are shown in **Figure 7-7** for different inlet average velocities. The result shows that average EQSs for MCF7 are approximately 1.4 and 1.5 times greater than MCF10A for cytoplasm and nucleus respectively. Hence, hydrodynamic forces which are transmitted through the cells of MCF7 are much more at the same conditions in comparison to another cell line. It can be seen from this figure that the average equivalent elastic strain is increased with respect to inlet average velocities.

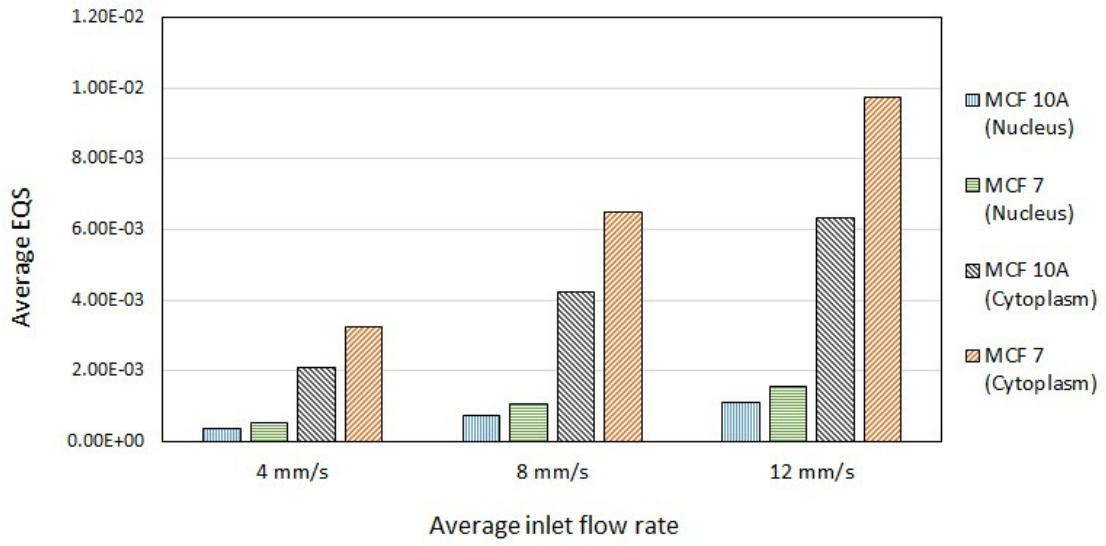

Figure 7-7. *Average equivalent elastic strain (EQS) over nucleus and cytoplasm of the cells under different average inlet velocities.*

As mentioned in **Equation 7-3)**, total forces acting on the membrane of the cell is a combination of viscous and pressure forces. Due to different pressure between the surfaces of fluid flow, the pressure gradient force is produced, while due to friction between layers of fluid flow, the viscous forces are produced in the opposite direction of flow. Deformation of cells does not determine the contribution of each force to the total force, so it would be useful if we can quantify the contribution of each force to the total forces acting on the cells. **Figure 7-8** illustrates the amplitude and direction of pressure and viscous forces applying to the adherent cell under fluid flow inside microchannel. Viscous forces are tangent to the fluid-cell interface boundary, and it is clear that the maximum forces due to viscosity is applied at the top of cell, and its values are decreased significantly by moving toward the sides of the cells. The length of the arrows at different points express the amplitude of forces at those points. Pressure forces are normal to the fluid- cell interface boundary, and its values are more uniform compared with the viscous forces. **Figure 7-9** compares the values of total viscous and pressure forces along both MCF7 and MCF10A cells. It is evident that pressure forces are much greater in comparison with viscous forces, so their contribution to the deformation of cells would be more significant. For the setting boundary conditions and the geometry of channel, the pressure forces are more than ten times than viscous forces. These results emphasize the significant role of pressure on the deformation of cells compared to viscous forces. **Figure 7-9** also highlights the different magnitude of loads arising

from pressure forces acting on the membrane of the cells compared to the viscous forces under different inlet velocities. By increasing the average inlet velocity, both total pressure and total viscous forces are increased, but due to more contact area between MCF10A and surrounding fluid flow, they are subjected to more forces in comparison to the MCF7 cells.

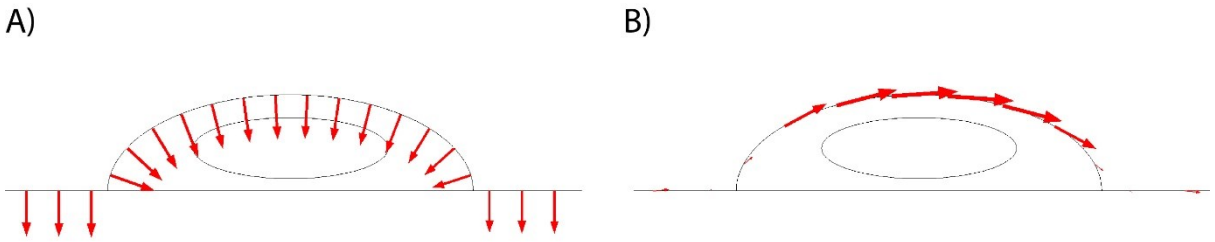

***Figure 7-8**. Pressure and viscous forces (arrows are proportional to the magnitude of forces at the indicated points). **(A)** Pressure force acting on the membrane of cell; **(B)** Viscous force acting on the membrane of cell (the scales of arrows for pressure and viscous forces are not identical).*

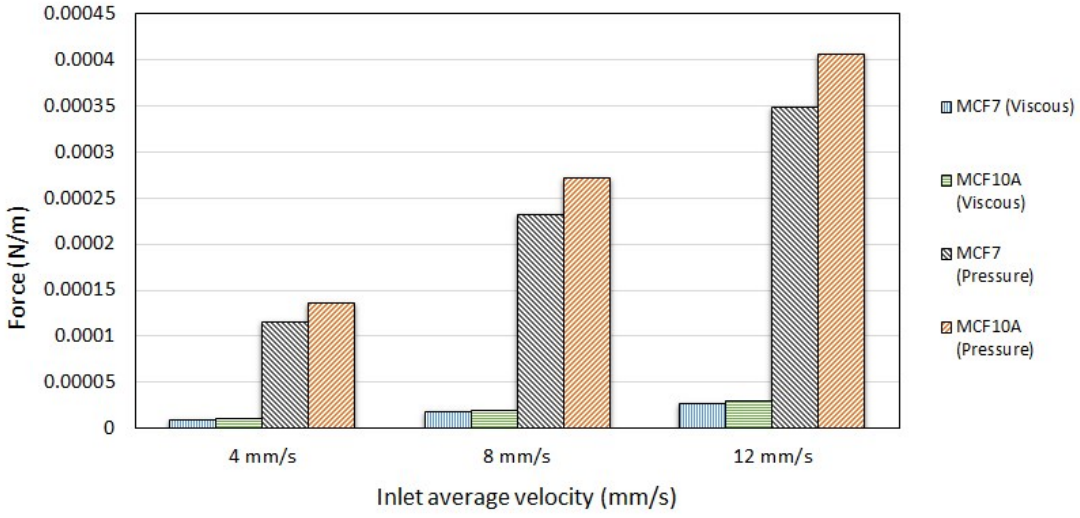

***Figure 7-9.** Total pressure and total viscous forces acting on the membrane of two cell lines under various average inlet velocities.*

Due to reduced cell surface adhesion molecules in cancerous cells, most of them are less adhesive (focal adhesion) compared to their normal counterparts. As a result, cancer cells are not restrained completely by interaction with tissue components or their substrate, giving them the ability to invade and metastasize. Reduced adhesiveness to the substrate causes morphological and cytoskeletal changes of cancerous cells, so they are rounder than normal cells [341][342]. For previously obtained results, it was assumed that the cell attaches to the substrate completely, so there is no deflection at the interface of the cell and substrate. In order to study the effects of

adhesion on the deformation of cells and mimic their microenvironment, the simulation was performed assuming that cells partially adhere to the substrate so that cells are free to deform at the two sides in X-direction only while still they are fixed in the y-direction. **Figure 7-10** illustrates how cells were constrained on their cell-substrate interface for the simulation by considering various attached areas. As this figure shows, there is no deflection for the center of cells. However, at X_a distance away from two ends, it can be deformed only in x-direction.

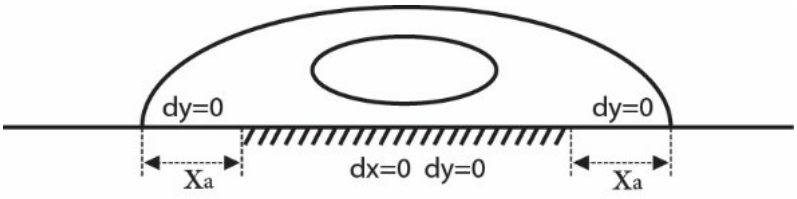

***Figure 7-10**. Schematic of fixation of a cell to the substrate*

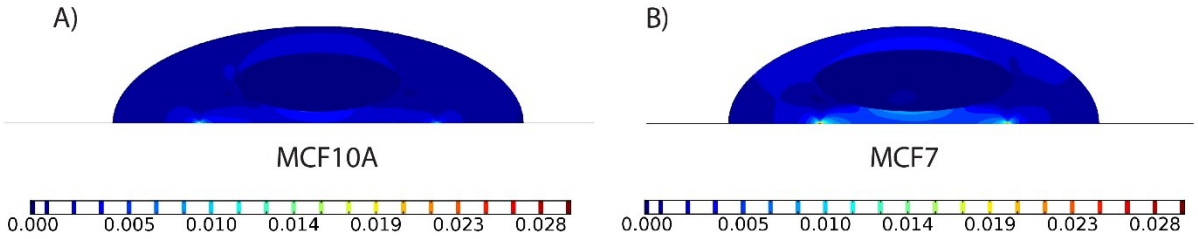

***Figure 7-11**. EQS contours when cells are adhered partially (X_a=3 μm). **(A)** MCF10A, **(B)** MCF7 (inlet average velocity: 4 mm/s).*

To study the effect of X_a, the average equivalent elastic strains of the two cell lines were computed for different values of X_a, and the results are shown in **Figure 7-11** and **Figure 7-12**. The average EQS increases by increasing the X_a, but the increase in deformation is not similar for both cytoplasm and nucleus of two cell lines. **Figure 7-12B** compares the increased percentage in EQS with respect to the X_a. This figure clearly demonstrates that the nucleus EQS of the cell under constant inlet average velocity is influenced more by increasing X_a compared to the cytoplasm. Due to the shorter attached area of cells to the bottom plate, more stresses are experienced by them under same boundary conditions. It was shown that the maximum stresses occur on the cell-substrate interface, and the maximum value of stress was measured to understand the effect of various attached areas on it. **Figure 7-13** shows the maximum stress estimated in two cell lines when X_a changes from 0 to 4 μm. The maximum stress can be increased from 5 Pa when X_a = 0 to 15 Pa when X_a = 4 for MCF7 cells.

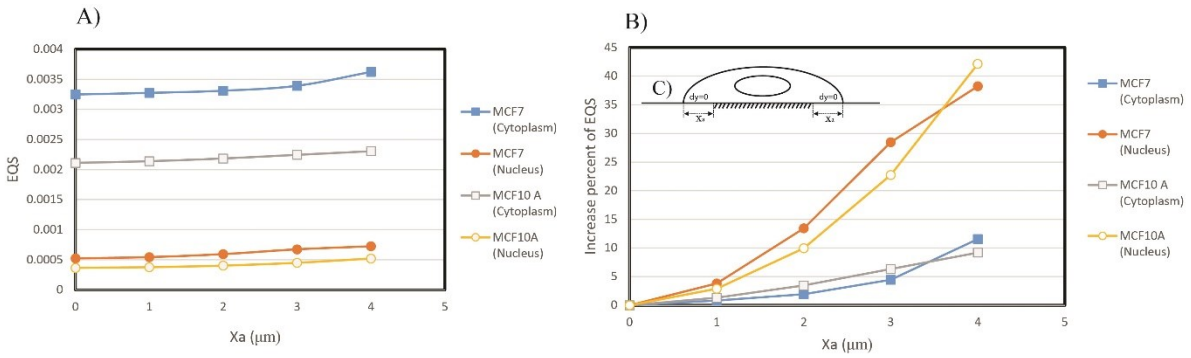

Figure 7-12. ***(A)*** *Average EQS for cytoplasm and nucleus of both cell lines versus different X_a as shown in* ***(C)****;* ***(B)*** *Increased percentage of EQS versus different X_a compared with EQS of two cell lines when X_a=0 (inlet average velocity: 4 mm/s).*

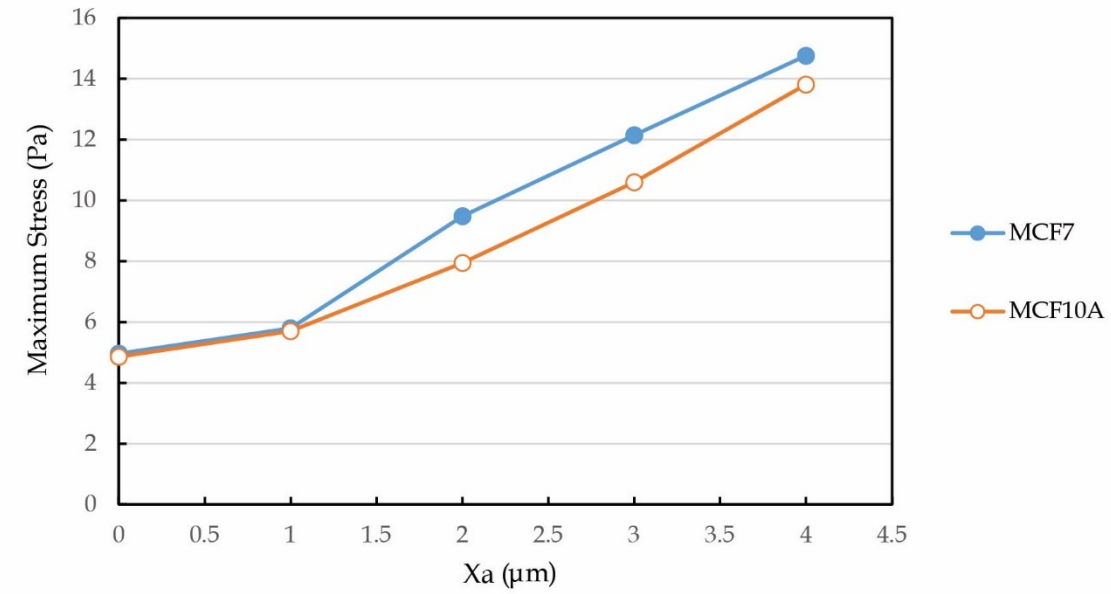

Figure 7-13. *Maximum stress estimated in the two cell lines for different X_a (inlet average velocity: 4 mm/s).*

7.4. Conclusions

Biological function of cells and their behavior are affected by biomechanical forces such as shear stress in their environment. These mechanical stimulations can also alter the phenotype of those cells. Cells respond to fluid shear stresses by mechanotransduction mechanism, and they exhibit various deformations with respect to their mechanical properties such as elasticity and density. In this study, a fluid-structure interaction model was developed to quantify the deformation of both normal and cancerous cells under flow-induced hydrodynamic loads including viscous and

pressure forces. It was observed that the maximum stresses take place at cell-substrate and the minimum at cytoplasm- nucleus interface. The obtained results show that the nucleus and cytoplasm of MCF7 cancer cells undergo almost one and half times more deformation than MCF10A benign cells under the same conditions. To differentiate the effects of viscous and pressure forces individually on the deformation of cells, the contribution of each force was estimated numerically. The adherent cells undergo the hydrodynamic force which is a combination of pressure and viscous forces, but our numerical study reveals that the imposing total pressure on the membrane of the cells due to the flow field, is much more (ten times greater) than total viscous forces within channel. It suggests that the pressure field provides a major contribution to the deformation of the adherent cells. Moreover, the FSI model was used to study the effect of partial adhesion of the cells on their deformation. By reducing the cell adhesion, the deformations of both MCF10A and MCF7 increased under the constant inlet velocity, but the amount of increase is not identical for both cytoplasm and nucleus. When the cell adhesion was reduced, the physical deformation of cell increased considerably in response to forces. This study can provide useful insight into the behavior of individual cancerous and normal cells under flow conditions.

In this chapter, we discussed how cells depending on their mechanobiological properties sense external hydrodynamic forces. In the next chapter, a new model is introduced to characterize the mobility ability of cells based on their mechanobiological properties particularly cells stiffness. This model helps to understand the different migratory behaviors of healthy and cancer cells.

Chapter 8
Effects of Cellular Bulk Stiffness on Migratory Potential of Cells

This chapter is based on the following submitted paper:

- **Kashani, Ahmad Sohrabi**, and Muthukumaran Packirisamy. "Effects of Cellular Bulk Stiffness on Migratory Potential of Cells." *Submitted to Journal of the Royal Society Interface* - March 2020

Cancer progression is associated with alternations in the cytoskeletal architecture of cells and, consequently, their mechanical properties such as stiffness. Changing the mechanics of cells enables cancer cells to migrate and invade to distant organ sites. This process, metastasis, is the main reason for cancer-related mortality. Cell migration is an essential step toward increasing the invasive potential of cells. Although many studies have shown that the migratory speed and the invasion of cells can be inversely correlated to the stiffness of cells, some other investigations indicate exactly opposing results. In the current work, based on the strain energy stored in cells due to the contractile forces, we defined an energy-dependent term, migratory index, to approximate how changes in the mechanical properties of cells influence cell migration required for cancer progression. Cell migration involves both cell deformation and force transmission within cells. The effects of these two parameters can be represented equally by the migratory index. Our mechanical modeling and computational study show that cells depending on their shape, size, and other physical parameters, have a maximum migratory index taking place at a specific range of cell stiffness, indicating the most favorable conditions for invasive mobility. This approximate model can be used to explain why the stiffness of cells varies during cancer progression. We believe that the stiffness of invasive cells depending on the stiffness of their non-invasive counterparts is either decreased or increased to reach the critical condition in which the mobility potential of cells is approximated to be maximum.

8.1. Introduction

Over two past decades, many researchers have revealed that mechanical properties at the cellular level, mechanobiological properties, can provide diagnostic information on various abnormalities like cancer. Cells are the smallest, dynamic, and functional living unit of human

organs and many diseases like cancer cells originate from alternations at the cellular level[343][344]. There is mounting evidence suggesting that biological functions of cells can be correlated to the mechanical properties[87], [130], [345], and this growing knowledge has motivated many bioengineers to investigate on how physical and mechanical properties of cells contribute to migration, progression, and invasiveness of cancers. Alternation in mechanobiological properties of cells will influence functional characteristics of cells such as cellular proliferation, progressions, growths, mobility, invasiveness, and differentiation[65]. Living cells possess different mechanobiological properties such as stiffness and viscosity, which have been found to be significant mechanical biomarkers for cancer detection at early stage. Stiffness is a fundamental mechanical property of structures or components and is defined by material properties such as Young's Modulus and geometrical configuration. Generally, the resistance of materials to deformation under the action of an applied force is defined as stiffness[346]. Soft structures are more deformable than stiff structures, while stiff structures show more resistance to deformation in response to the applied force[347]. Several scientific surveys have shown that cancerous and invasive cells are softer compared to non-invasive and healthy cells[131]. However, their tumors, including the surrounding environments of cells, are more rigid as cancer cells undergo mesenchymal-epithelial transition[140]. Deformability coupled with less adhesion in cancer cells enables them to change their positions within body tissues through cell migration and invasion[348][349]. This phenomenon, metastasis, is the main threat of cancer to human health. According to the most reported results on the mechanics of various cancers, softness is a striking characteristic of cells, and its degrees can give an estimation of cancer migration and invasiveness[130]. For example, it has been reported that the metastatic activities of human breast cancer cells can be increased by lowering the stiffness of cells[83][350]. Findings of *Probhun et al.* [351] showed that the actin organization of malignant thyroid cells is disrupted, giving the malignant cells 2-5 times smaller bulk Young's Modulus in comparison to the primary normal thyroid cells. In other work *Xu et al.* [131]used AFM technique to examine the stiffness of highly-invasive ovarian cancer cells (HEY A8) in comparison to benign ovarian epithelial cells (HEY), suggesting that malignant cells display a lower intrinsic stiffness than non-malignant cells by re-modeling their actin organizations. These findings suggest that the invasiveness and migration speed of cells can be related to the softness-level of cells, and this correlation is believed can be used as an indicator to estimate the invasiveness and migration speed of cancers[352]. Despite

many findings on the softening of cancer cells and their subsequent increase in the migratory and invasive capability, it is not appropriate to draw a firm conclusion about the invasiveness and the softening of different types of cancers[353][83]. There are few contradictory results in which it was shown that cancerous and invasive cells are stiffer compared to normal and non-invasive cells[353]. In work done with *Palmieri et al.* [354], their findings showed exactly a reverse stiffness-invasiveness relationship. Their AFM measurements confirmed that, in colorectal cancer cells, non-invasive (R-type) cells have smaller Young's Modulus compared to the invasive cells (E-type). In another work performed with *Bastatas et al.* [355], it was also revealed that stiffness of invasive or metastatic prostate cancer cells is significantly increased compared to their non-invasive counterparts. The study of *Kim et al.* [356], also recently revealed that β-adrenergic activation causes cancer cells to become less deformable while their invasiveness is increased. Based on these results, invasive cells are not necessarily softer compared to their non-invasive counterparts. It is thought that invasive cancer cells can be either stiff or soft. Stiff cancer cells cannot deform themselves and soft cancer cells cannot generate and transmit forces to squeeze through pores of highly crosslinked collagen fibres in their microenvironment[357]. **Figure 8-1** schematically shows how relatively stiff or soft cancer cells can move into their local microenvironment.

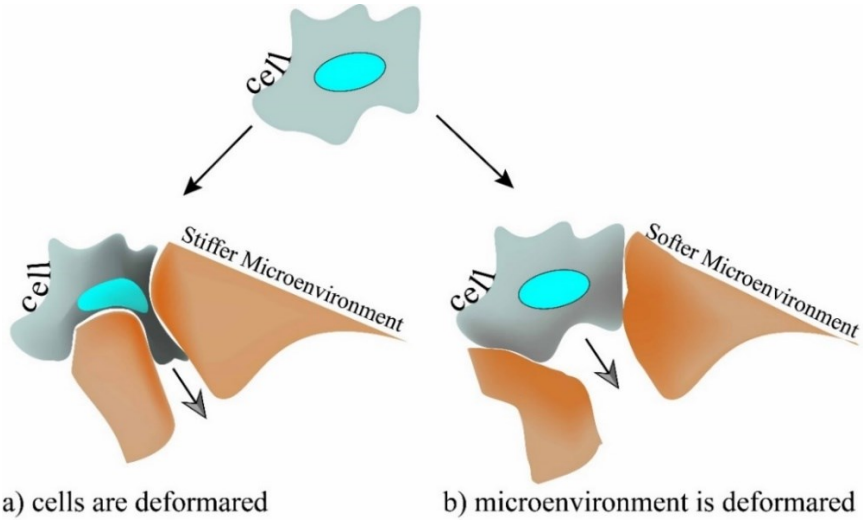

Figure 8-1. *Cancerous cells can be relatively either softer or stiffer compared to their microenvironment. Depending on the rigidity of cells and their microenvironment,* ***a)*** *they can be deformed, or* ***b)*** *they can deform their microenvironment.*

Similar contradictory results might also be observed in different responses of cancer cells to anti-cancer drugs. Some studies have shown that treated cells with anti-cancer drugs or

nanoparticles regulate the progress and migration of cancer by reducing their stiffness values while other investigations are suggesting exactly an inverse relationship, treated cells are stiffer and less invasive and motile compared to the non-treated cells. The structural properties of cells, such as stiffness are determined by complex, dynamic filamentous proteins [56]. This organized system, cytoskeleton, consists of different proteins such as actin-filament, microtubule, and intermediate filament. The cytoskeleton is responsible for different cell functions, including spreading, polarity, migration, differentiation, and division[358]. Generating force, and changing shape to move are two important roles of the cytoskeletal architecture, and any change in these structures might influence the cellular function negatively. Many anti-cancer drugs, like chemotherapeutic agents, are purposely designed to target the cytoskeleton and mechanics of cancer to control cell migration and consequently cell metastasis [65][359]. Different investigations have shown that the effects of these anti-cancer drugs on the stiffness of cells are not consistent. Several studies have demonstrated that anti-cancer drugs could disrupt the cytoskeleton organization, and make them softer. *Babhosseini et al.* [138] used a microfluidic to evaluate the effects of sphingosine kinase inhibitors (SphKIs)[12], an inhibitor to halt the metastasis, on cancer cell by measuring their velocities and passage time when they pass through a narrow microchannel. Their findings showed that the highly invasive human breast cancer cells become more deformable once they are treated with SphKI6, suggesting that the cancer invasiveness can be controlled by reducing the stiffness. Recently, *Qin et al.* [119] observed that the migratory and invasive abilities of highly invasive human breast cancer cells (MDA-MB-231) could be weakened by treating cancer cells with small fullerenol nanoparticles while their stiffness values are decreased compared to untreated cells. Some other studies are proving exactly the opposing results in which the migratory and invasive capability of malignant cancer cells is managed by increasing the stiffness of cells. *Ren et al.* [360] tested the effects of different anti-cancer drugs on human prostate cancer cells. Their AFM measurements revealed that for all tested anti-cancer agents, the Young's Modulus of cancer cells is substantially increased in comparison to non-treated cancer cells. Using AFM analysis, in another similar investigation, *Mustafa et al.* [139] found that gold nanorods particle designed to target the nucleus of ovarian cancer cells can be effective in increasing the stiffness of cells. Along

[12] Human cancer tissues elevate sphingosine kinase, which results in increased production of sphingosine-1-phosphate (S1P) from sphingosine[422].

with this increase in mechanical resistance of the cells, they observed that this treatment has strong inhibitory effects on the migratory and invasive ability of cancer cells.

As we discussed, some cancer and invasive cells can be softer than their normal and non-invasive counterparts, while few other invasive cells are stiffer than their healthy and non-invasive counterparts. The similar behavior also has been observed in the treated cells, showing that the cell migration speed and invasiveness can be reduced either by increasing or decreasing the rigidity of cells. These different behaviors can be presented with the rigidity index. For cancer or invasive cells, the rigidity index is defined with respect to the elasticity of their normal or non-invasive counterparts as follow:

$$r = Log_{10}\left(\frac{E_c}{E_n}\right) \qquad 8\text{-}1$$

Where r is the rigidity index, E_c is the elasticity of cancer or invasive cells, and E_n is the elasticity of the normal or non-invasive counterparts with the same unit. The variation of r is given in **Figure 8-2** for different types of cancer. For fluid-like cancer cells that are softer than normal cells, the rigidity index is negative ($E_c < E_n$), and for rigid-like cancer cells that are stiffer than normal cells, the rigidity index is positive ($E_c > E_n$). Looking at these non-consistent results, some fundamental questions might be raised on the reliability of cell stiffness measurements to evaluate the invasiveness and migration of cells and the efficacy of anti-cancer drugs designed to target the cellular structures. How cells stiffness could be used to predict the migratory and invasive ability of cells? If cancerous and invasive cells are softer compared to healthy cells, is it always effective to design anti-cancer drugs to increase the cell stiffness to control the migration and invasiveness of cancer? It seems that cell stiffness alone is not capable of answering these key questions. In the context of cell mechanics, force transmission and deformation of cells are influenced by the elasticity of their bodies [56], [361], [362]. For a relatively stiffer environment, the cancer cells need to be deformed largely to squeeze through the microenvironment, while cancer cells need to be relatively stiffer to move into the softer microenvironment. In the process of metastasis, cell migration is essential to regulate many biological processes required for cancer invasion, and invasive cells are more migratory than non-invasive cells [363]–[367]. Besides, as mentioned earlier, under some treatments, the invasive ability of invasive cancers is reduced along with a reduction in their migratory ability[119][139]. To compare the migration ability of cells required

for cell invasion, we need to account the two mentioned important parameters, namely force transmission, and cell deformation.

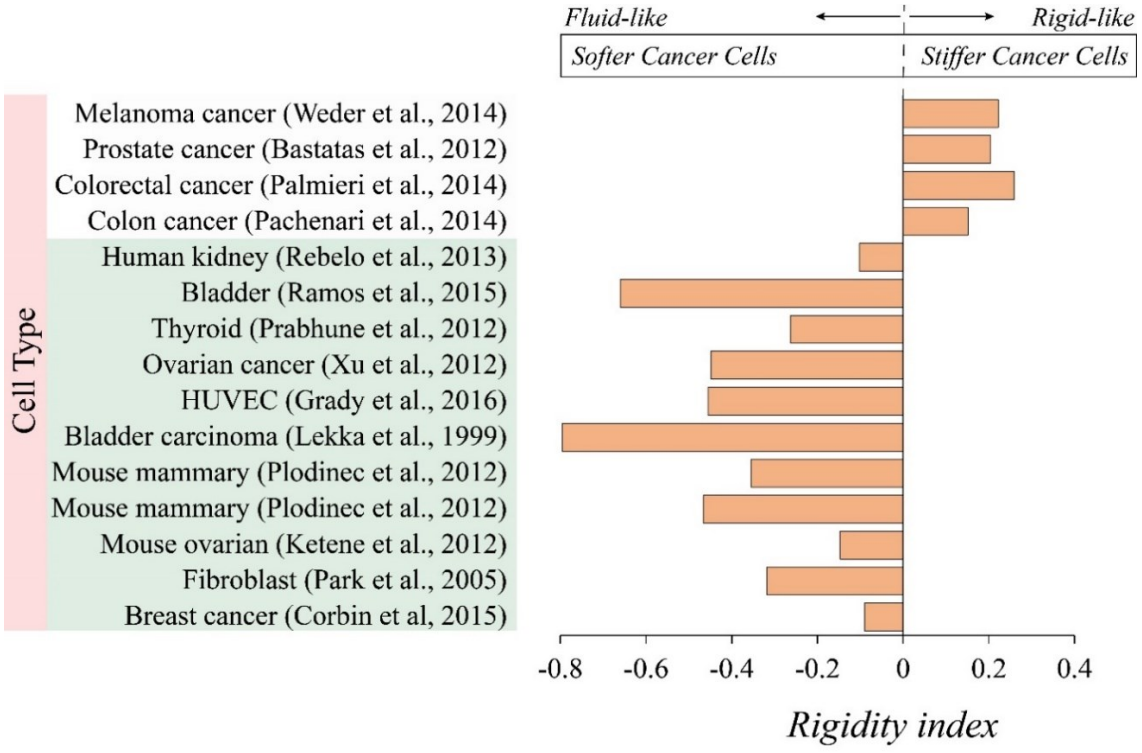

Figure 8-2*. Increasing or decreasing the stiffness of cancer cells can enhance the invasive and migratory abilities of cells. Those changes might be happened either during cancer progression or once they are treated with different drugs (stiffer:* [354][355] [368][369]*, softer :* [130][131][83] [351][370][371][372][71][373][374]*)*

We need to model both force-based migration and deformation-based migration through cancer mechanobiological behavior in a unique way to model and understand the migratory behaviors of cancer cells under different microenvironments. Once a force is generated in cells, it is propagated throughout the cell body. Depending on the structural and material properties of cells, the body of cells is deformed, and a portion of that force reaches the cell-microenvironment contact points, trying to overcome resisting-forces at those points and making cells to move forward. All these phenomena, force generation, and transmission, and the subsequent deformation are energy-dependent processes. Once cells are deformed due to the internal force, mechanical energy is stored in cells. The stored energy can be changed in other forms of energy, and under ideal conditions can approximate the potential of the system (cell body) to do work (cell movement). Under ideal conditions, the stored energy could be used to represent both deformation and force transmission

in cells. Although cell migration and cell invasion are complex phenomena, with the energy model, the migration behavior of cancer cells can be approximated to compare their migratory abilities globally based on their stiffness values. It is thought that the energy model can answer mechanobiological questions about stiffness-migration interactions.

In the current work, we developed a computational study to test our hypotheses about the stored energy potential in cancer cells due to the internal force to approximate the migratory potential of cancer cells. The higher energy potential implies increased migration as this energy of cells is transformed either through deformation or force and can represent the degree of migration and can be called "migratory energy". Our objective is to use computational techniques to approximate the migratory ability of cells in terms of force and deformation through cancer mechanobiological behavior in the absence of biological contributions from cell and microenvironment that are negligible for this study. We modeled a single cell and studied its migratory energy by varying its bulk stiffness to show how cell mechanics influence the migratory ability of cells. It was assumed that cell mechanics contribute mainly to the migration of cells, and the bulk stiffness of cells is assumed to remain constant over cell migration to simplify the modeling. Based on this approximate model, cells depending on physical factors such as shape and size have critical stiffness values or ranges in which the cell migration is approximated to be high. Beyond that range, cells might lose their capability to migrate fast and potentially move into other parts of the body. It is believed that healthy and non-invasive cells possess a bulk stiffness in distant from the critical range, while cancerous and invasive cells tend to modulate their stiffness to a value in the critical range to maximize their migratory potential required for cancer progression. Our hypothesis and approximate model can interpret the earlier mentioned contradictory results accurately and shed light on the reported results about cell stiffness and their migratory and invasive potentials.

8.2. Mechanical Modeling of Migratory Energy for Cancer Cells

8.2.1. Cell Modeling and Force Generation

Cells have a heterogeneous complex material, and each region of cells has different mechanical properties and stiffness. Generally, eukaryotic cells have a nucleus placed at the center of the cytoplasm. The cytoplasm includes all material between the nucleus membrane and the edge of cells enclosed by cell membrane. In our modeling, for simplicity, the biological factors that vary

during migration and invasion are not considered, and cells are considered as pure elastic mechanical body with a bulk stiffness[56]. Although the bulk stiffness of cells might change during the migration, the initial bulk stiffness was assumed to be constant to approximate the migratory potential of cells. Furthermore, to approximate the migratory ability of cells, we assumed that the contractile force and the bulk stiffness of cells are independent. In this study, as shown in **Figure 8-3**, the body of cancer cells is discretized into two zones; the nucleus with bulk stiffness of K_1 and the cytoplasm with bulk stiffness of K_2. The nucleus of cells are 4~10 times stiffer compared to the cytoplasm[315], [375], [376]. The shape and dimensions of cells in this study were assumed to be as similar to human breast cancer cells described in [315]. The microenvironment of cancer cells is modeled with a substrate (with specific elasticity), and cancer cells are linked to their microenvironment (substrate) with adhesion complexes (**Figure 8-3c**). For migration, cells need to generate a force to deform cells and transmit that force to the cell-substrate interface to overcome moving-resistance forces and make cells to move forward. These two actions are dependent on the rigidity of cells in different regions. The internal force for the movement of cells is generated by polymerization of actin-filament and molecular interactions between F-actin and non-muscle myosin II at the rear-back of the cells [377] (**Figure 8-3b**). The generation of the internal force occurs by converting chemical energy to mechanical work. In our simulation, a force at the rear-back of cells was considered as the contractile force to quantify cell deformation and stress transmission within cells bodies (**Figure 8-3a**).

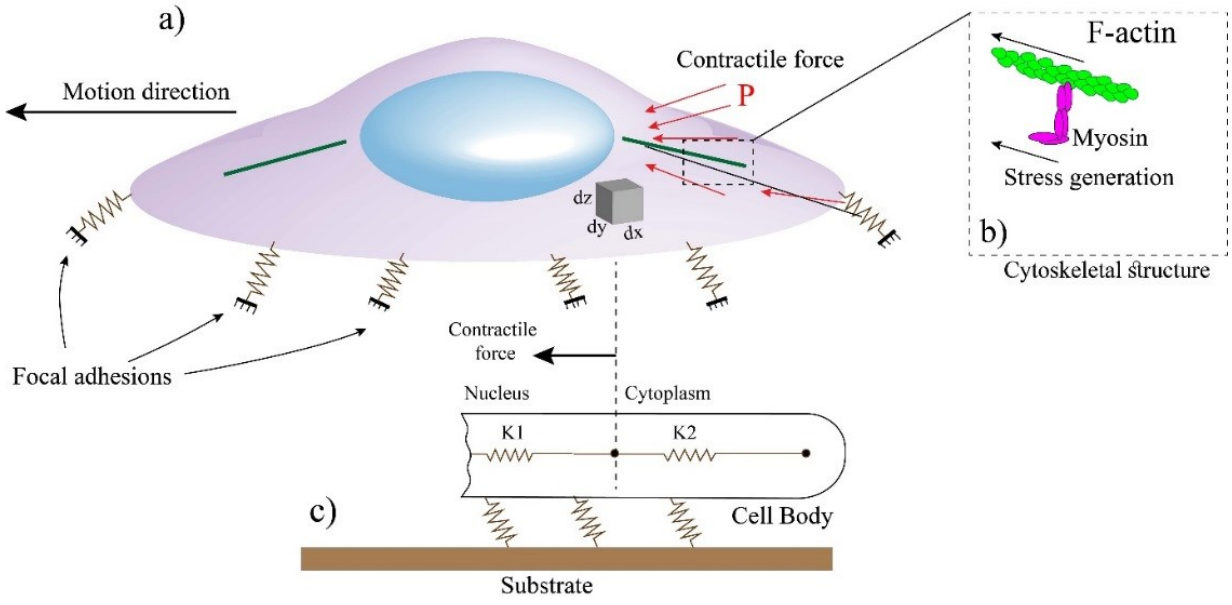

Figure 8-3. *A schematic of a single cell showing how contractile force* ***(a)*** *is applied for migration in cells due to stresses generated in myosin network* ***(b)****. The cell is attached to the substrate* ***(c)****, and different regions of cells have different elasticities which can be simulated with a spring with a specific stiffness.*

8.2.2. Strain Energy for Cancer Cells

As already mentioned, the two parameters, namely deformation and transmitted force, play pivotal roles in the movement of cells[377][378]. Displacement field can be calculated in different regions of cells by considering the deformation throughout the cells, and the propagated force in each region can be quantified by computing the stress in different regions of cells. Displacement field or stress field alone cannot predict the migration ability of cells as for migration, the contribution of each needs to be taken into account. For softer material, under a constant contractile force and at the specific time, more deformations take place in cells while at the same time, the force cannot be transmitted fast within cells. However, in stiffer cells, under a specific rate of stress, the body of cells undergo less deformation, whereas the generated force is transmitted faster to the substrate to overcome moving-resistance forces. In order to capture both phenomena, namely deformation and force transmission, strain energy formulation is used. This energy is the potential energy stored in cells, and for migration, it is transferred to the microenvironment to distort it and help the cell move forward. The strain energy can be calculated by the strain field (ε) and stress field (σ). To find the total strain energy (U), we need to measure the summation of strain energy over the entire cell [379]. Here we simplify the energy formulation for 2D as follows; however, it can be extended for 3D formulation.

$$U = \frac{1}{2}\iint \sigma(x.y).\varepsilon(x,y)dxdy \qquad 8\text{-}2$$

Where $\sigma(x.y)$ is the stress field in x and y directions and $\varepsilon(x.y)$ is the strain field in x and y directions. Here, we define the migratory index to approximate the migration ability of cells. This term represents the energy stored at those adhesion complexes, which link cells to the microenvironment when contractile forces are generated in cells. During the cell movement, this energy is directly transferred to the surrounding microenvironment to distort it. In order to study the migratory index of non-invasive and invasive cells, we assumed that all parameters of cells are identical except the bulk stiffness of cells (K_1=10K_2, **Figure 8-3c**). The role of stiffness alone was studied in migration by assessing their migratory index. It should be mentioned that living cells

have complex rheological properties due to their complex cross-linked networks and cannot purely be translated in the cell mechanic. However, assuming cells as a pure mechanic system was proven to be sufficient to understand the global behavior of cells [380].

8.2.3. Strain Energy for Hyperelastic Material

In our simulation, cells (both nucleus and cytoplasm) were assumed as homogeneous and isotropic material. The hyperelastic model can be used to describe the constitutive behavior of cells[56][380][317]. For isotropic Neo-Hookean hyperplastic materials, the strain energy density (U) can be expressed by the following equation, and the first variation of this strain energy gives Piola stress[380][317].

$$U = \frac{\mu_o}{2}\left(\overline{\lambda_1} + \overline{\lambda_2} + \overline{\lambda_3} - 3\right) + \frac{k_o}{2}(\lambda_1\,\lambda_2\lambda_3 - 1)^2 \qquad 8\text{-}3$$

where λ_i are principal stretches, $\overline{\lambda_i}$ are deviatoric principal stretches and k_o and μ_o are initial bulk and shear moduli, respectively. The initial shear and bulk moduli can be determined by standard linear elastic equations:

$$\mu_o = \frac{E}{1+v} \qquad 8\text{-}4$$

$$k_o = \frac{E}{3(1-2v)} \qquad 8\text{-}5$$

Where E is the elastic modulus and v is Poisson ratio. The cell was assumed to be incompressible material with Poisson's ratio of 0.49 [381], and stress field, and displacement field were calculated by varying the bulk elasticity of the cells. The deformation of cells and stress in cells can be characterized by the equivalent elastic strain (ε^*) and Von Mises stress (σ^*) respectively [315]:

$$\varepsilon^* = \frac{1}{\sqrt{2}(1+v)}\left[\left(\varepsilon_{xx} - \varepsilon_{yy}\right)^2 + (\varepsilon_{xx} - \varepsilon_{zz})^2 + \left(\varepsilon_{yy} - \varepsilon_{zz}\right)^2\right]^{0.5} \qquad 8\text{-}6$$

$$\sigma^* = \frac{1}{\sqrt{2}}\left[\left(\sigma_{xx} - \sigma_{yy}\right)^2 + (\sigma_{xx} - \sigma_{zz})^2 + \left(\sigma_{yy} - \sigma_{zz}\right)^2\right]^{0.5} \qquad 8\text{-}7$$

Where v is the Poisson ratio, ε_{ii} are principle strains in different directions, and σ_{ii} are principle stresses in different directions. In our simulation, the averages of ε^* and σ^* were computed for

different bulk Young's Modulus of cells by averaging ε^* and σ^* over the entire cells respectively ($\overline{\varepsilon^*}$ and $\overline{\sigma^*}$).

8.2.4. Numerical Simulation

In order to calculate the migratory index for different stiffness values, we developed a 2D finite element model to solve the governing equations (stress field and displacement field). The mechanical module at COMSOL Multiphysics was used to model cells, generate mesh over the entire cell, and compute the stored energy by considering the hyperelastic formulation and using above-described physical and material properties. A fully coupled solution method was used to carry out all the simulations and solve the system of equations when the internal contractile forces are applied.

8.2.5. Boundary Conditions and Mesh Model

In order to characterize the cellular deformations and force distributions in cells under contractile forces, cells were considered to be fixed on a substrate (the stiffness of the substrate, representing a real microenvironment, and can be changed) as shown in **Figure 8-3a**. Zero displacements were set at the bottom of the substrate, and free condition was assumed for the top surface of cells. Based on the available data in the literature, to simulate the contractile force, a constant pressure toward the center of cells in the range of 1~100 Pa [382][383] was applied at the periphery of cells (**Figure 8-4a**). For covering both normal and cancer cells, the average or bulk Young's Modulus of cells was assumed to vary between 20 to 1000 Pa, and the density of cytoplasm and nucleus were assumed to be 1050 kg/m^3 and 1300 kg/m^3 respectively[338]. The average length of cells and the height of cells were set to be 14 μm and 3.5 μm. The nucleus for simplicity is assumed to be in ellipsoid shape with length of the major axis 6 μm and half of the minor axis 2 μm.

A free triangular mesh was used to generate mesh over the cells (**Figure 8-4b**). A 2D mesh independency study was performed to choose an efficient mesh type for our simulations. Different mesh sizes were generated (**Figure 8-4d**), and the σ^*on the top surface of the cell for a short distance was computed and plotted in **Figure 8-4c** to compare their differences. By decreasing the size element and increasing the freedom degree, the differences between results were calculated to reach negligible differences for two successive results. As can be seen in **Figure 8-4c**, the

differences between “extra fine” and “extremely fine” mesh types are very small, so “extra fine” was chosen for an efficient computation run and the following simulation.

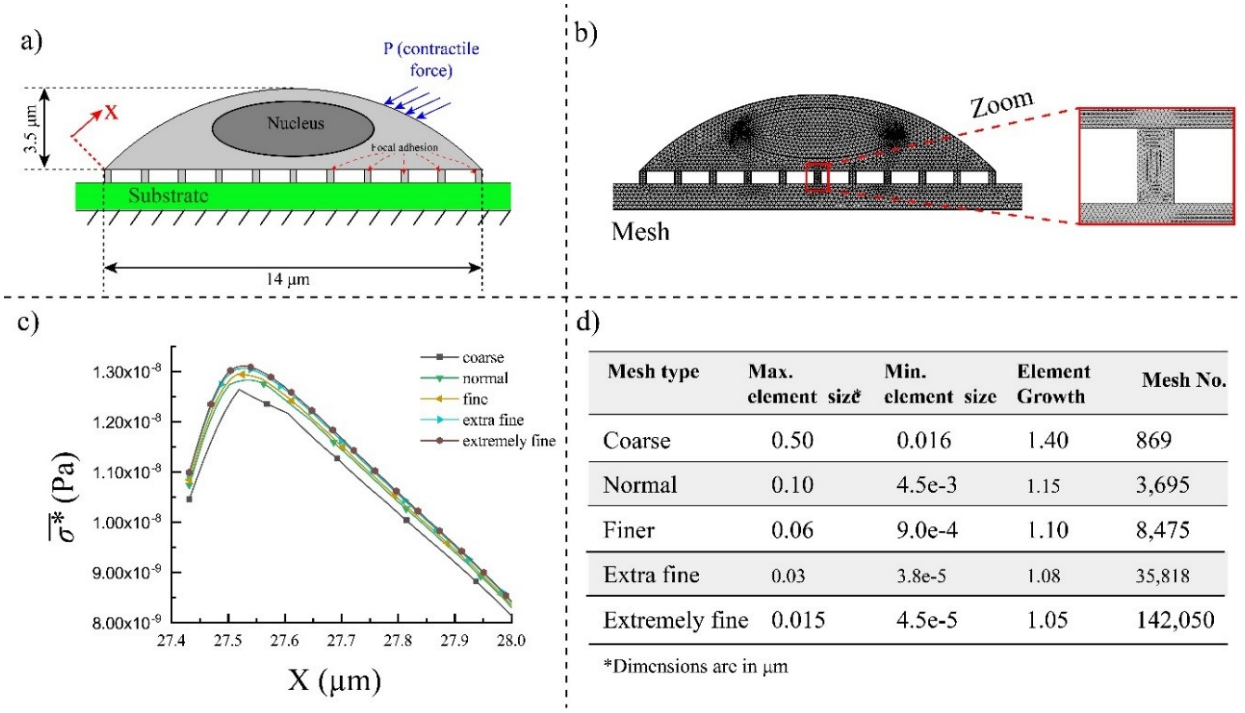

Mesh type	Max. element size	Min. element size	Element Growth	Mesh No.
Coarse	0.50	0.016	1.40	869
Normal	0.10	4.5e-3	1.15	3,695
Finer	0.06	9.0e-4	1.10	8,475
Extra fine	0.03	3.8e-5	1.08	35,818
Extremely fine	0.015	4.5e-5	1.05	142,050

*Dimensions are in µm

Figure 8-4. a) *Cell modeling in COMSOL, showing where forces are applied,* ***b)*** *mesh elements distributions for the computational study,* ***c)*** *mesh dependency study by measuring σ^* on top of cells for different mesh types,* ***d)*** *different parameters used for different mesh types*

8.3. Results and Discussion

8.3.1. Cellular Deformation and Stress

COMSOL Multiphysics ® was used to solve the governing equation and quantify the deformation of the whole cells when a constant contractile force is applied at the periphery of cells (rear-middle) [368]. Stress values generated in actin filaments originate from the activity of the molecular motors, myosin II, which are connected to the actin filaments[377][383]. In the following simulations, the physical properties of human breast cancer cells available in the literature were used to numerically calculate the stress within cells and characterize their deformations[315]. Cells with smaller stiffness cannot resist the applied force, so the applied force is reflected in a higher level of deformation. Stiffer cells can propagate the mechanical signal better compared to relatively softer cells, and softer cells can display more deformation compared to the relatively stiffer cells.

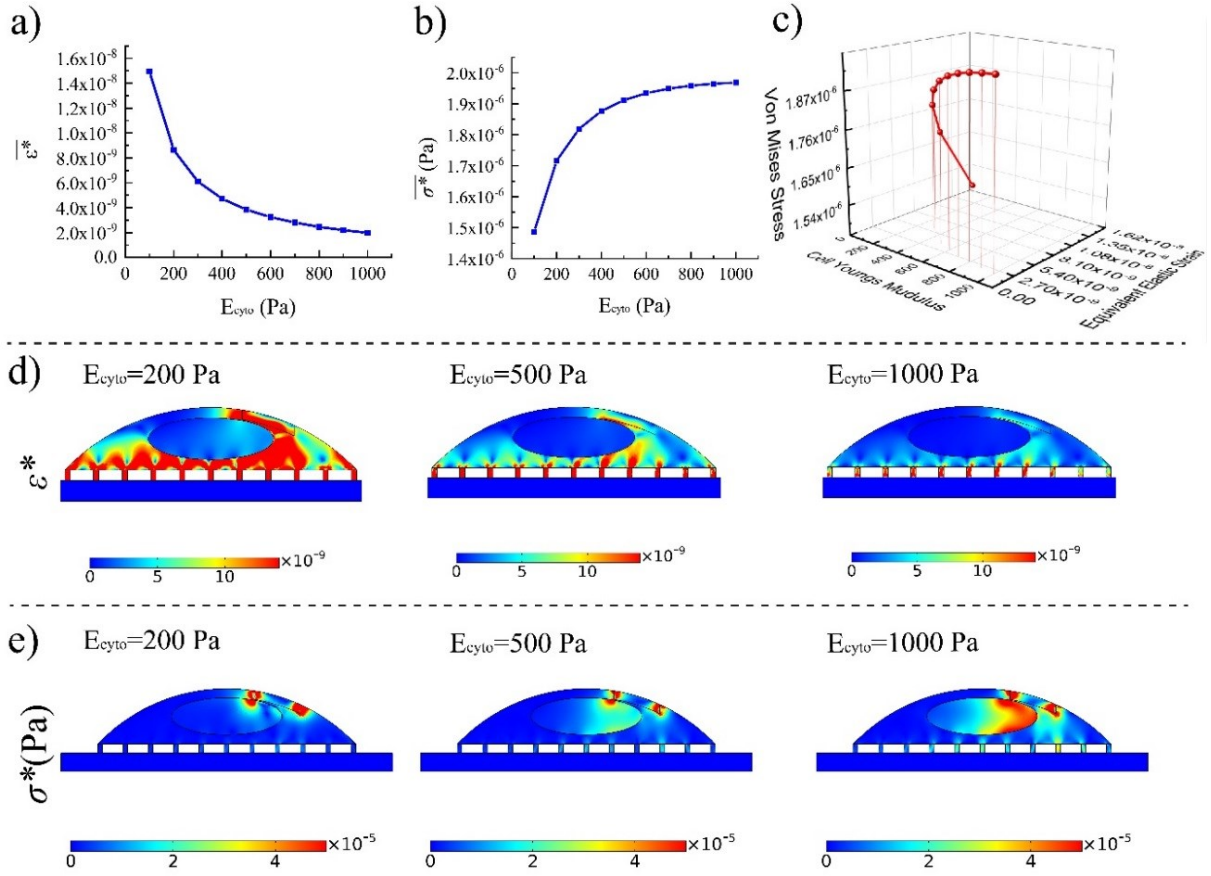

Figure 8-5. *Deformation (ε*) and stress (σ*) distribution in cells due to the generated force at actin filaments for different bulk Young's Modulus (E_{cyto}: 100 to 1000 Pa).* ***a)*** *Deformation at the cell-substrate interface is decreased by increasing the stiffness of cells,* ***b)*** *Stress-induced at the cell-substrate due to the contractile force for different E_{cyto},* ***c)*** *A 3D plot showing the correlation between ε*and σ* for different E_{cyto},* ***d)*** *ε* contours by increasing the cell stiffness,* ***e)*** *σ* contours with increasing the stiffness of cell (we assumed the substrate is rigid)*

The variations of cellular deformation (ε^*) and stress (σ^*) within cell under the contractile forces (for a short time) can be seen in **Figure 8-5a** and **b** when the bulk elasticity of cytoplasm (E_{cyto}) is varied between 100 and 1000 Pa (the bulk elasticity of the nucleus is 10 times of the cytoplasm's). At a low E_{cyto}, cells undergo a considerable deformation while at a high E_{cyto}, cells feel higher stress at their bodies. These different responses are evident in the 3D graph presented in **Figure 8-5c** where cellular ε^* and σ^* are compared to each other with respect to E_{cyto}**. Figure 8-5d** compares the deformation of the same single cell for three different E_{cyto} (200, 500, and 1000 Pa) once a contractile force is applied in a short time. As can be seen in the surface contour, for very soft cells, a wider surface area of cells undergoes deformation. For relatively stiffer cells, only regions very close to the location of the force are deformed, while at the central region, the nucleus undergoes

less deformation. **Figure 8-5e** shows the σ^* distributions and their values for three different Young's Modulus. In contrary to ε^*, with increasing the cell elasticity, higher values of stress are distributed within cells in the distance from the place of the applied force. Force transmission in cells is determined by the architecture and mechanics of the F-actin networks. These two parameters can be reflected in the bulk stiffness of cells. Therefore, the force transmission level can be estimated by cell bulk stiffness whose level is influenced by type and quantity of crosslinking proteins. For efficient migration, cells need to transmit the generated force efficiently to the cell-substrate interface at a shorter time. As can be noticed in **Figure 8-5e**, for stiffer cells (E_{cyto}=1000 Pa) at the same time, the nucleus feels higher values of stress in the left side from the contractile forces generated in the back-middle of cells. The average deformation and the average transmitted stress were quantified separately over cytoplasm and cell nucleus and plotted in **Figure 8-6a** and **b**. The nucleus of cells is stiffer compared to other regions of cells, so they undergo less deformation (one order less) compared to the cytoplasm, and its deformation is reduced by increasing the rigidity of the cells (**Figure 8-6a**). The average transmitted stress over the cytoplasm also is higher compared to the nucleus; however, its trend is ascending, unlike deformation.

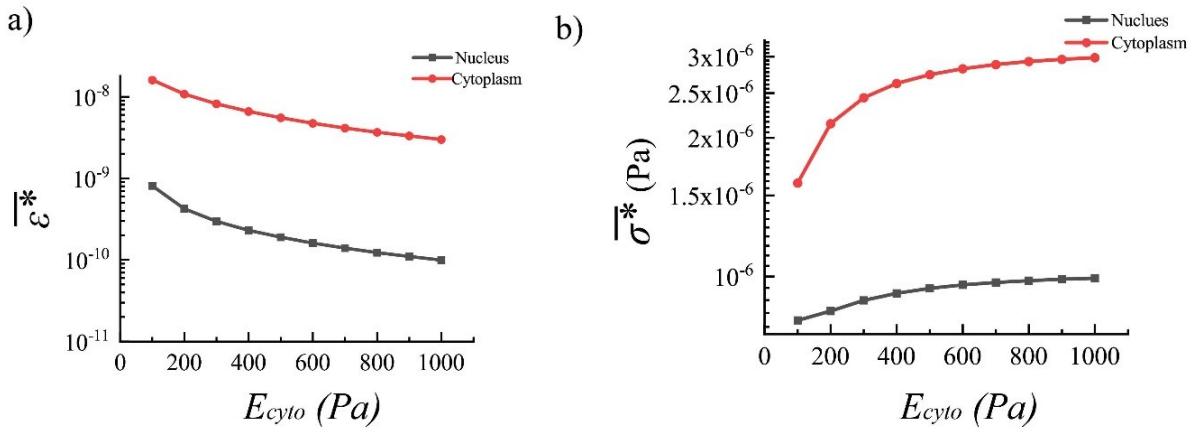

Figure 8-6. a) *Average equivalent elastic strain ($\overline{\varepsilon^*}$) for cytoplasm and nucleus when a contractile force is applied,* ***b)*** *average stress ($\overline{\sigma^*}$) in the cytoplasm and the nucleus when a contractile force is generated. Contractile pressure: 6 Pa, E_{nuc}(elasticity of nucleus)=10 E_{cyto})*

8.3.2. Migratory Index (μ)

Neither very stiff nor very soft cells can provide conditions for fast migration, which occurs in the cancer progression. A higher level of deformability disrupts the mechanical signaling within

cells, and a higher level of rigidity impede the cell deformation and, consequently, its movement. It should be a balance between the transmitted stress and deformation in cells to enable them to migrate fast, and any unbalance between these two parameters can suppress the progress of cancer. Therefore, we need to take into account the contributions of both cellular deformation and the cellular stress in our model at the same time to approximate the capacity of cancer cells for migration. It is necessary to define a unique parameter that covers the contributions of both phenomena. As earlier discussed, with the aid of migratory energy, we can uniquely characterize the migratory capacity of cancer cells. This term captures both phenomena and shows the potential ability of cells to do work for the movement. Focal adhesions connect cells to their microenvironment. These thin structures have a critical role in migration and clinically are approved to drive cancer cell metastasis[384]. So, the stored energy or migratory energy can be specifically computed at focal adhesions, migratory index (μ), to approximate the migratory capacity of cancer cells.

$$\mu = \frac{\iint \varepsilon . \sigma \, dA_{adhesion\ complexes}}{2A_{adhesion\ complexes}} \qquad 8\text{-}8$$

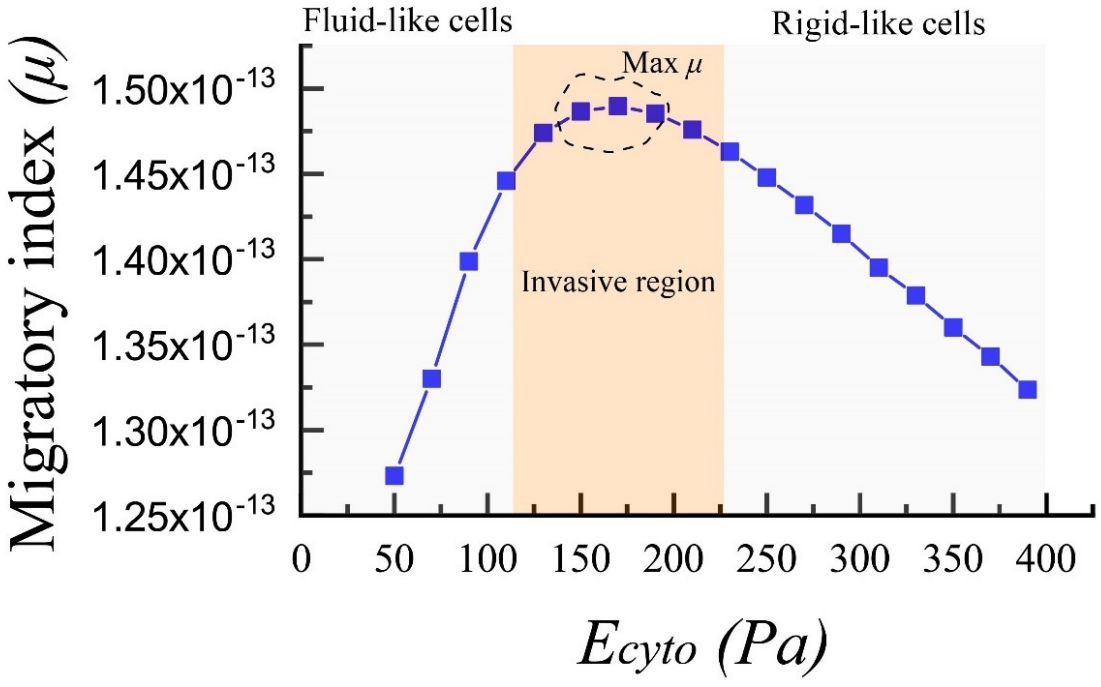

Figure 8-7*. Migratory index quantification of a cell concerning its different bulk Young's Modulus when it adheres to a rigid substrate and a contractile force is applied (Substrate is completely rigid, contractile pressure 6 Pa, effective time: 0.001)*

Where μ is the migratory index or stored energy density, ε and σ are strain and stress in the focal adhesions when a contractile force is applied for a short time. Once a force is produced in cells, under a stationary condition, when time goes to infinity, regardless of the cell stiffness, the effects of the applied forces will be all transferred to the cell-substrate interface. Hence, with the stationary study, we cannot comprehend the mechanical signaling capacity of the cell. The ability of cells for mechanical signaling needs to be examined by quantifying the transmitted forces for a limited time. So, the mechanical stress values at the cell-substrate interface (adhesion complexes) need to be quantified by applying contractile forces for a short time. Depending on the stiffness of cells, forces are transmitted fast or slow.

Figure 8-7 shows a typical migratory index responses, energy stored in the focal adhesions, of the same cell when a contractile force is applied for 1 ms. It is very interesting to observe an optimum range for the cell migratory index when E_{cyto} is varying between 150-200 Pa. The peak shows that depending on the physical properties of cells, there is an optimum range of stiffness at which the cell has a maximum potential to migrate on a rigid substrate. It is believed that the optimum range is a critical region as it provides cancer cells with mechanically favorable conditions to enhance their migratory abilities required for cancer progression. By increasing or decreasing the stiffness, as shown in **Figure 8-7**, the migratory index of cells or the maximum potential of cells for migration is reduced, indicating that a mismatch occurs between the deformation and the transmitted force. Fluid-like cells with lower stiffness are soft with low capacity to transmit force or deform its environment, while rigid-like cells with high stiffness can deform the environment while undergoing less deformation. Hence, cells with either very low or very high stiffness have low capacity to strain the environment, leading to the low migratory index. Therefore, for a very low and very high stiffness, the migratory capacity of cells is low. Cells for fast migration need to have a higher migratory index. At a specific stiffness/range (maximum migratory index), not only contractile forces sufficiently deform the cells, but also they are transmitted well to the adhesion complexes wherein cells are linked to the substrate. We believe that in cancer, the cytoskeletal organization of cells is changed in a way that the bulk elasticity of cells is fallen in the critical range at which the migratory index is very high. Based on this approximate model, cells with a higher migratory index could migrate faster under a constant contractile force. It is thought that cancer cells know how to modulate their stiffness to a critical value (stiffness) in which cell mobility is maximum. Estimating this critical stiffness is necessary

to understand the behavior of cancer cells and develop anti-cancer drugs to potentially control the migration of cancer cells, which is essential for cancer progression.

As can be noticed in **Figure 8-7**, this peak is almost broad, showing a range for maximum migratory index. The stiffness of normal cells and non-invasive cancer cells should be placed somewhere outside of the critical range. This behavior can correctly interpret the contradictory response of cells discussed in the introduction. Many normal and non-invasive cells have been proven to be stiffer compared to their cancerous counterparts and based on the migratory index model, their stiffness should be on the right side of the peak where the migratory index is smaller. However, the migratory index suggests that normal and non-invasive cells with normal migration even could have smaller stiffness compared to malignant cells (on the left side of the critical range), which are in agreement with a few reported studies[354], [355], [368]. The critical stiffness can be influenced by any parameters affecting the cell mechanics such as cell size, cell configuration, and external parameters such as substrate stiffness.

8.3.3. Effects of Substrate Elasticity on the Migratory Index

Cells can sense their extracellular matrix, and any change in their microenvironment might affect their ability for migration. Substrate elasticity has shown to be an important factor for the migration and invasiveness of cancer cells. Some investigations have proved that the capability of cells for migration is boosted by increasing the substrate rigidity[385]. It has also been substantiated that cells tend to migrate directionally toward places with stiffer substrates (Durotaxis)[385]. In order to examine the effects of substrate elasticity computationally, the deformations at focal adhesion and transmitted forces within cells were quantified by varying the stiffness of the substrate. **Figure 8-8a** indicates the average ε^* when cells are placed on various substrates with different elasticities. As can be seen in the results, cells under a constant contractile force undergo more deformation at their adhesion complexes when the stiffness of the substrate is decreased. However, their differences in $\overline{\varepsilon^*}$ are only prominent at very low substrate stiffness, and for substrate elasticity higher than 5 kPa, their differences in $\overline{\varepsilon^*}$ are almost insignificant. For the transmitted stress (σ^*), the trend is completely in reverse, by increasing the substrate stiffness, cells at their interface with the substrate sense a higher level of stress. This behavior can be seen in **Figure 8-8b**. A stiff substrate resists to the local deformation induced by the transmitting force from the internal contractile force, and this resistance is reflected in the form of higher stress at the

cell-substrate interface. For a soft substrate, forces internally generated in cells provide more deformations at the substrate and consequently cause less stress at the cell-substrate interface. As already discussed, both deformation and stress at cell-substrate contribute to cell migration and the migratory index. So, any change in either deformation or stress responses of cells (due to the different cell substrate) influences the migratory index, its critical range, as well as the balance between deformation and the stress for optimum migration.

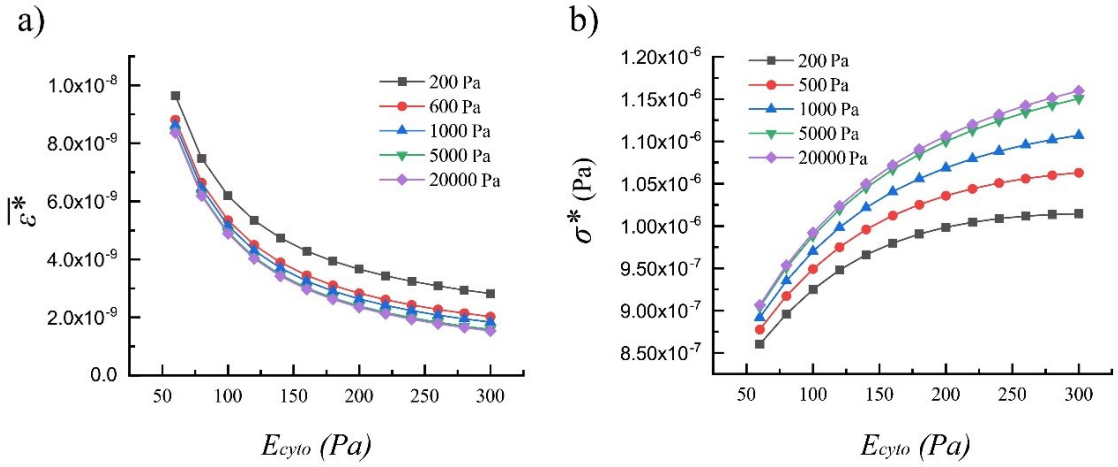

Figure 8-8. a) *Average elastic strain of cell focal adhesions versus cells' Young's Modulus by increasing the elasticity of substrate (between 200 to 20000Pa),* ***b)*** *Average stress taking place due to a constant contractile force versus cells' Young's Modulus by increasing the substrate elasticity (contractile pressure: 6 Pa, time:0.001, substrate elastic modulus in Pa)*

In order to see the effect of the substrate stiffness on the maximum migratory index, we measured the migratory index by changing the substrate stiffness between 0.02 – 20 kPa [386], and plotted the results in **Figure 8-9a**. It clearly shows that the migratory index is increased by increasing the substrate stiffness, and for the current cell model, its effects on the migratory index are saturated by increasing substrate elasticity above 5 kPa. So, a stiffer substrate could enhance the mobility potential of cells, and they could migrate faster. During the solid tumor progression, the extracellular matrix becomes rigid due to increasing the collagen deposition and cross-linking in the tumor stroma [387] and provides a favorable condition for cancer progression by giving them a higher mobility potential. Interestingly, it can be observed that the migratory index peak is shifted to the right by stiffening the substrate, suggesting that the migration of cancer cells can be regulated by altering the mechanical properties of the extracellular matrix as well. These results indicate that on a stiffer substrate, the critical migratory index takes place at a higher stiffness of cells. In fact,

for each substrate stiffness, there is a different critical migratory index. As shown in **Figure 8-9a**, for substrate rigidity higher than 5 kPa, no significant change is noticeable in the migratory index. It seems healthy and non-invasive cells depending on their substrate (microenvironment) stiffness can control their migration by changing their stiffness, and during cancer, cells try to regulate their stiffness to a value at which the migratory index is maximum.

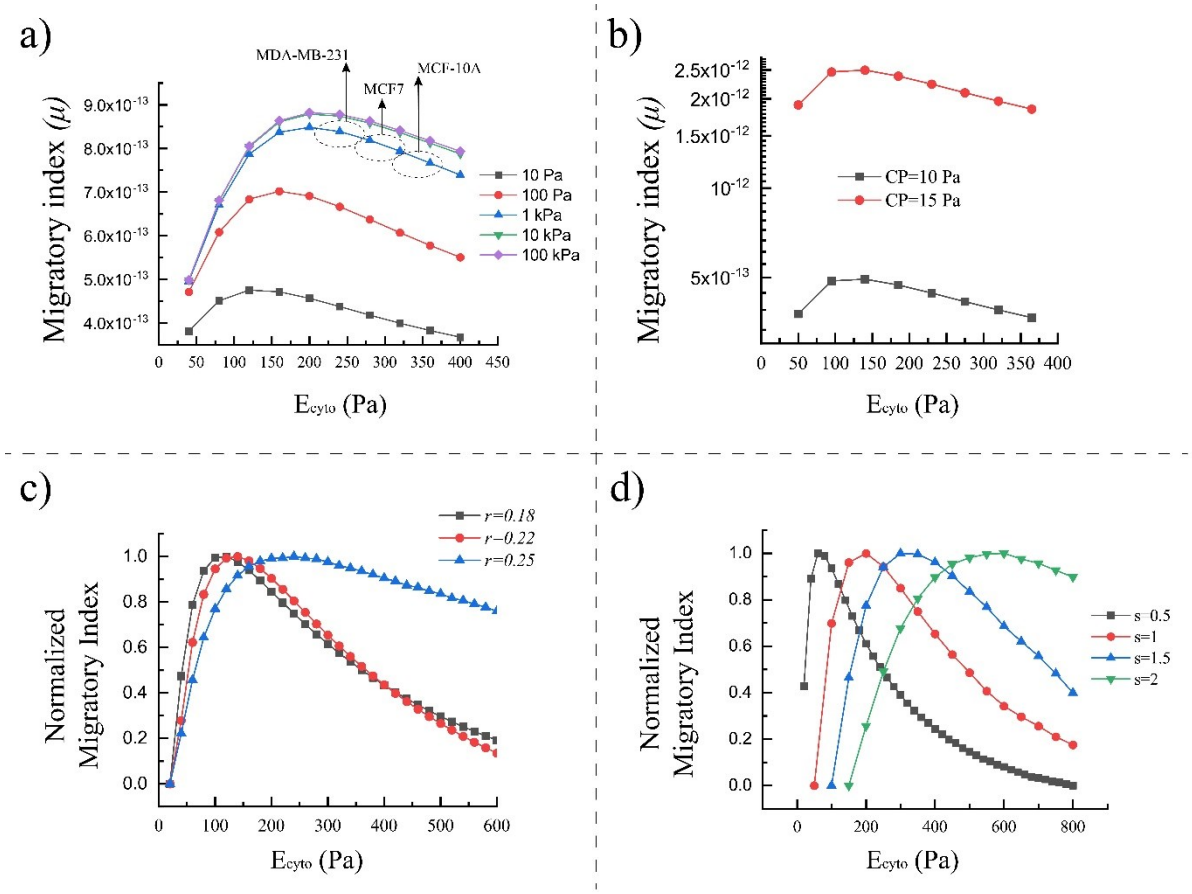

***Figure 8-9**. **a)** the effects of substrate elasticity on the migratory index changes versus cell bulk Young's Modulus, **b)** migratory index versus cell elasticity increased with the contractile force (CP: contractile force), **c)** Normalized migratory index showing the effects of aspect ratio on the migratory index peak (r=height/diameter), **d)** effects of cells size on the migratory index (s: scale, for s=1: diameter=14 μm, height=3.5 μm)*

We used the physical parameters of human breast cancer in the current simulations. Here we can approximate and compare the migratory capability of human breast cancer with different malignancy levels, MCF10A (benign and non-invasive cells), MCF7 (invasive cancer cells), and MDA-MB-231 (highly invasive cells) by knowing their *in vitro* elasticities[388]. Based on our model (in the case of a stiff substrate), the critical condition for a higher migratory capability is

approximated to occur for cells with elasticity of 200-240 Pa (**Figure 8-9a)** which is in good agreement with elasticity of the highly invasive human breast cancer cells (277.3 Pa) previously reported by *Corbin et al.* [388] by AFM measurements. Based on the same study, the average elasticity of the non-invasive human breast cancer cells (MCF-10A) is ~341 Pa, which is far from the critical range while reaches down to 277.3 Pa for MDA-MB-231[388]. The same study showed that the elasticity of invasive cells (MCF7) is somewhere between two other cells line, but very close to the highly invasive cell lines (285.1 Pa). Based on the migratory model, the migratory potential of highly invasive cells (MDA-MB-231) is in critical range and higher compared to invasive and non-invasive cells. As discussed earlier, invasive cells are assumed to be highly migratory and vice versa[119], [357], [363]–[367], suggesting that our model can be also useful to predict the invasiveness of cells based on their bulk stiffness.

8.3.4. Effects of Physical Parameters on the Migratory Index

Furthermore, the effects of other parameters also were studied on the migratory index. Internal contractile force directly affects the migratory index level; however, it does not affect the migratory critical position (**Figure 8-9b**). With a higher contractile force, more energy could be stored in cells for migration. The migratory index might be influenced by geometrical factors such as shape, size, and aspect ratio. **Figure 8-9c** displays the normalized migratory index and its critical range by changing the cells aspect ratio (height/ diameter). With increasing the cell height, the position of the critical range is shifted to the right, suggesting that for rounder cells, the critical migratory index takes place at a higher cell stiffness compared to the flat cells. The same behavior can be seen in the migratory index of larger cells (**Figure 8-9d**). The size of cells was increased with the same aspect ratio, and their migratory index values were plotted. The migratory index critical range is shifted to the right by increasing the size of cells, showing that for larger cells, the critical migratory index occurs at a higher stiffness.

8.4. Migratory Index of Normal Cells and Cancer Cells

The ability to predict the migration behavior of cells is necessary to study cancer invasiveness and control cancer progression. Earlier it was discussed and shown that cells depending on their physical characteristics and mechanical properties of their environment, exhibit a critical stiffness range for cell movement. This approximate model is based on the fact that cells for migration need to have enough deformation and generate sufficient traction forces to overcome

adhesion forces between cells and their extracellular environment[389]. The main driving-forces are generated in actomyosin networks and are distributed within cells to drag the body of cells forward[377]. The spatiotemporal force distribution within cells is dependent on the cytoskeletal structures and their mechanical properties such as stiffness. Cells have a complex network of subcellular filaments that allow individual cells to impose mechanical forces to their microenvironment and sustain external forces[378]. These structures of cells and mechanical properties of individual filaments provide a bulk stiffness for each cell.

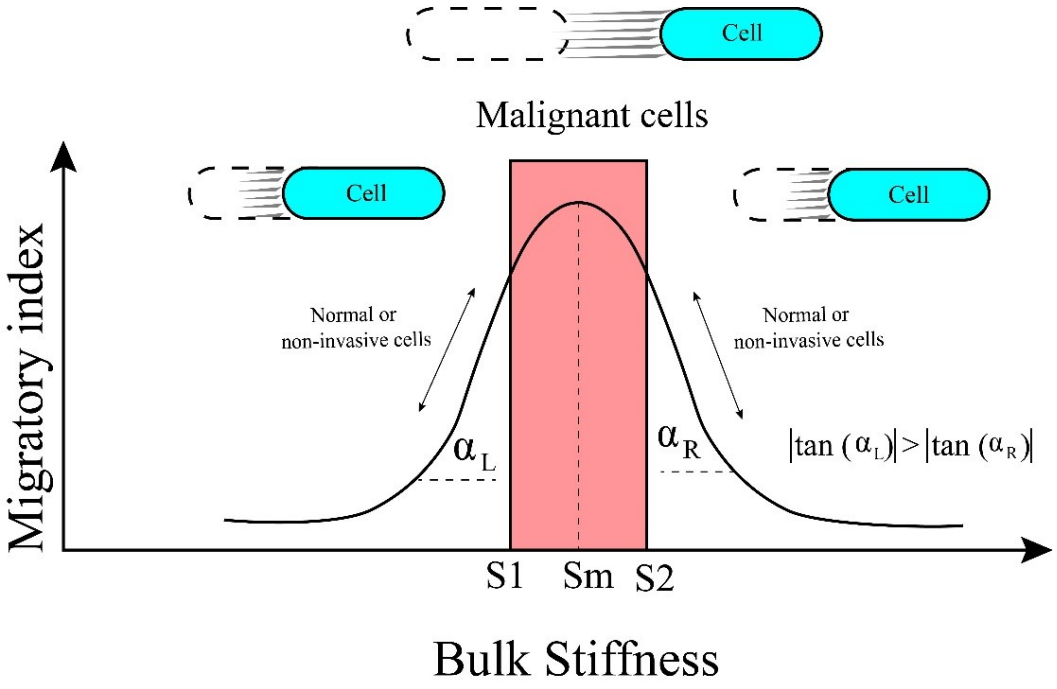

***Figure 8-10**. A typical migratory index responses of cells and their changes by altering cell stiffness. At the critical value/range (red region) the migratory index is maximum, and cells could move fast, outside of the critical range, cell movement is reduced either by reducing cells stiffness or enhancing the stiffness of the cell*

It is believed that in the context of cell mechanics, the migration ability of cells can be approximated by the migratory index, which is dependent on the bulk stiffness of cells. It was showed that for each cell, there is a critical stiffness value/range at which the mobility ability is predicted to be high. This high value is dependent on the size and shape of cells as well. In this range, as shown in the schematic (**Figure 8-10**), under a constant internal force, not only the contractile force is effectively transmitted through cytoskeletal networks, but also cells have enough deformation, allowing cells to spread fast. Migration plays a central role in cancer progression and metastasis[357], [363]–[366], and based on the migratory index, it is thought that

cancerous and invasive cells tend to possess a bulk stiffness in the critical range (between S1 and S2) at which they have the maximum migratory potential. This critical range is essential to interpret the behavior of cells based on their cell mechanics; however, further detailed computational and experimental studies are required to determine the extent of the critical migratory index (S1 and S2).

Many healthy cells (or non-invasive cells) were experimentally proved to have stiffer bodies compared to their counterparts'. Based on our approximate model, they are thought to be at the right side of the critical range with a low migratory index, as shown in **Figure 8-10**. Cells have dynamic structures that can be softened or stiffened in response to external cues [56]. This nature of cells enables them to control their migration by changing mechanical properties. Based on our approximate model, as can be seen in **Figure 8-10**, the migration ability of cells (migratory index) can be regulated by a small variation in bulk stiffness of normal cells. It is thought that normal and non-invasive cells based on their permanent local microenvironment tend to have a stable and tuneable migratory index, which is far enough from the critical range. By a small change in their stiffness once is necessary, they can either reduce their migration ability or accelerate their migration ability. Based on the migratory model, normal cells (or non-invasive cells) can even have smaller elasticity versus invasive cells (left side of the critical region), and for a fast migration, cells need to become stiff to have a higher migratory index. As discussed in the introduction, few cancerous and invasive cells were proved to be stiffer compared to healthy and non-invasive cells[354], [355], [368]. The migratory model suggests that all invasive cancer cells are not necessarily soft compared to non-invasive cells.

8.5. Non-invasive Cells Have Tuneable Migratory Index

Moreover, as was observed in **Figure 8-7** (based on the approximate model), the pace of changes in the migratory index at the right side of the critical range is slower (smaller slope) compared to the left side, providing the normal and non-invasive cells with more control on their migrations. However, the rate of the migratory index at the left side of the critical range is higher (higher slope), which reduces the control resolution on the migratory index. These behavioral changes of the migratory index can interestingly express the reason why many normal cells are stiffer compared to cancer cells and tend to be on the right side. In contrast to the normal cells (or non-invasive cells), in invasive or metastatic cells, the bulk stiffness is reduced until reaching the

critical range (the broad peak point), and at that point, any small variation in the bulk stiffness will not affect the movement capacity of cells significantly. Therefore, it is predicted that cancer cells with critical stiffness have less control over their movement abilities, and they lose their ability to adjust their potentials for migrations. At the critical range, small variations in the bulk stiffness cannot be effective in controlling the mobility potential of cells.

8.6. Migratory Index Model for Developing Anti-Cancer Drugs

Based on the approximate model, the migratory potential of cells can be controlled through increasing or decreasing the bulk stiffness to a value beyond the critical range. Targeting the cytoskeletal structures and altering the mechanical properties of cells can be a useful strategy to manage cell migration required for cancer progression. This process can be occurred by designing anti-cancer drugs or nanoparticles-based drugs to disrupt the cytoskeletal organization of cells to reduce the stiffness of cells. Or, through enhancing cell stiffness by stimulating the overexpression of proteins which are responsible for cell mechanics. Both ways can be effective to suppress migratory levels of malignant cells by modulating the mechanobiological properties of cells[119][139]. Based on the migratory index model, measuring the elasticity of both treated and non-treated cells allows us to approximate the efficacy of anti-cancer drugs designed to control cancer migration. The migratory index model can be implemented to develop effective drugs to control cancer migration. By measuring the migratory index of cells when they are treated with anti-cancer drugs, we can monitor whether antic-cancer drugs are effective or not. Then, we can optimize the effectiveness of anti-cancer drugs by either increasing the cell elasticity from Sm to S2 or decreasing the elasticity from Sm to S1 to control cancer migration required for cancer progression. To inhibit the migratory ability of cancer cells, we need to design anti-cancer drugs with anti-elastic properties in order to reduce their migratory ability. In the context of cell mechanics, an anti-elastic drug will help us to alter the elasticity of cancer cells such that the migratory index is reduced. In the literature, some investigations have proved that anti-cancer drugs or nanoparticles can be used to control the cancer migration and invasiveness by either softening or stiffening their elasticities [27], [119], [139], [390].

8.7. Conclusions

In this study, we introduced our “migratory index” on the migration ability of cells based on their mechanical proprieties, particularly cell stiffness, to find out the approximate correlation

between cancer migration and their deformability levels. In our study, to approximate the mobility potential of cells, we assumed that the initial bulk stiffness of cells and the adhesion force remained constant during migration, and the internal force is independent from the bulk stiffness of cells. Cell migration is essential for cancer cells to be invasive, and it is thought that the migratory index could provide a platform to approximate the invasive level of cancer. The migratory index is defined based on the bulk stiffness of cells and stored strain energy in cells when internal contractile forces are generated. Our mechanical modeling and computational studies showed that non-invasive cells (or normal cells) should not necessarily be stiffer than invasive cells (or cancer cells). However, our results showed that rigid-like normal cells have more control over their movements compared to fluid-like normal cells. Based on the suggested model, stiffness of invasive cells provides them a critical migratory index that allows them to migrate fast and spread to other parts of the body. Based on the migratory index model, during the cancer progression (mesenchymal-like state), cells can become either soft or stiff, depending on their normal conditions in the migratory index profile. Our 2D model can also predict the contradictory responses of anti-cancer drugs targeting cell mechanics. From the mechanics point of view, the migratory levels of cells can be controlled by designing drugs to either stiffen or soften cells. However, the level of the required changes needs further detailed study. In this work, we developed a simplified 2D model to show the potential of this concept to predict the migratory potential of cells based on their bulk stiffness. However, in 2D model, we did not simulate all parameters existing *in vivo* environment such as other forces influencing cells. For future work, a 3D model can be developed to measure migratory index in a more realistic environment while other parameters are considered. The migratory index model provides valuable information to understand why the stiffness of cells is increased or decreased during cancer progression and helps to take different strategies to control migration of cancer cells potentially.

In this chapter, we learned how mechanobiological properties of cells and their changes affect the migratory ability of cells. In the next chapter, the same model is used to study how nanoparticles by changing the mechanobiology of cells can control the migration of cells.

Chapter 9
Modeling and Regulation of Migratory Capabilities of Human Lung Cancer Cells through Nano-Bio-Interaction

This chapter is based on the following submitted manuscript:

- **Ahmad Sohrabi Kashani**, Alisa Piekny and Muthukumaran Packirisamy, "Modelling and Regulation of Metastatic Capabilities of Human Lung Cancer Cells through Nano-Bio-Interaction ", Submitted to *RSC Nanoscale Advances*, March 2020

During cancer progression, the mechanobiological properties of cells are altered compared to healthy cells. They detach from the primary tumor and enter the circulatory system to invade other parts of the body. This process, metastasis, is the main reason for cancer-related mortality. Therefore, developing novel therapeutic strategies to control metastasis could be an effective cancer treatment. With advances in nanotechnology, nanomaterials such as gold may have valuable applications in suppressing cancer metastasis by regulating the mechanobiological properties of cells required for their migration. In the present study, we utilized two different unmodified gold nanoparticles with different morphologies to examine their potential to inhibit cancer cell migration. First, we employed a hyperspectral technique as well as SEM and wide-field fluorescence microscopy to determine the localization and distribution of nanospheres and nanostars in human lung cancer cells. Particles appeared to be distributed differently in cells depending on their morphology, with nanospheres being more uniformly distributed in cells compared to nanostars. A migration assay revealed that internalized gold nanoparticles suppress cell migration. In support of this, biomechanical measurements showed that gold particles lowers the stiffness of cells. This suggests that gold particles impacts the cytoskeletal organization required for migration. Furthermore, according to our modeling, it is thought that gold nanoparticles could inhibit the migratory capability of the human lung cancer cells by altering their elasticity to a value beyond the critical range at which cells lose their potential to migrate efficiently.

9.1. Introduction

Cancer is one of the main causes of death globally, and many methodologies have been developed to increase our understanding of cancer and its progression. During metastasis, which is responsible for more than 80% of cancer-related mortality, cells undergo a multi-step process,

enabling them to migrate from the primary tumor site and enter vascular systems to spread out into secondary sites[1][2]. Increasing evidence shows that during cancer progression, the stiffness of cells is changed, allowing them to facilitate their motility and invasiveness[391]. These changes in the mechanobiological properties of cancer cells stem from alterations in their cytoskeletal organization. Changes in the mechanobiological properties of cells during progression alter their interpretation of forces from the surrounding environment, which may help them to migrate more effectively [392][393]. Nanotechnology has provided a revolutionary platform for cancer therapy, diagnosis, and management [394]. In recent years, the applications of nanotechnology in medicine and drug delivery have increased rapidly. Nanotechnology has provided us with a great opportunity to design and develop nanoparticles (NPs) with favorable characteristics (physical, chemical and optical properties) for use as nanomedicines, to be able to move within biological systems and deliver biomedical entities to the site of diseased cells for diagnosis, treatment and prevention [149][395]. Nanomedicines have the potential to overcome limitations associated with conventional drug therapies.

The textbook model of cell migration describes how F-actin is organized and has different dynamics in the front vs. rear of the cell. For example, Arp2/3 mediates the assembly of branched F-actin at the front and is controlled by Rac and/or Cdc42 via WAVE/WASP to form lamellipodia or filopodia. These structures help cells navigate over the substrate. Behind this region of branched F-actin that highly turns over, is a region of more stable F-actin. In this area, cells associate with the underlying substrate via integrins to form focal adhesions. Further, toward the back of the cell, which has mature focal adhesions, large stress fibers are formed from long, unbranched F-actin and associate with active non-muscle myosin regulated by active RhoA via mDia1 and Rho kinase, respectively. This is where force is generated to displace the nucleus and propel the back of the cell forward[396][397][398]. Most cancers arise from the epithelial cell population, which tend to be highly proliferative. In healthy tissue, these cells have a cuboid-like shape are tethered to neighboring cells via adhesion complexes. These cells are highly polarized and static. However, as cancer progresses, these cells undergo epithelial-mesenchymal transition (EMT) where changes in their transcriptional program lead to the downregulation of cell-cell adhesion proteins and the upregulation of genes required for cell migration[399][400][401].

Several studies revealed the potential use of NPs to influence cancer cell migration. They hypothesized that by suppressing cancer cell migration, NPs could be used to block metastasis

[401][402][142]. After cellular uptake, NPs could escape from lysosomal and endosomal compartments where they have opportunities to interact with the cytoskeleton. One hypothesis is that they disturb cytoskeletal organization, or interfere with force generation and affect cell migration[403][126]. In a study by *Furong et al.*, it was shown that the morphology of human fibroblast cells is changed upon their interaction with single-wall carbon nanotubes. They observed that these nanomaterials directly interact with actin networks after entering cells [123]. Different parameters such as the physicochemical properties of NP (size, morphology, and surface chemistry), NP concentration, incubation time, and cell type can influence how NPs induce cytoskeletal changes. *Holt et al.* [107] demonstrated that silica nanorods (NRs) with a high aspect ratio could influence the organization of actin filaments in the vicinity of the membrane compared to silica nanospheres. In another study, *Yang and co-workers*[403] showed that the migration of prostate carcinoma cells (PC3) is reduced in the presence of gold NPs, while the migration of human dermal fibroblasts (HDF) depended on surface charges and shape of gold NPs. *Tarsiana et al.* [25] showed that cellular uptake of gold NPs might induce a disruption in the filamentous structures of HDF cells depending on size, incubation time, and concentration of gold NPs. *Zhou et al.* [142] investigated the impact of serum-coated gold nanorods (AuNRs) on the migration of three cancer cell lines. They showed that although the AuNRs caused no change in viability, cell migration was reduced. *Wen et al.* [112] used different biochemical techniques to study the interaction of silver NPs (AgNPs) with purified actin vs. tubulin. They observed that AgNPs bound to actin compared to tubulin, and both of them undergo conformational changes upon their interaction with these NPs. All the above-mentioned works focused on the cytoskeletal changes; however, still is not clearly known and understood how NPs-induced cytoskeletal changes and the following dynamic change inhibit the migratory capability of cells, and could potentially control cancer progression.

During migration, cells produce mechanical forces to move over their substrate but also need to detach from the substrate to propel forward. Cells also are subject to deformation during migration, as their leading edges are typically flat, while their nucleus provides ‘bulk’ and causes the middle-back of cells to be more round. Interactions between the resisting and driving forces, as well as deformation of cells are influenced by mechanobiological properties of cells[404][405]. As described above, the mechanobiological properties of cells are determined by actin and myosin, and altering these proteins changes the mechanobiological properties of cells[102][406].

Measuring the mechanobiological properties of cancer cells provides a label-free technique to evaluate how changes in these properties could influence their migration (and potentially their metastatic abilities). During metastasis, prior studies showed that the stiffness of cells changes as their migration speed increases [407]. Since NPs could interact directly with actin, they could induce changes in mechanobiological properties and migration [126]. Some prior studies showed that NPs increased the stiffness of cells. In 2010, *Buyukhatipoglue et al*. [135] showed that the actin cytoskeleton of endothelial cells changed upon interaction with iron oxide NPs, and observed a significant increase in their stiffness. In another study, *Ogneva et al.* [124] demonstrated that the stiffness of mesenchymal stem cells increased by 61% after incubation with silica NPs. *Ramesh et al.* [125] showed that the treatment of the human alveolar epithelial cells, mouse fibroblasts cells, and human bone marrow stromal cells with hybrid silver nanoparticles considerably changed their morphology, and cells had a higher average Young's Modulus (a term describing stiffness) in their cytoplasm regions. In a recent work, *El-Sayed et al.* showed that targeting NPs to the nucleus of Ovarian cancer cells could increase the stiffness and slow down the migration and invasion speed of cancer cells[139]. However, other studies contradict this and showed that the stiffness of cells decreased after incubation with nanoparticles. *Jiang Pi et al*.[111] observed that selenium NPs disrupted the cytoskeletal organization and significantly increased the softness of MCF-7. *Babhosseini et al*. [138] showed that internalization of poly lactic-co-glycolic acid (PLGA) NPs coated with an anti-cancer drug (sphingosine kinase inhibitor) caused a reduction in stiffness. In recent studies by *Qin et al*.[119], a reduction in the Young's modulus of malignant breast cancer cells was observed after incubation with small size fullerenol NPs. They also observed that upon the interaction of cells and NPs, cell migration decreased. Though many confirmed the mechanobiological changes due to the NPs internalization, it is not yet known how both increasing and decreasing the elasticity could regulate the migratory capability of cells.

In this research, we used two different morphologies of unmodified gold NPs (nanospheres, nanostars) to study their interaction with human lung cancer cells (A549) and determine their impact on cell mechanics. Scanning Electron Microscopy (SEM) and immunofluorescence imaging showed the location of NPs in cells. These images, together with hyperspectral images and spectral information of gold particles in cells revealed different distribution patterns of gold NPs in cells depending on their sizes and morphologies. Cell migration assays revealed that migration was impaired when cells were treated with both nanostar and nanosphere particles.

However, the effects of nanospheres were stronger compared to nanostars. To determine their impact on the mechanobiological responses of cells, we measured the mechanical properties of cells using atomic force microscopy (AFM). We found that the rigidity of cells was significantly reduced upon their interaction with nanospheres while gold nanostars had less impact. Furthermore, we used a computational model to study the relationship between migration and mechanobiological properties. Our modeling revealed that there is an optimal stiffness associated with maximal migration, and as stiffness deviates from this optimal value, the rate of migration is predicted to decrease. Besides, our modeling suggests the importance of the NPs distribution within cells to be effective in influencing the cellular deformations during cell migration. The findings of this work highlight the potential application of using gold nanomedicines to control cancer progression by regulating the mechanobiological properties of cells.

9.2. Materials and Methods

9.2.1. Gold Nanoparticles Synthesis

Turkevich method[152] was used to synthesize gold nanospheres by reduction of a gold hydrochloric acid with sodium citrate. Briefly, 75 ml of $HAuCl_4.3H_2O$ solution containing 45 µg/ml of gold was heated until boiling and then reduced by adding 5 ml of 1% sodium citrate. The solution was heated until its color turned to purple; it was then boiled for more 15 minutes. Next, the solution was left to cool to room temperature. Inductively-Coupled Plasma Mass Spectroscopy (ICP-MS) was used to determine the elemental composition of the synthesized gold NPs. The shape and size of the gold NPs were characterized using a Hitachi S 3400 N Scanning Electron Microscope (SEM).

A seed-mediated method was used in order to prepare star-shaped nanoparticles[158]. For preparing the seed solution, 15 of sodium citrate (1%) as a reducing agent was added to 100 ml of boiling 1 mM $HAuCl_4$ solution. With continuing boiling for 30 min, the color of the solution turns from yellow, first to deep blue, and purple at the final step. In order to synthesize the nanostars, 10 ml of 0.25 mM gold precursor ($HACl_4.3H_2O$), 10 µl of 1M hydrochloric acid (HCl), and 100 µl of seed solution were mixed in an Erlenmeyer flask and stirred for 5 minutes. Then, 50 µl 100 mM ascorbic acid ($C_6H_8O_6$) and 100 µl 1mM silver nitrate ($AgNO_3$) solution were added at the same time and stirred for one minute. The color of the solution immediately turned form light pink to

blue [408]. The shape and size of NPs were characterized by SEM and dynamic light scattering (DLS).

9.2.2. Cell Preparation and Fixation

A549 cells (a human epithelial cell line derived from a carcinomatous lung tissue) were cultured in F-12 Medium containing 10% (v/v) fetal bovine serum (FBS; ThermoFisher Scientific), 100 units/ml Penicillin and 100 µg/ml streptomycin (Wisent). Cells were incubated at 37°C in a humidified chamber with 5% CO2 and passaged at 70-90% confluency or as needed for studying gold NPs in cells. Cells after 24 hours, were treated with 45 µg/ml (9 µg) of gold NPs solution for 24 hours. In order to fix cells for hyperspectral images (HIS) and immunofluorescent (IF) imagings, cells were pre-incubated with gold NPs and plated on acid-washed coverslips in six-well plates. 10% TCA (trichloracetic acid) was next used to fix the cells, and for IF images, they were immune-stained for microtubules and myosin[167]. An Epifluorescence Leica microscope (DM1600B) with 63x oil immersion objective was used for IF imaging of the fixed cells. Volocity and ImageJ software were used for cellular imaging and analyses.

9.2.3. Migration Assays

Standard migration assay was used to measure the migration ability of cells. A confluent monolayer of A549 cells was pre-cultured with gold NPs in a six-well plate. After 24 hours of incubation, a p200 pipette tip was used to create a straight free-cell zone to provide an empty gap. At the edges of the wound, cells can migrate and fill the gap. Cells then were imaged with a Nikon TiE inverted microscope after 24, 48, and 72 hours. After each interval, the area of the gap was measured using ImageJ and compared to control cells to determine the migration ability of treated cells.

9.2.4. Hyperspectral Imaging System (HSI)

In order to precisely determine the presence and distribution of gold NPs in cells, a hyperspectral imaging system, CytoViva (USA, Aruban), coupled with a dark-field imaging system was used to differentiate gold particles inside and outside of cells by considering the localized surface plasmon resonance (LSPR) band of gold NPs. With the CytoViva technology, gold NPs can be optically observed as they interact with cells, and their localizations can be confirmed by measuring their spectra. In comparison to other similar systems, not only the presence

of NPs can be confirmed, but also their interactions with cells can be studied by collecting and measuring the visible and near-infrared (VNIR) spectral data (400-1000 nm with 2.8 nm resolution) from each pixel of the scanned area. Experimental measurements were performed on fixed cells at room temperature. For spectral imaging, the intensity was set to a value between 1000 and 5000 and each spectral area was exposed to 0.15~0.25s to collect the VNIR spectral data. Regions of interest (ROI) were determined (for ~70 pixels, each pixel is 225 nm^2) to create spectral libraries for NPs and identify them in cells. The spectral libraries were filtered against non-treated cells to eliminate the spectral data not coming from gold NPs (from cells), and spectral mapping was performed (with threshold value of 0.1) to localize particles within the cells. We used ENVI 4.8 to perform post-processing on HSI image and ImageJ for other analyses.

9.2.5. SEM Images

For SEM imaging, the cells were fixed with Trichloroacetic acid (TCA) and washed with TBST [270]. Cells then were dehydrated by using a series of ethanol solutions. They were incubated with 50% (v/v) ethanol in water for 15 minutes, then in 60%, 70%, 80%, 90% and 100% ethanol, respectively. The coverslips were added face up to glass slides and left to dry in a fume hood overnight. Samples were coated with gold and palladium, and they were imaged by SEM using a Hitachi S 3400N system.

9.2.6. Atomic Force Microscopy Measurement

The Dimension FastScan Atomic Force Microscopy with nanoscope V controller (Bruker, Camarillo, CA) was used in order to quantify the mechanobiological properties of single adherent cancer cells immersed in the culture medium. A soft V-shaped silicon nitride cantilever with a nominal length of 210 μm and a nominal spring constant of 0.02 N/m was utilized to probe the cells. The pyramidal tip had a half angle of 25°, and the radius of curvature of the point of angle was 20 nm. Before performing the experiments, the actual spring constant of the cantilever was measured by thermal noise fluctuation[409], yielding the practical spring constant of the cantilever, 0.015-0.100 N/m. Twenty-four hours before performing the AFM experiment, the cells were plated on round glass coverslips (diameter 12 mm), and before seeding the cells, the coverslips were coated with 0.1 mg/ml collagen type IV (Sigma) to allow cells to fully adhere the substrate [410]. All measurements were done on single cells in the culture media at room temperature. The approach velocity and force trigger were set at 0.5 μm/sec and 1-2 nN respectively to avoid

hydrodynamic effects [80] and make sure that maximum 30% of the total height of cells is intended[411]. By considering these parameters, the Hertz model can be applied for calculating the stiffness of cells accurately. The indentation was carried out at the cell's nucleus and peri-nuclei regions. In order to calculate the mechanobiological properties, the cantilever deflection versus piezo displacement data were recorded by probing both gold NPs-treated and untreated cells. The schematic of the AFM measurement is illustrated in **Figure 9-1**.

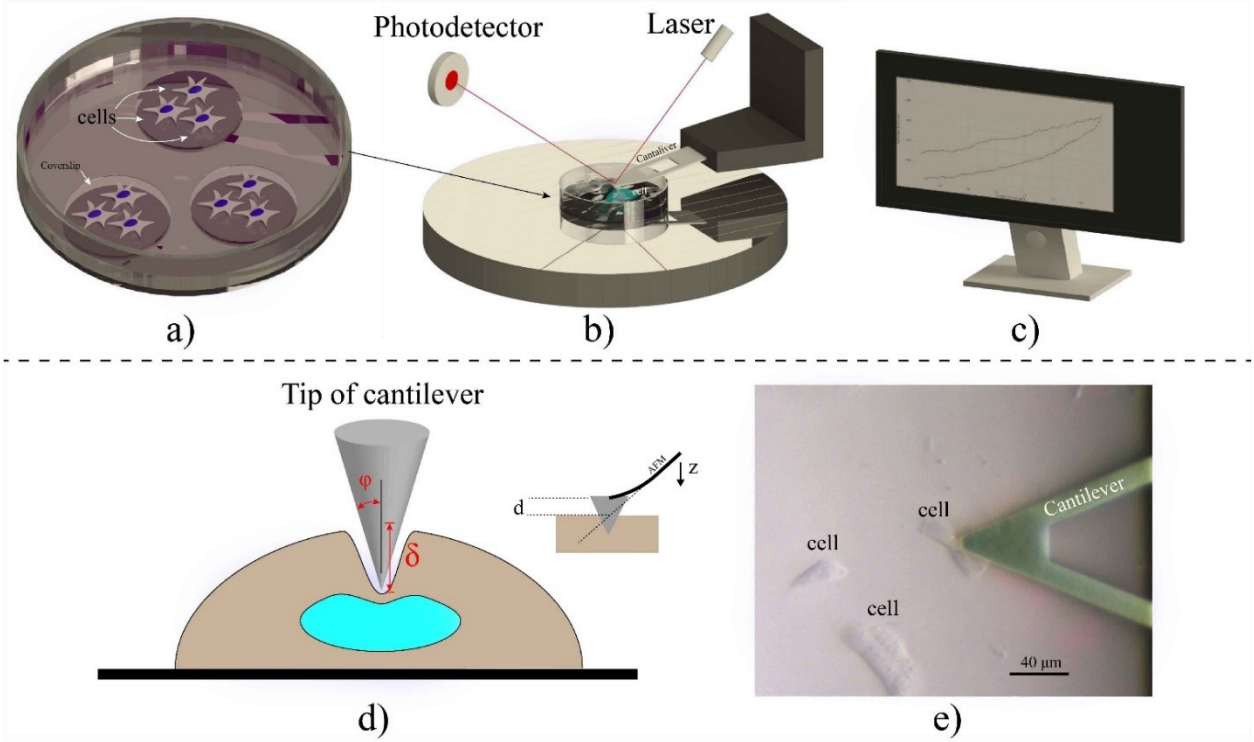

***Figure 9-1**. **a)** Cells seeded on coverslips, **b)** probing cells immersed in the culture medium with AFM tip and measuring its deflection, **c)** collecting the data, **d)** schematic showing the indentation of a single cell, **e)** optical image of the actual cantilever form the top view.*

9.2.7. Data Analysis for Mechanobiological Characterization

AFM as a powerful technique that has been widely used for mechanobiological characterization of living cells and tissues[388][72]. This tool provides a high-resolution measurement for the mechanical properties of cells. The cantilever is deflected after approaching the target cell and indenting the cell. The deflection of the cantilever (d) with respect to its vertical location (z) is recorded by an optical method (**Figure 9-1 b** and **d**). By considering the cantilever as an elastic beam, the cantilever deflection (d) is proportional to the force (F) applied on cells by the spring constant of the cantilever (k). The cell indentation remains zero until the tip of the

cantilever makes contact with the cells. The indentation (δ) continues until the cantilever deflection reaches the set point. The cantilever is then withdrawn from the cells and returns to initial locations. The elastic modulus can be computed by considering a proper contact model theory (Hertz) for F-δ relationship. For soft materials like cells, Young's Modulus can be calculated by fitting the indenting force and the indentation with a Hertzian contact model [412][413]. According to this model, the applied force and corresponding indentation for a sharp cone tip of opening angle 2φ can be predicted as follow[80][72]:

$$F = \frac{2E\tan(\varphi)}{\pi(1-v^2)}\delta^2 \qquad 9\text{-}1$$

where E and v are the elastic moduli and Poisson's ratio of cells, respectively. Poisson's ratio is considered as 0.49 for incompressible biological cells[315]. Sample indentation and indenting force are calculated as follow:

$$\delta = z^* - d^* \qquad 9\text{-}2$$

$$F = kd^* \qquad 9\text{-}3$$

where z* and d* are the relative vertical position of the cantilever and the cantilever deflection respectively with respect to the initial contact point of the tip (z_0, d_0) with the cells, and k is the spring constant of the cantilever. The least-square fitting was applied to fit F-δ relation to the Hertz model to calculate Young's Modulus. Statistical analyses of data were done using OriginPro 2016. The student t-test was used in order to compare statistical data with control cells, and differences were considered significant at $p<0.05$.

9.2.8. Dynamic Light Scattering and Zeta Potential Measurements

Zetasizer Nano ZS90 (Malvern Instruments, UK) was utilized to characterize the size of gold NPs using dynamic laser scattering (DLS). A Helium-Neon laser with 4 mW (633 nm) at 25° C was used for our measurements. Brookhaven Zeta Plus electrophoresis instrument was also used to characterize the zeta potential of particles under the ambient temperature. For our measurements, the PH was set 7.4. We averaged ten data points and reported their average in this study.

9.2.9. Simulation

In order to calculate the migratory index for different stiffness values, we developed an approximate 2D finite element model to solve the governing equations (stress field and

displacement field). The mechanical module at COMSOL Multiphysics was used to model cells, generate mesh over the entire cell, and compute the stored energy. We used the hyperelastic materials model[56], physical and biomechanical properties of A549 cells to approximate the mechanical behavior of cells, and assumed the initial bulk stiffness remains constant during the migration. A free boundary condition and a fixed boundary condition were used for the top surface and bottom of cells, respectively. We assumed that cells are migrating on solid substrates, so the effects of the substrates' stiffness were not considered in our calculations. A fully coupled solution method was used to carry out all the simulations and solve the system of equations when the internal contractile forces are applied. The deformation of cells and stress values within cells were quantified by averaging the equivalent elastic strain (ε^*), and von mises stress (σ^*), respectively, over a single cell.

9.3. Results and Discussion

9.3.1. Characterization of Gold Nanoparticles

First, we characterized the size and morphology of synthesized gold nanospheres and nanostars using Scanning Electron Microscopy (SEM) and Dynamic Light Scattering (DLS). **Figure 9-2a and d** show the SEM images of nanospheres and nanostars respectively, dried on the microscopic glasses. Nanospheres appeared to be more uniform, and a few clusters of them can be seen in a range of 50-150 nm in their SEM images **(Figure 9-2d)**. SEM images of nanostars showed multiple branches growing from the core particles (**Figure 9-2a**). Nanostars tended to aggregate and form agglomerates with larger diameters (100-300 nm), and showed a higher level of aggregation compared to nanospheres, likely due to their instability. The localized surface plasmon resonance (LSPR) of gold nanostars showed a broad band at 684 nm (**Figure 9-2b**), although the position varied depending on the branch aspect ratio and the number of branches [414]. Because of different morphologies of branches, and different sizes of gold nanostars, their LSPR band displayed a wide peak band. The absorbance spectra of nanospheres displayed a narrow band at 521nm (**Figure 9-2e),** with a more uniform particle size compared to nanostars. We then used DLS to determine the size of both types of NPs. DLS studies revealed that most nanostars had an average size of 78 nm (**Figure 9-2c**), while the average size of nanospheres was 21 nm (**Figure 9-2f**). In our previous studies[167][230], the size of synthesized nanospheres determined by their UV-Visible spectra was around 32 nm.

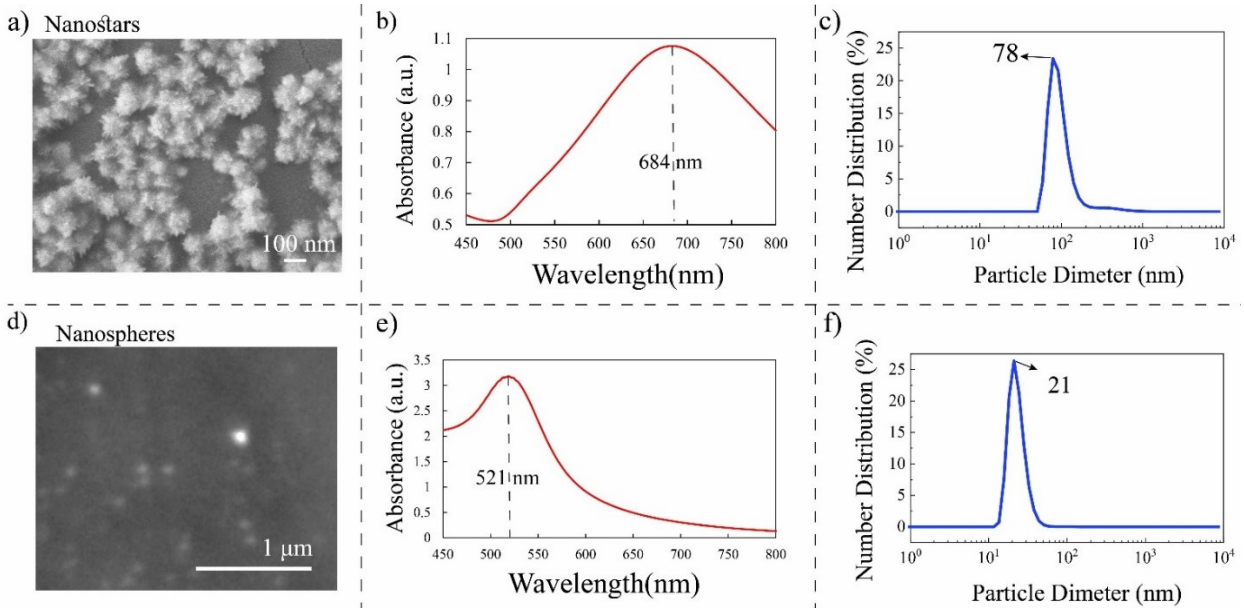

***Figure 9-2**. Characterization of gold nanoparticles: **a)** SEM image of nanostars dried on a glass substrate showing their morphology and aggregation, **b)** LSPR band corresponding to colloidal gold nanostars measured by UV-vis spectrometer, **c)** gold nanostars size measurement using DLS, **d)** SEM image of gold nanospheres dried on a microscopic glass, **e)** LSPR band of gold nanospheres measured by UV-vis spectrometer, **f)** gold nanospheres size measurement using DLS*

Zeta potential measurements (**Table 9-1**) also showed that both gold NPs have negative surface charges, and nanospheres were more negative compared to gold nanostars. During the preparation of gold NPs, citrate ions (as the stabilizer) surround the gold NPs, causing particles to have a negative surface charge. The higher zeta potential values (negative charge) of nanospheres confirmed their higher stability compared to the nanostars[415].

***Table 9-1**. Characterization of gold nanoparticles*

Gold Nanoparticles	Size (DLS)	Zeta Potential (mV)	LSRP-peak wavelength
Nanospheres	15-25 nm	-53.22±6.77	521nm
Nanostars	70~80 nm	-34.59±1.01	684 nm

9.3.2. Characterization of Nanoparticles in Cells with HSI

To characterize the gold NPs, both particles (stars and spheres) were dried on a cover glass and imaged with the CytoViva system to measure their spectra at the nanoscale. **Figure 9-3a** and **c** show the dark-field (DK) imaging of nanostars and nanospheres, respectively. The particles and

their aggregations can be seen clearly in brighter colors in the images. Depending on their size and aggregation, they can be seen as different colors. Both shapes of particles tend to aggregate, and smaller aggregates of particles are more difficult to see in the DK images. Navigating over the HSI images, the LSPR spectra of the desired particles/aggregates were measured. **Figure 9-3b** and **d** show the spectra of individual nanostars and nanospheres. Nanospheres exhibit a peak band at 558 nm, and nanostars display a peak band at 710 nm, which are in agreement with the LSPR bands measured earlier by UV-vis spectrometer.

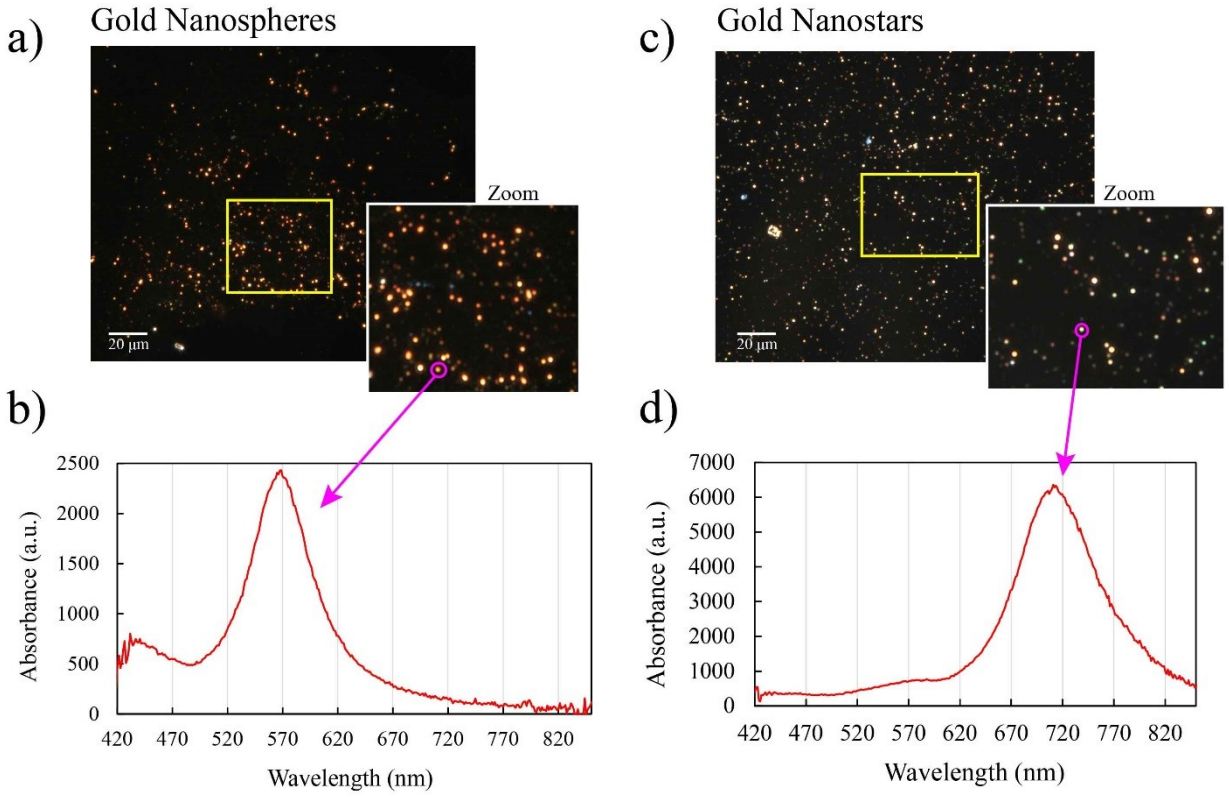

***Figure 9-3**. **a, b)** Dark-field images of nanospheres dried on a glass substrate and their corresponding spectra showing a band at 546 nm, **c, d)** a dark-field image of nanostar particles dried on a glass cover and the corresponding spectra at 570 nm and 710 nm– All spectra were filtered against the spectra of the CytoViva halogen light source (Scale bar is 20 µm)*

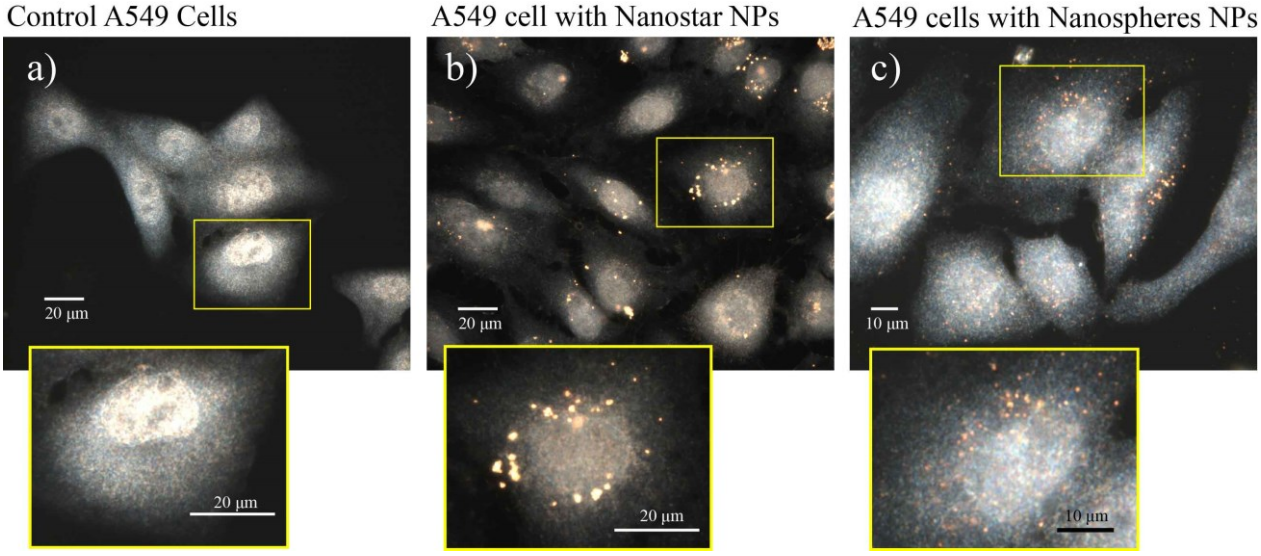

Figure 9-4. *Distribution and internalization of both nanospheres and nanostars in A549 cells compared to control cells,* ***a)*** *control,* ***b)*** *nanostars-treated cell,* ***c)*** *nanosphere-treated cells*

Using the enhanced DK imaging, the distribution and localization of both shapes of gold NPs in A549 cells were compared to control (non-treated) A549 cells in **Figure 9-4**. Particles are visualized as the brighter signals, so in **Figure 9-4** we can optically identify the aggregates within cells. **Figure 9-4a** displays no particle within or outside of control cells, and the nucleus region can be distinguished in the central region of cancer cells, which is denser and brighter than other regions of the cell. Both nanostars and nanospheres were observed throughout cells. However, as shown in the zoomed image (**Figure 9-4b**), nanostars formed large aggregates in and at the periphery of cells, while nanospheres formed smaller clusters in cells, and localized mainly at the periphery of the nucleus, with a few inside the nucleus. A549 cells appeared to uptake more nanospheres than nanostars during the first 24 hours, likely due to their size. As can be seen in **Figure 9-4c**, all cancer cells had nanospheres, while not all cancer cells had nanostars, and their distribution was more variable.

To further characterize gold NPs in cancer cells, we collected HSI images of the particles in A549 cells. HSIs provide VNIR spectral and spatial information of gold NPs in cells. HSI allows us to accurately analyze nanoscale features (NPs and molecular structures) in a biological environment that are not possible with traditional microscopic techniques[264]. **Figure 9-5a** shows a typical HSI image of cells with nanospheres, and similar to DK images, particles in cells have greater optical contrast. Each pixel includes spectral information for the VNIR range at that point. For gold nanospheres, a region of interest was precisely selected in the HSI images, and

Figure 9-5b shows the maximum, minimum, mean, and standard deviation of the selected spectra. The spectral information of this region was used to build a reference spectral library (RSL). The RSL was filtered against the spectra of control cells (without NPs) to make sure that the RSL includes only the scattering spectrum of gold (F-RSL), not cells. The spectral Angle Mapper (SAM) algorithm was then used to map the f-RSL on the same hyperspectral image (**Figure 9-5c**) to mark gold nanospheres with green color. This algorithm scans the entire HSI image to find pixels matched to the reference spectra (F-RSL). The green dots in **Figure 9-5c** show the gold particles in cells whose spectra are matched with the f-RSL when the threshold value is 0.1. As can be seen in the enlarged view of a single cell (**Figure 9-5c**), aggregates of gold nanospheres were marked in the nuclear region, confirming that gold nanospheres localize to the periphery of the nucleus after entering cells.

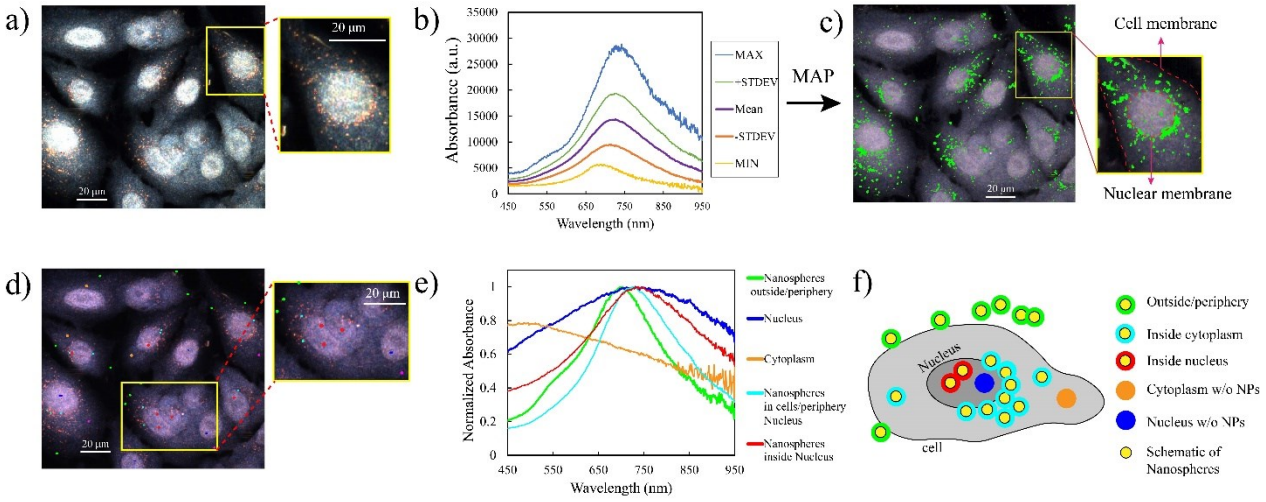

***Figure 9-5**. Characterization of gold nanospheres in cancer cells. **a)** a hyperspectral image of gold nanospheres-treated cancer cells showing the particles in different regions of cells, **b)** Spectral information of the ROI for gold nanospheres, **c)** spectral mapping of the same HSI image using the shown spectra range in "**b**" after filtering against control cells, and an enlarged view of a single A549 cell (gold nanoparticles are shown in green dots), **d, e)** labeling particles in different locations of cells and their corresponding spectra, **f)** a schematic illustrating particles in different regions of cells: green for particles outside of cells or at the periphery, cyan for particles inside and at the periphery of the nucleus, red for particles inside of the nucleus, blue for nucleus region without particles, and orange for cytoplasm region without gold particles- All spectra were filtered against the spectra of the CytoViva halogen light source.*

Changes in the LSPR band of gold NPs can be used to confirm their presence in cells and to characterize changes in their properties due to their surrounding microenvironment [230][416]. The properties of solutions can influence the energy associated with electric field oscillation,

altering the LSPR band. In particular, gold NPs in a simple solution with low salinity would be predicted to display a specific LSPR band. However, this band can change due to differences in their physicochemical properties such as size, morphology, level of aggregation, and surface charge. In addition, their spectral responses also could be influenced by the surrounding microenvironment in cells, which would include nucleic acids, proteins, lipids and salts in addition to changes in pH [230][201]. In **Figure 9-5d,** we marked particles with different colors depending on their location in cells, and their corresponding mean spectral profiles were plotted in **Figure 9-5e**. Particles on the outside of cells or close to the cell periphery displayed a plasmonic band between 650~700 nm. However, NPs located in the cytoplasm or at the periphery of the nucleus had plasmon band shifts of 700~750 nm. Thus, inside the cells, as indicated above interactions with intracellular components alter the plasmon band position of the gold NPs. Moreover, particles located inside the nucleus displayed a broader band and their position was slightly shifted. The nuclear environment is more electron-dense than the cytoplasm due to the enrichment of nucleic acids, which could influence the plasmon band. As shown in **Figure 9-5e**, nuclear absorption is greater than that of the cytoplasm. The intracellular location-dependent spectral responses of gold NPs confirms their presence in cells and provides a platform to characterize particles within cells.

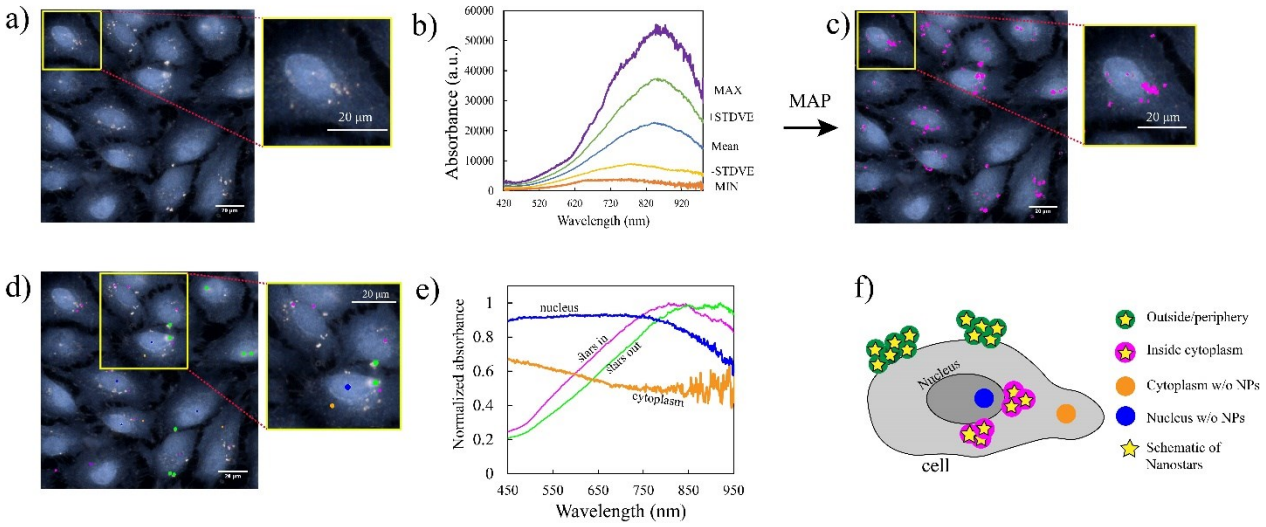

Figure 9-6. *Characterizations of nanostars in cancer cells,* ***a)*** *an HSI image of cells with nanostars,* ***b)*** *Mean spectra of the ROI of nanostars in cells,* ***c)*** *Spectral mapping of the same HSI image with respect to the f-SPL created with ROI shown in* ***(b)****,* ***d, e)*** *Marking nanostars in different regions of cells (green: nanostars outside or at the periphery of cells, purple: nanostars inside of the cells, dark blue: cell nucleus, and orange: cell spectra), and corresponding spectral responses,* ***f)*** *a*

schematic showing the nanostars in different regions of cells- All spectra were filtered against the spectra of the CytoViva halogen light source.

We also similarly analyzed A549 cells treated with nanostars as shown in **Figure 9-6a-f**. As seen earlier, the level of uptake was reduced for nanostars compared to nanospheres. **Figure 9-6c** shows the mapping of nanostars in cells for the spectra plotted in **Figure 9-6b**. As described before, nanostars formed larger aggregates in cells, many of which localized at the periphery of cells. **Figure 9-6e** compares the band position of nanostars outside and inside cells. In contrast to nanospheres, the plasmon band of nanostars outside or at the edge of cells was red-shifted. Larger aggregates of nanostars situated to the periphery of cells and only fewer small aggregates could enter into cells. So, the shifts were likely due to their physicochemical properties vs. the surrounding microenvironment. **Figure 9-7a** presents the spectra of two different morphologies of gold particles depending on their subcellular locations. The distributions of both morphologies of NPs in cells are shown schematically in **Figure 9-7b**. Nanospheres formed smaller clusters and localized at the periphery of the nucleus while nanostars aggregated upon interaction with cells, and fewer of them entered cells over 24 hours. Particles embedded in the cytoplasm or the nucleus could influence interactions with their microenvironment, and these effects are reflected in their optical responses. For example, smaller particles (nanospheres) could sense their surrounding medium better compared to larger particles (nanostars), and their LSPR bands could reflect this sensitivity[230].

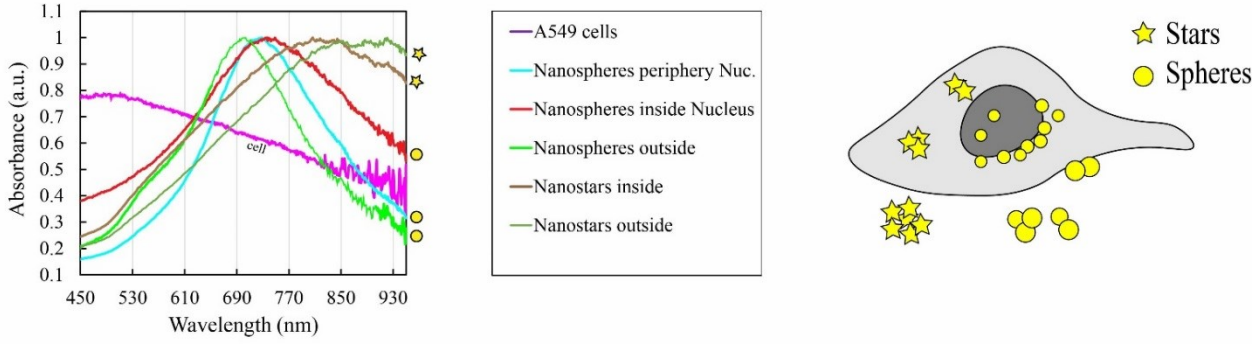

Figure 9-7. *comparison of spectral responses of two different particles depending on their positions inside cells and a schematic showing the distributions of nanospheres and nanostars in A549 cells*

9.3.3. Immunofluorescence Imaging of Cells

In the previous section, with the help of DK images and HSI images, we confirmed that gold NPs could access intracellular locations; however, their localization near cytoskeletal

structures was not visible with these methods. To visualize the location of gold NPs (spheres) compared to microtubules and actomyosin, A549 cells were treated with NPs, then were stained with antibodies against tubulin and myosin, as well as DAPI to visualize chromatin. As shown in **Figure 9-8** myosin was distorted around the clusters of nanospheres (visualized as black dots), which was not observed in the non-treated cells above. These deformations likely reflect vesicles, which are actin-derived. As described earlier, their location in the vicinity of the nucleus could cause changes in cell mechanics required for migration. For example, here they could interfere with deformation, as well as the ability to transmit force from the rear of the cell to propel cells forward over substrate.

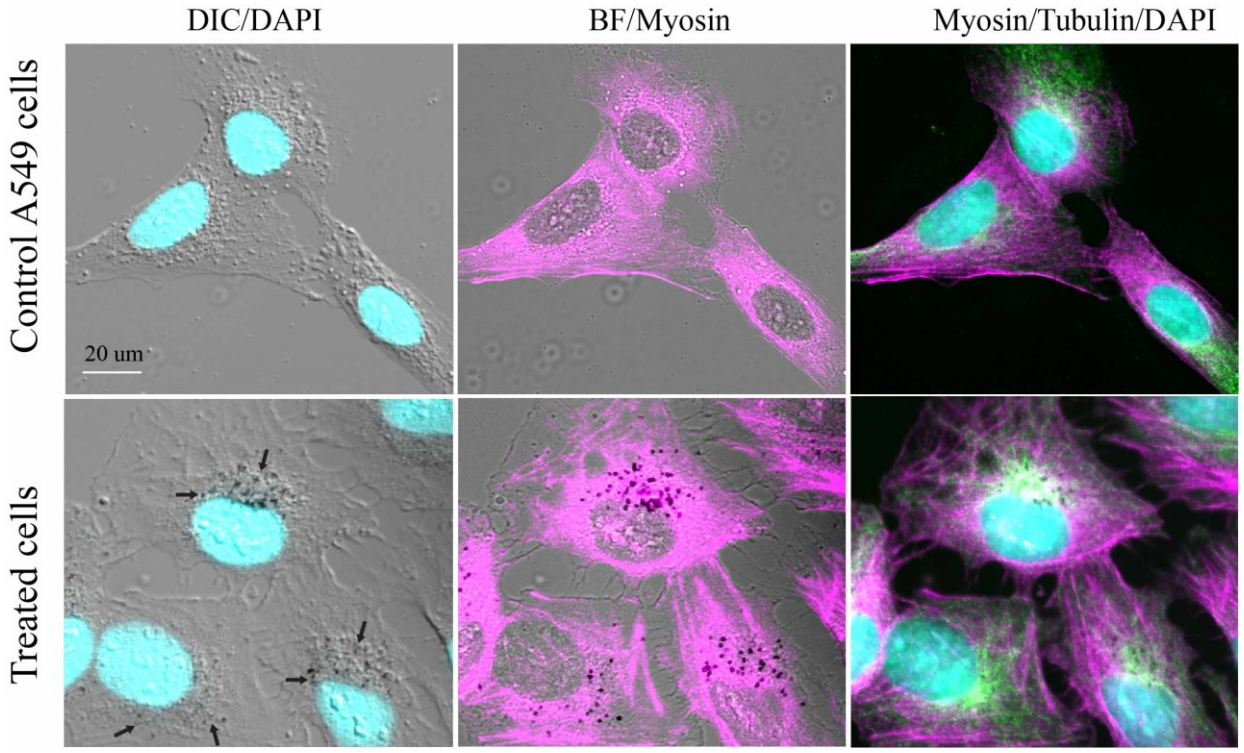

Figure 9-8. *Immunofluorescence images of A549 cancer cells after treatment with gold nanospheres. The cells were stained for DAPI (cyan), Myosin (magenta), and Microtubules (Green)*

9.3.4. Characterization of Gold Nanoparticles in Cells with SEM

To further characterize NPs in cells, we imaged treated and untreated cells with SEM. SEM provides increased resolution and greater contrast compared to immunofluorescence microscopy. As shown in **Figure 9-9**, both types of NPs were taken up by cells. Clusters of gold nanostars and nanospheres can be seen in the cells, while additional smaller clusters of nanospheres also were

seen in cells. Although this was not quantified, it appeared that some of the A549 cells had a more rounded morphology compared to control, non-treated cells as seen in **Figure 9-9**.

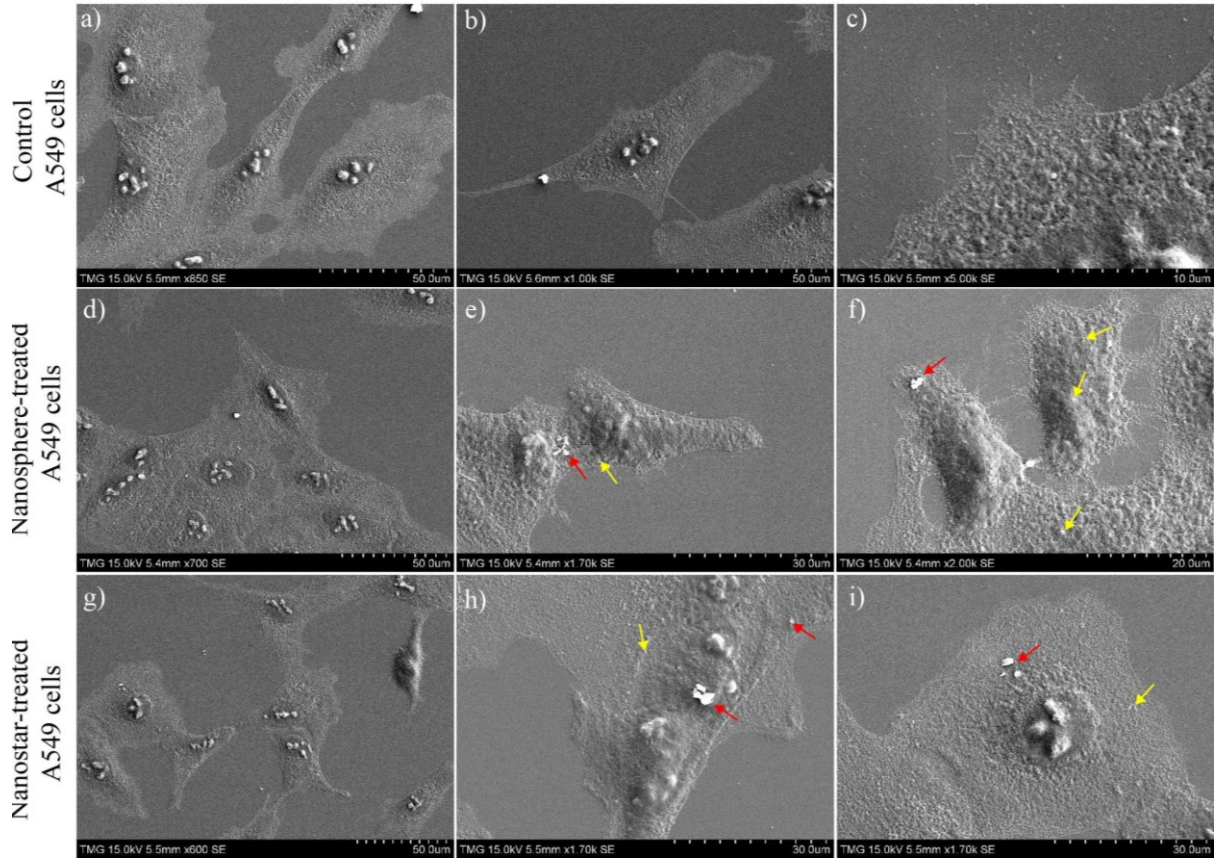

Figure 9-9. *SEM images of control cells versus treated cells.* ***a, b, c)*** *control cells in different magnifications showing the normal, extended and flat shape of cells,* ***d, e, f)*** *cells after treatment with nanospheres, showing the distribution of them in cells and morphological changes of cells,* ***g, h, i)*** *larger clusters of gold nanostars in cells and their morphological changes. (Red arrows show larger clusters and yellow arrows show the smaller clusters of gold nanoparticles)*

9.3.5. Migration of Cancer Cells

We observed that NPs could induce changes in the arrangement of cytoskeletal proteins and the morphology of cells. To examine the effects of these changes on migration, we used a standard scratch assay [417] to quantify the migration of control and NP-treated cells. Cells were grown in 2D to confluency, then a cell-free area was created (**Figure 9-10a**). The rate at which cells migrated from either side to recover this region was imaged every 24 hours for 3 days. Migration was quantified by measuring the change in area over time as shown in **Figure 9-10b**. After 72 hours,

the gap was significantly smaller indicating that the control cells migrated significantly over this time. However, cells treated with NPs had larger gaps remaining, suggesting that migration was compromised. **Figure 9-10c** shows a graph comparing control cells with NP-treated cells. While nanospheres had an immediate impact on migration, nanostars only impacted migration after 72 hours. It is not clear why the nanospheres had a stronger impact, although as described earlier, cells took up nanospheres to a greater extent compared to nanostars, and thus, would more likely impact their cytoskeleton compared to nanostars.

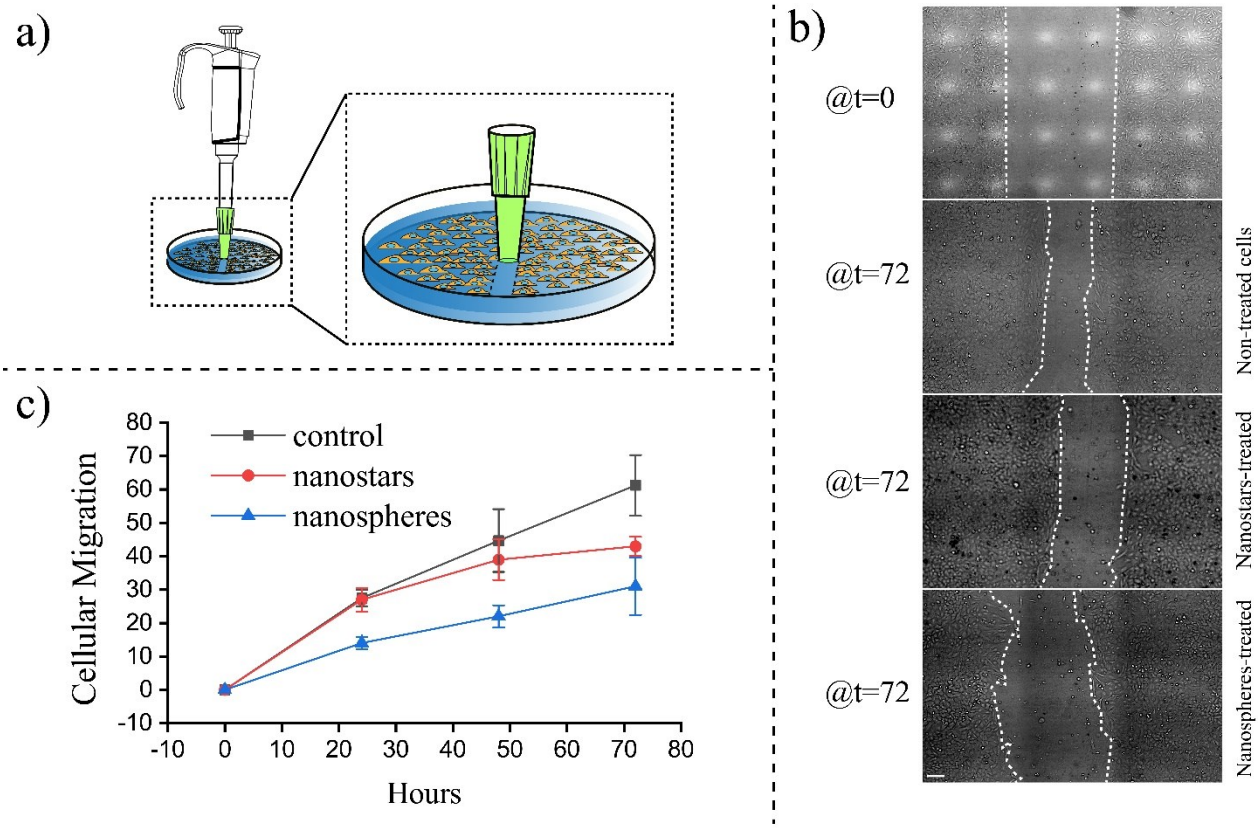

Figure 9-10. *Scratch assays to study the inhibitory effects of gold nanoparticles on A549 cells,* ***a)*** *schematic showing the scratch assays experiment,* ***b)*** *Migration assay for different shapes of gold particles @ t=72 hours(scale bar is 200 µm),* ***c)*** *migration ability (in mm^2/hour) of treated cells compared to control cells (without NPs) at different intervals*

9.3.6. Mechanobiological Measurements of Cancer Cells

We used AFM instrument to characterize the deformability of A549 cells before and after interaction with both types of gold NPs. We predict that NPs could influence the mechanobiological properties of cells[126]. Myosin converts chemical energy into mechanical

energy to produce force and movement. Therefore, myosin plays a significant role in the mechanics of cells, and any changes in its activity or organization could change properties such as stiffness. AFM measurements on adherent A549 cells revealed that A549 cells with gold NPs had reduced elasticity, or lower stiffness compared to non-treated cancer cells. In particular, the AFM results (**Figure 9-11a-c**) showed that after 24-30 hours of incubation with both morphologies of gold NPs, cells were softer and had less resistance to the force applied by the AFM cantilever (**Figure 9-11e**). However, the level of reduction in the stiffness of A549 cells was not identical for both nanostars and nanospheres.

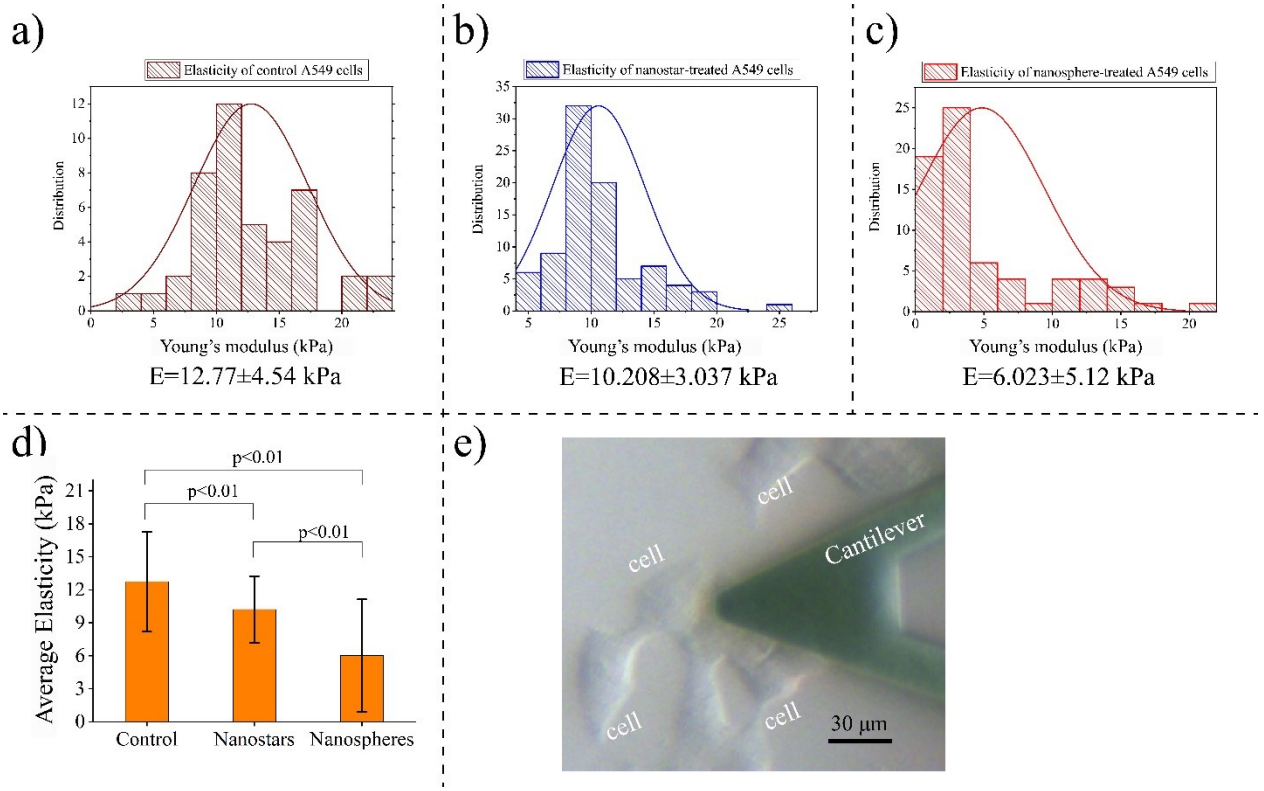

Figure 9-11. (a-c) *Histogram of elastic modulus computed from AFM mechanical measurement for control, nanostar-treated, and nanosphere-treated A549 cells.* ***d)*** *The average elastic modulus for treated and untreated cells and the corresponding standard deviations, and* ***e)*** *actual image of AFM probing of cells after incubating them with gold nanostars (arrows shows the NPs)*

The elasticity of cells incubated with gold nanospheres (**Figure 9-11a-c**) showed a major reduction in their deformability compared to the nanostar-treated cells. As shown in **Figure 9-11d**, on average, nanospheres reduced the stiffness of A549 cells by 50% while, on average, nanostar-treated cells were 16% softer compared to control cells. As described above, we observed that gold nanospheres more effectively suppressed A549 cell migration compared to nanostars, and these

mechanical measurements confirm that nanospheres also more strongly reduce the mechanical stiffness of cells compared to nanostars. Several reasons could explain why nanospheres elicit a stronger effect. First, their internalization was higher compared to nanostars, where they would have more opportunity to impact the cytoskeleton. Second, their smaller size compared to nanostars (higher surface area to the volume) could permit them to interact more effectively with subcellular components [37][36].

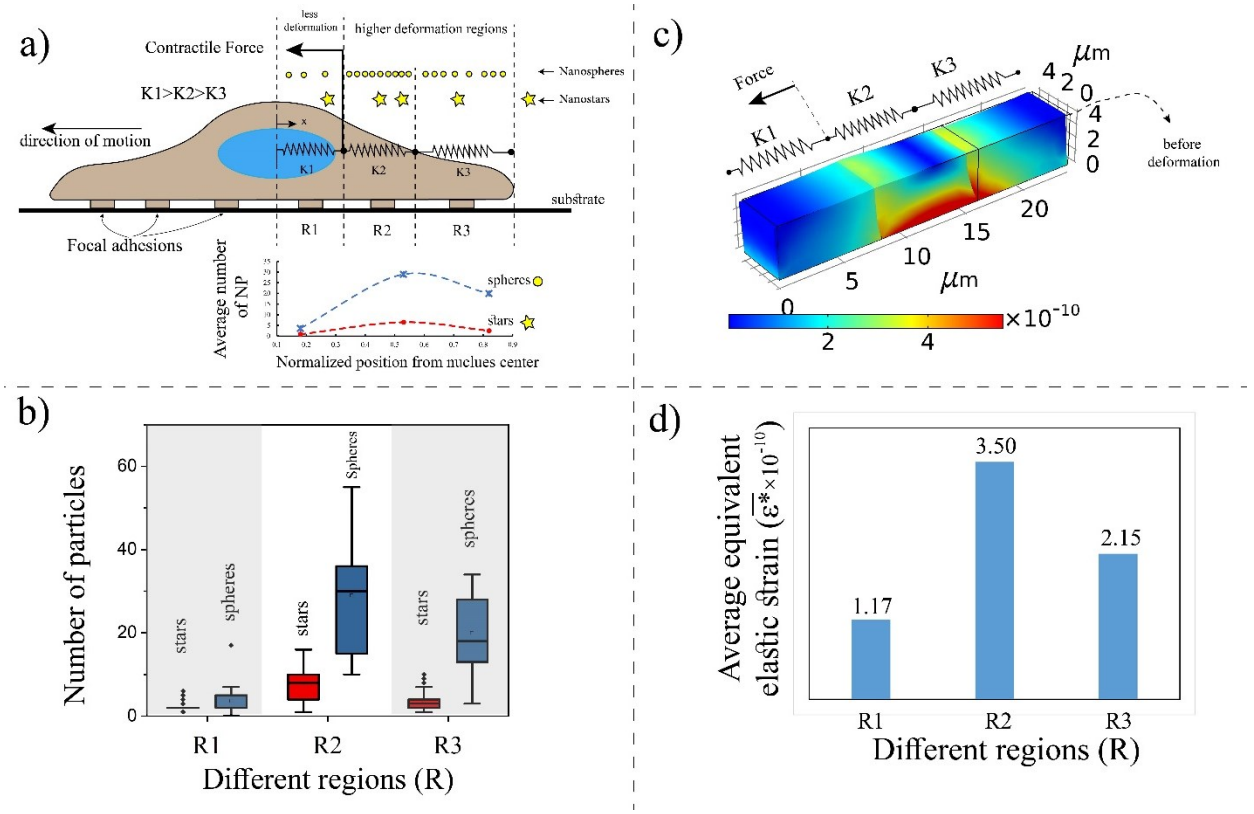

Figure 9-12. a) *the stiffness of cells is schematically modeled with three springs with different constants and average number of nanoparticles in different regions (R),* ***b)*** *distribution of both types of nanoparticles in different regions of cells (R1: nucleus, R2: peri-nucleus, R3: in distance from nucleus),* ***c)*** *deformation modeling of three springs connected in series under a force at rear middle (K1=24kPa, K2=12kPa, K3=6kPa, F=2μN),* ***d)*** *total elastic deformation of each spring expressed in the equivalent elastic strain*

How could nanospheres affect the stiffness of cells? Filamentous structures are not distributed uniformly. As described earlier, stress fibers from around and behind the nucleus toward the cell rear, while dynamic, branched F-actin filaments are found at the front. In addition, the nucleus is encapsulated by cytoskeletal components to resist mechanical rupture caused by deformation during migration, particularly when moving between small spaces. Hence, the stiffness of cells is

not constant and the nucleus is the stiffest region, being four to ten times higher compared to the cytoplasm[375][376], while the cell membrane is much softer. The net stiffness of a single cell can be modeled with different springs connected in series, as shown in **Figure 9-12a**, with different stiffness constants. We can discretize the cells into three regions with three different spring constants; nucleus with K1, cytoplasm and peri-nucleus with K2, and cell membrane with K3 such that K1>K2>K3. The distributions of both nanostars and nanospheres in three regions are statistically shown in **Figure 9-12b.** As observed, nanospheres localized in the K2 region, while nanostars did not show a specific distribution pattern. In addition, the average number of nanospheres was higher compared to nanostars. During cell migration, different levels of deformation take place in three different regions. We modeled three cubes (**Figure 9-12c**) representing the three regions with different elasticities to quantify the deformation of each portion under a constant force in the rear-center (K2) of the nucleus. We used a simple simulation to study deformation of the different regions when a contractile force is generated at the rear of cells during migration. The deformation of cells can be expressed as equivalent elastic strain (ε^*) showing the amount of strain in the cell[418]. As shown in **Figure 9-12d**, K2 (membrane) undergoes more deformation compared to K3 , which in turn deforms more compared to K1 (nucleus). The higher level of deformation at distances from the nucleus (K1 and K2) suggests that these regions need to deform to translate forces more effectively for migration. Due to the capability of nanospheres to potentially cause changes in the cytoskeleton, particularly in K2 and K3 regions where force is generated and translated, by reducing stiffness they could prevent the effective translation of force to the leading edge to move cells forward effectively.

9.3.7. Adhesion Characterization of Cells

To further investigate the effect of NPs on the mechanobiological properties of cancer cells, we measured the adhesion force between the membrane of cells and the AFM probe. We can study the adhesion force generated by measuring the AFM pull-off force when the membrane of cells is probed with an AFM tip and then subsequently is retracted [419] (**Figure 9-13**). The adhesion force for A549 cells treated with both nanostars and nanospheres is presented in a chart box shown in **Figure 9-13** (left panel). It is interesting to observe that the average adhesion force was reduced by almost 76% when cells were treated with gold nanospheres in comparison to control cells. Nanostar-treated cells also had reduced adhesion force, but it was higher than the nanosphere-treated cells.

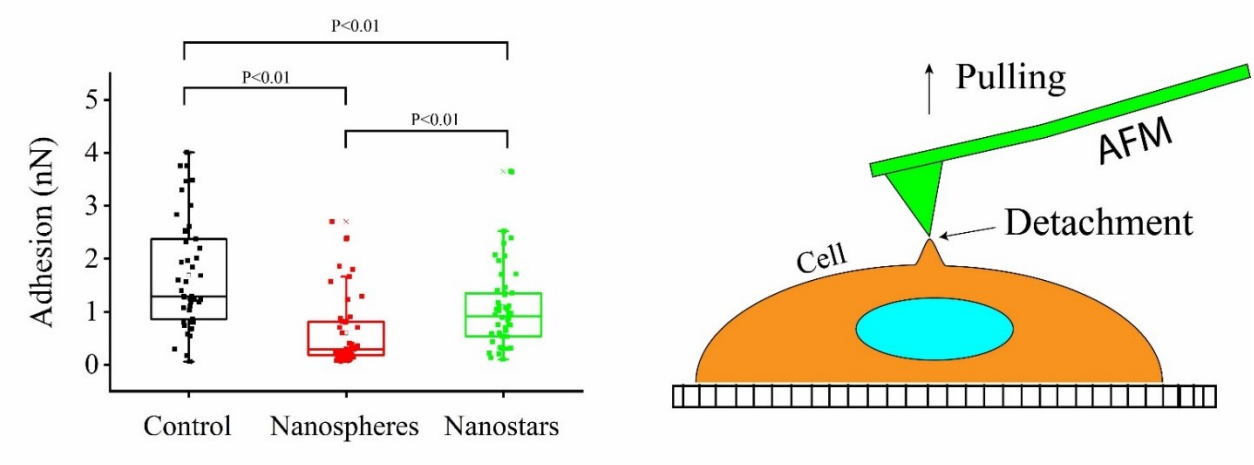

Figure 9-13. *The adhesion force between AFM tip and the membrane of A549 cells treated with two different morphologies of gold NPs compared to control cells*

Although this force does not reflect the adhesion of cells on a substrate, which can vary dramatically depending on the chemical composition (e.g. integrins) and stiffness (dura), the reduction in adhesion force measured by AFM could indicate that cell attachment is also impacted by the presence of gold NPs. In particular, nanosphere-treated A549 cells exhibited a significant reduction in their adhesion to the AFM tip, from 1.3 nN to 0.3 nN. These results demonstrate that gold NPs can modulate the mechanobiological properties of cells such as stiffness, adhesion, and migration. These changes are likely attributed to changes in the organization of actomyosin.

9.3.8. Cell Stiffness and Migratory Index

As mentioned earlier and demonstrated by AFM, after treatment with gold NPs, cancer cells exhibit a lower stiffness compared to non-treated cells and have reduced migration. Previous studies showed that softer cells could have the potential to be more invasive compared to stiff cells, while others reported the opposite. *El-Sayed et al*. [139] showed that increasing the stiffness of cells reduced their migratory ability; however, *Qin et al.* [119] showed, similar to the current work, that migrated decreased when stiffness was reduced. One explanation is that the relationship between stiffness and migration is not linear. We hypothesize that there is an optimal range of stiffness that supports efficient migration, and cells lose their capacity to migrate beyond this range. Two factors that influence migration are cell deformation and the generation of traction force to counteract the resisting forces at the cell-substrate interface. To migrate, cells need to deform their bodies and need to overcome this resisting stress[389]. The mechanical properties of cells, such as stiffness, contribute to these factors. Under a specific force, softer materials undergo more

deformation, and are not able to transmit the applied force rapidly to other regions, while stiffer materials can transmit force faster with fewer deformations. Uniquely, we can study these two phenomena by measuring the mechanical energy stored in cells, migratory index, when contractile forces are internally produced (unpublished data).

We used a simple 2D model of cancer cells shown in **Figure 9-14a** to approximate the migratory potential of cells and investigate the effect of cell stiffness on the deformation and stress of A549 cancer cells (the details of modeling can be found in [315][418]). Contractile stress (P=0.5~5 Pa)[382] is applied to the rear-center of cells (**Figure 9-14a**). We used the hyperelastic materials model to simulate the mechanical behavior of cells. We used the elastic properties of A549 cells measured in **Sec. 9.3.6** to extract the simulation data. **Figure 9-14b** shows the equivalent elastic strain (ε^*) of non-treated A549 cells and gold NP-treated cells when the contractile force is applied at the rear-center of cells for different bulk elasticities of cells cytoplasm (E_c). As shown in this figure, treated cells with a smaller elasticity exhibit higher deformation under a constant force over a specific time compared to control cells. As can be seen in the deformation contour shown in **Figure 9-14e**, nanosphere-treated cancer cells sense deformation in a wider region of their bodies. On the other hand, as can be seen in **Figure 9-14c**, nanosphere-treated cells with higher deformability transfer a smaller value of stress (σ^*) at their bottom (in the contact regions with substrate). Thus, they would be predicted to not transfer enough force to overcome the resisting force at their interface with the substrate, suggesting an imbalance between mechanical signaling and cellular deformation (**Figure 9-14d**). This mechanical behavior of treated cells could explain why their migration is reduced when they have gold NPs.

There is a range of stiffness for mobility at which cells can make a balance between their deformation and stress, which is necessary for migration. If we assume that the cellular deformation and the transmitted force in their contact regions with their microenvironment are two main factors for migrations, we can approximate the potential ability of cells for migration by measuring the "migratory index" in the adhesion complexes. Although as mentioned earlier, adhesion complexes are not same in rear vs. front of cells, in our model for simplicity we assumed them to be same. The migratory index is the potential mechanical energy stored in the physical systems of cells and could be transferred in contact regions for migration when a contractile force is applied[379]. This approximate model allows us to globally compare the mobility potential of cells. We can determine

the migratory index values by considering the displacement fields and stress filed in contact regions between cells and their microenvironment (substrate). The 2D migratory index for cells is defined based on the stored energy in contact regions as follow[420]:

$$\mu = \frac{1}{2}\frac{\iint \vec{\sigma}(x,y).\vec{\varepsilon}(x,y)dA_{adhesion\ complexes}}{A_{adhesion\ complexes}} \qquad 9\text{-}4$$

where μ is the migratory index, $\sigma(x,y)$ is the stress field in x- and y-directions, $\varepsilon(x,y)$ is the displacement field in x-, y-directions. Once contractile forces are generated in the rear center of cells, forces are transmitted and distributed into the whole body of the cell, causing deformation and stress in different regions of cells. **Figure 9-14f** shows the migratory index for A549 cells (considering its configuration) with different elasticities based on our approximate model. As can be seen in the same figure, control A549 cells and nanostars-treated A549 cells with bulk elasticities of 12 kPa ($\mu = 2.1 \times 10^{-14}$) and 10 kPa ($\mu = 2.07 \times 10^{-14}$), respectively, have almost same migratory index in the optimal range where the migration could be maximum. In this range, it is believed that the migratory potential of cells is higher. However, in the case of nanosphere-treated A549 cancer cells with the bulk elasticity of 6 kPa, the migratory index reached down to a value far from the optimal range ($\mu = 1.68 \times 10^{-14}$), which is a favourable condition to control cancer migration.

These mechanical behaviors of A549 cancer cells with different elasticities are in agreement with the experimental data presented in **Sec. 9.3.5.** As shown in **Figure 9-14f,** the migratory potential of cancer cells can be suppressed either by increasing or decreasing the stiffness of cancer cells. Together, our data suggest that gold nanospheres have effects on the mechanical properties of cells and could be considered as a treatment to slow down cancer cell migration required for metastasis. In particular, they reduce cell stiffness, which causes an increase in deformation and a reduction in the translation of forces and ability to overcome resistance thus slowing their migration. Gold NPs with the proper size and morphology could be used to modulate the stiffness of cancer cells to a value beyond the optimal range, and lead cells to lose their migratory capacity. **Figure 9-15** depicts a schematic graph showing the relationship between migration and the stiffness of cells based on our various measurements and the approximate model. In the highlighted area (first region), the stiffness of cells is in the critical range between s1 and s2, where cells could migrate fast. NPs reduce the stiffness of cells (region 2) to a point in which migration is slow and

is outside a region where they could be predicted to have less metastatic potential. The balance between deformation and overcoming stress can also be disrupted by increasing the stiffness to reduce migration (region 3)[139].

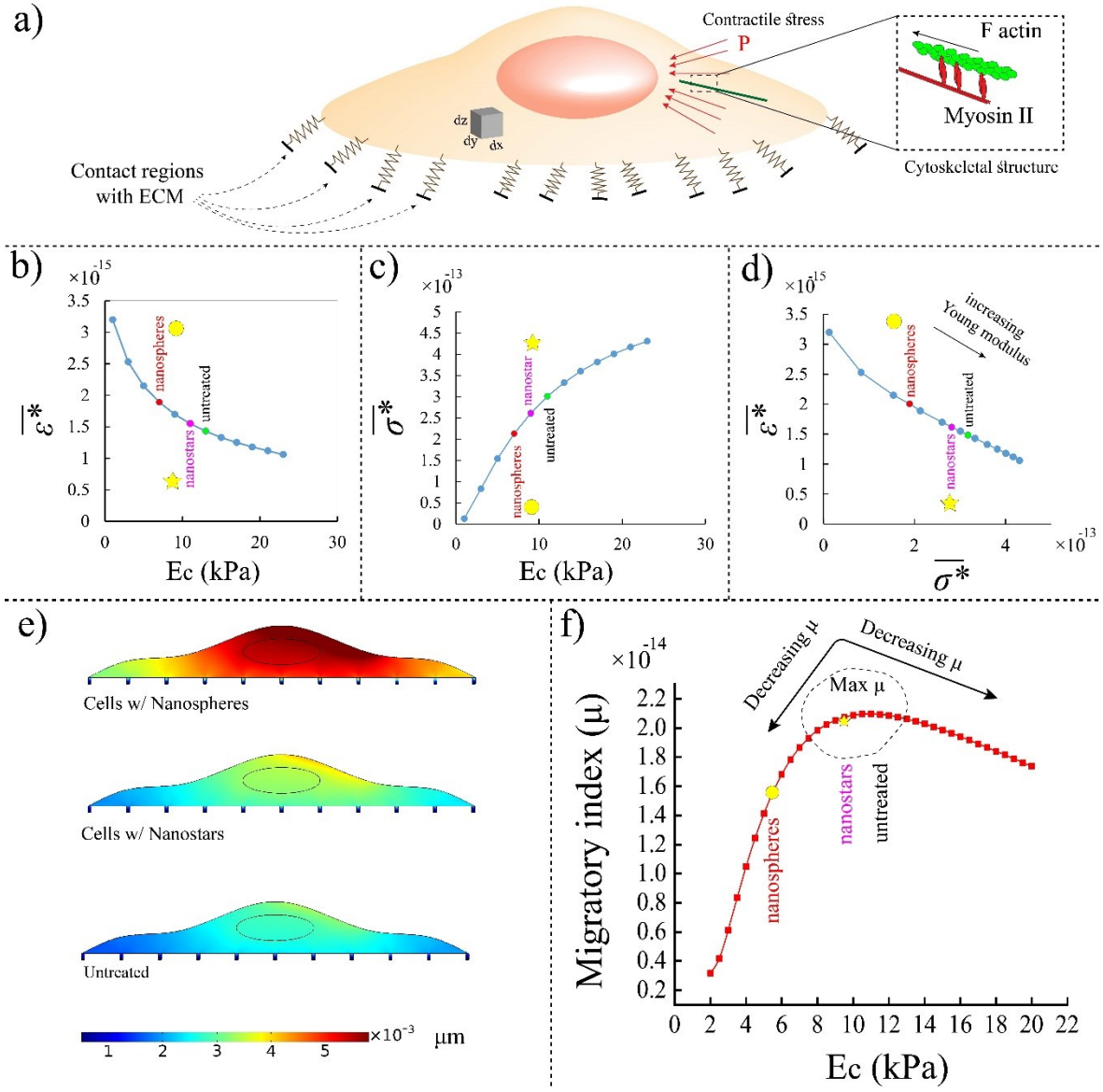

***Figure 9-14**. **a)** Schematic of a cell showing where the contractile force is applied (motion direction to left), **b)** stresses-induced by the contractile force at the cell-substrate interface by changing the elasticities of cells. stiffer cells, transmit more stress within a constant time, **c)** Equivalent elastic strain (ε*) of cells with respect to the elasticity of cells, softer cells provide a higher degree of deformation within a constant time, **d)** cell deformation is inversely proportional to the stress, once cells transmit more force, they undergo less deformation and vice versa, **e)** displacement contours of the treated cells compared to the untreated cell, **f)** migratory index of cells by increasing the stiffness, showing optimal range between 8~ 14 kPa.*

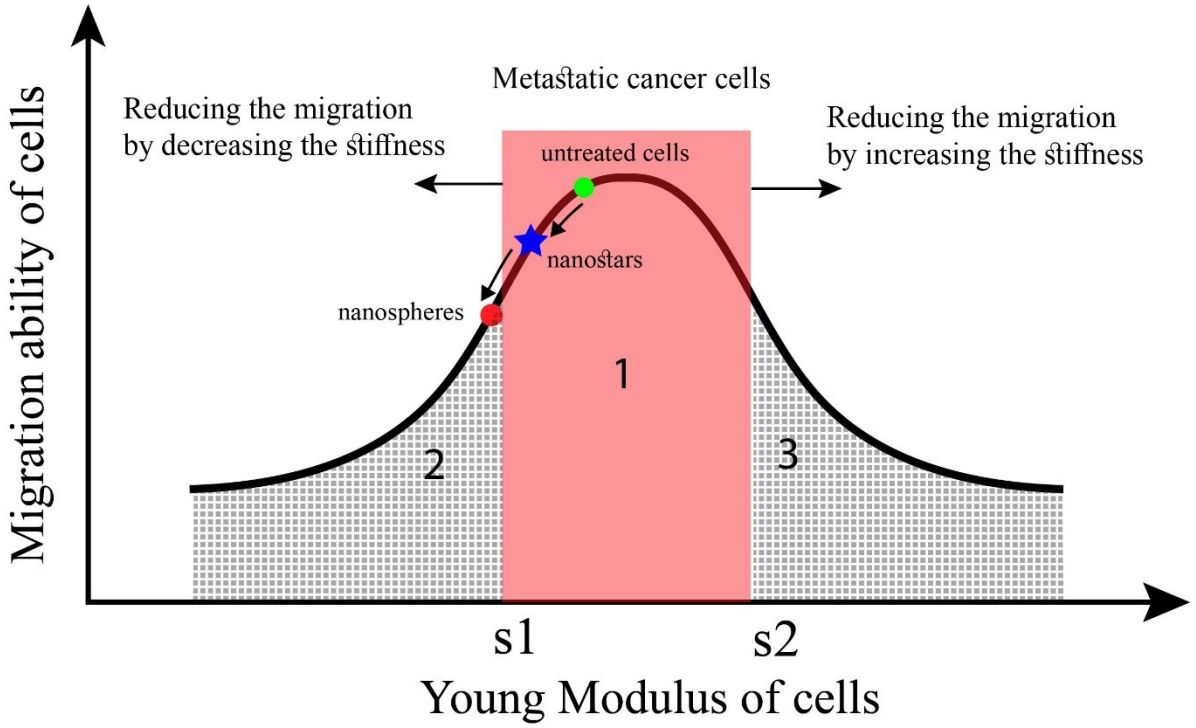

Figure 9-15. *A schematic showing the relationship between stiffness and migration of cells. The migration of cells can be controlled by increasing or decreasing the stiffness of cells to regions 2 and 3. Normal cells (region 3 or 2) when becoming cancerous, their stiffness values change to the region 1, in which it is believed that the migratory capacity of cells is high. Gold nanoparticles can regulate cell stiffness to control the migration of cells.*

9.4. Conclusions

Cancer cells undergo complex physiological changes to become migratory and gain metastatic potential. Cancer cells have mechanobiological properties to support efficient migration. Cell migration requires force generation and adhesion, and cells must be able to deform to overcome adhesion, but still be able to transmit force effectively to move forward. Here, we determined how the uptake of gold NPs with two different morphologies altered the mechanobiology of A549 cancer cells. First, we showed the cellular uptake of gold NPs in cancer cells with different microscopic and hyperspectral imaging techniques. With a novel hyperspectral technique and spectral information of gold NPs, we detected gold NPs in different regions of cells and showed how their spectral properties could shift depending on their location. IF and SEM images revealed that the structural and morphological changes take place in cancer cells after the uptake of NPs. In particular, vesicles of actin and myosin form around the NPs, which could cause changes in the nearby cytoskeleton. The effects of these structural changes were reflected in observed changes in the mechanobiological properties of cells.

Mechanobiological measurements showed that gold NPs softened cancer cells, and migration assays confirmed that gold NPs also slowed down their migration. We used approximate modeling to determine why reducing stiffness would decrease cell migration. Deformation and traction force are two determining factors in the migration of cells. Understanding their relationship could shed light on the contribution of cancer cells stiffness to their migratory capabilities. Our computational simulations showed that stiffness has contradictory effects on deformation and overcoming force at the cell-substrate interface. The computational results revealed that the migratory potential of NP-treated A549 cells with lower stiffness is reduced compared to the non-treated A549 cells with a stiffer body. Our modeling also highlighted the effects of the NPs distribution patterns within cells in controlling cell migration, particularly, in regions where force is generated and translated. Our data support that gold nanospheres could decrease the stiffness of cancer cells outside of the optimal range for efficient migration, and we hypothesize that this could suppress their metastatic potential. Thus, our study suggests that gold nanomedicines with the proper morphology and size could be designed to control cancer progression by regulating the migratory capability of cancer cells. These nanomedicines need to alter the elasticity of cancer cells so that the migratory index decreases.

In this chapter, our model developed in the previous chapter used to study the effects of nanoparticles on the migratory ability of cells. In the final chapter, the summary of this dissertation is discussed and futures works are suggested.

Chapter 10
Summary, Conclusions and Future Works

Developing efficient, novel, fast therapeutic methods for cancer treatment is one of the crucial challenges in the current century. New techniques are needed to improve the limitations of traditional methods such as chemotherapy, surgery, and radiotherapy. Every year, millions of people across the world are diagnosed with different types of cancer, and thousands of them are dying because of cancer. The advent of nanotechnology in biology and medicine field has provided scientists with varied opportunities to develop nano-based drugs, nanomedicines, to overcome limitations associated with the traditional therapies. To use these nanomedicines for cancer therapy, we need to answer many fundamental questions on their interactions with our bodies at the cellular level. Although various studies have enhanced our understanding of many biological aspects of nano-bio-interaction (NBI), the effects of these nanomedicines on the mechanobiology of cells have not been explored well. Before designing nanomedicines, we need to answer fundamental questions about nano-bio-interaction.

How could NPs enter cells? Do they kill cancer or healthy cells? In which region of cells, NPs tend to localize? How physicochemical properties of NPs affect the quality of the interactions in terms of the level of uptake, toxicity, and localization? Do NPs change the cellular structure of cells? Do they have any effects on cell mechanics? If so, how changes in cell mechanics influence the biological functions of cells such as migration? Any research that could help us to enhance our understanding of nano-bio-interaction by answering those questions are highly valuable to design nanomedicines. The work in this dissertation focused on the nano-bio-interaction of gold NPs and cancer cells from both two mentioned aspects while emphasized the importance of cell mechanobiology in cancer therapy. We used different imaging and nanotechnology methods to target those questions and argue on how NPs could modulate the mechanobiology of cells for cancer therapy.

With the aim of designing gold-based nanomedicine for cancer therapy, this thesis took three main steps to improve our understanding of different aspects of nano-bio-interaction: (a) Study the interaction of different gold NPs with healthy and cancer cells in terms of cellular uptake level, entry mechanics, and morphological changes, (b) study the distribution and localization of gold NPs within different cancer cells with optical and spectral measurements, and (c) mechanical measurement of cells to study the interactions of gold NPs and cancer cells from mechanobiological

point of view and to develop possible strategies to control cancer progression with gold NPs. Targeted cancer therapy, intracellular diagnosis, anti-cancer drug development (from mechanics point of view), and design of effective nanoparticle-based drug delivery systems are important potential applications of our findings in this thesis. The summary and the overall conclusion of each step is discussed separately in the following sections:

10.1. Summary and Conclusion

10.1.1. Gold NPs Characterizations and Their NBI with Cancer Cells (Objective #1)

Before using gold NPs for NBI studies, different nanotechnology techniques including SEM, SEM-EDS, UV-spectrometer, DLS, and ICP-MS were used to characterize the gold NPs in terms of size, shape, elemental composition, surface chemistry, and morphology. In the first step, we used two types of gold nanoparticles, which are prepared by two completely different methods. Citrate-capped gold NPs are in a sphere shape and are synthesized chemically by reduction of gold chloride. Another type of gold particles is Swarna Bhasma. These particles are metal-based medicines which are prepared based on the Ayurvedic technique by incineration of gold ribbons under very high temperature. At the same time, they are mixed with herbal extracts, which are thought to have healing effects for various diseases. SB particles are available commercially in powder format, and for our experiment, they suspended in de-ionized water. SEM-EDS and ICP-MS measurements revealed that Au is the main component of both types of particles; however, the measurements confirmed the presence of other elements such as silicon, sodium, oxygen, potassium in the trace elements. The DLS analysis showed the size of nanospheres is in the range of 12-20 nm, and under the same analysis, the average size of SB particles/aggregates were estimated to be in the range of 1~4 μm while their crystals might reach down to 60 nm. Although SBs, due to their larger average size is not in the range of nanoparticles, the smaller size of them could be found in the SEM image. Zeta potential measurements showed negative charges for both type of particles, and nanospheres displayed a higher negative value of charge, proving that they are very stable.

NPs' characterization enabled us to analyze the behavior of NPs within cells with respect to their properties. One normal cell line, HFF-1 (derived from the fibroblast), and one cancer cell line, HeLa (from cervical cancer), were employed to examine both types of gold particles, SB and nanospheres under the same conditions. Analytical imaging techniques, light imaging, and SEM allowed us to perform a detailed study of NBI. We aimed to test the effects of both types of NPs in

both cell lines in terms of compatibility. Two strategies were chosen to examine their compatibility by exposing them to the different dosages of NPs under different exposure times. Light imaging revealed that both SB and nanospheres are not toxic to both normal and cancer cells as no cell death was observed under different incubation times (24, 48, and 72 hours). Besides, with increasing the NPs concentrations, although cells took up more particles, both cells showed no reduced activity in their divisions, appearing both particles are not toxic. One of the most noticeable differences between citrate-capped gold particles and SB in cells is their different levels of internalization. We could see many more nanospheres within cells while distributed uniformly in a specific pattern. However, both cancer and healthy cells took up only a few SB distributed randomly. Microscopic images showed that nanospheres tend to enter cells through receptor-mediated methods while move along microtubules to reach subcellular organelles. They localized mostly at the periphery of the nucleus at the centrosome where cell microtubules are originated from. We performed another comparative study to investigate how both types of NPs enter to healthy and cancer cells. Based on the cellular entry assays, SBs with larger size tended to enter cells by micro-phagocytosis method while citrate-capped particles entered by the receptor-mediated method. When we mechanically broke SBs to smaller sizes, we observed that broken and smaller SBs could enter both cell lines in the same pattern as nanospheres did. Furthermore, staining different parts of cells, including microtubules and nucleus, revealed that the micro-tubular structures of cells remained intact after interaction with nanospheres. However, in the case of SBs, microtubules appeared to be slightly changed. Despite the larger size of SBs, nucleus assays identified a few of them localized in the nucleus. It seems this phenomenon occurs during the cell division when the already entered SBs in the cytoplasm could access the nucleus.

By considering the results as mentioned earlier, it can be concluded that gold nanospheres possess a higher capability to enter cells compared to SBs likely due to their size and shape. Many nanospheres localized at the periphery of the nucleus when they entered cells in the form of vesicles. However, fewer of them appeared scattering in different regions of cells. These nanospheres seemed to escape from vesicles and entered directly into the cytoplasm. These NPs have a chance to directly interact with structural filaments such as F-actin and myosin or other organelles in cells and change the cellular function. We observed their effects on A549 cancer cells in **Chapter 9** in which they altered the mechanobiological properties of cells. Although unbroken SBs could enter cancer cells, they are too large to be effective in delivering herbal extract (or other

reagents) within cancer cells, and due to their larger size, their engulfing process is much longer [13] compared nanospheres or broken SBs. Their random distribution in cancer cells indicates that unlike nanospheres, they are not moving along microtubules and could escape from their vesicles and damage the filamentous networks of cells. SBs are traditionally thought to be effective in fighting various diseases, while our *in vitro* studies showed that they are not toxic to the HeLa cells. Nevertheless, we cannot draw a firm conclusion about their ineffectiveness in cancer cells, and further detailed study is necessary to examine their effects on other different cancer cell lines. All in all, it can be said that even with their larger size, they could enter the cells (both cytoplasm and nucleus), so they can be used as carriers to deliver a higher amount of drugs to cells.

10.1.2. Detection and Localization of Gold NPs in Cancer Cells (Objective #2)

After evaluating the overall behavior of gold NPs in cancer and healthy cells, in the next step, the focus was given to the localization of NPs in cancer cells. In the designing NPs, their precise intracellular localizations are essential as for some diseases and effective therapy, we need to deliver the anti-cancer reagents at specific intracellular regions. We used two different optical techniques not only to confirm the presence of NPs in cells but also to understand the localization of them in cells. We employed Surface-enhanced Raman spectroscopy and hyperspectral imaging for understanding the localization of nanoparticles in cells and characterize their interaction with different subcellular components. We compared these two methods in [2]. We incubated two different cancer cell lines, HepG2 and HeLa cells, with both gold nanospheres and nanostars for a specific time, then fixed them for optical imaging. Nanostars are in a star shape and prepared with the seed-mediated method, and during the preparation process, sharp branches are extruded from their core surface. Raman spectroscopy provides information about different chemical structures of cells whose vibrational frequencies are very weak when they are illuminated with a monochromatic laser. The illuminated light is shifted while producing different peaks. Each peak represents a different chemical structure. Gold NPs could enhance those weak peaks due to their LSPR properties when they localize at very close regions to those structures. Single spectra measurements showed that the enhancement degree is changed depending on the morphology of particles, and the type of cell lines. The Raman spectra showed that HeLa cells took up more nanostars as their enhancement degrees are higher compared to the nanospheres. Raman enhancement signals proved that the SERS effects are not identical for all bands, suggesting that each type of particle interacts differently with different molecular structures. In most bands,

nanostars showed a higher level of enhancement compared to nanospheres due to the specific shape and their higher level of aggregations. We also performed Raman mappings over the entire of single cells to detect the gold NPs spatially by monitoring SERS signals at different regions to find where maximum enhancement happens. We could not perform the mapping with high resolution as we observed that cells are burnt out due to the overexposure. On the other hand, at a lower intensity or at a shorter exposure time, the NPs do not display detectable peaks. Although the SERS method provides valuable information about the interactions of NPs to different components, this method has significant limitations in detecting particles.

Besides Raman spectroscopy, we used a new 2D hyperspectral-based method to detect and localize gold particles. In contrary to the SERS method, the hyperspectral technique provides the visible-near infrared spectral information of thousands of pixels at a shorter time. This advantage of HSI images along LSPR properties of gold NPs allowed us to develop a new approach to diagnose particles at the intracellular level. With this method, we could detect particles within cells while we could estimate their localizations. This technique is based on the fact that the LSPR band is sensitive to the surrounding microenvironment of NPs. Once noble particles are situated in a different environment, the behavior of LSPR is changed in terms of band position and band broadness. We could exploit this phenomenon of noble particles to estimate their localization in cancer cells by comparing their LSPR bands. 2D dark-field images visualize particles with a high contrast resolution, while cannot prove the presence of particles in a biological environment correctly. Hyperspectral images allow confirming their presence by study their spectral information. This technique is a straightforward, reliable, and fast approach for detecting NPs within different intracellular environments. We used this technique to study NBI of there different types of gold NPs in HepG2 and HeLa cell lines. SB particles and two chemically synthesized gold nanoparticles, nanospheres, and nanostars were used to investigate how these NPs could be used to detect intracellular regions. We studied the localization of three different NPs by analyzing their hyperspectral images. The mapping technique was used to explore the distribution of each type of NPs in cells by comparing the spectral information of each pixel with the reference spectra. This technique allows us to even diagnose embedded particle in cells which are not optically visible in the dark-field images. Dark-field images along hyperspectral images revealed the presence of many nanospheres within cells, which were distributed everywhere of cancer cells. Nanostars mostly aggregated within cells and distributed in a random fashion while only a few SBs were detectable

in cells. To prove the feasibility of this technique, we compared the spectra of NPs at different regions in cells: outside, at the periphery (membrane), inside the cytoplasm, and in the nucleus. These regions provide different microenvironments for NPs once they are localized. The spectra of gold NPs reflect the effect of their environment by shifting their band position as well as their broadness. NPs located in the nucleus expressed a broader and larger shift band compared to those in the cytoplasm and the periphery cells. We observed similar behavior for all three types of NPs; however, it depends on the physicochemical properties of cells such as size and shape. Among them, sphere-shaped particles showed a consistent behavior in two different cancer cell lines with higher quality factors.

In the context of this thesis and considering the second objective described in **Chapter 1**, two main conclusions can be drawn, which might be valuable for the development of nanomedicines. Raman measurements suggest the importance of choosing gold NPs with proper shape and size to mediate the affinity of gold nanoparticles to different chemical structures in cells. Nanospheres and nanostars showed different affinities to different molecular structures of cells. This shape-dependent tendencies of gold NPs need to be considered in designing gold nanomedicines as drugs may have different efficacies depending on their molecular targets in cells. Although the SERS technique offers detailed information on the gold NPs-molecular structures, this technique does not provide high-throughput measurements, and the interpretation of their results is not straightforward. The hyperspectral technique is a fast approach for NBI study and not only allows the detection of gold NPs inside cells but also gives an estimation on their microenvironment. This property is highly important, specifically for 2D measurements. This method opens a new avenue in the NBI field, cancer therapy, and diagnosis as it allows us to detect nanoparticles in different regions inside cells with a fast, straightforward, and non-invasive technique. The mapping of the hyperspectral images allowed us to determine the distribution of three different particles correctly within cells. The predictable distributions of nanospheres showed their great potentials to be used for the development of nanomedicines compared to two other types. On the other hand, they are promising candidates for intracellular diagnosis due to their consistent behavior in cells. As a proof-of-concept, we considered only three main regions of cells (periphery of cells, the periphery of nucleus, and inside nucleus) for intracellular plasmonics; however, this technique can be further developed to detect other organelles in cells by creating a library of

plasmonic shifts for different intracellular components. This can happen when gold nanoparticles with consistent behavior is used to move into different intracellular localizations.

SB particles showed no significant cellular uptake in cancer cells, and few of them only could enter while distributed randomly, so we did not investigate their effects on the Mechanobiology of cancer in **Chapter 9**. Due to the larger size of SBs and their non-specific shape, their hyperspectral images do not provide further information on their localizations as their spectral changes cannot reflect perfectly the effects of their microenvironment. As we suggested in **Chapter 3**, we need to break them mechanically to enhance their effectiveness in cells. For future works, the live hyperspectral and Raman measurements of cells are recommended to investigate the dynamic NBI between cancer cells and gold NPs. This study can be performed with the introduced microfluidic in **Chapter 6**. This efficient micro-chip can be used to gently trap cancer cells to study the dynamic interaction of nanoparticles and cells.

10.1.3. Gold NPs for Fighting Metastasis through Mechanobiological Changes (Objective #3 and #4)

After our fundamental investigation in NBI between gold NPs and cancer cells in the first two steps of this dissertation, we aimed to study their potential to be used for cancer therapy in the context of cell mechanics. We observed that gold particles are not biologically toxic to the cancer cells, suggesting that they could be used as nano-carriers for cancer therapy. In this step of my research, we investigated the potential of unmodified gold NPs for cancer therapy from a different point of view.

Before studying the effects of NPs on the mechanobiology of cells, we developed a fluid-structure interaction model to computationally study the mechanobiology of both cancer and healthy cells when they are exposed to the hydrodynamic forces. The softness level of cancer cells was reported by many researchers to be essential for cell mechanosensing. Our model revealed that benign and malignant breast cancer cells express different levels of deformation under the hydrodynamic shear stress as they have different elasticities. Cellular deformation is critical in biological functions such as cell division and cell migration. The model showed that under a stationary condition, the invasive human breast cancer cells experience low values of stress on their membrane compared to the benign and non-invasive cells. In the channel which mimics the interstitial fluid flow (**Chapter 7**), the effects of normal forces (pressure) were found higher compared to the viscous forces on the membrane of cells. Our simulation highlights the importance

of cell stiffness on the mechanobiology of cells. In this regard, in **Chapter 9**, we studied how the mechanobiology of cells contributes to cancer migration and progression. The stiffness of cells has been proved to be changed during the cancer progression (mesenchymal-like state), and several works have shown that cancerous and invasive cells become softer compared to their counterparts. These types of cells are fluid-like cancer cells, such as human breast cancer cells and ovarian cancer cells. However, cancer cells with the opposing behavior (stiffer) are called rigid-like cancer cells such as cortical and prostate cancer cells. Metastatic cancer cells are highly invasive and could move to other organs and spread cancer throughout the body. This requires mechanobiological changes in cancer cells. Cell deformation and force transmission are two necessary phenomena for cell migration. F-actins in connection with myosin networks generate the contractile force required for cell movement. Depending on the configuration of cells and their stiffness, the force is transmitted while the cell body undergoes deformation. Our approximate model showed that these two phenomena are correlated inversely to each other. For fast migration, it should be a balance between deformation and force transmission. Elastic strain energy could express the effects of these two parameters in a unique way. This stiffness-dependent parameter, migratory index, approximates the migration of cancer cells required for cancer invasiveness. Cancerous cells need to either increase or decrease their stiffness to reach a higher migratory index, while normal and non-invasive cells tend to have a lower migratory index. The migratory model and the numerical study showed that there is a range of elasticity in which the migratory ability of cells is approximated to be maximum. This range is critical because it allows cancer cells to become highly motile, which is essential for metastasis in the body. Any strategy which could reduce the migratory index can be useful to inhibit cell migration required for cancer progression. Based on the approximate migratory model, benign and non-invasive cells even could be softer than invasive cells. Many works mentioned that stiffness of cells could be used as a mechanical biomarker for diagnosis of cancer and invasiveness, while based on our study, measuring the migratory index could provide a more precise evaluation of the cancer progression. In **Chapter 9,** we validated this concept by measuring the mechanobiological properties of A549 cancer cells.

In the last chapter of my dissertation, the potential of gold NPs for cancer therapy was studied. We used two different morphologies of gold NPs, which already showed better internalization in cancer cells. Immunofluorescent imaging revealed that gold NPs localize where they could directly interact with myosin networks and change their organizations. The reflection

of these changes can be seen in the mechanobiology of cancer cells as myosin networks are molecular motors that help cells to generate forces and move forward. AFM measurements proved that the nanospheres and nanostars could reduce the elasticity of A549 cells compared to the control or non-treated cells. Further study showed that NPs-treated cells lose their adhesion (membrane adhesion) with their AFM tip. We also observed less activity in the migration of the treated and softer cells compared to control cells. The results suggest that gold nanospheres could potentially control cancer migration required for metastatic of A549 cancer cells by softening their bodies. Our approximate migratory model verified that the migratory ability of NP-treated cancer cells is reduced compared to control cells when their elasticity is reduced to 6 kPa.

The last step of this dissertation highlights the importance of cell mechanobiology in the NBI field and cancer therapy. In designing nanomedicines for cancer therapy, the mechanobiology of cancer cells has received little attention while they play key roles in cancer progression. This thesis showed how even unmodified gold NPs could be used for the treatment of cancer by reducing their migratory potential of cells. Although gold nanospheres cannot kill the cancer cells, they could potentially slow down the migratory potential of cells required for the metastatic process in the body, which is the main reason of the cancer-related mortality. This potential of gold nanoparticles opens a new avenue to design more effective gold-based nanomedicines to be used for cancer therapy. We could determine the efficacy of gold nanoparticles by measuring the migratory index of treated cells. Our migratory index model showed that nanomedicine with anti-elastic properties (a property to change the elasticity of cells) could be designed to control the cancer migration. Many researchers showed normal and non-invasive cells are stiffer than cancer and invasive cells, so we can reduce the risk of cancer progression by stiffening the cancer cells[139][421]. However, this is not always a correct statement. There are plenty of works that contradict this belief, showing that softer cells are less invasive or stiffer cells are more invasive[119][368][138][356]. These contradictory results indicate that always, cell stiffness cannot predict the risk of cancer correctly. We highlighted the importance of the migratory index rather than stiffness for predicting cancer progression. In **Chapter 1**, we discussed different microfluidic chips to measure the mechanical properties of single cells as a biomarker for cancer detection. Those microsystems can be tuned to directly measure the migratory index based on the configuration and bulk elasticity of cells to detect cancer at early stage.

10.2. Future Works

The main objective of this dissertation was to investigate the NBI between gold NPs and cancer to figure out their potential for regulating the mechanobiology of cancer cells for cancer therapy. As was described above, we accomplished different steps to fulfill the objectives of this thesis. Among different gold NPs, gold nanospheres appeared to be more effective for cancer therapy, intracellular plasmonics, and intracellular diagnosis. In each step of this thesis, there are some recommendations that would be helpful for future investigations.

10.2.1. Studying the Effects of Other Physicochemical Parameters on NBI

a) For future investigations, the effects of other important physicochemical parameters of gold NPs can be studied. The surface chemistry of gold NPs influences the quality of their interaction with cancer cells in terms of toxicity and internalization. In our experiments in this thesis, synthesized gold particles were coated with citrate. We used sodium citrate as reducing agents and non-aggregation agents for preparing gold NPs. This citrate provides negatively charged ions and gets absorbed on the gold NPs. So, their interactions with the negatively charged membrane of cells cannot be very effective. For future studies, the surface of NPs can be coated with positive ligands such as polyethylene glycol (PEG). They are expected to have more effective interaction which might impact the toxicity, bio-distribution of NPs as well as the cellular structures of cancer cells.

b) We observed that SBs are not good in internalization, and only a few of them could enter cells even after a longer incubation time. Due to their low level of cellular entry, their therapeutic effects might not be explored well. We understood that by breaking SBs, we could enhance their internalization while still, the cellular uptake of broken SBs are low compared to gold nanospheres. For future works, nanospheres can be designed such that they have similar therapeutic effects of SBs. We can make this condition happened by coating nanospheres with the therapeutic agents either mechanically or chemically. During the preparation of SBs, gold particles are mixed with herbal extracts, which are believed to be useful for curing diseases. With this strategy, we exploit the higher ability of nanospheres for internalization while coating them with herbal extract allows us to take advantage of their therapeutic effects. For

future works, the designing and testing such modified gold NPs in cells can be considered for cancer therapy.

c) The nanostars showed a higher level of aggregation in cells, and we could see only few of them individually within cells. Due to their low stability, they tend to become more stable by transforming their shape to spheres or shorting the length of their branches. So, after a longer incubation time, they might not show their real potential perfectly in cells. For future works, different strategies can be taken to stabilize them and study their longer effects in cells. For future studies, it is worth considering rod-shaped gold NPs in cells. Gold nanorods could solely mimic the effects of nanostars branches in cells.

10.2.2. Designing Consistent Nanospheres for Intracellular Diagnosis

a) We showed that nanospheres are good candidates for intracellular diagnosis. Despite of the more consistent size and shape of nanospheres, in our experiment, it was difficult to find two identical particles in the same size and shape to compare their LSPR bands for intracellular diagnosis. Nanospheres could be prepared under controllable conditions to produce identical particles and perform precise intracellular detections with the hyperspectral concept. Synthesizing inside microfluidics could provide a better environment to prepare more consistent NPs for really applicable intracellular diagnosis.

b) For future works, by preparing more consistent NPs in size and shape, the optical properties of different regions of cells can be predicted by hyperspectral imaging. We observed that LSPR band shifts of particles could provide information about their microenvironment. With the modeling of gold particles and their microenvironment, and performing a reverse calculation, we can predict the optical properties (e.g. refractive index) in different intracellular regions of cells. In reverse modeling, the optical properties of the desired regions can be changed to get a similar band shift in the experiments. For instance, for this method, we can determine the refractive index of the nucleus, cytoplasm, and membrane.

c) In the current work, we studied the NBI of different types of gold NPs with cancer cells while they are fixed on the microscopic glasses. This method cannot provide the dynamic interactions between gold NPs and cells. The combination of SERS with microfluidic can provide online label-free bio-sensing methods to study the dynamic

interaction of cells and nanoparticles. With microfluidic, under controllable conditions, the particles can be loaded to channels for interactions with the desired cells. In **Chapter 6**, we introduced a microfluidic to position cells at already defined trapping sites. Due to the gentle trapping, cells undergo no damaging stress values under flowing conditions. For future works, this microsystem can be implemented to capture cancer cells for SERS or hyperspectral detections in the fluidic channel.

10.2.3. Designing Microfluidics to Study the Effects of Drugs on Migratory Index

a) In **Chapter 8**, we developed a simplified 2D model to approximate the migratory potential of cells based on their bulk stiffness. For future works, one can develop a 3D model for the migratory index to study the migratory index in a more *in vivo*-like environment. Moreover, more parameters such as forces from the environment can be taken into account.

b) In **Chapter 6**, we introduced a new concept to approximate the mobility potential of cells by measuring their migratory index values. This concept can approximate the migratory potential of cells, which is essential for cancer progression. For future works, a microfluidic device is recommended to measure stiffness and, consequently, the migratory index of cells to evaluate the efficacy of the anti-cancer drugs. In the context of cell mechanics, effective anti-cancer drugs need to reduce the migratory potential of cells and inhibit cancer progression. A successful drug has to be able to either reduce or increase the elasticity of cells while the migratory index is decreased. In this system, cancer cells undergo a known force to measure the cellular deformation and estimate the elasticity of cells, then based on their shapes, their migratory values are calculated. This device can be used to design or optimize anti-cancer drugs to either increase the cell elasticity from Sm to S2 or decrease the elasticity from Sm to S1 to control the migratory potential of cells (**Figure 8-10**).

c) The gold nanoparticles can be conjugated with anti-cancer compounds, and their efficacy can be evaluated with the microfluidic presented in **Chapter 6** by measuring the cellular deformation, elasticity of cells, and using the migratory index concept.

d) In **Chapter 9,** we used the scratch assay to evaluate the migrating ability of cells. This experiment happened at the bottom of the six-well petri dish. This experiment can be done inside microfluidic by designing different channels for culturing cells. The free-

gaps between very confluent cells can be performed by precisely loading the remover chemical to the desired place. Then, the migration ability of cells can be done in a controllable environment.

e) Our results revealed that the gold nanospheres could reduce the migration potential of cancer cells by changing the organization of cells. For future study, the organization changes can be investigated by confocal live imaging to characterize the F-actin networks of cancer cells with further detailed information. Study the random migration of single treated cancer cells is also recommended to get more detailed information on the migration of cells. Moreover, it is worth to study the effects of the same gold nanospheres into healthy cells to investigate whether they have any negative effects on the mechanobiology of healthy cells.

10.3. Contributions

10.3.1. Journal papers

1. **Ahmad Sohrabi Kashani**, Kevin Larocque, Alisa Piekny and Muthukumaran Packirisamy, "Regulation of Migratory Capabilities of Human Lung Cancer Cells through Nano-Bio-Interaction" (Submitted to ***RCS Nanoscale Advances*** Journal- March **2020**)

2. **Ahmad Sohrabi Kashani**, Alisa Piekny and Muthukumaran Packirisamy, "Using intracellular plasmonic to characterize nano-morphology in Human cells" (Submitted to ***Nature - Microsystem And Nanoengineering*** Journal- December **2019**)

3. **Ahmad Sohrabi Kashani**, Simona Badilescu, Alisa Piekny, and Muthukumaran Packirisamy, "Differing Affinities of Gold Nanostars and Nanospheres toward HeLa and HepG2 Cells: Implications for Cancer Therapy" (Revision, ***ACS Applied Nano Material*** Journal- January **2020**)

4. **Ahmad Sohrabi Kashani**, Alisa Piekny and Muthukumaran Packirisamy, "Effects of Cellular Bulk Stiffness on Migratory Potential of Cells" (Submitted to ***Royal Society Interface*** Journal- March **2020**)

5. **Ahmad Sohrabi Kashani**, and Muthukumaran Packirisamy, "Efficient low shear flow-based trapping of biological entities", **(2019)**, ***Nature Scientific Reports*****,** 9 (1), pp.1-15.

6. **Ahmad Sohrabi Kashani**, Simona Badilescu, Alisa Piekny, and Muthukumaran Packirisamy, **(2019)**" Perspective- Nano-bio-interaction in treatment and management of cancer", **(2019)**, ***Journal of the Electrochemical Society***, 166(9), p.B3007.

7. **Ahmad Sohrabi Kashani**, Kiran Kuruvinashetti, Daniel Beaudet, Simona Badilescu, Alisa Piekny, Muthukumaran Packirisamy, **(2018)**, "Enhanced Internalization of Indian Ayurvedic Swarna Bhasma (Gold Nanopowder) in Human Cells", ***Nanoscience and Nanotechnology*** - ASP, pp. 6791-6798, v. 18, no. 10

8. **Ahmad Sohrabi Kashani**, Muthukumaran Packirisamy, **(2017),** "cellular deformation characterization of human breast cancer cells under hydrodynamic forces, ***AIMS Biophys,*** 4 (2017): 400-414.

9. Kiran Kuruvinashetti, **Ahmad Sohrabi Kashani,** Simona Badilescu, Daniel Beaudet, Alisa Piekny, and Muthukumaran Packirisamy, **(2018)**. Intracellular Localized Surface Plasmonic Sensing for Subcellular Diagnosis. ***Plasmonics Journal*** **-Springer** , 13(5), pp.1639-1648.

10. Daniel Beaudet, Simona Badilescu, Kiran Kuruvinashetti, **Ahmad Sohrabi Kashani**, Dilan Jaunky, Sylvie Ouellette, Alisa Piekny, Muthukumaran Packirisamy, **(2017)**, "Comparative study on cellular entry of incinerated ancient gold particles (Swarna Bhasma) and chemically synthesized gold particles", ***Nature Scientific Report*****,** 7(1), pp.1-12.

10.3.2. Conference papers

1. Subha Parimalam, **Ahmad Sohrabi Kashani**, Simona Badilescu, Rama Bhat, Alisa Piekny, and Muthukumaran Packriisamy, Indian medicine incinerated silver particles and their application in cancer therapy. 3th international conference on theoretical and applied nanoscience and nanotechnology. Ottawa, Canada (12-14 June 2019)
2. **Ahmad Sohrabi Kashani**, Simona Badilescu, Alisa Piekny, and Muthukumaran Packirisamy, Gold nanoparticles modulate the mechanobiological properties of human lung cancer cells, 35th annual meeting of the Canadian biomaterial society, Quebec city, Canada (May - 2019)
3. **Ahmad Sohrabi Kashani**, Simona Badilescu, Alisa Piekny, and Muthukumaran Packirisamy, Nano-Bio-Interaction of Gold nanoparticles with cancer cells and Impact on

biophysical properties, 4th world congress on recent advances in nanotechnology, Rome, Italy (April- 2019)

4. **Ahmad Sohrabi Kashani**, Simona Badilescu, Alisa Piekny, and Muthukumaran Packirisamy. Uptake of Medium-size Gold Nanoparticles in the Nucleus of Living cells. 2th International Conference on Theoretical and Applied Nanoscience and Nanotechnology (June- 2018), Niagara Fall, Canada
5. Vahid KaramZadeh., Shervin Foroughi, **Ahmad Sohrabi Kashani**, and Muthukumaran Packirisamy, Characterization of a 3D Printed Mold for a Cell Culturing Microfluidic Device, International Conference of Fluid Flow, Heat and Mass Transfer, (June- 2018), Niagara Fall, Canada
6. **Ahmad Sohrabi Kashani**, Simona Badilescu, Alisa Piekny, and Muthukumaran Packirisamy. A Non-Invasive Method for Intracellular Localization of Gold Nanoparticles in Cancer Cells, North Photonic (July- 2018), Montreal, Canada
7. **Ahmad Sohrabi Kashani**, Muthukumaran Packirisamy, Javad Dargahi, Quality factor optimization of microcantilever sensors immerses in viscous fluids. 4th international conference on knowledge-based engineering and innovation. Tehran, December (2017)
8. **Ahmad Sohrabi Kashani**, Muthukumaran Packirisamy. Effect of Geometry of Microfluidic on Hydrodynamic SingleCell Trapping, 14th U.S. National Congress on Computational Mechanics July, (2017), Montreal, Quebec, Canada

References

[1] E. Pérez-Herrero and A. Fernández-Medarde, "Advanced targeted therapies in cancer: Drug nanocarriers, the future of chemotherapy," *Eur. J. Pharm. Biopharm.*, vol. 93, no. March, pp. 52–79, 2015.

[2] M. TATEMICHI, "Global cancer data," *J. Med. Soc. Toho Univ.*, vol. 50, no. 1, pp. 106–107, 2003.

[3] P. Mehlen and A. Puisieux, "Metastasis: A question of life or death," *Nat. Rev. Cancer*, vol. 6, no. 6, pp. 449–458, 2006.

[4] B. A. Chabner and T. G. Roberts Jr, "Chemotherapy and the war on cancer," *Nat. Rev. Cancer*, vol. 5, no. 1, p. 65, 2005.

[5] C.-Y. Zhao, R. Cheng, Z. Yang, and Z.-M. Tian, "Nanotechnology for Cancer Therapy Based on Chemotherapy," *Molecules*, vol. 23, no. 4, p. 826, Apr. 2018.

[6] W. H. Gmeiner and S. Ghosh, "Nanotechnology for cancer treatment," *Nanotechnol. Rev.*, vol. 3, no. 2, pp. 111–122, Jan. 2014.

[7] A. Jurj, C. Braicu, L. A. Pop, C. Tomuleasa, C. D. Gherman, and I. Berindan-Neagoe, "The new era of nanotechnology, an alternative to change cancer treatment," *Drug Des. Devel. Ther.*, vol. 11, pp. 2871–2890, 2017.

[8] J. D. Byrne, T. Betancourt, and L. Brannon-Peppas, "Active targeting schemes for nanoparticle systems in cancer therapeutics," *Adv. Drug Deliv. Rev.*, vol. 60, no. 15, pp. 1615–1626, 2008.

[9] M. F. Attia, N. Anton, J. Wallyn, Z. Omran, and T. F. Vandamme, "An overview of active and passive targeting strategies to improve the nanocarriers efficiency to tumour sites," *J. Pharm. Pharmacol.*, vol. 71, no. 8, pp. 1185–1198, Aug. 2019.

[10] T. Sun, Y. S. Zhang, B. Pang, D. C. Hyun, M. Yang, and Y. Xia, "Engineered nanoparticles for drug delivery in cancer therapy," *Angew. Chemie - Int. Ed.*, vol. 53, no. 46, pp. 12320–12364, 2014.

[11] S. Suri, H. Fenniri, and B. Singh, "Nanotechnology-based drug delivery systems," *J.*

Occup. Med. Toxicol., vol. 2, no. 1, p. 16, 2007.

[12] Y. Wang, R. Cai, and C. Chen, "The Nano-Bio Interactions of Nanomedicines: Understanding the Biochemical Driving Forces and Redox Reactions," *Acc. Chem. Res.*, vol. 52, no. 6, pp. 1507–1518, 2019.

[13] S. Behzadi *et al.*, "Cellular uptake of nanoparticles: Journey inside the cell," *Chem. Soc. Rev.*, vol. 46, no. 14, pp. 4218–4244, 2017.

[14] B. Yameen, W. Il Choi, C. Vilos, A. Swami, J. Shi, and O. C. Farokhzad, "Insight into nanoparticle cellular uptake and intracellular targeting," *J. Control. Release*, vol. 190, pp. 485–499, Sep. 2014.

[15] S. Valetti, S. Mura, B. Stella, and P. Couvreur, "Rational design for multifunctional non-liposomal lipid-based nanocarriers for cancer management : theory to practice," vol. 11, no. Suppl 1, pp. 1–17, 2013.

[16] T. F. Martens, K. Remaut, J. Demeester, S. C. De Smedt, and K. Braeckmans, "Intracellular delivery of nanomaterials: How to catch endosomal escape in the act," *Nano Today*, vol. 9, no. 3, pp. 344–364, 2014.

[17] L. C. Cheng, X. Jiang, J. Wang, C. Chen, and R. S. Liu, "Nano-bio effects: Interaction of nanomaterials with cells," *Nanoscale*, vol. 5, no. 9, pp. 3547–3569, 2013.

[18] N. D. Donahue, H. Acar, and S. Wilhelm, "Concepts of nanoparticle cellular uptake, intracellular trafficking, and kinetics in nanomedicine," *Adv. Drug Deliv. Rev.*, 2019.

[19] X. Li, L. Wang, Y. Fan, Q. Feng, and F. Cui, "Biocompatibility and Toxicity of Nanoparticles and Nanotubes," *J. Nanomater.*, vol. 2012, pp. 1–19, 2012.

[20] D. F. Williams, "On the mechanisms of biocompatibility," *Biomaterials*, vol. 29, no. 20, pp. 2941–2953, 2008.

[21] S. Naahidi, M. Jafari, F. Edalat, K. Raymond, A. Khademhosseini, and P. Chen, "Biocompatibility of engineered nanoparticles for drug delivery," *J. Control. Release*, vol. 166, no. 2, pp. 182–194, 2013.

[22] Z. Aguilar, *Nanomaterials for Medical Applications*. Newnes, 2013.

[23] S. Ahn, E. Seo, K. H. Kim, and S. J. Lee, “Physical property control on the cellular uptake pathway and spatial distribution of nanoparticles in cells,” *J. Biomed. Nanotechnol.*, vol. 11, no. 6, pp. 1051–1070, 2015.

[24] V. Serpooshan *et al.*, “Effect of Cell Sex on Uptake of Nanoparticles: The Overlooked Factor at the Nanobio Interface,” *ACS Nano*, vol. 12, no. 3, pp. 2253–2266, 2018.

[25] T. Mironava, M. Hadjiargyrou, M. Simon, V. Jurukovski, and M. H. Rafailovich, “Gold nanoparticles cellular toxicity and recovery: effect of size, concentration and exposure time,” *Nanotoxicology*, vol. 4, no. 1, pp. 120–137, 2010.

[26] Z. J. Zhu *et al.*, “The interplay of monolayer structure and serum protein interactions on the cellular uptake of gold nanoparticles,” *Small*, vol. 8, no. 17, pp. 2659–2663, 2012.

[27] A. S. Kashani, S. Badilescu, A. Piekny, and M. Packirisamy, “Bio-nano-interaction in treatment and management of cancer,” *J. Electrochem. Soc.*, vol. 166, no. 9, pp. B3007–B3011, 2019.

[28] S. Zhang, H. Gao, and G. Bao, “Physical Principles of Nanoparticle Cellular Endocytosis,” *ACS Nano*, vol. 9, no. 9, pp. 8655–8671, 2015.

[29] M. Zhu, G. Nie, H. Meng, T. Xia, A. Nel, and Y. Zhao, “Physicochemical properties determine nanomaterial cellular uptake, transport, and fate,” *Acc. Chem. Res.*, vol. 46, no. 3, pp. 622–631, 2013.

[30] B. D. Chithrani, A. A. Ghazani, and W. C. W. Chan, “Determining the size and shape dependence of gold nanoparticle uptake into mammalian cells,” *Nano Lett.*, vol. 6, no. 4, pp. 662–668, 2006.

[31] B. Marrow, S. Secreted, and C. Protect, “Insight into nanoparticle cellular uptake and intracellular targeting,” *J Control Release*, vol. 71, no. 11, pp. 3831–3840, 2014.

[32] W. Jiang, B. Y. S. Kim, J. T. Rutka, and W. C. W. Chan, “Nanoparticle-mediated cellular response is size-dependent,” *Nat. Nanotechnol.*, vol. 3, no. 3, pp. 145–150, 2008.

[33] K. Huang *et al.*, “Size-dependent localization and penetration of ultrasmall gold nanoparticles in cancer cells, multicellular spheroids, and tumors in vivo,” *ACS Nano*, vol.

6, no. 5, pp. 4483–4493, 2012.

[34] W. K. Ko *et al.*, “The effect of gold nanoparticle size on osteogenic differentiation of adipose-derived stem cells,” *J. Colloid Interface Sci.*, vol. 438, pp. 68–76, 2015.

[35] A. Albanese and W. C. W. Chan, “Effect of gold nanoparticle aggregation on cell uptake and toxicity,” *ACS Nano*, vol. 5, no. 7, pp. 5478–5489, 2011.

[36] Y. P. Jia, B. Y. Ma, X. W. Wei, and Z. Y. Qian, “The in vitro and in vivo toxicity of gold nanoparticles,” *Chinese Chem. Lett.*, vol. 28, no. 4, pp. 691–702, 2017.

[37] S. J. Soenen *et al.*, “Cytotoxic effects of gold nanoparticles: A multiparametric study,” *ACS Nano*, vol. 6, no. 7, pp. 5767–5783, 2012.

[38] Y. Pan *et al.*, “Size-dependent cytotoxicity of gold nanoparticles,” *Small*, vol. 3, no. 11, pp. 1941–1949, 2007.

[39] P. M. Favi *et al.*, “Shape and surface effects on the cytotoxicity of nanoparticles: Gold nanospheres versus gold nanostars,” *J. Biomed. Mater. Res. - Part A*, vol. 103, no. 11, pp. 3449–3462, 2015.

[40] B. D. Chithrani, A. A. Ghazani, and W. C. W. Chan, “Determining the size and shape dependence of gold nanoparticle uptake into mammalian cells,” *Nano Lett.*, vol. 6, no. 4, pp. 662–668, 2006.

[41] X. Xie, J. Liao, X. Shao, Q. Li, and Y. Lin, “The Effect of shape on Cellular Uptake of Gold Nanoparticles in the forms of Stars, Rods, and Triangles,” *Sci. Rep.*, vol. 7, no. 1, pp. 1–9, 2017.

[42] H. Herd, N. Daum, A. T. Jones, H. Huwer, H. Ghandehari, and C.-M. Lehr, “Nanoparticle Geometry and Surface Orientation Influence Mode of Cellular Uptake,” *ACS Nano*, vol. 7, no. 3, pp. 1961–1973, Mar. 2013.

[43] A. A. Salyers and D. D. Whitt, “A molecular approach,” *Bact. Pathog.*, pp. 53–100, 2002.

[44] Y. Li and N. Gu, “Thermodynamics of charged nanoparticle adsorption on charge-neutral membranes: A simulation study,” *J. Phys. Chem. B*, vol. 114, no. 8, pp. 2749–2754, 2010.

[45] E. C. Cho, J. Xie, P. A. Wurm, and Y. Xia, “Understanding the role of surface charges in

cellular adsorption versus internalization by selectively removing gold nanoparticles on the cell surface with a I 2/KI etchant," *Nano Lett.*, vol. 9, no. 3, pp. 1080–1084, 2009.

[46] R. R. Arvizo *et al.*, "Effect of nanoparticle surface charge at the plasma membrane and beyond," *Nano Lett.*, vol. 10, no. 7, pp. 2543–2548, 2010.

[47] T. S. Hauck, A. A. Ghazani, and W. C. W. Chan, "Assessing the effect of surface chemistry on gold nanorod uptake, toxicity, and gene expression in mammalian cells," *Small*, vol. 4, no. 1, pp. 153–159, 2008.

[48] Y. Jiang *et al.*, "The Interplay of Size and Surface Functionality on the Cellular Uptake of Sub-10 nm Gold Nanoparticles," *ACS Nano*, vol. 9, no. 10, pp. 9986–9993, 2015.

[49] Y.-C. Yeh, K. Saha, B. Yan, O. R. Miranda, X. Yu, and V. M. Rotello, "The role of ligand coordination on the cytotoxicity of cationic quantum dots in HeLa cells," *Nanoscale*, vol. 5, no. 24, p. 12140, Feb. 2013.

[50] D. Bartczak and A. G. Kanaras, "Diacetylene-containing ligand as a new capping agent for the preparation of water-soluble colloidal nanoparticles of remarkable stability," *Langmuir*, vol. 26, no. 10, pp. 7072–7077, 2010.

[51] A. Chompoosor *et al.*, "The Role of Surface Functionality on Acute Cytotoxicity, ROS Generation and DNA Damage by Cationic Gold Nanoparticles," *Small*, vol. 6, no. 20, pp. 2246–2249, Oct. 2010.

[52] M. Krieg *et al.*, "Atomic force microscopy-based mechanobiology," *Nat. Rev. Phys.*, vol. 1, no. 1, pp. 41–57, Jan. 2019.

[53] K. A. Jansen, D. M. Donato, H. E. Balcioglu, T. Schmidt, E. H. J. Danen, and G. H. Koenderink, "A guide to mechanobiology: Where biology and physics meet," *Biochimica et Biophysica Acta - Molecular Cell Research*, vol. 1853, no. 11. Elsevier B.V., pp. 3043–3052, 2015.

[54] D.-H. Kim, P. K. Wong, J. Park, A. Levchenko, and Y. Sun, "Microengineered Platforms for Cell Mechanobiology," *Annu. Rev. Biomed. Eng.*, vol. 11, no. 1, pp. 203–233, 2009.

[55] K. A. Jansen, D. M. Donato, H. E. Balcioglu, T. Schmidt, E. H. J. Danen, and G. H.

Koenderink, “A guide to mechanobiology: Where biology and physics meet,” *Biochim. Biophys. Acta - Mol. Cell Res.*, vol. 1853, no. 11, pp. 3043–3052, 2015.

[56] M. L. Rodriguez, P. J. McGarry, and N. J. Sniadecki, “Review on Cell Mechanics: Experimental and Modeling Approaches,” *Appl. Mech. Rev.*, vol. 65, no. 6, p. 060801, Nov. 2013.

[57] Y. Zheng, J. Nguyen, Y. Wei, and Y. Sun, “Recent advances in microfluidic techniques for single-cell biophysical characterization,” *Lab Chip*, vol. 13, no. 13, pp. 2464–2483, 2013.

[58] G. Y. H. Lee and C. T. Lim, “Biomechanics approaches to studying human diseases,” *Trends Biotechnol.*, vol. 25, no. 3, pp. 111–118, 2007.

[59] D. E. Ingber, “Tensegrity I. Cell structure and hierarchical systems biology,” *J. Cell Sci.*, vol. 116, no. 7, pp. 1157–1173, 2003.

[60] M. Fechheimer, “ Cell and Molecular Biology: Concepts and Experiments . Gerald Karp ,” *Q. Rev. Biol.*, vol. 75, no. 4, pp. 454–454, Dec. 2000.

[61] K. Lykov, Y. Nematbakhsh, M. Shang, C. T. Lim, and I. V. Pivkin, “Probing eukaryotic cell mechanics via mesoscopic simulations,” *PLoS Comput. Biol.*, vol. 13, no. 9, pp. 1–22, 2017.

[62] K. N. Dahl, A. J. S. Ribeiro, and J. Lammerding, “Nuclear shape, mechanics, and mechanotransduction,” *Circ. Res.*, vol. 102, no. 11, pp. 1307–1318, 2008.

[63] P. A. Pullarkat, P. A. Fernández, and A. Ott, “Rheological properties of the eukaryotic cell cytoskeleton,” *Phys. Rep.*, vol. 449, no. 1–3, pp. 29–53, 2007.

[64] F. A. Cotton, G. Wilkinson, C. a. Murillo, and M. Bochmann, *Advanced Inorganic Chemistry, 6th Edition*. 1999.

[65] S. Suresh, “Biomechanics and biophysics of cancer cells,” *Acta Mater.*, vol. 55, no. 12, pp. 3989–4014, 2007.

[66] D. A. Fletcher and R. D. Mullins, “Cell mechanics and the cytoskeleton,” *Nature*, vol. 463, no. 7280, pp. 485–492, Jan. 2010.

[67] H. Hatami-Marbini and M. R. K. Mofrad, “Cytoskeletal Mechanics and Cellular

Mechanotransduction: A Molecular Perspective," no. February 2011, 2010, pp. 3–27.

[68] D. Sears, "Protein structure prediction: Concepts and applications," *Biochem. Mol. Biol. Educ.*, vol. 35, no. 1, pp. 79–80, Jan. 2007.

[69] L. E. Ford, "Mechanics of Motor Proteins and the Cytoskeleton (review)," *Perspect. Biol. Med.*, vol. 45, no. 2, pp. 305–307, 2002.

[70] S. Pellegrin and H. Mellor, "Actin stress fibers," *J. Cell Sci.*, vol. 120, no. 20, pp. 3491–3499, 2007.

[71] M. Lekka, P. Laidler, D. Gil, J. Lekki, Z. Stachura, and A. Z. Hrynkiewicz, "Elasticity of normal and cancerous human bladder cells studied by scanning force microscopy," *Eur. Biophys. J.*, vol. 28, no. 4, pp. 312–316, 1999.

[72] M. Li, D. Dang, L. Liu, N. Xi, and Y. Wang, "Atomic force microscopy in characterizing cell mechanics for biomedical applications: A review," *IEEE Trans. Nanobioscience*, vol. 16, no. 6, pp. 523–540, 2017.

[73] W. R. Trickey, G. M. Lee, and F. Guilak, "Viscoelastic properties of chondrocytes from normal and osteoarthritic human cartilage," *J. Orthop. Res.*, vol. 18, no. 6, pp. 891–898, 2000.

[74] N. Bellini *et al.*, "Femtosecond laser fabricated monolithic chip for optical trapping and stretching of single cells," *Opt. Express*, vol. 18, no. 5, p. 4679, 2010.

[75] M. F. Coughlin, M. Puig-de-Morales, P. Bursac, M. Mellema, E. Millet, and J. J. Fredberg, "Filamin-A and rheological properties of cultured melanoma cells," *Biophys. J.*, vol. 90, no. 6, pp. 2199–2205, 2006.

[76] S. Byun *et al.*, "Characterizing deformability and surface friction of cancer cells," *Proc. Natl. Acad. Sci.*, vol. 110, no. 19, pp. 7580–7585, 2013.

[77] D. R. Gossett *et al.*, "Hydrodynamic stretching of single cells for large population mechanical phenotyping," *Proc. Natl. Acad. Sci.*, vol. 109, no. 20, pp. 7630–7635, 2012.

[78] G. Binnig, C. F. Quate, and C. Gerber, "Atomic Force Microscope," *Phys. Rev. Lett.*, vol. 56, no. 9, pp. 930–933, Mar. 1986.

[79] S. Senapati and S. Lindsay, “Recent Progress in Molecular Recognition Imaging Using Atomic Force Microscopy,” *Acc. Chem. Res.*, vol. 49, no. 3, pp. 503–510, 2016.

[80] G. Thomas, N. A. Burnham, T. A. Camesano, and Q. Wen, “Measuring the Mechanical Properties of Living Cells Using Atomic Force Microscopy,” *J. Vis. Exp.*, no. 76, pp. 1–8, 2013.

[81] Q. S. Li, G. Y. H. Lee, C. N. Ong, and C. T. Lim, “AFM indentation study of breast cancer cells,” *Biochem. Biophys. Res. Commun.*, vol. 374, no. 4, pp. 609–613, Oct. 2008.

[82] S. Byun *et al.*, “Characterizing deformability and surface friction of cancer cells,” *Proc. Natl. Acad. Sci.*, vol. 110, no. 19, pp. 7580–7585, 2013.

[83] E. A. Corbin, F. Kong, C. T. Lim, W. P. King, and R. Bashir, “Biophysical properties of human breast cancer cells measured using silicon MEMS resonators and atomic force microscopy,” *Lab Chip*, vol. 15, no. 3, pp. 839–847, 2015.

[84] M. Godin, A. K. Bryan, T. P. Burg, K. Babcock, and S. R. Manalis, “Measuring the mass, density, and size of particles and cells using a suspended microchannel resonator,” *Appl. Phys. Lett.*, vol. 91, no. 12, pp. 17–19, 2007.

[85] Z. Y. Luo *et al.*, “Deformation of a single mouse oocyte in a constricted microfluidic channel,” *Microfluid. Nanofluidics*, vol. 19, no. 4, pp. 883–890, 2015.

[86] Q. Guo, S. Park, and H. Ma, “Microfluidic micropipette aspiration for measuring the deformability of single cells,” *Lab Chip*, vol. 12, no. 15, pp. 2687–2695, 2012.

[87] D. R. Gossett *et al.*, “Hydrodynamic stretching of single cells for large population mechanical phenotyping,” *Proc. Natl. Acad. Sci.*, vol. 109, no. 20, pp. 7630–7635, 2012.

[88] J. Rajagopalan and M. T. A. Saif, “MEMS sensors and microsystems for cell mechanobiology,” *J. Micromechanics Microengineering*, vol. 21, no. 5, p. 054002, May 2011.

[89] D. B. Weibel, W. R. DiLuzio, and G. M. Whitesides, “Microfabrication meets microbiology,” *Nat. Rev. Microbiol.*, vol. 5, no. 3, pp. 209–218, Mar. 2007.

[90] J. P. Shelby, J. White, K. Ganesan, P. K. Rathod, and D. T. Chiu, “A microfluidic model

for single-cell capillary obstruction by Plasmodium falciparum-infected erythrocytes," *Proc. Natl. Acad. Sci.*, vol. 100, no. 25, pp. 14618–14622, 2003.

[91] A. Valizadeh and A. Y. Khosroushahi, "Single-cell analysis based on lab on a chip fluidic system," *Anal. Methods*, vol. 7, no. 20, pp. 8524–8533, 2015.

[92] J. S. Dudani, D. R. Gossett, H. T. K. Tse, and D. Di Carlo, "Pinched-flow hydrodynamic stretching of single-cells," *Lab Chip*, vol. 13, no. 18, pp. 3728–3734, 2013.

[93] Y. Zheng and Y. Sun, "Microfluidic devices for mechanical characterisation of single cells in suspension," *Micro Nano Lett.*, vol. 6, no. 5, p. 327, 2011.

[94] N. Bao, Y. Zhan, and C. Lu, "Microfluidic electroporative flow cytometry for studying single-cell biomechanics," *Anal. Chem.*, vol. 80, no. 20, pp. 7714–7719, 2008.

[95] M. Krieg *et al.*, "Atomic force microscopy-based mechanobiology," *Nat. Rev. Phys.*, vol. 1, no. 1, pp. 41–57, 2019.

[96] M. Unal *et al.*, "Micro and Nano-Scale Technologies for Cell Mechanics," *Nanobiomedicine*, vol. 1, no. October, p. 5, Sep. 2014.

[97] L. Avraham-Chakim, D. Elad, U. Zaretsky, Y. Kloog, A. Jaffa, and D. Grisaru, "Fluid-Flow Induced Wall Shear Stress and Epithelial Ovarian Cancer Peritoneal Spreading," *PLoS One*, vol. 8, no. 4, pp. 0–8, 2013.

[98] J. R. Lange *et al.*, "Microconstriction Arrays for High-Throughput Quantitative Measurements of Cell Mechanical Properties," *Biophys. J.*, vol. 109, no. 1, pp. 26–34, 2015.

[99] M. Mak and D. Erickson, "A serial micropipette microfluidic device with applications to cancer cell repeated deformation studies," *Integr. Biol. (United Kingdom)*, vol. 5, no. 11, pp. 1374–1384, 2013.

[100] J. S. Bagnall *et al.*, "Deformability of Tumor Cells versus Blood Cells," *Sci. Rep.*, vol. 5, no. 1, p. 18542, Dec. 2015.

[101] J. Huang, F. Lin, and C. Xiong, "Mechanical characterization of single cells based on microfluidic techniques," *TrAC Trends Anal. Chem.*, vol. 117, pp. 47–57, Aug. 2019.

[102] D. A. Fletcher and R. D. Mullins, “Cell mechanics and the cytoskeleton,” *Nature*, vol. 463, no. 7280, pp. 485–492, 2010.

[103] D. A. Fletcher and R. D. Mullins, “cell mechanics and cytoskeleton,” vol. 463, no. 7280, pp. 485–492, 2010.

[104] N. Pernodet *et al.*, “Adverse effects of citrate/gold nanoparticles on human dermal fibroblasts,” *Small*, vol. 2, no. 6, pp. 766–773, 2006.

[105] H. K. Patra, S. Banerjee, U. Chaudhuri, P. Lahiri, and A. K. Dasgupta, “Cell selective response to gold nanoparticles,” *Nanomedicine Nanotechnology, Biol. Med.*, vol. 3, no. 2, pp. 111–119, 2007.

[106] T. R. Pisanic II, J. D. Blackwell, V. I. Shubayev, R. R. Finones, and S. Jin, “Nanotoxicity of iron oxide nanoparticle internalization in growing neurons,” *Biomaterials*, vol. 28, no. 16, pp. 2572–2581, 2007.

[107] X. Huang, X. Teng, D. Chen, F. Tang, and J. He, “The effect of the shape of mesoporous silica nanoparticles on cellular uptake and cell function,” *Biomaterials*, vol. 31, no. 3, pp. 438–448, 2010.

[108] B. D. Holt *et al.*, “Altered Cell Mechanics from the Inside: Dispersed Single Wall Carbon Nanotubes Integrate with and Restructure Actin,” *J. Funct. Biomater.*, vol. 3, no. 4, pp. 398–417, 2012.

[109] Y. Wu, T. Yu, T. A. Gilbertson, A. Zhou, H. Xu, and K. T. Nguyen, “Biophysical assessment of single cell cytotoxicity: Diesel exhaust particle-treated human aortic endothelial cells,” *PLoS One*, vol. 7, no. 5, pp. 1–10, 2012.

[110] D. Choudhury *et al.*, “Unprecedented inhibition of tubulin polymerization directed by gold nanoparticles inducing cell cycle arrest and apoptosis,” *Nanoscale*, vol. 5, no. 10, pp. 4476–4489, 2013.

[111] J. Pi *et al.*, “Selenium nanoparticles induced membrane bio-mechanical property changes in MCF-7 cells by disturbing membrane molecules and F-actin,” *Bioorganic Med. Chem. Lett.*, vol. 23, no. 23, pp. 6296–6303, 2013.

[112] Y. Wen *et al.*, “Binding of cytoskeletal proteins with silver nanoparticles,” *RSC Adv.*, vol. 3, no. 44, pp. 22002–22007, 2013.

[113] M. A. I. Rasel *et al.*, “Biophysical response of living cells to boron nitride nanoparticles: uptake mechanism and bio-mechanical characterization,” *J. Nanoparticle Res.*, vol. 17, no. 11, pp. 1–13, 2015.

[114] R. J. Cooper and N. Spitzer, “Silver nanoparticles at sublethal concentrations disrupt cytoskeleton and neurite dynamics in cultured adult neural stem cells,” *Neurotoxicology*, vol. 48, pp. 231–238, May 2015.

[115] M. R. K. Ali *et al.*, “Targeting cancer cell integrins using gold nanorods in photothermal therapy inhibits migration through affecting cytoskeletal proteins,” *Proc. Natl. Acad. Sci. U. S. A.*, vol. 114, no. 28, pp. E5655–E5663, Jul. 2017.

[116] Y. Liu *et al.*, “Nanoparticle size-specific actin rearrangement and barrier dysfunction of endothelial cells,” *Nanotoxicology*, vol. 11, no. 7, pp. 846–856, 2017.

[117] L. F. de A. Vieira, M. P. Lins, I. M. M. N. Viana, J. E. dos Santos, S. Smaniotto, and M. D. dos S. Reis, “Metallic nanoparticles reduce the migration of human fibroblasts in vitro,” *Nanoscale Res. Lett.*, vol. 12, no. 1, p. 200, Dec. 2017.

[118] M. Ibrahim, J. Schoelermann, K. Mustafa, and M. R. Cimpan, “TiO 2 nanoparticles disrupt cell adhesion and the architecture of cytoskeletal networks of human osteoblast-like cells in a size dependent manner,” *J. Biomed. Mater. Res. Part A*, vol. 106, no. 10, pp. 2582–2593, Oct. 2018.

[119] Y. Qin *et al.*, “Small size fullerenol nanoparticles suppress lung metastasis of breast cancer cell by disrupting actin dynamics,” *J. Nanobiotechnology*, vol. 16, no. 1, pp. 1–14, 2018.

[120] M. Geiser *et al.*, “Ultrafine particles cross cellular membranes by nonphagocytic mechanisms in lungs and in cultured cells,” *Environ. Health Perspect.*, vol. 113, no. 11, pp. 1555–1560, 2005.

[121] Y. L. Wu *et al.*, “Biophysical responses upon the interaction of nanomaterials with cellular interfaces,” *Acc. Chem. Res.*, vol. 46, no. 3, pp. 782–791, 2013.

[122] M. Lundqvist *et al.*, “The evolution of the protein corona around nanoparticles: A test study,” *ACS Nano*, vol. 5, no. 9, pp. 7503–7509, 2011.

[123] F. Tian, D. Cui, H. Schwarz, G. G. Estrada, and H. Kobayashi, “Cytotoxicity of single-wall carbon nanotubes on human fibroblasts,” *Toxicol. Vitr.*, vol. 20, no. 7, pp. 1202–1212, 2006.

[124] I. V. Ogneva, S. V. Buravkov, A. N. Shubenkov, and L. B. Buravkova, “Mechanical characteristics of mesenchymal stem cells under impact of silica-based nanoparticles,” *Nanoscale Res. Lett.*, vol. 9, no. 1, pp. 1–10, 2014.

[125] R. Subbiah *et al.*, “Evaluation of cytotoxicity, biophysics and biomechanics of cells treated with functionalized hybrid nanomaterials,” *J. R. Soc. Interface*, vol. 10, no. 88, p. 20130694, Nov. 2013.

[126] D. Septiadi, F. Crippa, T. L. Moore, B. Rothen-Rutishauser, and A. Petri-Fink, “Nanoparticle–Cell Interaction: A Cell Mechanics Perspective,” *Adv. Mater.*, vol. 30, no. 19, pp. 1–30, 2018.

[127] N. Pernodet *et al.*, “Adverse effects of citrate/gold nanoparticles on human dermal fibroblasts,” *Small*, vol. 2, no. 6, pp. 766–773, 2006.

[128] M. Ibrahim, J. Schoelermann, K. Mustafa, and M. R. Cimpan, “TiO 2 nanoparticles disrupt cell adhesion and the architecture of cytoskeletal networks of human osteoblast-like cells in a size dependent manner,” *J. Biomed. Mater. Res.*, pp. 1–30, 2018.

[129] R. J. Cooper and N. Spitzer, “Silver nanoparticles at sublethal concentrations disrupt cytoskeleton and neurite dynamics in cultured adult neural stem cells,” *Neurotoxicology*, vol. 48, pp. 231–238, 2015.

[130] M. Plodinec *et al.*, “The nanomechanical signature of breast cancer,” *Nat. Nanotechnol.*, vol. 7, no. 11, pp. 757–765, Nov. 2012.

[131] W. Xu, R. Mezencev, B. Kim, L. Wang, J. McDonald, and T. Sulchek, “Cell Stiffness Is a Biomarker of the Metastatic Potential of Ovarian Cancer Cells,” *PLoS One*, vol. 7, no. 10, 2012.

[132] S. Tojkander, G. Gateva, and P. Lappalainen, “Actin stress fibers - Assembly, dynamics and biological roles,” *J. Cell Sci.*, vol. 125, no. 8, pp. 1855–1864, 2012.

[133] A. Calzado-Martín, M. Encinar, J. Tamayo, M. Calleja, and A. San Paulo, “Effect of Actin Organization on the Stiffness of Living Breast Cancer Cells Revealed by Peak-Force Modulation Atomic Force Microscopy,” *ACS Nano*, vol. 10, no. 3, pp. 3365–3374, 2016.

[134] C. Rotsch and M. Radmacher, “Drug-induced changes of cytoskeletal structure and mechanics in fibroblasts: An atomic force microscopy study,” *Biophys. J.*, vol. 78, no. 1, pp. 520–535, 2000.

[135] K. Buyukhatipoglu and A. M. Clyne, “Superparamagnetic iron oxide nanoparticles change endothelial cell morphology and mechanics via reactive oxygen species formation,” *J. Biomed. Mater. Res. - Part A*, vol. 96 A, no. 1, pp. 186–195, 2011.

[136] W. Zhang, J. Hughes, and Y. Chen, “Impacts of hematite nanoparticle exposure on biomechanical, adhesive, and surface electrical properties of escherichia coli cells,” *Appl. Environ. Microbiol.*, vol. 78, no. 11, pp. 3905–3915, 2012.

[137] A. Pietuch *et al.*, “Mechanical properties of MDCK II cells exposed to gold nanorods,” *Beilstein J. Nanotechnol.*, vol. 6, no. 1, pp. 223–231, 2015.

[138] H. Babahosseini *et al.*, “The impact of sphingosine kinase inhibitor-loaded nanoparticles on bioelectrical and biomechanical properties of cancer cells,” *Lab Chip*, vol. 16, no. 1, pp. 188–198, 2016.

[139] M. R. K. Ali *et al.*, “Nuclear Membrane-Targeted Gold Nanoparticles Inhibit Cancer Cell Migration and Invasion,” *ACS Nano*, vol. 11, no. 4, pp. 3716–3726, 2017.

[140] J. Banyard and D. R. Bielenberg, “The role of EMT and MET in cancer dissemination,” *Connective Tissue Research*, vol. 56, no. 5. pp. 403–413, 2015.

[141] K. Cai *et al.*, “Effects of titanium nanoparticles on adhesion, migration, proliferation, and differentiation of mesenchymal stem cells,” *Int. J. Nanomedicine*, vol. 8, p. 3619, Sep. 2013.

[142] T. Zhou *et al.*, “Inhibition of cancer cell migration by gold nanorods: Molecular

mechanisms and implications for cancer therapy," *Adv. Funct. Mater.*, vol. 24, no. 44, pp. 6922–6932, 2014.

[143] Y. Pan, Q. Wu, L. Qin, J. Cai, and B. Du, "Gold Nanoparticles Inhibit VEGF 165 -Induced Migration and Tube Formation of Endothelial Cells via the Akt Pathway," *Biomed Res. Int.*, vol. 2014, pp. 1–11, 2014.

[144] H. Zare-Zardini *et al.*, "Nanotechnology and Pediatric Cancer: Prevention, Diagnosis and Treatment.," *Iran. J. Pediatr. Hematol. Oncol.*, vol. 5, no. 4, pp. 233–48, 2015.

[145] G. Morgan, R. Ward, and M. Barton, "The contribution of cytotoxic chemotherapy to 5-year survival in adult malignancies," *Clin. Oncol.*, vol. 16, no. 8, pp. 549–560, 2004.

[146] S. Jorfi *et al.*, "Inhibition of microvesiculation sensitizes prostate cancer cells to chemotherapy and reduces docetaxel dose required to limit tumor growth in vivo," *Sci. Rep.*, vol. 5, no. 1, p. 13006, Oct. 2015.

[147] S. Pernas and S. M. Tolaney, "HER2-positive breast cancer: new therapeutic frontiers and overcoming resistance," *Therapeutic Advances in Medical Oncology*, vol. 11. p. 175883591983351, 19-Jan-2019.

[148] M. D. Wang, D. M. Shin, J. W. Simons, and S. Nie, "Nanotechnology for targeted cancer therapy," *Expert Rev. Anticancer Ther.*, vol. 7, no. 6, pp. 833–837, 2007.

[149] V. Sanna, N. Pala, and M. Sechi, "Targeted therapy using nanotechnology: Focus on cancer," *Int. J. Nanomedicine*, vol. 9, no. 1, pp. 467–483, 2014.

[150] P. Singh, S. Pandit, V. R. S. S. Mokkapati, A. Garg, V. Ravikumar, and I. Mijakovic, "Gold nanoparticles in diagnostics and therapeutics for human cancer," *Int. J. Mol. Sci.*, vol. 19, no. 7, 2018.

[151] J. Li, H. Mao, N. Kawazoe, and G. Chen, "Insight into the interactions between nanoparticles and cells," *Biomater. Sci.*, vol. 5, no. 2, pp. 173–189, 2017.

[152] J. Turkevich, P. C. Stevenson, and J. Hillier, "A study of the nucleation and growth processes in the synthesis of colloidal gold," *Discuss. Faraday Soc.*, vol. 11, no. c, pp. 55–75, 1951.

[153] J. Chamberlain, M. N. Afsar, and J. B. Hasted, "© 1973 Nature Publishing Group," *Nature*, vol. 244, pp. 47–49, 1973.

[154] N. Wenxin, Z. Ling, and X. Guobao, "Seed-mediated growth method for high-quality noble metal nanocrystals," *Science China Chemistry*, vol. 55, no. 11. pp. 2311–2317, 2012.

[155] W. Niu, L. Zhang, and G. Xu, "Seed-mediated growth of noble metal nanocrystals: Crystal growth and shape control," *Nanoscale*, vol. 5, no. 8, pp. 3172–3181, 2013.

[156] P. R. Sajanlal, T. S. Sreeprasad, A. K. Samal, and T. Pradeep, "Anisotropic nanomaterials: structure, growth, assembly, and functions," *Nano Rev.*, vol. 2, no. 1, p. 5883, 2011.

[157] G. Chirico, M. Borzenkov, and P. Pallavicini, *Gold nanostars: Synthesis, properties and biomedical application*. Cham: Springer International Publishing, 2015.

[158] H. L. Wu, C. H. Chen, and M. H. Huang, "Seed-mediated synthesis of branched gold nanocrystals derived from the side growth of pentagonal bipyramids and the formation of gold nanostars," *Chem. Mater.*, vol. 21, no. 1, pp. 110–114, 2009.

[159] S. Pal, "The Ayurvedic Bhasma: The Ancient Science of Nanomedicine," *Recent Patents Nanomed.*, vol. 5, no. 1, pp. 12–18, 2015.

[160] K. Thakur, R. Gudi, M. Vahalia, S. Shitut, and S. Nadkarni, "Preparation and Characterization of Suvarna Bhasma Parada Marit," *J. Pharmacopuncture*, vol. 20, no. 1, pp. 36–44, 2017.

[161] K. Yadav and A. Chaudhary, "Percentage of Swarna Bhasma in medicaments of Ayurveda to treat disorders of different origin," *Int. J. Green Pharm.*, vol. 9, no. 2, p. 90, 2015.

[162] S. Khedekar, Anupriya, R. Galib, B. Patgiri, and P. K. Prajapati, "Chemical characterization of incinerated gold (Swarna Bhasma)," *Adv. Appl. Sci. Res.*, vol. 6, no. 12, pp. 89–95, 2015.

[163] N. Singh and C. Anand, "Swarna Bhasma and gold compounds: An innovation of pharmaceutics for illumination of therapeutics," *International Journal of Research in Ayurveda and Pharmacy*, vol. 3, no. 1. pp. 5–9, 2012.

[164] P. K. Sarkar and A. K. Chaudhary, "Ayurvedic bhasma: The most ancient application of

nanomedicine," *J. Sci. Ind. Res. (India).*, vol. 69, no. 12, pp. 901–905, 2010.

[165] A. A and K. BR, "Elemental Analysis of Ayurvedic Drugs (Bhasmas) By Atomic Absorption Spectrometer," *Asian J. Pharm. Clin. Res.*, no. July, pp. 545–549, Feb. 2019.

[166] C. L. Brown *et al.*, "Nanogold-pharmaceutics: (i) The use of colloidal gold to treat experimentally-induced arthritis in rat models; (ii) Characterization of the gold in Swarna bhasma, a microparticulate used in traditional Indian medicine," *Gold Bull.*, vol. 40, no. 3, pp. 245–250, 2007.

[167] D. Beaudet *et al.*, "Comparative study on cellular entry of incinerated ancient gold particles (Swarna Bhasma) and chemically synthesized gold particles," *Sci. Rep.*, vol. 7, no. 1, p. 10678, 2017.

[168] V. A. Ogarev, V. M. Rudoi, and O. V. Dement'eva, "Gold Nanoparticles: Synthesis, Optical Properties, and Application," *Inorg. Mater. Appl. Res.*, vol. 9, no. 1, pp. 134–140, 2018.

[169] S. Eustis and M. A. El-Sayed, "Why gold nanoparticles are more precious than pretty gold: Noble metal surface plasmon resonance and its enhancement of the radiative and nonradiative properties of nanocrystals of different shapes," *Chem. Soc. Rev.*, vol. 35, no. 3, pp. 209–217, 2006.

[170] M. Hassellöv and R. Kaegi, *Analysis and Characterization of Manufactured Nanoparticles in Aquatic Environments*. 2009.

[171] A. K. Singh, *Engineered nanoparticles: structure, properties and mechanisms of toxicity*. Academic Press, 2015.

[172] A. Kim, W. B. Ng, W. Bernt, and N. J. Cho, "Validation of Size Estimation of Nanoparticle Tracking Analysis on Polydisperse Macromolecule Assembly," *Sci. Rep.*, vol. 9, no. 1, pp. 1–14, 2019.

[173] M. Joshi, A. Bhattacharyya, and S. W. Ali, "Characterization techniques for nanotechnology applications in textiles," *Indian J. Fibre Text. Res.*, vol. 33, no. 3, pp. 304–317, 2008.

[174] B. Sarecka-Hujar, R. Balwierz, A. Ostrozka-Cieslik, R. Dyja, D. Lukowiec, and A. Jankowski, “Scanning electron microscopy and X-ray energy dispersive spectroscopy-useful tools in the analysis of pharmaceutical products,” *J. Phys. Conf. Ser.*, vol. 931, no. 1, 2017.

[175] M. Scimeca, S. Bischetti, H. K. Lamsira, R. Bonfiglio, and E. Bonanno, “Energy Dispersive X-ray (EDX) microanalysis: A powerful tool in biomedical research and diagnosis,” *Eur. J. Histochem.*, vol. 62, no. 1, Mar. 2018.

[176] M. Joshi, A. Bhattacharyya, and S. W. Ali, “Characterization techniques for nanotechnology applications in textiles,” *Indian J. Fibre Text. Res.*, vol. 33, no. 3, pp. 304–317, 2008.

[177] S. Ebnesajjad, “Surface and material characterization techniques,” in *Handbook of Adhesives and Surface Preparation*, Elsevier, 2011, pp. 31–48.

[178] R. Allabashi, W. Stach, A. De La Escosura-Muñiz, L. Liste-Calleja, and A. Merkoçi, “ICP-MS: A powerful technique for quantitative determination of gold nanoparticles without previous dissolving,” *J. Nanoparticle Res.*, vol. 11, no. 8, pp. 2003–2011, 2009.

[179] L. Jitkang, Y. S. Pin, C. H. Xin, and L. S. Chun, “Characterization of magnetic nanoparticle by dynamic light scattering,” *Nanoscale Res. Lett.*, vol. 8, no. 1, p. 381, 2013.

[180] D. Titus, E. James Jebaseelan Samuel, and S. M. Roopan, “Nanoparticle characterization techniques,” in *Green Synthesis, Characterization and Applications of Nanoparticles*, Elsevier, 2019, pp. 303–319.

[181] G. W. Lu and P. Gao, “Emulsions and microemulsions for topical and transdermal drug delivery,” in *Handbook of non-invasive drug delivery systems*, Elsevier, 2010, pp. 59–94.

[182] A. Sikora *et al.*, “A systematic comparison of different techniques to determine the zeta potential of silica nanoparticles in biological medium,” *Anal. Methods*, vol. 7, no. 23, pp. 9835–9843, 2015.

[183] J. I. Goldstein *et al.*, *Scanning Electron Microscopy and X-ray Microanalysis*, vol. 215, no. 4532. Boston, MA: Springer US, 2003.

[184] S. Mourdikoudis, R. M. Pallares, and N. T. K. Thanh, “Characterization techniques for nanoparticles: Comparison and complementarity upon studying nanoparticle properties,” *Nanoscale*, vol. 10, no. 27, pp. 12871–12934, 2018.

[185] P.-C. Lin, S. Lin, P. C. Wang, and R. Sridhar, “Techniques for physicochemical characterization of nanomaterials,” *Biotechnol. Adv.*, vol. 32, no. 4, pp. 711–726, Jul. 2014.

[186] R. A. Petros and J. M. DeSimone, “Strategies in the design of nanoparticles for therapeutic applications.,” *Nat. Rev. Drug Discov.*, vol. 9, no. 8, pp. 615–27, Aug. 2010.

[187] M. Kodiha, Y. M. Wang, E. Hutter, D. Maysinger, and U. Stochaj, “Off to the organelles - killing cancer cells with targeted gold nanoparticles.,” *Theranostics*, vol. 5, no. 4, pp. 357–70, 2015.

[188] Y. C. Yeh, B. Creran, and V. M. Rotello, “Gold nanoparticles: Preparation, properties, and applications in bionanotechnology,” *Nanoscale*, vol. 4, no. 6. pp. 1871–1880, 21-Mar-2012.

[189] Galib, M. Barve, M. Mashru, C. Jagtap, B. J. Patgiri, and P. K. Prajapati, “Therapeutic potentials of metals in ancient India: A review through Charaka Samhita,” *Journal of Ayurveda and Integrative Medicine*, vol. 2, no. 2. Elsevier B.V., pp. 55–63, 2011.

[190] A. Chaudhary, “Ayurvedic bhasma: nanomedicine of ancient India--its global contemporary perspective.,” *J. Biomed. Nanotechnol.*, vol. 7, no. 1, pp. 68–9, Feb. 2011.

[191] A. Dance, “Medical histories.,” *Nature*, vol. 537, no. 7619, pp. S52-3, 2016.

[192] P. K. Mukherjee *et al.*, “Development of Ayurveda – Tradition to trend,” *J. Ethnopharmacol.*, vol. 197, pp. 10–24, Feb. 2017.

[193] Y. S. Jaiswal and L. L. Williams, “A glimpse of Ayurveda - The forgotten history and principles of Indian traditional medicine.,” *J. Tradit. Complement. Med.*, vol. 7, no. 1, pp. 50–53, Jan. 2017.

[194] M. M. Pandey, S. Rastogi, and A. K. S. Rawat, “Indian traditional ayurvedic system of medicine and nutritional supplementation,” *Evidence-based Complementary and*

Alternative Medicine, vol. 2013. 2013.

[195] W. Paul and C. P. Sharma, "Blood compatibility studies of Swarna bhasma (gold bhasma), an Ayurvedic drug," *Int. J. Ayurveda Res.*, vol. 2, no. 1, pp. 14–22, 2011.

[196] S. K. Santosh, "Bhasma and Nanomedicine," *Int. Res. J. pharm*, vol. 4, no. 4, pp. 10–16, 2013.

[197] S. Alex and A. Tiwari, "Functionalized gold nanoparticles: Synthesis, properties and applications-A review," *J. Nanosci. Nanotechnol.*, vol. 15, no. 3, pp. 1869–1894, 2015.

[198] A. Mitra *et al.*, "Evaluation of chemical constituents and free-radical scavenging activity of Swarnabhasma (gold ash), an ayurvedic drug," *J. Ethnopharmacol.*, vol. 80, no. 2–3, pp. 147–153, 2002.

[199] R. B. Saper *et al.*, "Heavy metal content of Ayurvedic herbal medicine products," *J. Am. Med. Assoc.*, vol. 292, no. 23, pp. 2868–2873, 2004.

[200] N. R. Panyala, E. M. Peña-Méndez, and J. Havel, "Gold and nano-gold in medicine: Overview, toxicology and perspectives," *Journal of Applied Biomedicine*, vol. 7, no. 2. pp. 75–91, 2009.

[201] A. M. Alkilany and C. J. Murphy, "Toxicity and cellular uptake of gold nanoparticles: What we have learned so far?," *J. Nanoparticle Res.*, vol. 12, no. 7, pp. 2313–2333, 2010.

[202] G. J. Doherty and H. T. McMahon, "Mechanisms of Endocytosis," *Annu. Rev. Biochem.*, vol. 78, no. 1, pp. 857–902, Jun. 2009.

[203] J. P. Lim and P. A. Gleeson, "Macropinocytosis: An endocytic pathway for internalising large gulps," *Immunology and Cell Biology*, vol. 89, no. 8. pp. 836–843, Nov-2011.

[204] S. Mayor and R. E. Pagano, "Pathways of clathrin-independent endocytosis," *Nature Reviews Molecular Cell Biology*, vol. 8, no. 8. pp. 603–612, 2007.

[205] J. Swanson, C. W.-T. in cell Biology, and U. 1995, "Macropinocytosis," *Elsevier*.

[206] A. Albanese and W. C. W. Chan, "Effect of gold nanoparticle aggregation on cell uptake and toxicity," in *ACS Nano*, 2011, vol. 5, no. 7, pp. 5478–5489.

[207] E. C. Cho, Q. Zhang, and Y. Xia, “The effect of sedimentation and diffusion on cellular uptake of gold nanoparticles,” *Nat. Nanotechnol.*, vol. 6, no. 6, pp. 385–391, 2011.

[208] X. Cheng *et al.*, “Protein Corona Influences Cellular Uptake of Gold Nanoparticles by Phagocytic and Nonphagocytic Cells in a Size-Dependent Manner,” *ACS Appl. Mater. Interfaces*, vol. 7, no. 37, pp. 20568–20575, Sep. 2015.

[209] R. Grosjean *et al.*, “High pressures pathway toward boron-based nanostructured solids,” *Dalt. Trans.*, vol. 47, no. 23, pp. 7634–7639, 2017.

[210] J. Gilleron *et al.*, “Image-based analysis of lipid nanoparticle–mediated siRNA delivery, intracellular trafficking and endosomal escape,” *Nat. Biotechnol.*, vol. 31, no. 7, pp. 638–646, Jul. 2013.

[211] A. R. Bayles, H. S. Chahal, D. S. Chahal, C. P. Goldbeck, B. E. Cohen, and B. A. Helms, “Rapid cytosolic delivery of luminescent nanocrystals in live cells with endosome-disrupting polymer colloids,” *Nano Lett.*, vol. 10, no. 10, pp. 4086–4092, 2010.

[212] A. Jhaveri and V. Torchilin, “Intracellular delivery of nanocarriers and targeting to subcellular organelles,” *Expert Opin. Drug Deliv.*, vol. 13, no. 1, pp. 49–70, Jan. 2016.

[213] A. Wongrakpanich, S. M. Geary, M. L. A. Joiner, M. E. Anderson, and A. K. Salem, “Mitochondria-targeting particles,” *Nanomedicine*, vol. 9, no. 16. Future Medicine Ltd., pp. 2531–2543, 01-Nov-2014.

[214] C. J. Yang and D. B. Chithrani, “Nuclear Targeting of Gold Nanoparticles for Improved Therapeutics,” *Curr. Top. Med. Chem.*, vol. 16, no. 3, pp. 271–280, 2015.

[215] J. Kimling, M. Maier, B. Okenve, V. Kotaidis, H. Ballot, and A. Plech, “Turkevich method for gold nanoparticle synthesis revisited,” *J. Phys. Chem. B*, vol. 110, no. 32, pp. 15700–15707, Aug. 2006.

[216] J. Turkevich, P. C. Stevenson, and J. Hillier, “A study of the nucleation and growth processes in the synthesis of colloidal gold,” *Discussions of the Faraday Society*, vol. 11. pp. 55–75, 1951.

[217] A. G. Patel and S. H. Kaufmann, “How does doxorubicin work?,” *Elife*, vol. 2012, no. 1,

2012.

[218] D. Gewirtz, “A critical evaluation of the mechanisms of action proposed for the antitumor effects of the anthracycline antibiotics adriamycin and daunorubicin,” *Biochem. Pharmacol.*, vol. 57, no. 7, pp. 727–741, Apr. 1999.

[219] A. P. Ramos, M. A. E. Cruz, C. B. Tovani, and P. Ciancaglini, “Biomedical applications of nanotechnology,” *Biophys. Rev.*, vol. 9, no. 2, pp. 79–89, Apr. 2017.

[220] M. A. Kamal, N. Jabir NR, Tabrez, Ashraf, Shakil, and Damanhouri, “Nanotechnology-based approaches in anticancer research,” *Int. J. Nanomedicine*, vol. 7, p. 4391, Aug. 2012.

[221] C. S. O. Paulo, R. Pires das Neves, and L. S. Ferreira, “Nanoparticles for intracellular-targeted drug delivery,” *Nanotechnology*, vol. 22, no. 49, p. 494002, Dec. 2011.

[222] X. Wang *et al.*, “Influence of cell size on cellular uptake of gold nanoparticles,” *Biomater. Sci.*, vol. 4, no. 6, pp. 970–978, 2016.

[223] N. Gong, S. Chen, S. Jin, J. Zhang, P. C. Wang, and X.-J. Liang, “Effects of the physicochemical properties of gold nanostructures on cellular internalization,” *Regen. Biomater.*, vol. 2, no. 4, pp. 273–280, 2015.

[224] S. R. Panikkanvalappil, N. Hooshmand, and M. A. El-Sayed, “Intracellular assembly of nuclear-targeted gold nanosphere enables selective plasmonic photothermal therapy of cancer by shifting their absorption wavelength toward near-infrared region,” *Bioconjug. Chem.*, vol. 28, no. 9, pp. 2452–2460, 2017.

[225] M. A. M. Abo-Zeid, T. Liehr, A. M. Gamal-Eldeen, M. Zawrah, M. Ali, and M. A. K. Othman, “Potential of rod, sphere and semi-cube shaped gold nanoparticles to induce cytotoxicity and genotoxicity in human blood lymphocytes in vitro,” *Eur. J. Nanomedicine*, vol. 7, no. 1, pp. 63–75, 2015.

[226] C. W. Kuo, J. J. Lai, K. H. Wei, and P. Chen, “Studies of surface-modified gold nanowires inside living cells,” *Adv. Funct. Mater.*, vol. 17, no. 18, pp. 3707–3714, 2007.

[227] C. G. Khoury and T. Vo-Dinh, “Gold nanostars for surface-enhanced Raman scattering: synthesis, characterization and optimization,” *J. Phys. Chem. C*, vol. 112, no. 48, pp.

18849–18859, 2008.

[228] A. D'Hollander *et al.*, "Development of nanostars as a biocompatible tumor contrast agent: Toward in vivo SERS imaging," *Int. J. Nanomedicine*, vol. 11, pp. 3703–3714, 2016.

[229] A. Espinosa *et al.*, "Cancer Cell Internalization of Gold Nanostars Impacts Their Photothermal Efficiency In Vitro and In Vivo: Toward a Plasmonic Thermal Fingerprint in Tumoral Environment," *Adv. Healthc. Mater.*, vol. 5, no. 9, pp. 1040–1048, 2016.

[230] K. Kuruvinashetti, A. S. Kashani, S. Badilescu, D. Beaudet, A. Piekny, and M. Packirisamy, "Intracellular Localized Surface Plasmonic Sensing for Subcellular Diagnosis," *Plasmonics*, vol. 13, no. 5, pp. 1639–1648, Oct. 2018.

[231] N. D. Israelsen, C. Hanson, and E. Vargis, "Nanoparticle Properties and Synthesis Effects on Surface-Enhanced Raman Scattering Enhancement Factor: An Introduction," *Sci. World J.*, vol. 2015, pp. 1–12, 2015.

[232] A. Paudel, D. Raijada, and J. Rantanen, "Raman spectroscopy in pharmaceutical product design," *Adv. Drug Deliv. Rev.*, vol. 89, pp. 3–20, 2015.

[233] N. B. Shah, J. Dong, and J. C. Bischof, "Cellular Uptake and Nanoscale Localization of Gold Nanoparticles in Cancer Using Label-Free Confocal Raman Microscopy," *Mol. Pharm.*, vol. 8, no. 1, pp. 176–184, Feb. 2011.

[234] J. Zhu *et al.*, "Surface-enhanced Raman spectroscopy investigation on human breast cancer cells," *Chem Cent J*, vol. 7, no. 1, p. 37, 2013.

[235] J. Huang, S. Liu, Z. Chen, N. Chen, F. Pang, and T. Wang, "Distinguishing Cancerous Liver Cells Using Surface-Enhanced Raman Spectroscopy," *Technol. Cancer Res. Treat.*, vol. 15, no. 1, pp. 36–43, 2016.

[236] L. F. Leopold *et al.*, "Assessment of PEG and BSA-PEG gold nanoparticles cellular interaction," *Colloids Surfaces A Physicochem. Eng. Asp.*, vol. 532, no. June, pp. 70–76, 2017.

[237] I. Estrela-Lopis, G. Romero, E. Rojas, S. E. Moya, and E. Donath, "Nanoparticle uptake and their co-localization with cell compartments - A confocal Raman microscopy study at

single cell level," in *Journal of Physics: Conference Series*, 2011, vol. 304, no. 1.

[238] J. Dorney, F. Bonnier, A. Garcia, A. Casey, G. Chambers, and H. J. Byrne, "Identifying and localizing intracellular nanoparticles using Raman spectroscopy," *Analyst*, vol. 137, no. 5, pp. 1111–1119, 2012.

[239] P. Knief *et al.*, "Raman spectroscopy - A potential platform for the rapid measurement of carbon nanotube-induced cytotoxicity," *Analyst*, vol. 134, no. 6, pp. 1182–1191, 2009.

[240] J. Kimling, M. Maier, B. Okenve, V. Kotaidis, H. Ballot, and A. Plech, "Turkevich method for gold nanoparticle synthesis revisited," *J. Phys. Chem. B*, vol. 110, no. 32, pp. 15700–15707, 2006.

[241] N. Anand *et al.*, "Fabrication of a Gold Nanostar-Embedded Porous Poly (dimethylsiloxan) Platform for Sensing Applications," *Sensors & Transducers*, vol. 149, no. 2, p. 20, 2013.

[242] S. Bhattacharjee, "DLS and zeta potential – What they are and what they are not?," *J. Control. Release*, vol. 235, pp. 337–351, Aug. 2016.

[243] A. Goldstein, Y. Soroka, M. Frušić-Zlotkin, I. Popov, and R. Kohen, "High resolution SEM imaging of gold nanoparticles in cells and tissues," *J. Microsc.*, vol. 256, no. 3, pp. 237–247, 2014.

[244] S. Verrier, H. Romanska, J. M. Polak, A. E. Bishop, I. Notingher, and L. L. Hench, "In situ Characterisation of Living Cells by Raman Spectroscopy ," *Spectroscopy*, vol. 16, no. 2, pp. 43–51, 2012.

[245] K. W. Short, S. Carpenter, J. P. Freyer, and J. R. Mourant, "Raman spectroscopy detects biochemical changes due to proliferation in mammalian cell cultures," *Biophys. J.*, vol. 88, no. 6, pp. 4274–4288, 2005.

[246] Z. Farhane, F. Bonnier, A. Casey, and H. J. Byrne, "Raman micro spectroscopy for in vitro drug screening: Subcellular localisation and interactions of doxorubicin," *Analyst*, vol. 140, no. 12, pp. 4212–4223, 2015.

[247] I. Notingher, S. Verrier, H. Romanska, A. E. Bishop, J. M. Polak, and L. L. Hench, "In situ

characterisation of living cells by Raman spectroscopy," *Spectroscopy*, vol. 16, no. 2, pp. 43–51, 2002.

[248] E. Fazio *et al.*, "A micro-Raman spectroscopic investigation of leukemic U-937 cells in aged cultures," *Spectrochim. Acta Part A Mol. Biomol. Spectrosc.*, vol. 159, pp. 21–29, Apr. 2016.

[249] M. Altunbek, G. Kuku, and M. Culha, "Gold nanoparticles in single-cell analysis for surface enhanced Raman scattering," *Molecules*, vol. 21, no. 12, pp. 1–18, 2016.

[250] F. Tian, F. Bonnier, A. Casey, A. E. Shanahan, and H. J. Byrne, "Surface enhanced Raman scattering with gold nanoparticles: Effect of particle shape," *Anal. Methods*, vol. 6, no. 22, pp. 9116–9123, 2014.

[251] G. Villaverde and A. Baeza, "Targeting strategies for improving the efficacy of nanomedicine in oncology," *Beilstein J. Nanotechnol.*, vol. 10, no. 1, pp. 168–181, 2019.

[252] K. O. Shittu, M. T. Bankole, A. S. Abdulkareem, O. K. Abubakre, and A. U. Ubaka, "Application of gold nanoparticles for improved drug efficiency," *Adv. Nat. Sci. Nanosci. Nanotechnol.*, vol. 8, no. 3, p. 035014, Jul. 2017.

[253] A. Ostrowski *et al.*, "Overview about the localization of nanoparticles in tissue and cellular context by different imaging techniques," *Beilstein J. Nanotechnol.*, vol. 6, no. 1, pp. 263–280, 2015.

[254] M. D'Acunto, "Detection of Intracellular Gold Nanoparticles: An Overview," *Materials (Basel).*, vol. 11, no. 6, p. 882, May 2018.

[255] E. Pancani *et al.*, "High-Resolution Label-Free Detection of Biocompatible Polymeric Nanoparticles in Cells," *Part. Part. Syst. Charact.*, vol. 35, no. 3, p. 1700457, Mar. 2018.

[256] B. Drasler, D. Vanhecke, L. Rodriguez-Lorenzo, A. Petri-Fink, and B. Rothen-Rutishauser, "Quantifying nanoparticle cellular uptake: Which method is best?," *Nanomedicine*, vol. 12, no. 10. Future Medicine Ltd., pp. 1095–1099, 01-May-2017.

[257] K. Shapero, F. Fenaroli, I. Lynch, D. C. Cottell, A. Salvati, and K. A. Dawson, "Time and space resolved uptake study of silica nanoparticles by human cells," *Mol. Biosyst.*, vol. 7,

no. 2, pp. 371–378, 2011.

[258] E. Efeoglu, M. Keating, J. McIntyre, A. Casey, and H. J. Byrne, “Determination of nanoparticle localisation within subcellular organelles in vitro using Raman spectroscopy,” *Anal. Methods*, vol. 7, no. 23, pp. 10000–10017, 2015.

[259] S. Chen *et al.*, “Direct Observation of Nanoparticles within Cells at Subcellular Levels by Super-Resolution Fluorescence Imaging,” *Anal. Chem.*, vol. 91, no. 9, pp. 5747–5752, 2019.

[260] J. Taylor, A. Huefner, L. Li, J. Wingfield, and S. Mahajan, “Nanoparticles and intracellular applications of surface-enhanced Raman spectroscopy,” *Analyst*, vol. 141, no. 17, pp. 5037–5055, 2016.

[261] I. W. Schie and T. Huser, “Methods and applications of Raman microspectroscopy to single-cell analysis,” in *Applied Spectroscopy*, 2013, vol. 67, no. 8, pp. 813–828.

[262] J. M. Hermida-Ramon, L. Guerrini, and R. A. Alvarez-Puebla, “Analysis of the SERS spectrum by theoretical methodology: Evaluating a classical dipole model and the detuning of the excitation frequency,” *J. Phys. Chem. A*, vol. 117, no. 22, pp. 4584–4590, 2013.

[263] N. J. Crane, S. W. Huffman, F. A. Gage, I. W. Levin, and E. A. Elster, “Evidence of a heterogeneous tissue oxygenation : renal ischemia / reperfusion injury in a large animal,” *J. Biomed. Opt.*, vol. 18, no. 3, pp. 035001–7, 2003.

[264] N. Mehta, S. Shaik, R. Devireddy, and M. R. Gartia, “Single-Cell Analysis Using Hyperspectral Imaging Modalities,” *J. Biomech. Eng.*, vol. 140, no. 2, p. 020802, 2018.

[265] J. Juan-Colás, I. S. Hitchcock, M. Coles, S. Johnson, and T. F. Krauss, “Quantifying single-cell secretion in real time using resonant hyperspectral imaging,” *Proc. Natl. Acad. Sci.*, vol. 115, no. 52, pp. 13204–13209, 2018.

[266] G. Lu and B. Fei, “Medical hyperspectral imaging: a review,” *J. Biomed. Opt.*, vol. 19, no. 1, p. 010901, 2014.

[267] G. Lu, L. Halig, D. Wang, X. Qin, Z. G. Chen, and B. Fei, “Spectral-spatial classification for noninvasive cancer detection using hyperspectral imaging,” *J. Biomed. Opt.*, vol. 19,

no. 10, p. 106004, 2014.

[268] A. Mahadevan-Jansen, “Raman spectroscopy for the detection of cancers and precancers,” *J. Biomed. Opt.*, vol. 1, no. 1, p. 31, 1996.

[269] R. Smith, K. L. Wright, and L. Ashton, “Raman spectroscopy: an evolving technique for live cell studies,” *Analyst*, vol. 141, no. 12, pp. 3590–3600, 2016.

[270] A. S. Kashani, K. Kuruvinashetti, D. Beauet, S. Badilescu, A. Piekny, and M. Packirisamy, “Enhanced Internalization of Indian Ayurvedic Swarna Bhasma (Gold Nanopowder) for Effective Interaction with Human Cells,” *J. Nanosci. Nanotechnol.*, vol. 18, no. 10, pp. 6791–6798, Oct. 2018.

[271] E. D. SoRelle, O. Liba, J. L. Campbell, R. Dalal, C. L. Zavaleta, and A. de la Zerda, “A hyperspectral method to assay the microphysiological fates of nanomaterials in histological samples,” *Elife*, vol. 5, Aug. 2016.

[272] J. F. L. Duval, R. M. Town, and H. P. Van Leeuwen, “Poisson-Boltzmann Electrostatics and Ionic Partition Equilibration of Charged Nanoparticles in Aqueous Media,” *J. Phys. Chem. C*, vol. 122, no. 30, pp. 17328–17337, Aug. 2018.

[273] L. Xiao and E. S. Yeung, “Optical Imaging of Individual Plasmonic Nanoparticles in Biological Samples,” *Annu. Rev. Anal. Chem.*, vol. 7, no. 1, pp. 89–111, Jun. 2014.

[274] N. Fairbairn, A. Christofidou, A. G. Kanaras, T. A. Newman, and O. L. Muskens, “Hyperspectral darkfield microscopy of single hollow gold nanoparticles for biomedical applications,” *Phys. Chem. Chem. Phys.*, vol. 15, no. 12, pp. 4163–4168, Mar. 2013.

[275] K. A. Willets and R. P. Van Duyne, “Localized Surface Plasmon Resonance Spectroscopy and Sensing,” *Annu. Rev. Phys. Chem.*, vol. 58, no. 1, pp. 267–297, 2007.

[276] A. Dmitriev, *Nanoplasmonic Sensors*. New York, NY: Springer New York, 2012.

[277] T. N. G. Adams, P. A. Turner, A. V Janorkar, F. Zhao, and A. R. Minerick, “Characterizing the dielectric properties of human mesenchymal stem cells and the effects of charged elastin-like polypeptide copolymer treatment,” *Biomicrofluidics*, vol. 8, no. 5, pp. 1–14, 2014.

[278] L. Guo, J. A. Jackman, H.-H. Yang, P. Chen, N.-J. Cho, and D.-H. Kim, “Strategies for enhancing the sensitivity of plasmonic nanosensors,” *Nano Today*, vol. 10, no. 2, pp. 213–239, Apr. 2015.

[279] F. X. Theillet *et al.*, “Physicochemical properties of cells and their effects on intrinsically disordered proteins (IDPs),” *Chem. Rev.*, vol. 114, no. 13, pp. 6661–6714, 2014.

[280] D. K. Sasmal, S. Ghosh, A. K. Das, and K. Bhattacharyya, “Solvation dynamics of biological water in a single live cell under a confocal microscope,” *Langmuir*, vol. 29, no. 7, pp. 2289–2298, 2013.

[281] G. Lilley, M. Messner, and K. Unterrainer, “Improving the quality factor of the localized surface plasmon resonance,” *Opt. Mater. Express*, vol. 5, no. 10, p. 2112, Oct. 2015.

[282] P. Johns, G. Beane, K. Yu, and G. V. Hartland, “Dynamics of Surface Plasmon Polaritons in Metal Nanowires,” *J. Phys. Chem. C*, vol. 121, no. 10, pp. 5445–5459, Mar. 2017.

[283] G. V. Hartland, “Optical studies of dynamics in noble metal nanostructures,” *Chemical Reviews*, vol. 111, no. 6. pp. 3858–3887, 08-Jun-2011.

[284] M. Hu *et al.*, “Dark-field microscopy studies of single metal nanoparticles: Understanding the factors that influence the linewidth of the localized surface plasmon resonance,” *J. Mater. Chem.*, vol. 18, no. 17, pp. 1949–1960, 2008.

[285] M. Mehling and S. Tay, “Microfluidic cell culture,” *Curr. Opin. Biotechnol.*, vol. 25, pp. 95–102, 2014.

[286] D. Mark, S. Haeberle, G. Roth, F. von Stetten, and R. Zengerle, “Microfluidic lab-on-a-chip platforms: requirements, characteristics and applications,” *Chem. Soc. Rev.*, vol. 39, no. 3, p. 1153, 2010.

[287] H. Yun, K. Kim, and W. G. Lee, “Cell manipulation in microfluidics,” *Biofabrication*, vol. 5, no. 2, p. 22001, 2013.

[288] A. Karimi, S. Yazdi, and A. M. Ardekani, “Hydrodynamic mechanisms of cell and particle trapping in microfluidics,” *Biomicrofluidics*, vol. 7, no. 2, p. 021501, Mar. 2013.

[289] M. A. M. Ali, K. K. Ostrikov, F. A. Khalid, B. Y. Majlis, and A. A. Kayani, “Active

bioparticle manipulation in microfluidic systems," *RSC Adv.*, vol. 6, no. 114, pp. 113066–113094, 2016.

[290] Z. H. Fan, *Circulating Tumor Cells: isolation and analysis*, vol. 184. John Wiley & Sons, 2016.

[291] A. H. J. Yang, S. D. Moore, B. S. Schmidt, M. Klug, M. Lipson, and D. Erickson, "Optical manipulation of nanoparticles and biomolecules in sub-wavelength slot waveguides," *Nature*, vol. 457, no. 7225, p. 71, 2009.

[292] C. Zhang, K. Khoshmanesh, A. Mitchell, and K. Kalantar-zadeh, "Dielectrophoresis for manipulation of micro/nano particles in microfluidic systems," *Anal. Bioanal. Chem.*, vol. 396, no. 1, pp. 401–420, 2010.

[293] J. H. Kang, S. Krause, H. Tobin, A. Mammoto, M. Kanapathipillai, and D. E. Ingber, "A combined micromagnetic-microfluidic device for rapid capture and culture of rare circulating tumor cells," *Lab Chip*, vol. 12, no. 12, pp. 2175–2181, 2012.

[294] X. Ding *et al.*, "On-chip manipulation of single microparticles, cells, and organisms using surface acoustic waves," *Proc. Natl. Acad. Sci.*, vol. 109, no. 28, pp. 11105–11109, 2012.

[295] M. Ghanbari, A. S. Nezhad, C. G. Agudelo, M. Packirisamy, and A. Geitmann, "Microfluidic positioning of pollen grains in lab-on-a-chip for single cell analysis," *J. Biosci. Bioeng.*, vol. 117, no. 4, pp. 504–511, 2014.

[296] I. Kumano, K. Hosoda, H. Suzuki, K. Hirata, and T. Yomo, "Hydrodynamic trapping of Tetrahymena thermophila for the long-term monitoring of cell behaviors," *Lab Chip*, vol. 12, no. 18, pp. 3451–3457, 2012.

[297] M. Tanyeri and C. M. Schroeder, "Manipulation and confinement of single particles using fluid flow," *Nano Lett.*, vol. 13, no. 6, pp. 2357–2364, 2013.

[298] X. Xu, Z. Li, and A. Nehorai, "Finite element simulations of hydrodynamic trapping in microfluidic particle-trap array systems," *Biomicrofluidics*, vol. 7, no. 5, p. 54108, 2013.

[299] M. Tanyeri, M. Ranka, N. Sittipolkul, and C. M. Schroeder, "A microfluidic-based hydrodynamic trap: design and implementation," *Lab Chip*, vol. 11, no. 10, pp. 1786–

1794, 2011.

[300] W.-H. Tan and S. Takeuchi, “A trap-and-release integrated microfluidic system for dynamic microarray applications,” *Proc. Natl. Acad. Sci.*, vol. 104, no. 4, pp. 1146–1151, 2007.

[301] D. Di Carlo, L. Y. Wu, and L. P. Lee, “Dynamic single cell culture array,” *Lab Chip*, vol. 6, no. 11, pp. 1445–1449, 2006.

[302] A. Guan, A. Shenoy, R. Smith, and Z. Li, “Streamline based design guideline for deterministic microfluidic hydrodynamic single cell traps,” *Biomicrofluidics*, vol. 9, no. 2, p. 24103, 2015.

[303] A. A. Nawaz *et al.*, “Sub-micrometer-precision, three-dimensional (3D) hydrodynamic focusing via ‘microfluidic drifting,’” *Lab Chip*, vol. 14, no. 2, pp. 415–423, 2014.

[304] M. Akbari, D. Sinton, and M. Bahrami, “Viscous flow in variable cross-section microchannels of arbitrary shapes,” *Int. J. Heat Mass Transf.*, vol. 54, no. 17–18, pp. 3970–3978, 2011.

[305] M. J. Fuerstman, A. Lai, M. E. Thurlow, S. S. Shevkoplyas, H. A. Stone, and G. M. Whitesides, “The pressure drop along rectangular microchannels containing bubbles,” *Lab Chip*, vol. 7, no. 11, pp. 1479–1489, 2007.

[306] A. Ahmad Khalili, M. R. Ahmad, M. Takeuchi, M. Nakajima, Y. Hasegawa, and R. Mohamed Zulkifli, “A microfluidic device for hydrodynamic trapping and manipulation platform of a single biological cell,” *Appl. Sci.*, vol. 6, no. 2, p. 40, 2016.

[307] H. Bruus, *Theoretical microfluidics. oxford master series in condensed matter physics*. Oxford University Press, 2007.

[308] M. J. Rhodes and M. Rhodes, *Introduction to particle technology*. John Wiley & Sons, 2008.

[309] B. Ma, V. Ruwet, P. Corieri, R. Theunissen, M. Riethmuller, and C. Darquenne, “CFD simulation and experimental validation of fluid flow and particle transport in a model of alveolated airways,” *J. Aerosol Sci.*, vol. 40, no. 5, pp. 403–414, 2009.

[310] L.-S. Fan and C. Zhu, *Principles of gas-solid flows*. Cambridge University Press, 2005.

[311] T. A. Duncombe, A. M. Tentori, and A. E. Herr, "Microfluidics: reframing biological enquiry," *Nat. Rev. Mol. Cell Biol.*, vol. 16, no. 9, p. 554, 2015.

[312] Y. Zhou *et al.*, "A microfluidic platform for trapping, releasing and super-resolution imaging of single cells," *Sensors Actuators B Chem.*, vol. 232, pp. 680–691, 2016.

[313] A. S. Nezhad *et al.*, "Optimization of flow assisted entrapment of pollen grains in a microfluidic platform for tip growth analysis," *Biomed. Microdevices*, vol. 16, no. 1, pp. 23–33, 2013.

[314] J. Wang, J. Heo, and S. Z. Hua, "Spatially resolved shear distribution in microfluidic chip for studying force transduction mechanisms in cells," *Lab Chip*, vol. 10, no. 2, pp. 235–239, 2010.

[315] A. S. Kashani and M. Packirisamy, "Cellular deformation characterization of human breast cancer cells under hydrodynamic forces," *AIMS Biophys.*, vol. 4, no. 3, pp. 400–414, 2017.

[316] J. Shemesh, I. Jalilian, A. Shi, G. H. Yeoh, M. L. K. Tate, and M. E. Warkiani, "Flow-induced stress on adherent cells in microfluidic devices," *Lab Chip*, vol. 15, no. 21, pp. 4114–4127, 2015.

[317] T. J. Vaughan, M. G. Haugh, and L. M. McNamara, "A fluid–structure interaction model to characterize bone cell stimulation in parallel-plate flow chamber systems," *J. R. Soc. Interface*, vol. 10, no. 81, p. 20120900, Apr. 2013.

[318] Q. D. Tran, T. F. Kong, D. Hu, and R. H. W. Lam, "Deterministic sequential isolation of floating cancer cells under continuous flow," *Lab Chip*, vol. 16, no. 15, pp. 2813–2819, 2016.

[319] F. Yesilkoy *et al.*, "Highly efficient and gentle trapping of single cells in large microfluidic arrays for time-lapse experiments," *Biomicrofluidics*, vol. 10, no. 1, p. 14120, 2016.

[320] M. Martinelli and V. Viktorov, "Modelling of laminar flow in the inlet section of rectangular microchannels," *J. Micromechanics Microengineering*, vol. 19, no. 2, p. 025013, Feb. 2009.

[321] N. Sakamoto, “Responses of living cells to hydrodynamic stimuli due to fluid flow,” *Lect. Notes Comput. Vis. Biomech.*, vol. 12, pp. 165–180, 2014.

[322] W. Yao and G. H. Ding, “Interstitial fluid flow: Simulation of mechanical environment of cells in the interosseous membrane,” *Acta Mech. Sin. Xuebao*, vol. 27, no. 4, pp. 602–610, Aug. 2011.

[323] D. Brindley, K. Moorthy, J.-H. Lee, C. Mason, H.-W. Kim, and I. Wall, “Bioprocess forces and their impact on cell behavior: implications for bone regeneration therapy.,” *J. Tissue Eng.*, vol. 2011, p. 620247, 2011.

[324] R. Fan, T. Emery, Y. Zhang, Y. Xia, J. Sun, and J. Wan, “Circulatory shear flow alters the viability and proliferation of circulating colon cancer cells.,” *Sci. Rep.*, vol. 6, p. 27073, 2016.

[325] H. W. Hou, W. C. Lee, M. C. Leong, S. Sonam, S. R. K. Vedula, and C. T. Lim, “Microfluidics for applications in cell mechanics and mechanobiology,” *Cell. Mol. Bioeng.*, vol. 4, no. 4, pp. 591–602, 2011.

[326] E. A. Corbin, F. Kong, C. T. Lim, W. P. King, and R. Bashir, “Biophysical properties of human breast cancer cells measured using silicon MEMS resonators and atomic force microscopy,” *Lab Chip*, vol. 15, no. 3, pp. 839–847, 2015.

[327] J. G. McGarry, J. Klein-Nulend, M. G. Mullender, and P. J. Prendergast, “A comparison of strain and fluid shear stress in stimulating bone cell responses--a computational and experimental study.,” *FASEB J.*, vol. 19, no. 3, pp. 482–4, Mar. 2005.

[328] A. Ni, T. A. Cheema, and C. W. Park, “Numerical Study of RBC Motion and Deformation through Microcapillary in Alcohol Plasma Solution,” *Open J. Fluid Dyn.*, vol. 05, no. 01, pp. 26–33, 2015.

[329] M. J. Mitchell and M. R. King, “Computational and experimental models of cancer cell response to fluid shear stress.,” *Front. Oncol.*, vol. 3, p. 44, 2013.

[330] R. A. Foty, C. M. Pfleger, G. Forgacs, and M. S. Steinberg, “Surface tensions of embryonic tissues predict their mutual envelopment behavior,” *Development*, vol. 122, no. 5, pp. 1611–1620, 1996.

[331] Y. Ding, G.-K. Xu, and G.-F. Wang, “On the determination of elastic moduli of cells by AFM based indentation.,” *Sci. Rep.*, vol. 7, p. 45575, 2017.

[332] T. D. Brown, “Techniques for mechanical stimulation of cells in vitro: A review,” *Journal of Biomechanics*, vol. 33, no. 1. pp. 3–14, Jan-2000.

[333] F. K. Benra, H. J. Dohmen, J. Pei, S. Schuster, and B. Wan, “A comparison of one-way and two-way coupling methods for numerical analysis of fluid-structure interactions,” *J. Appl. Math.*, vol. 2011, 2011.

[334] S. Basak, A. Raman, and S. V. Garimella, “Hydrodynamic loading of microcantilevers vibrating in viscous fluids,” *J. Appl. Phys.*, vol. 99, no. 11, 2006.

[335] J. Guck *et al.*, “Optical deformability as an inherent cell marker for testing malignant transformation and metastatic competence,” *Biophys. J.*, vol. 88, no. 5, pp. 3689–3698, 2005.

[336] Z. Liu *et al.*, “Microfluidic cytometric analysis of cancer cell transportability and invasiveness,” *Sci. Rep.*, vol. 5, Sep. 2015.

[337] N. Caille, O. Thoumine, Y. Tardy, and J. J. Meister, “Contribution of the nucleus to the mechanical properties of endothelial cells,” *J. Biomech.*, vol. 35, no. 2, pp. 177–187, 2002.

[338] A. Geltmeier *et al.*, “Characterization of dynamic behaviour of MCF7 and MCF10A cells in ultrasonic field using modal and harmonic analyses,” *PLoS One*, vol. 10, no. 8, pp. 1–20, 2015.

[339] ANSYS, “ANSYS Mechanical APDL Theory Reference,” *ANSYS Inc*, vol. Release15, no. November, pp. 1–909, 2013.

[340] T. J. Vaughan, C. A. Mullen, S. W. Verbruggen, and L. M. McNamara, “Bone cell mechanosensation of fluid flow stimulation: a fluid–structure interaction model characterising the role integrin attachments and primary cilia,” *Biomech. Model. Mechanobiol.*, vol. 14, no. 4, pp. 703–718, Aug. 2015.

[341] N. W. Blackstone, “The Cell: A Molecular Approach . Seventh Edition. By Geoffrey M. Cooper and Robert E. Hausman. Sunderland (Massachusetts): Sinauer Associates.

$155.95. xxv + 832 p.; ill.; index. ISBN: 978-1-60535-290-9. [A companion website is available.] 2016.," *Q. Rev. Biol.*, vol. 92, no. 2, pp. 202–202, Jun. 2017.

[342] and W. G. J. Tracey A. Martin, Lin Ye, Andrew J. Sanders, Jane Lane, *Cancer Invasion and Metastasis: Molecular and Cellular Perpective*. 2000.

[343] A. V. Nguyen *et al.*, "Differential Contributions of Actin and Myosin to the Physical Phenotypes and Invasion of Pancreatic Cancer Cells," *Cell. Mol. Bioeng.*, 2019.

[344] S. Yadav, M. J. Barton, and N.-T. Nguyen, "Biophysical properties of cells for cancer diagnosis," *J. Biomech.*, vol. 86, no. February, pp. 1–7, Mar. 2019.

[345] N. I. Nikolaev, T. Müller, D. J. Williams, and Y. Liu, "Changes in the stiffness of human mesenchymal stem cells with the progress of cell death as measured by atomic force microscopy," *J. Biomech.*, vol. 47, no. 3, pp. 625–630, 2014.

[346] M. Lekka, "Discrimination Between Normal and Cancerous Cells Using AFM," *Bionanoscience*, vol. 6, no. 1, pp. 65–80, 2016.

[347] J. A. Belgodere, C. T. King, J. B. Bursavich, M. E. Burow, E. C. Martin, and J. P. Jung, "Engineering Breast Cancer Microenvironments and 3D Bioprinting," *Front. Bioeng. Biotechnol.*, vol. 6, no. MAY, May 2018.

[348] P. S. Steeg, "Targeting metastasis," *Nat. Rev. Cancer*, vol. 16, no. 4, pp. 201–218, Apr. 2016.

[349] S. Valastyan and R. A. Weinberg, "Tumor metastasis: Molecular insights and evolving paradigms," *Cell*, vol. 147, no. 2, pp. 275–292, 2011.

[350] R. Omidvar, M. Tafazzoli-shadpour, M. A. Shokrgozar, and M. Rostami, "Atomic force microscope-based single cell force spectroscopy of breast cancer cell lines: An approach for evaluating cellular invasion," *J. Biomech.*, vol. 47, no. 13, pp. 3373–3379, 2014.

[351] M. Prabhune, G. Belge, A. Dotzauer, J. Bullerdiek, and M. Radmacher, "Comparison of mechanical properties of normal and malignant thyroid cells," *Micron*, vol. 43, no. 12, pp. 1267–1272, 2012.

[352] N. Zuela-Sopilniak and J. Lammerding, "Engineering approaches to studying cancer cell

migration in three-dimensional environments," *Philos. Trans. R. Soc. B Biol. Sci.*, vol. 374, no. 1779, p. 20180219, Aug. 2019.

[353] C. Alibert, B. Goud, and J.-B. Manneville, "Are cancer cells really softer than normal cells?," *Biol. Cell*, vol. 109, no. 5, pp. 167–189, May 2017.

[354] V. Palmieri *et al.*, "Biomechanical investigation of colorectal cancer cells," *Appl. Phys. Lett.*, vol. 105, no. 12, 2014.

[355] L. Bastatas *et al.*, "AFM nano-mechanics and calcium dynamics of prostate cancer cells with distinct metastatic potential," *Biochim. Biophys. Acta - Gen. Subj.*, vol. 1820, no. 7, pp. 1111–1120, 2012.

[356] T. H. Kim *et al.*, "Cancer cells become less deformable and more invasive with activation of β-adrenergic signaling," *J. Cell Sci.*, vol. 129, no. 24, pp. 4563–4575, 2016.

[357] C. T. Mierke, *Physics of Cancer*. IOP Publishing, 2015.

[358] C. Zhu, G. Bao, and N. Wang, "Cell Mechanics: Mechanical Response, Cell Adhesion, and Molecular Deformation," *Annu. Rev. Biomed. Eng.*, vol. 2, no. 1, pp. 189–226, 2000.

[359] S. Brayford, G. Schevzov, J. Vos, and P. Gunning, "The Role of the Actin Cytoskeleton in Cancer and Its Potential Use as a Therapeutic Target," in *The Cytoskeleton in Health and Disease*, New York, NY: Springer New York, 2015, pp. 373–391.

[360] J. Ren, H. Huang, Y. Liu, X. Zheng, and Q. Zou, "An atomic force microscope study revealed two mechanisms in the effect of anticancer drugs on rate-dependent Young's modulus of human prostate cancer cells," *PLoS One*, vol. 10, no. 5, May 2015.

[361] N. Guz, M. Dokukin, V. Kalaparthi, and I. Sokolov, "If Cell Mechanics Can Be Described by Elastic Modulus: Study of Different Models and Probes Used in Indentation Experiments," *Biophys. J.*, vol. 107, no. 3, pp. 564–575, Aug. 2014.

[362] J. R. Lange and B. Fabry, "Cell and tissue mechanics in cell migration," *Exp. Cell Res.*, vol. 319, no. 16, pp. 2418–2423, Oct. 2013.

[363] X. Liu, D. A. Vargas, D. Lü, Y. Zhang, M. H. Zaman, and M. Long, "Computational modeling of stem cell migration: A mini review," *Cell. Mol. Bioeng.*, vol. 7, no. 2, pp.

196–204, 2014.

[364] O. Jonas, C. T. Mierke, and J. A. Käs, “Invasive cancer cell lines exhibit biomechanical properties that are distinct from their noninvasive counterparts,” *Soft Matter*, vol. 7, no. 24, pp. 11488–11495, Dec. 2011.

[365] C. R. Justus, N. Leffler, M. Ruiz-Echevarria, and L. V. Yang, “In vitro cell migration and invasion assays,” *J. Vis. Exp.*, no. 88, Jun. 2014.

[366] C.-P. Spatarelu *et al.*, “Biomechanics of Collective Cell Migration in Cancer Progression: Experimental and Computational Methods,” *ACS Biomater. Sci. Eng.*, vol. 5, no. 8, pp. 3766–3787, Aug. 2019.

[367] N. V Krakhmal, M. V Zavyalova, E. V Denisov, S. V Vtorushin, and V. M. Perelmuter, “Cancer Invasion: Patterns and Mechanisms,” *Acta Naturae*, vol. 7, no. 2, pp. 17–28, Jun. 2015.

[368] G. Weder *et al.*, “Increased plasticity of the stiffness of melanoma cells correlates with their acquisition of metastatic properties,” *Nanomedicine Nanotechnology, Biol. Med.*, vol. 10, no. 1, pp. 141–148, Jan. 2014.

[369] M. Pachenari, S. M. Seyedpour, M. Janmaleki, S. B. Shayan, S. Taranejoo, and H. Hosseinkhani, “Mechanical properties of cancer cytoskeleton depend on actin filaments to microtubules content: Investigating different grades of colon cancer cell lines,” *J. Biomech.*, vol. 47, no. 2, pp. 373–379, Jan. 2014.

[370] L. M. Rebelo, J. S. de Sousa, J. Mendes Filho, and M. Radmacher, “Comparison of the viscoelastic properties of cells from different kidney cancer phenotypes measured with atomic force microscopy.,” *Nanotechnology*, vol. 24, no. 5, p. 055102, Feb. 2013.

[371] J. R. Ramos, J. Pabijan, R. Garcia, and M. Lekka, “The softening of human bladder cancer cells happens at an early stage of the malignancy process,” *Beilstein J. Nanotechnol.*, vol. 5, no. 1, pp. 447–457, 2014.

[372] M. E. Grady, R. J. Composto, and D. M. Eckmann, “Cell elasticity with altered cytoskeletal architectures across multiple cell types,” *J. Mech. Behav. Biomed. Mater.*, vol. 61, pp. 197–207, Aug. 2016.

[373] A. N. Ketene, E. M. Schmelz, P. C. Roberts, and M. Agah, “The effects of cancer progression on the viscoelasticity of ovarian cell cytoskeleton structures.,” *Nanomedicine*, vol. 8, no. 1, pp. 93–102, Jan. 2012.

[374] S. Park, D. Koch, R. Cardenas, J. Kas, and C. K. Shin, “Cell motility and local viscoelasticity of fibroblasts,” *Biophys. J.*, vol. 89, no. 6, pp. 4330–4342, Dec. 2005.

[375] J. Lammerding, “Mechanics of the nucleus,” *Compr. Physiol.*, vol. 1, no. 2, pp. 783–807, 2011.

[376] H. Liu *et al.*, “In situ mechanical characterization of the cell nucleus by atomic force microscopy,” *ACS Nano*, vol. 8, no. 4, pp. 3821–3828, 2014.

[377] M. Murrell, P. W. Oakes, M. Lenz, and M. L. Gardel, “Forcing cells into shape: the mechanics of actomyosin contractility,” *Nat. Rev. Mol. cell Biol.*, vol. 16, no. 8, p. 486, 2015.

[378] E. Moeendarbary and A. R. Harris, “Cell mechanics: Principles, practices, and prospects,” *Wiley Interdiscip. Rev. Syst. Biol. Med.*, vol. 6, no. 5, pp. 371–388, 2014.

[379] J. P. Butler, I. M. Toli-Nørrelykke, B. Fabry, and J. J. Fredberg, “Traction fields, moments, and strain energy that cells exert on their surroundings,” *Am. J. Physiol. - Cell Physiol.*, vol. 282, no. 3 51-3, pp. 595–605, 2002.

[380] A. Agosti, D. Ambrosi, and S. Turzi, “Strain energy storage and dissipation rate in active cell mechanics,” *Phys. Rev. E*, vol. 97, no. 5, pp. 1–6, 2018.

[381] E. Spedden and C. Staii, “Neuron biomechanics probed by atomic force microscopy,” *Int. J. Mol. Sci.*, vol. 14, no. 8, pp. 16124–16140, 2013.

[382] R. Zielinski, C. Mihai, D. Kniss, and S. N. Ghadiali, “Finite Element Analysis of Traction Force Microscopy: Influence of Cell Mechanics, Adhesion, and Morphology,” *J. Biomech. Eng.*, vol. 135, no. 7, p. 071009, 2013.

[383] R. Ananthakrishnan and A. Ehrlicher, “The forces behind cell movement,” *International Journal of Biological Sciences*, vol. 3, no. 5. pp. 303–317, 2007.

[384] G. Jacquemet, H. Hamidi, and J. Ivaska, “Filopodia in cell adhesion, 3D migration and

cancer cell invasion," *Current Opinion in Cell Biology*, vol. 36. Elsevier Ltd, pp. 23–31, 01-Oct-2015.

[385] C. M. Lo, H. B. Wang, M. Dembo, and Y. L. Wang, "Cell movement is guided by the rigidity of the substrate," *Biophys. J.*, vol. 79, no. 1, pp. 144–152, 2000.

[386] S. E. Reid *et al.*, "Tumor matrix stiffness promotes metastatic cancer cell interaction with the endothelium," *EMBO J.*, vol. 36, no. 16, pp. 2373–2389, Aug. 2017.

[387] F. Bordeleau *et al.*, "Matrix stiffening promotes a tumor vasculature phenotype," *Proc. Natl. Acad. Sci. U. S. A.*, vol. 114, no. 3, pp. 492–497, 2017.

[388] E. A. Corbin, F. Kong, C. T. Lim, W. P. King, and R. Bashir, "Biophysical properties of human breast cancer cells measured using silicon MEMS resonators and atomic force microscopy," *Lab Chip*, vol. 15, no. 3, pp. 839–847, 2015.

[389] J. R. Lange and B. Fabry, "Cell and tissue mechanics in cell migration," *Exp. Cell Res.*, vol. 319, no. 16, pp. 2418–2423, 2013.

[390] A. J. S. Ribeiro, P. Khanna, A. Sukumar, C. Dong, and K. N. Dahl, "Nuclear Stiffening Inhibits Migration of Invasive Melanoma Cells," *Cell. Mol. Bioeng.*, vol. 7, no. 4, pp. 544–551, 2014.

[391] M. R. Zanotelli, F. Bordeleau, and C. A. Reinhart-King, "Subcellular regulation of cancer cell mechanics," *Curr. Opin. Biomed. Eng.*, vol. 1, pp. 8–14, 2017.

[392] P. Katira, R. T. Bonnecaze, and M. H. Zaman, "Modeling the Mechanics of Cancer: Effect of Changes in Cellular and Extra-Cellular Mechanical Properties," *Front. Oncol.*, vol. 3, no. June, pp. 1–7, 2013.

[393] J. I. Lopez, J. K. Mouw, and V. M. Weaver, "Biomechanical regulation of cell orientation and fate," *Oncogene*, vol. 27, no. 55, pp. 6981–6993, 2008.

[394] D. Peer, J. M. Karp, S. Hong, O. C. Farokhzad, R. Margalit, and R. Langer, "Nanocarriers as an emerging platform for cancer therapy," *Nat. Nanotechnol.*, vol. 2, no. 12, pp. 751–760, 2007.

[395] T. Sun, Y. S. Zhang, B. Pang, D. C. Hyun, M. Yang, and Y. Xia, "Engineered

nanoparticles for drug delivery in cancer therapy," *Angew. Chemie Int. Ed.*, vol. 53, no. 46, pp. 12320–12364, 2014.

[396] C. D. Lawson and A. J. Ridley, "Rho GTPase signaling complexes in cell migration and invasion," *Journal of Cell Biology*, vol. 217, no. 2. pp. 447–457, 2018.

[397] J. Stricker, Y. Beckham, M. W. Davidson, and M. L. Gardel, "Myosin II-Mediated Focal Adhesion Maturation Is Tension Insensitive," *PLoS One*, vol. 8, no. 7, p. e70652, Jul. 2013.

[398] M. L. Gardel, I. C. Schneider, Y. Aratyn-Schaus, and C. M. Waterman, "Mechanical Integration of Actin and Adhesion Dynamics in Cell Migration," *Annu. Rev. Cell Dev. Biol.*, vol. 26, no. 1, pp. 315–333, Nov. 2010.

[399] J. Terzić, S. Grivennikov, E. Karin, and M. Karin, "Inflammation and Colon Cancer," *Gastroenterology*, vol. 138, no. 6, pp. 2101-2114.e5, May 2010.

[400] F. Bocci *et al.*, "Toward understanding cancer stem cell heterogeneity in the tumor microenvironment," *Proc. Natl. Acad. Sci. U. S. A.*, vol. 116, no. 1, pp. 148–157, Jan. 2019.

[401] C. L. Chaffer and R. A. Weinberg, "A perspective on cancer cell metastasis," *Science (80-.).*, vol. 331, no. 6024, pp. 1559–1564, Mar. 2011.

[402] E. A. Murphy *et al.*, "Nanoparticle-mediated drug delivery to tumor vasculature suppresses metastasis," *Proc. Natl. Acad. Sci. U. S. A.*, vol. 105, no. 27, pp. 9343–9348, Jul. 2008.

[403] J. A. Yang, H. T. Phan, S. Vaidya, and C. J. Murphy, "Nanovacuums: nanoparticle uptake and differential cellular migration on a carpet of nanoparticles," *Nano Lett.*, vol. 13, no. 5, pp. 2295–2302, 2013.

[404] J. R. Lange and B. Fabry, "Cell and tissue mechanics in cell migration," *Experimental Cell Research*, vol. 319, no. 16. Elsevier, pp. 2418–2423, 2013.

[405] M. F. Fournier, R. Sauser, D. Ambrosi, J. J. Meister, and A. B. Verkhovsky, "Force transmission in migrating cells," *J. Cell Biol.*, vol. 188, no. 2, pp. 287–297, 2010.

[406] R. Krishnan *et al.*, "Reinforcement versus fluidization in cytoskeletal

mechanoresponsiveness.," *PLoS One*, vol. 4, no. 5, p. e5486, May 2009.

[407] V. Swaminathan, K. Mythreye, E. Tim O'Brien, A. Berchuck, G. C. Blobe, and R. Superfine, "Mechanical Stiffness grades metastatic potential in patient tumor cells and in cancer cell lines," *Cancer Res.*, vol. 71, no. 15, pp. 5075–5080, 2011.

[408] K. Watanabe *et al.*, "A ROCK inhibitor permits survival of dissociated human embryonic stem cells," *Nat. Biotechnol.*, vol. 25, no. 6, pp. 681–686, Jun. 2007.

[409] R. Lévy and M. Maaloum, "Measuring the spring constant of atomic force microscope cantilevers: Thermal fluctuations and other methods," *Nanotechnology*, vol. 13, no. 1, pp. 33–37, 2002.

[410] H. Babahosseini, P. C. Roberts, E. M. Schmelz, and M. Agah, "Bioactive sphingolipid metabolites modulate ovarian cancer cell structural mechanics," *Integr. Biol. (United Kingdom)*, vol. 5, no. 11, pp. 1385–1392, 2013.

[411] F. Rico, P. Roca-Cusachs, N. Gavara, R. Farré, M. Rotger, and D. Navajas, "Probing mechanical properties of living cells by atomic force microscopy with blunted pyramidal cantilever tips," *Phys. Rev. E - Stat. Nonlinear, Soft Matter Phys.*, vol. 72, no. 2, pp. 1–10, 2005.

[412] A. Vinckier and G. Semenza, "Measuring elasticity of biological materials by atomic force microscopy," *FEBS Lett.*, vol. 430, no. 1–2, pp. 12–16, Jun. 1998.

[413] E. K. Dimitriadis, F. Horkay, J. Maresca, B. Kachar, and R. S. Chadwick, "Determination of elastic moduli of thin layers of soft material using the atomic force microscope," *Biophys. J.*, vol. 82, no. 5, pp. 2798–2810, 2002.

[414] H. Yuan, A. M. Fales, C. G. Khoury, J. Liu, and T. Vo-Dinh, "Spectral characterization and intracellular detection of Surface-Enhanced Raman Scattering (SERS)-encoded plasmonic gold nanostars," *J. Raman Spectrosc.*, vol. 44, no. 2, pp. 234–239, 2013.

[415] A. Ostróżka-Cieślik and B. Sarecka-Hujar, "The Use of Nanotechnology in Modern Pharmacotherapy," in *Multifunctional Systems for Combined Delivery, Biosensing and Diagnostics*, Elsevier, 2017, pp. 139–158.

[416] R. E. Messersmith, G. J. Nusz, and S. M. Reed, “Using the localized surface plasmon resonance of gold nanoparticles to monitor lipid membrane assembly and protein binding,” *J. Phys. Chem. C*, vol. 117, no. 50, pp. 26725–26733, 2013.

[417] J. E. N. Jonkman *et al.*, “Cell Adhesion & Migration An introduction to the wound healing assay using livecell microscopy An introduction to the wound healing assay using livecell microscopy,” *Cell Adhes. Migr.*, vol. 8, no. 5, pp. 440–451, 2014.

[418] A. Sohrabi Kashani and M. Packirisamy, “Efficient Low Shear Flow-based Trapping of Biological Entities,” *Sci. Rep.*, vol. 9, no. 1, p. 5511, 2019.

[419] Y. Jiang and K. T. Turner, “Measurement of the strength and range of adhesion using atomic force microscopy,” *Extrem. Mech. Lett.*, vol. 9, pp. 119–126, 2016.

[420] B. L. Bangasser *et al.*, “Shifting the optimal stiffness for cell migration,” *Nat. Commun.*, vol. 8, no. May, pp. 1–10, 2017.

[421] M. Suganuma *et al.*, “Biophysical Approach to Mechanisms of Cancer Prevention and Treatment with Green Tea Catechins,” *Molecules*, vol. 21, no. 11, p. 1566, Nov. 2016.

[422] S. Pyne, R. Bittman, and N. J. Pyne, “Sphingosine kinase inhibitors and cancer: Seeking the golden sword of hercules,” *Cancer Research*, vol. 71, no. 21. pp. 6576–6582, 2011.